Zofia Michalewska
Jerzy Nawrocki
Editors

Atlas of Swept Source Optical Coherence Tomography

Springer

Atlas of Swept Source Optical Coherence Tomography

Zofia Michalewska • Jerzy Nawrocki
Editors

Atlas of Swept Source Optical Coherence Tomography

Springer

Editors
Zofia Michalewska, MD, PhD
Jasne Blonia Ophthalmic Clinic
Lodz
Poland

Jerzy Nawrocki, MD, PhD
Jasne Blonia Ophthalmic Clinic
Lodz
Poland

ISBN 978-3-319-49839-3 ISBN 978-3-319-49840-9 (eBook)
DOI 10.1007/978-3-319-49840-9

Library of Congress Control Number: 2017933286

© Springer International Publishing AG 2017
This work is subject to copyright. All rights are reserved by the Publisher, whether the whole or part of the material is concerned, specifically the rights of translation, reprinting, reuse of illustrations, recitation, broadcasting, reproduction on microfilms or in any other physical way, and transmission or information storage and retrieval, electronic adaptation, computer software, or by similar or dissimilar methodology now known or hereafter developed.
The use of general descriptive names, registered names, trademarks, service marks, etc. in this publication does not imply, even in the absence of a specific statement, that such names are exempt from the relevant protective laws and regulations and therefore free for general use.
The publisher, the authors and the editors are safe to assume that the advice and information in this book are believed to be true and accurate at the date of publication. Neither the publisher nor the authors or the editors give a warranty, express or implied, with respect to the material contained herein or for any errors or omissions that may have been made. The publisher remains neutral with regard to jurisdictional claims in published maps and institutional affiliations.

Printed on acid-free paper

This Springer imprint is published by Springer Nature
The registered company is Springer International Publishing AG
The registered company address is: Gewerbestrasse 11, 6330 Cham, Switzerland

Preface

Ophthalmology is a unique specialty in medicine in which usually we can directly see the disease. But this was not enough for many generations of ophthalmologists who documented their observations with drawings. The first real step forward was the introduction of fundus photography and fluorescein angiography. This enabled better quality documentation and improved understanding of the diseases. Also histopathological examinations of the affected eye were an important source of knowledge about different pathologies.

The revolutionary introduction of time-domain optical coherence tomography (OCT) in the 1990s by James Fujimoto, David Huang, and Eric Swanson (Massachusetts Institute of Technology) with insights for their clinical ocular application by Carmen Puliafito (University of Southern California) and Joel Schuman (University of Pittsburgh) became a milestone for improvement in both examination and documentation of retinal diseases. The third generation of time-domain OCT (Stratus OCT, Zeiss, Oberkochen, Germany) rapidly became a standard of care worldwide. It was our pleasure to witness the progress in the field of imaging when we introduced the first commercially available spectral-domain OCT (SD-OCT) device (Copernicus, Optopol, Zawiercie, Poland) into our clinic in January 2006 and presented the first case series of patients examined with this device at the combined American Society of Retina Surgeons (ASRS)–European VitreoRetinal Society (EVRS) Meeting in Cannes in 2006 and published the first papers on commercially available SD-OCT in 2007.

Since that time, developments in the field have continued to accelerate. As early as 2008, Richard Spaide presented enhanced depth imaging OCT (EDI-OCT), which enabled visualization of the choroid. The high quality of the new SD-OCT devices made in vivo semi-histopathological examination of the eye possible.

SD-OCT had become a worldwide standard of care by the end of 2012 when a revolutionary swept-source OCT (SS-OCT) device was commercially introduced (DRI-OCT, Topcon, Tokyo, Japan). The new technology enabled us to achieve wider images of even higher quality and allowed simultaneous three-dimensional examination of the vitreous, retina, and choroid. When we switched to SS-OCT in our clinic, in January 2013, we did not expect that just 2 years later, in 2015, SS-OCT angiography (SS-OCTA) would emerge (Atlantis and, later, Triton, Topcon, Tokyo, Japan).

SS-OCT and SS-OCTA not only allowed us to see the retina, vitreous, and choroid in higher quality and with greater detail than ever before. It additionally enhanced our knowledge of many diseases and changed our point of view in many diagnostic challenges.

The chapters of this atlas present basic information on SS-OCT and SS-OCTA examination for many pathologies. The authors discuss the advantages (and occasional difficulties) of the emerging technologies and present beautiful images of their findings to assist the reader with research and interpretation of SS-OCT images. We also offer a glance into the future of this technology as currently being developed under the leadership of Jay Duker and James Fujimoto et al.

In this book, authors from three continents share with you their knowledge not only in retina diseases but also in glaucoma. We hope that by drawing attention to the importance of glaucoma in retinology, we are providing an additional interdisciplinary advantage.

It has been our honor, pleasure, and privilege to work with such a distinguished group of experts and Springer to produce this atlas. We hope that the atlas will offer new information on current technology, add to the knowledge of general ophthalmologists as well as retina specialists, and be a pleasure to read.

Lodz, Poland — Zofia Michalewska
Lodz, Poland — Jerzy Nawrocki

Contents

1 **Introduction to Swept Source OCT** 1
Zhenguo Wang, Charles Reisman, Jonathan Liu, and Kinpui Chan

2 **Clinical Applications and Advantages of Swept Source OCT** 9
Netan Choudhry and Michael J. Sinai

3 **Swept Source OCT Angiography in Different Diseases** 23
Ricardo Noguera Louzada, Eric M. Moult, Emily Cole, James G. Fujimoto, and Jay S. Duker

4 **Healthy Retinal Vasculature** 37
Mayss Al-Sheikh and SriniVas R. Sadda

5 **Swept Source OCT in Pseudodrusen** 43
Hideyasu Oh

6 ***En Face* Swept Source OCT Study of Neovascular Age-Related Macular Degeneration** 49
Ignacio Flores-Moreno, Luis Arias-Barquet, Jorge Ruiz-Medrano, José M. Ruiz-Moreno, and Josep M. Caminal

7 **Neovascular Age-Related Macular Degeneration Studied with Swept Source OCT** 57
Ignacio Flores-Moreno, Luis Arias-Barquet, Jorge Ruiz-Medrano, José M. Ruiz-Moreno, and Josep M. Caminal

8 **Pathological Myopia** 65
Atsushi Maeda, Takafumi Hirashima, and Hideyasu Oh

9 **Vitreomacular Traction Syndrome** 73
Zofia Michalewska and Jerzy Nawrocki

10 **Epiretinal Membranes** 87
Zofia Michalewska and Jerzy Nawrocki

11 **Swept Source OCT for Macular Hole Treated with the Inverted Internal Limiting Membrane Flap Technique** 97
Jerzy Nawrocki and Zofia Michalewska

12 **Diabetic Macular Edema** 115
Takafumi Hirashima, Masanori Hagihara, and Hideyasu Oh

13 **Swept Source OCT in Retinal Vein Occlusion** 129
Mayss Al-Sheikh and SriniVas R. Sadda

14 **Swept Source OCT of Choroidal Nevi** 135
Kunal K. Dansingani and K. Bailey Freund

15 Intraocular Tumors Using Swept Source OCT 139
Ignacio Flores-Moreno, Luis Arias-Barquet, Josep M. Caminal, Jorge Ruiz-Medrano, and José M. Ruiz-Moreno

16 Intraocular Inflammation 149
Roberto Gallego-Pinazo, Rosa Dolz-Marco, Enrique España-Gregori, and Alejandro Fonollosa

17 Central Serous Chorioretinopathy, Polypoidal Choroidal Vasculopathy, and Rare Cases Imaged with Swept Source OCT and SS-OCTA 159
Zofia Michalewska and Jerzy Nawrocki

18 Swept Source OCT and Glaucoma 167
Kaweh Mansouri, Kirsten Hoskens, and Robert N. Weinreb

Index 175

Contributors

Mayss Al-Sheikh, MD Doheny Image Reading Center, Doheny Eye Institute, Los Angeles, CA, USA

Luis Arias-Barquet, MD, PhD Ophthalmology Unit, Bellvitge University Hospital, Hospitalet de Llobregat, Barcelona, Spain

Josep M. Caminal, MD, PhD Bellvitge University Hospital, Hospitalet de Llobregat, Barcelona, Spain

Castilla La Mancha University, Albacete, Spain

Kinpui Chan, MD Topcon Advanced Biomedical Imaging Laboratory, Oakland, NJ, USA

Netan Choudhry, MD Vitreous Retina Macula Specialists of Toronto, Etobicoke, ON, Canada

Department of Ophthalmology and Vision Sciences, University of Toronto, Toronto, ON, Canada

Emily Cole, MD New England Eye Center, Tufts University School of Medicine, Boston, MA, USA

Kunal K. Dansingani, MA, FRCOphth Vitreous Retina Macula Consultants of New York, New York, NY, USA

Jay S. Duker, MD New England Eye Center, Tufts University School of Medicine, Boston, MA, USA

Rosa Dolz-Marco, MD, PhD Unit of Macula, Department of Ophthalmology, University and Polytechnic Hospital La Fe, Valencia, Spain

Enrique España-Gregori, MD Department of Ophthalmology, Faculty of Medicine, University of Valencia, Valencia, Spain

Ignacio Flores-Moreno, MD, PhD Clinico San Carlos University Hospital, Madrid, Spain

Bellvitge University Hospital, Hospitalet de Llobregat, Barcelona, Spain

Alejandro Fonollosa, MD, PhD Department of Ophthalmology, BioCruces Health Research Institute, Cruces University Hospital, Vizcaya, Spain

James G. Fujimoto, PhD Department of Electrical Engineering and Computer Science, and Research Laboratory of Electronics, Massachusetts Institute of Technology, Cambridge, MA, USA

K. Bailey Freund, MD Vitreous Retina Macula Consultants of New York, New York, NY, USA

Roberto Gallego-Pinazo, MD Unit of Macula, Department of Ophthalmology,

University and Polytechnic Hospital La Fe, Valencia, Spain

Masanori Hagihara, MD Department of Ophthalmology, Hyogo Prefectural Amagasaki General Medical Center (AGMC), Amagasaki, Hyogo, Japan

Takafumi Hirashima, MD Department of Ophthalmology, Hyogo Prefectural Amagasaki General Medical Center (AGMC), Amagasaki, Hyogo, Japan

Kirsten Hoskens Glaucoma Center, Montchoisi Clinic, Lausanne, Switzerland

Jonathan Liu, PhD Topcon Advanced Biomedical Imaging Laboratory, Oakland, NJ, USA

Ricardo Noguera Louzada, MD Department of Ophthalmology, Federal University of Goiás, Goiânia, Goiás, Brazil

New England Eye Center, Tufts University School of Medicine, Boston, MA, USA

Atsushi Maeda, MD Department of Ophthalmology, Hyogo Prefectural Amagasaki General Medical Center (AGMC), Amagasaki, Hyogo, Japan

Kaweh Mansouri, MD Glaucoma Center, Montchoisi Clinic, Lausanne, Switzerland

Zofia Michalewska, MD, PhD Jasne Blonia Ophthalmic Clinic, Lodz, Poland

Eric M. Moult Department of Electrical Engineering and Computer Science, and Research Laboratory of Electronics, Massachusetts Institute of Technology, Cambridge, MA, USA

Harvard MIT Department of Health Science and Technology, Cambridge, MA, USA

Jerzy Nawrocki, MD, PhD Jasne Blonia Ophthalmic Clinic, Lodz, Poland

Hideyasu Oh, MD, PhD Department of Ophthalmology, Hyogo Prefectural Amagasaki General Medical Center (AGMC), Amagasaki, Hyogo, Japan

Charles Reisman Topcon Advanced Biomedical Imaging Laboratory, Oakland, NJ, USA

Jorge Ruiz-Medrano, MD Clinico San Carlos University Hospital, Madrid, Spain

José M. Ruiz-Moreno, MD Castilla-La Mancha University, Albacete, Spain

SriniVas R. Sadda, MD Department of Ophthalmology, David Geffen School of Medicine, University of California, Los Angeles, CA, USA

Michael J. Sinai, PhD Chief Clinical Affairs, R and D Planning Division, Topcon Corporation, Tokyo, Japan

Zhenguo Wang, PhD Topcon Advanced Biomedical Imaging Laboratory, Oakland, NJ, USA

Robert N. Weinreb, MD Department of Ophthalmology, Hamilton Glaucoma Center and Shiley Eye Center, University of California, San Diego, La Jolla, CA, USA

Introduction to Swept Source OCT

1

Zhenguo Wang, Charles Reisman, Jonathan Liu, and Kinpui Chan

Optical coherence tomography (OCT), first introduced in 1991, is an enabling optical, noninvasive imaging modality that provides cross-sectional visualization of biological tissues with resolutions one to two orders of magnitude better than conventional ultrasound [1]. Because the eye is optically accessible for visible and near-infrared light, ophthalmic OCT has been the most successful clinical application from the invention of OCT with an unparalleled combination of axial resolution (1–10 μm) and penetration depth (1–2 mm in tissue). This chapter presents a brief introduction of OCT, including the early time-domain OCT (TD-OCT) and the more recent Fourier-domain OCT (FD-OCT), which can be characterized into the two forms of spectral-domain OCT (SD-OCT) and swept source OCT (SS-OCT). Since the commercial launch of SD-OCT in 2006 by multiple manufacturers, including the world's first Topcon 3D OCT-1000, the significant practical advantages of both higher speed and higher sensitivity of SD-OCT over TD-OCT [2–4] have led to a widespread use of OCT instruments in ophthalmology [5]. On the other hand, SS-OCT, which employs the state-of-the-art high-speed wavelength tuning laser (swept source) as well as digital data acquisition and processing technology, offers further advantages of overcoming the signal roll-off observed for SD-OCT at a deeper range along with an unprecedented A-scan rate for wider field-of-view structural OCT and OCT angiography imaging [6, 7]. With advances in commercial wavelength tuning lasers, the first clinical 1 μm SS-OCT machine, Topcon DRI OCT-1 Atlantis, became commercially available for retinal imaging in 2012 [8].

As shown in Fig. 1.1, OCT measures the optical backscattering profile (intensity and time of flight of backscattered light) along the axial direction (A-scan), analogous to measuring echoes of sound waves in conventional ultrasound imaging. A two-dimensional cross-sectional image (B-scan) is produced by transversely scanning the incident optical beam and performing sequential A-scans. Similarly, volumetric data sets can be generated by acquiring sequential B-scans along the transverse direction.

Since the speed of light is much higher than that of sound waves, it is very challenging, if not impossible, to directly measure the time of flight for backscattered light. Instead, OCT is based on low coherence interferometry to measure the time of flight indirectly from optical interference generated by mixing the backscattered light with light from a reference mirror. A Michelson interferometer is most commonly employed in OCT systems. Light from the broadband light source is divided by a beam splitter into the reference and sample arms. The reflected light from these two arms are recombined again through the beam splitter and detected with a photodetector. Depending on the method used to reconstruct the intensity and time of flight of backscattered light, there are two types of OCT techniques, namely TD-OCT and FD-OCT.

In a TD-OCT system, a moving mirror is placed in the reference arm, and a single photodetector is employed. As the reference mirror in an OCT system moves along the axial direction, a corresponding depth-dependent backscattering profile of the sample is acquired. The axial resolution of OCT is determined by the coherence length of the light source, while the imaging speed is determined by how fast the reference mirror moves. Due to the relatively slow speed of the mechanical reference mirror, the imaging speed of commercial ophthalmic TD-OCT has been limited to 400 A-scans per second [9].

To further increase the imaging speed and the sensitivity, SD-OCT based on a fast linear detector array was demonstrated for retinal imaging in vivo in the early 2000s [10]. In a SD-OCT system, the reference mirror is stationary instead of moving. The imaging speed is determined by the speed of the linear detector array, which can be higher than tens of thousands of A-scans per second [11], yielding a roughly 100× improvement over that achieved with TD-OCT

Z. Wang, PhD (✉) • C. Reisman • J. Liu • K. Chan
Topcon Advanced Biomedical Imaging Laboratory, Oakland, NJ, USA
e-mail: zwang@topcon.com

© Springer International Publishing AG 2017

Z. Michalewska, J. Nawrocki (eds.), *Atlas of Swept Source Optical Coherence Tomography*,
DOI 10.1007/978-3-319-49840-9_1

systems. SD-OCT detects the interferogram as a function of wavelength (λ), in contrast to the direct detection of backscattering profile as a function of depth position of the reference mirror in TD-OCT. As illustrated in Fig. 1.2, the depth information, more precisely the depth difference between the reference mirror and the sample, is encoded as the frequency of the interferogram fringes. When the depth of the sample is near to that of the reference mirror, the frequency of interferogram fringes is low (Fig. 1.2a). And when the depth of the sample is far from that of the reference mirror, the frequency of interferogram fringes is high (Fig. 1.2b). Light backscattered from different depths along the axial direction are detected simultaneously using a linear detector array (Fig. 1.2c). By performing a Fourier transform on the detected interferogram in wavenumber (k), an A-scan profile can be readily acquired.

The higher speed and sensitivity of SD-OCT [2–4] has enabled volumetric imaging with better image quality. On the other hand, SD-OCT is subject to a signal-to-noise ratio (SNR) roll-off characteristic that occurs in the FD-OCT technique. As shown in Fig. 1.3, it is commonly observed in SD-OCT that the reconstructed sample signal intensity gets weaker when it is farther from the zero-delay position.

This SNR roll-off is primarily caused by the limited capability of SD-OCT to resolve the interferogram fringes. In an SD-OCT system using a broadband light source such as a superluminescent diode (SLD), the interferogram is generated by the spectrometer in the detection arm, which spreads the light at different wavelengths to be recorded by a linear detector array. However, due to the finite number of pixels on the linear detector array, the light of different wavelengths that are very close to each other fall on the same pixel and gets digitized without distinction, as illustrated in Fig. 1.4.

As a consequence, the resolvability of interferogram fringes is degraded. Mathematically, this constitutes an integration effect of the interferogram over the continuous spectrum of the light source across each element of the linear detector array. In other words, the resolvability of the interferogram fringes is affected differently during detection depending on frequency. As shown in Fig. 1.3, the higher the fringe frequency is, the more it is attenuated and the weaker its amplitude becomes. Accordingly, after Fourier transform, the amplitude of the reconstructed signal will be depth dependent. It was reported that the SNR roll-off for SD-OCT can be as high as 15 dB/mm [12]. Considering the typical 2 mm imaging range for commercial ophthalmic OCT instrument, an SNR drop of up to 30 dB is very significant and it is not unusual that the lower end of the imaging range is practically unusable.

By eliminating the use of the spectrometer and the linear detector array, SS-OCT employs a rapid-wavelength tuning laser and high-speed photodetector and signal digitizer. SS-OCT thereby offers a significant solution to the limitation of spectrometer spectral resolution as seen in SD-OCT, and thus enables deeper range imaging without compromising the sensitivity at a deeper position caused by the above-mentioned SNR roll-off. As illustrated in Fig. 1.5, the instantaneous line width of the laser light source used in SS-OCT, rather than the finite pixel size of the linear detector array used in SD-OCT, primarily determines the resolvability of the interferogram fringes.

The instantaneous line width characterizes how pure the laser mode is at one particular moment while it is swept through a range of individual wavelengths. Ideally, the tuning laser is emitting light at a single wavelength at any given moment. In reality, the emitted light is typically composed of photons of more than one wavelength spanning across a certain range that is characterized as instantaneous line width. Such wavelength impurity affects the interferogram similarly as finite pixel size of linear detector array in SD-OCT and causes SNR roll-off as well. However, with the recent advances in laser technology, the commercial tuning lasers have dramatically improved instantaneous line width [12]. Therefore, the interferogram fringes can be well-resolved across the entire imaging range. The SNR roll-off in SS-OCT systems enabled by the latest vertical-cavity surface emitting lasers (VCSEL) is virtually zero within the imaging range of up to 50 mm [13].

In addition, SS-OCT is able to operate in the 1 μm wavelength range. Besides low water absorption and minimal depth-dependent dispersion [14], 1 μm wavelength OCT is less susceptible to scattering in tissue such as cataract and hemorrhage [15]. It can also better penetrate the retina pigment epithelium (RPE) and visualize deeper structures in the choroid layer and sclera [16, 17]. The practical benefits of 1 μm wavelength SS-OCT can be appreciated by comparing retinal images at different depths acquired with an 800 nm wavelength SD-OCT system (Topcon 3D OCT-2000) and a 1 μm wavelength SS-OCT system (Topcon DRI-OCT Triton), as shown in Fig. 1.6.

The capability to obtain images with high quality at any depth within the imaging range not only makes it easier for patients and medical practitioners to take OCT images, but also facilitates a large imaging range that is able to accommodate the curvature of eyeball. More importantly, 1 μm wavelength SS-OCT enhances visualization of previously obscured features together with the retina in the same image without sophisticated imaging processing, as shown in Fig. 1.7.

This has helped choroidal imaging, posterior vitreous visualization [18], and ophthalmic research in new frontiers [19–22]. The recent development of OCT angiography based on 1 μm wavelength SS-OCT also demonstrated functional imaging ability by visualizing the choriocapillaris and

choroidal microvasculature in vivo in normal human subjects [23].

The development of SS-OCT technology has enabled many attributes for a better clinical ophthalmic imaging instrument, including higher speed [6, 7, 12, 13], deeper imaging range with uniform sensitivity, reduced fringe washout [24], less light-scattering by cataract tissue, deeper penetration for better visualization of choroid and beyond [16, 25], invisibility of the scanning light for less distraction to patients during imaging, fewer motion artifacts, and potential for eventual miniaturization and cost-reduction [26]. Commercial SS-OCT development results were first presented by Topcon at ARVO 2010 [27]. Prototype Topcon SS-OCT instruments for clinical research soon followed [28, 29]. Topcon continues to lead in clinical SS-OCT technology with the latest generation DRI-OCT Triton, which incorporates color fundus photography, fluorescein angiography, and fundus autofluorescence imaging, together with combined anterior and posterior eye OCT as well as OCT angiography. Cutting-edge SS-OCT technology opens the possibility for a new generation of multimodal ophthalmic instruments to image the entire eye, measure axial eye length [13], and acquire intraoperative OCT [30]. While SD-OCT is currently still dominant in the ophthalmic market, SS-OCT is expected to continue to grow and increasingly contribute to the medical community in the near future.

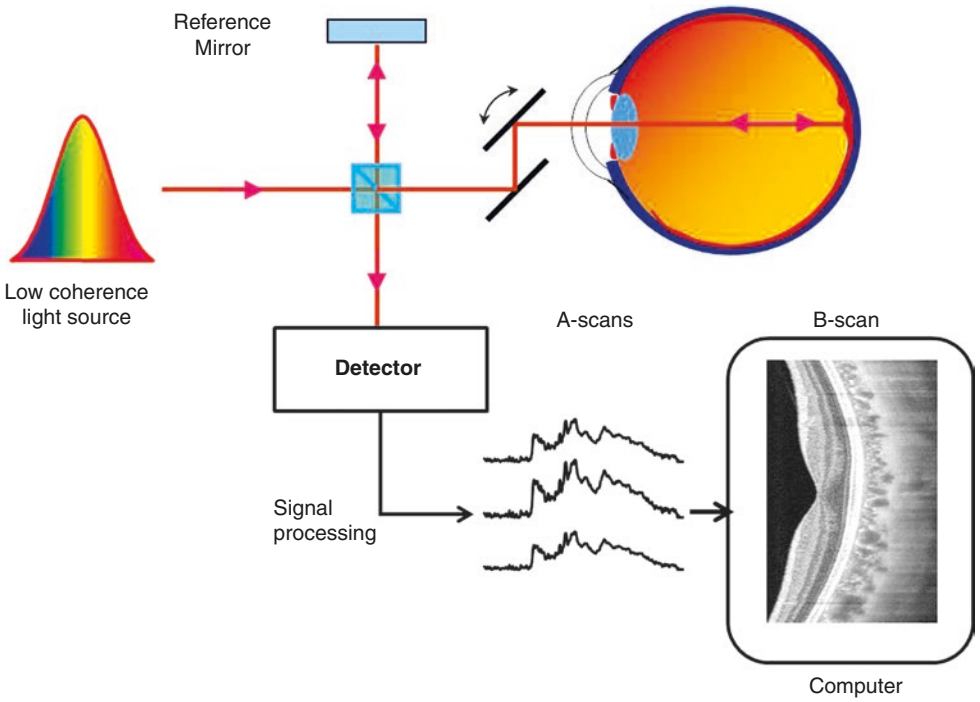

Fig. 1.1 Schematic of an OCT system based on low coherence interferometry using a Michelson interferometer design. Light from a broadband light source is divided by a beam splitter into the reference and sample arms. The reflected light from these two arms are recombined again through the beam splitter and detected with a photodetector. OCT images are produced by scanning the light in the sample arm to acquire sequential optical backscattering profiles along the axial direction. There are two types of OCT techniques, time-domain OCT (TD-OCT) and Fourier-domain OCT (FD-OCT), to reconstruct the intensity and time of flight of the backscattered light. In contrast to TD-OCT which uses a moving mirror in the reference arm, the reference mirror is stationary in FD-OCT, which includes spectral domain OCT and swept source OCT

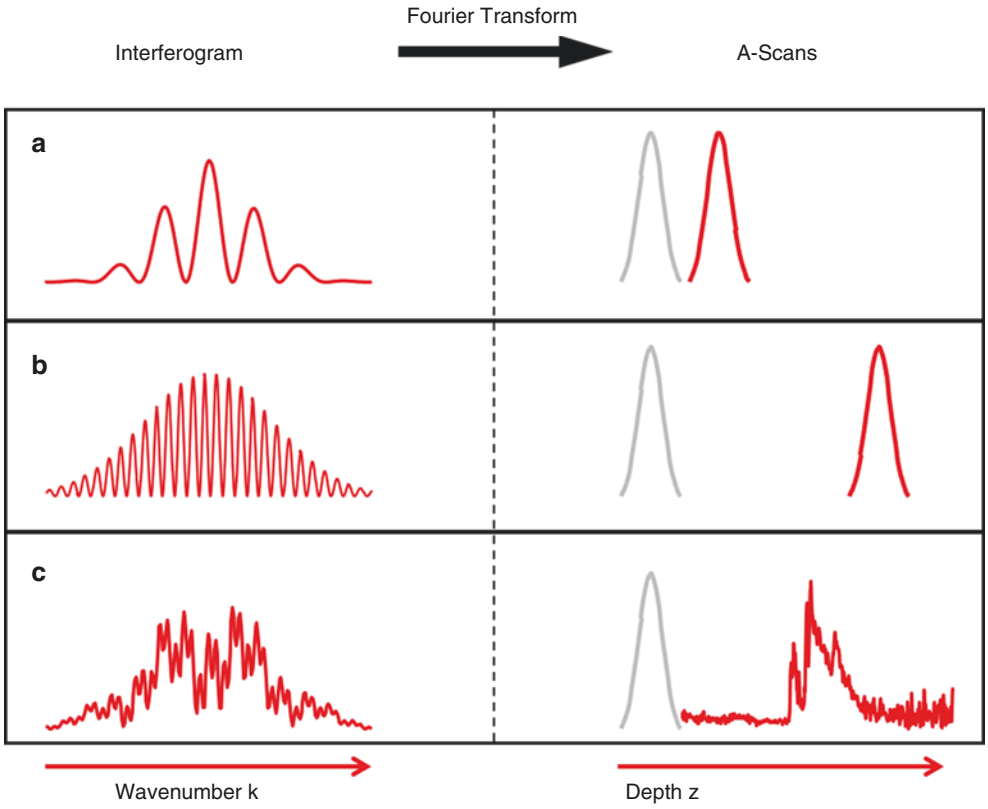

Fig. 1.2 Illustration of FD-OCT signal reconstruction. A-scans are generated by Fourier transforming the interferograms. (**a**) A low-frequency interferogram corresponds to a signal near the reference mirror. (**b**) A high-frequency interferogram corresponds to a signal far from the reference mirror. (**c**) OCT interferograms can have multiple frequency components comprised of signal from different depths as reconstructed in the A-scan profile

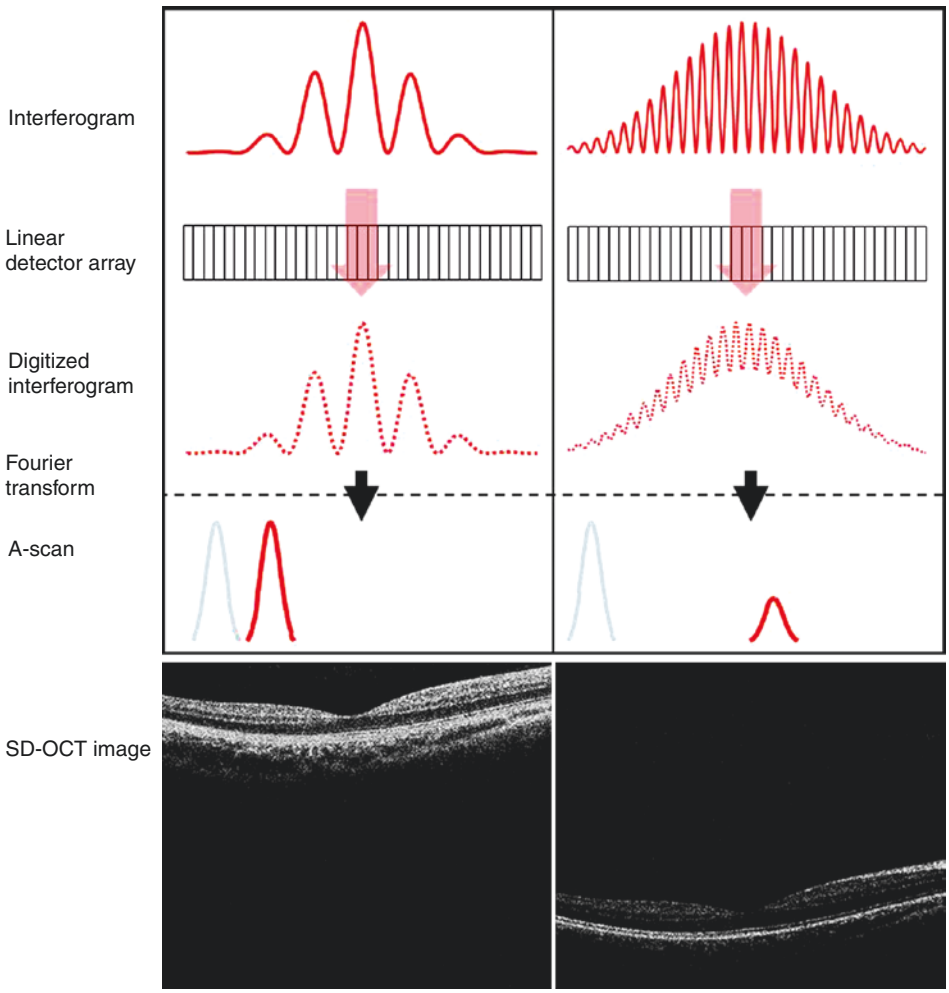

Fig. 1.3 Illustration of signal roll-off in SD-OCT. The spectral resolution of the interferograms is limited by the spectrometer linear detector array. Higher frequency interferograms suffer more signal attenuation. The amplitude of reconstructed A-scans is therefore depth-dependent in SD-OCT

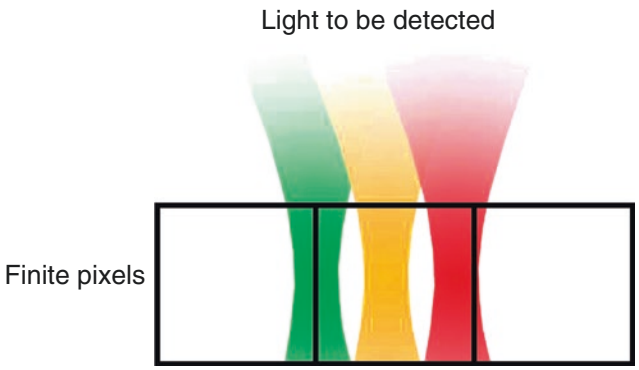

Fig. 1.4 Illustration of the limitation in resolvability of different wavelength light on finite pixels in a spectral domain OCT spectrometer

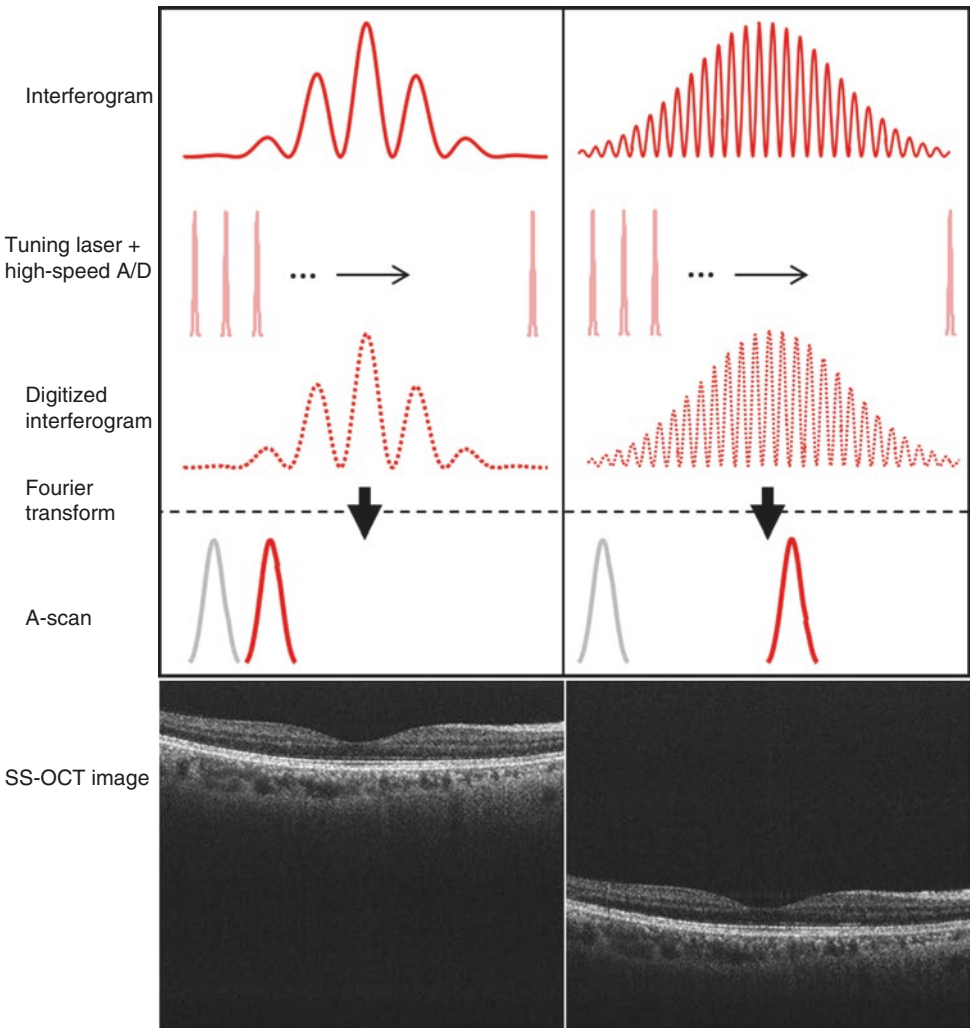

Fig. 1.5 Illustration of signal roll-off in SS-OCT. The tuning laser instantaneous line width and high-speed digitizer yields good resolvability of the interferograms. Higher frequency interferograms are well resolved without attenuation. The reconstructed A-scans therefore do not suffer from signal roll-off across the imaging range

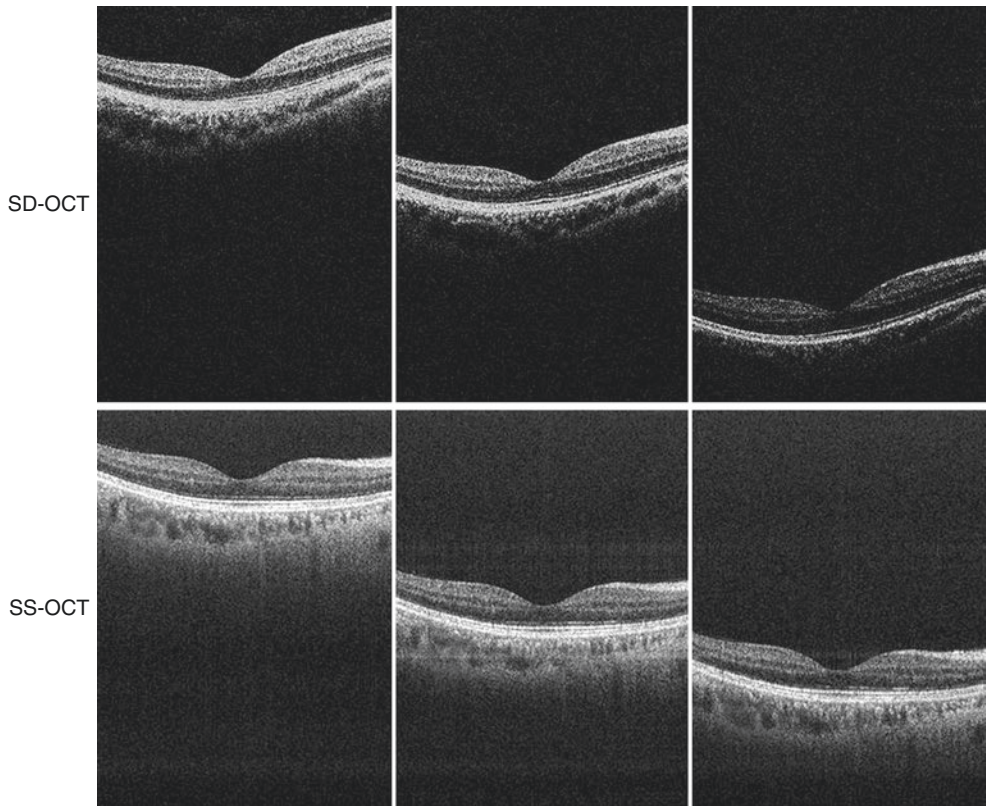

Fig. 1.6 Retinal images at different depths acquired with 800 nm wavelength SD-OCT and 1 μm wavelength SS-OCT. 1 μm wavelength SS-OCT not only can visualize deeper structures in the choroid and sclera, but is also capable of obtaining high-quality images at any depth within the imaging range

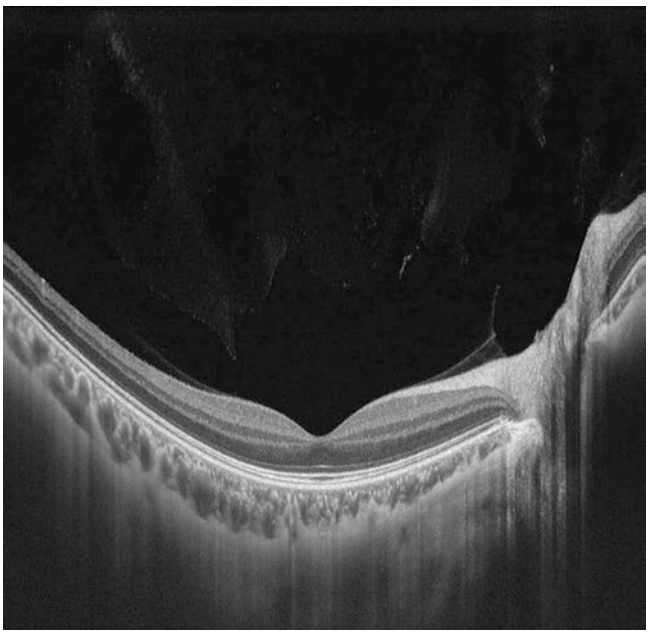

Fig. 1.7 1 μm wavelength SS-OCT enhances visualization of previously obscured features together with the retina in the same image without sophisticated imaging processing. The visibility of fine details in the vitreous, choroid, and sclera are enabled by 1 μm wavelength SS-OCT

References

1. Huang D, Swanson EA, Lin CP, Schuman JS, Stinson WG, Chang W, et al. Optical coherence tomography. Science. 1991;254(5035):1178–81.
2. Leitgeb R, Hitzenberger C, Fercher A. Performance of fourier domain vs. time domain optical coherence tomography. Opt Express. 2003;11(8):889–94.
3. De Boer JF, Cense B, Park BH, Pierce MC, Tearney GJ, Bouma BE. Improved signal-to-noise ratio in spectral-domain compared with time-domain optical coherence tomography. Opt Lett. 2003;28(21):2067–9.
4. Choma M et al. Sensitivity advantage of swept source and Fourier domain optical coherence tomography. Opt Express. 2003;11(18):2183–9.
5. Fujimoto J, Swanson E. The development, commercialization, and impact of optical coherence tomography. Invest Ophthalmol Vis Sci. 2016;57(9):OCT1–OCT13.
6. Klein T, Wieser W, Eigenwillig CM, Biedermann BR, Huber R. Megahertz OCT for ultrawide-field retinal imaging with a 1050 nm Fourier domain mode-locked laser. Opt Express. 2011;19(4):3044–62.
7. Klein T, Wieser W, Reznicek L, Neubauer A, Kampik A, Huber R. Multi-MHz retinal OCT. Biomed Opt Express. 2013;4(10):1890–908.
8. AAO New Product Report. Ophthalmology management. 2012;16:60–6. http://www.ophthalmologymanagement.com/articleviewer.aspx?articleID=107777.
9. Tearney GJ, Bouma BE, Fujimoto JG. High-speed phase- and group-delay scanning with a grating-based phase control delay line. Opt Lett. 1997;22(23):1811–3.
10. Wojtkowski M, Leitgeb R, Kowalczyk A, Bajraszewski T, Fercher AF. In vivo human retinal imaging by Fourier domain optical coherence tomography. J Biomed Opt. 2002;7(3):457–63.
11. Potsaid B, Gorczynska I, Srinivasan VJ, Chen Y, Jiang J, Cable A, et al. Ultrahigh speed spectral/Fourier domain OCT ophthalmic imaging at 70,000 to 312,500 axial scans per second. Opt Express. 2008;16(19):15149–69.
12. Potsaid B, Baumann B, Huang D, Barry S, Cable AE, Schuman JS, et al. Ultrahigh speed 1050 nm swept source/Fourier domain OCT retinal and anterior segment imaging at 100,000 to 400,000 axial scans per second. Opt Express. 2010;18(19):20029–48.
13. Grulkowski I, Liu JJ, Potsaid B, Jayaraman V, Lu CD, Jiang J, et al. Retinal, anterior segment and full eye imaging using ultrahigh speed swept source OCT with vertical-cavity surface emitting lasers. Biomed Opt Express. 2012;3(11):2733–51.
14. Wang Y, Nelson J, Chen Z, Reiser B, Chuck R, Windeler R. Optimal wavelength for ultrahigh-resolution optical coherence tomography. Opt Express. 2003;11(12):1411–7.
15. Esmaeelpour M, Povazay B, Hermann B, Hofer B, Kajic V, Kapoor K, et al. Three-dimensional 1060-nm OCT: choroidal thickness maps in normal subjects and improved posterior segment visualization in cataract patients. Invest Ophthalmol Vis Sci. 2010;51(10):5260–6.
16. Unterhuber A, Povazay B, Hermann B, Sattmann H, Chavez-Pirson A, Drexler W. In vivo retinal optical coherence tomography at 1040 nm-enhanced penetration into the choroid. Opt Express. 2005;13(9):3252–8.
17. Huber R, Adler DC, Srinivasan VJ, Fujimoto JG. Fourier domain mode locking at 1050 nm for ultra-high-speed optical coherence tomography of the human retina at 236,000 axial scans per second. Opt Lett. 2007;32(14):2049–51.
18. Spaide RF. Visualization of the posterior vitreous with dynamic focusing and windowed averaging swept source optical coherence tomography. Am J Ophthalmol. 2014;158(6):1267–74.
19. Spaide RF, Akiba M, Ohno-Matsui K. Evaluation of peripapillary intrachoroidal cavitation with swept source and enhanced depth imaging optical coherence tomography. Retina. 2012;32(6):1037–44.
20. Itakura H, Kishi S, Li D, Akiyama H. Observation of posterior precortical vitreous pocket using swept-source optical coherence tomography. Invest Ophthalmol Vis Sci. 2013;54(5):3102–7.
21. Stanga PE, Sala-Puigdollers A, Caputo S, Jaberansari H, Cien M, Gray J, et al. In vivo imaging of cortical vitreous using 1050-nm swept-source deep range imaging optical coherence tomography. Am J Ophthalmol. 2014;157(2):397–404.
22. Flores-Moreno I, Arias-Barquet L, Rubio-Caso MJ, Ruiz-Moreno JM, Duker JS, Caminal JM. En face swept-source optical coherence tomography in neovascular age-related macular degeneration. Br J Ophthalmol. 2015;99(9):1260–7.
23. Choi W, Mohler KJ, Potsaid B, Lu CD, Liu JJ, Jayaraman V, et al. Choriocapillaris and choroidal microvasculature imaging with ultrahigh speed OCT angiography. PLoS One. 2013;8(12):e81499.
24. Hendargo HC, McNabb RP, Dhalla AH, Shepherd N, Izatt JA. Doppler velocity detection limitations in spectrometer-based versus swept-source optical coherence tomography. Biomed Opt Express. 2011;2(8):2175–88.
25. Adhi M, Liu JJ, Qavi AH, Grulkowski I, Lu CD, Mohler KJ, et al. Choroidal analysis in healthy eyes using swept-source optical coherence tomography compared to spectral domain optical coherence tomography. Am J Ophthalmol. 2014;157(6):1272–81.
26. Wang Z, Lee HC, Vermeulen D, Chen L, Nielsen T, Park SY, et al. Silicon photonic integrated circuit swept-source optical coherence tomography receiver with dual polarization, dual balanced, in-phase and quadrature detection. Biomed Opt Express. 2015;6(7):2562–74.
27. Reisman CA, Yang Q, Wang Z, Tomidokoro A, Araie M, Hangai M, et al. Enhanced visualization and layer detection via averaging optical coherence tomography images. Invest Ophthalmol Vis Sci. 2010;51(13):3859. Presented at 2010 ARVO Annual Meeting.
28. Hirata M, Tsujikawa A, Matsumoto A, Hangai M, Ooto S, Yamashiro K, et al. Macular choroidal thickness and volume in normal subjects measured by swept-source optical coherence tomography. Invest Ophthalmol Vis Sci. 2011;52(8):4971–8.
29. Ohno-Matsui K, Akiba M, Moriyama M, Ishibashi T, Tokoro T, Spaide RF. Imaging retrobulbar subarachnoid space around optic nerve by swept-source optical coherence tomography in eyes with pathologic myopia. Invest Ophthalmol Vis Sci. 2011;52(13):9644–50.
30. Lu C, et al. Ultrahigh speed ophthalmic surgical OCT for intraoperative OCT angiography and widefield imaging. Invest Ophthalmol Vis Sci. 2016. Presented at 2016 ARVO Annual Meeting.

Clinical Applications and Advantages of Swept Source OCT

2

Netan Choudhry and Michael J. Sinai

The Topcon DRI Triton is an optical coherence tomographer (OCT) with a built-in color fundus camera. It utilizes swept source technology and has a central wavelength of 1050 nm. The scanning speed is 100 kHz and the depth resolution is 8 μm. It provides high-speed, high-resolution B-scans of the anterior and posterior segments of the human eye. It also provides 3D volumetric cubes that can be viewed in cross-sectional or in an *en face* format. Thickness maps are automatically generated for various retinal layers including: (1) full retinal thickness; (2) retinal nerve fiber layer (RNFL); (3) ganglion cell layer (GCL) plus the inner-plexiform layer (IPL); (4) RNFL plus GCL plus IPL; and (5) choroid layer. Due to the rapid speed of scanning, large areas of the retina can be imaged in a single scan including 3D scans covering areas as large as 12 × 9 mm, which includes both the macula and optic disc regions. The device has the capability to capture excellent anatomic detail beyond the traditional wide field (100°) (Fig. 2.1).

The Triton OCT has a normative reference database whereby thickness maps are compared and significant deviations from normal are automatically identified. A version of the Triton (Triton plus) is also capable of performing Fluorescein Angiography (FA), red-free imaging, and fundus autoflourescence (FAF). Most recently, the Triton also includes the capability to perform OCT-Angiography, which creates a 3D map of the microvasculature. It is a useful and indispensable tool to aid the clinician in the detection and management of many ocular pathologies. The Triton OCT is not approved for sale in the US yet.

N. Choudhry
Vitreous Retina Macula Specialists of Toronto, Etobicoke, ON, Canada

Department of Ophthalmology and Vision Sciences, University of Toronto, Toronto, ON, Canada

M.J. Sinai (✉)
Chief Clinical Affairs, R and D Planning Division, Topcon Corporation, Tokyo, Japan
e-mail: msinai@topcon.com

The Triton is part of the third generation of OCTs. The first-generation OCT was developed more than 20 years ago at Massachusetts Institute of Technology by Jim Fujimoto, David Huang, Michael Hee, and others [1]. This OCT was slow, had poor resolution, and operated on a time domain principle. That is, it utilized a moving reference mirror in the interferometer, which limited the speed. The light source was not very broad-band (±25 nm) and so the depth resolution was limited (10–20 μm). Despite these limitations, the time-domain OCT was a commercial success and it became the standard of care for retina and glaucoma. More recently, a second-generation OCT was developed, which utilized Fourier Domain (also referred to as Spectral Domain) methodology. It is faster (20–70 kHz) and has an improved depth resolution (5–8 μm) primarily because it utilized a stationary reference mirror and had a broader-band light source (±50 nm). The third-generation OCT, swept source OCT (SS-OCT), includes several major advances in technology. First, SS-OCT utilizes a swept source technology in combination with a light source with a longer wavelength. Swept source utilizes a narrow band wavelength laser and is swept across a broad range of wavelengths. This eliminates the need for a spectrometer, which allows for much faster scanning speeds (100 kHz). The longer wavelength light source (centered on 1050 nm) provides greater penetration due to the nature of longer wavelengths (less scatter, better penetration). This subsequently allows imaging and quantitative evaluation of the choroid for the first time [2–11] as well as better penetration through cataracts and other media opacities. SS-OCT also has a shallower drop in sensitivity with depth, which means there is high sensitivity throughout the entire image from top to bottom compared to time domain or Fourier domain OCT (Fig. 2.2). This allows imaging of the vitreous [12–16] while maintaining good visibility of the choroid in the same scan. Another advantage of the longer wavelength is that it is less visible to the human eye, as it is centered at 1050 nm with a range of ±50 nm. This is advantageous because the patient typically does not see the scanning

© Springer International Publishing AG 2017

Z. Michalewska, J. Nawrocki (eds.), *Atlas of Swept Source Optical Coherence Tomography*,
DOI 10.1007/978-3-319-49840-9_2

light and so they are not distracted and are less likely to move the eye to follow the scan beam. Over the years, OCT technology has continued to advance and this third-generation OCT, SS-OCT, is the latest iteration and offers many advantages over the older versions.

The Triton OCT also allows the user to visualize the retina and optic nerve using an *en face* approach. In *en face* mode the user can view a 3D cube of data from a top-down, or *en face* perspective. This allows for detailed surface evaluation. The software allows the user to view not only the top surface, but at any plane down into the deepest layers of the retina including the choroid and lamina cribrosa. The user also has the option to select the depth of the layer to be visualized, which further enhances any desired structure (Fig. 2.3).

In addition to the *en face* viewing capability, the Triton also offers the opportunity to better visualize the vitreous using the Enhanced Vitreous Visualization (EVV) mode. This proprietary method improves the signal-to-noise ratio at all levels in the image, which greatly enhances the visualization of structures, especially in the vitreous (Fig. 2.4).

Another helpful software feature, known as SMARTTrack™, is the ability to perform real-time tracking for line scanning and OCT-Angiography. This feature utilizes the live fundus image to lock on and track eye movements (through the use of landmarks such as blood vessels and the optic disc). It updates in real time such that once activated, the scan will move to compensate for eye movements, staying in the same place on the retina. A related software feature, called fundus guided acquisition™ (FGA), allows the user to identify and indicate a precise location on the fundus image where the OCT scan will be taken. The tracking feature keeps the scan locked onto this location during scanning, and follow-up features allow the user to take the scan again at a later time in the same location.

There are numerous advantages of SS-OCT over SD-OCT. Traditional spectral domain OCT (SD-OCT) utilizes a shorter wavelength (850 nm) and subsequently image quality can be negatively affected by media opacities such as nuclear sclerosis (cataract), hemorrhage, intravitreal gas, and oil. The use of a 1050 nm wavelength with SS-OCT, in contrast, offers the unique advantage of increased depth of penetration through a variety of media opacities.

A novel application of SS-OCT is the integration of OCT angiography (OCT-A). OCT-A is a novel and non-invasive imaging approach to visualizing the human ocular microvascular network. This method provides vascular information, in fine detail, of all retinal layers beyond what can be seen with conventional fluorescein angiography (FA), but without the use of a dye injection (a full 3D microvasculature map can be generated in 3–4 s). This is achieved by scanning the same location in a repeated fashion and then detecting intensity differences over time. These intensity changes over time can be attributed to motion (i.e., bloodflow within the vasculature). The method utilized in the Triton system is known as OCTARA™, which stands for OCTA Ratio Analysis. This name describes the basic process Topcon uses to detect the retinal and choroidal microvascular pattern (it is a ratio analysis of the intensity changes over time). The algorithm represents a relative measurement of OCT signal amplitude change that optimizes angiographic visualization over both the retina and choroid and also enhances the minimum detectable signal.

Similar to the *en face* software, the vasculature can be visualized at any depth using the modifiable segmentation lines. Four key retinal vascular layers are presented by default: (1) the Superficial Capillary Plexus (SCP), which is segmented from the internal limiting membrane (ILM) to approximately the inner plexiform layer/inner nuclear layer border (IPL/INL); (2) the Deep Capillary Plexus (DCP), which is segmented from approximately the IPL/INL border down 70 μm; (3) the Outer retina, which is segmented from 70 μm below the IPL/INL border to Bruch's Membrane (BM); and (4) the Choriocapillaris, which is segmented from BM down 10 μm (Fig. 2.5).

Figure 2.6 shows an example of the OCT Angiography image in the superficial layers of a normal eye and an eye with BRVO. Scan areas can be selected from 3 × 3 mm^2, 4.5 × 4.5 mm^2, and 6 × 6 mm^2. Several inherent advantages of the Triton swept source methodology also help with the OCT Angiography imaging method, including the faster speed and better depth penetration compared to spectral-domain OCT. These have been found to facilitate better detection of choroidal neovascular membranes (CNVMs) [17].

The Triton software also comes with a wide array of scan types and clinical reports. One important new scan is a wide-field (12 × 9 mm) protocol with 256 b-scans of high resolution (512 a-scans) It provides thickness maps over a large area (over 30 × 40°) and high resolution B scans in the same report (Fig. 2.7). There are also detailed 3D macula reports and glaucoma reports, including the new Hood Report.

The Hood Report is a new one-page report specialized for glaucoma assessment developed by Don Hood, professor, Columbia University, NY (Fig. 2.8). This report has several key features that make it especially helpful for guiding clinical decisions related to glaucoma detection and management. The layout of the report is designed to guide the clinician through several key aspects of the OCT results to improve evaluation. On the top left of the report is a large B scan image of the peripapillary RNFL surrounding the optic disc at a distance of 3.45 mm. Below this image is the peripapillary RNFL thickness profile (black curve) from this B scan superimposed on the normative limits (color regions) of the reference database. Unlike the typical RNFL thickness profile, the temporal side of the RNFL profile is in the center of the image. That is, the RNFL circumpapillary B scan (and thickness profile map) begins at the nasal side of the optic disc, then works its way superiorly, temporally, inferiorly, and then back to nasal again (NSTIN). In the past, most imaging

devices start this display on the temporal side and move superiorly, nasally, inferiorly, then back temporally (TSNIT). There is an important advantage of the NSTIN view [18]. In particular, the clinician can easily relate the changes in the RNFL thickness to changes in the visual field. In fact, the horizontal lines with arrows indicate the portion of the NSTIN plot associated with the central ±8° and the central ±15° of the visual field. These are the regions of the macula and perimacula most often affected by glaucomatous damage [19].

The bottom left image is an *en face* slab view (top-down view) of the intensity reflectance map of the RNFL layer. This *en face* view enhances visualization of RNFL defects common in glaucoma. Often the RNFL defects can be more readily viewed in the *en face* reflectance map than in the standard RNFL thickness map shown next to it (bottom left of report) [20]. In addition, it allows for easy identification of epiretinal membranes and peri-vascular defects [21].

The bottom center of the report shows the RNFL summary parameters by quadrant and clock hour. These are color-coded based on the comparison to the reference database of healthy eyes. At the bottom, and to the right of these summary parameters, the macular ganglion cell plus inner-plexiform (GC+) thickness map is displayed.

Most important, on the far right side of this report are the RNFL and GCL+ probability maps with the 24-2 (large symbols) and 10-2 (small symbols) of the HFA visual field test locations superimposed. These probability maps (for the OCT), which show the statistical significance of the RNFL and GCL+ thinning, are inverted/flipped to match the proper perspective of the visual field locations. That is, the structural deviation maps are flipped superiorly and inferiorly so the structure locations match the functional locations. In addition, the visual field test locations are adjusted to take into account the displacement of the ganglion cells away from the fovea. With these probability maps, the clinician can easily compare the thinning in the GCL+ layer and RNFL to changes in the probability maps of the 10-2 and/or 24-2 visual fields [18]. This arrangement has been shown to be very effective in aiding in the interpretation and diagnosis of glaucomatous damage [22]. Together with the RNFL thickness profile, it focuses the clinician on the key structural aspects most often affected by glaucoma, while enhancing the comparison to functional changes seen on visual fields.

The Triton OCT includes a normative reference database for statistical comparisons of the thickness maps and parameters. Thickness and parameter measurements are compared to the normal range or distribution from this reference database and patient values that are statistically outside the normal range are identified and flagged. Four statistical levels are used from the normal distribution, 1, 5, 95, and 99%. Values below 1% or above 99% are flagged in red to indicate the patient's measurement is outside the normal limits. Values below 5% or above 95% are flagged in yellow to indicate a "borderline" result. The reference database is made up of 360 individuals who were certified to be free from any ocular pathology based on a detailed clinical examination that included biomicroscopy, ophthalmoscopy, visual field testing, IOP measurement, and other factors. The age range was between 22 and 87. A significant correlation with age was observed in many parameters, so an adjustment for age effects was included in the statistical comparisons.

Finally, the Anterior Segment imaging capability of the Triton OCT is another example of the superior quality SS-OCT offers. The anterior segment module on the front of the Triton changes the focal plane from the posterior aspect of the eye to the anterior aspect of the eye for anterior segment imaging. This allows for high resolution imaging of the cornea, angle, and lens. Scan lengths up to 16 mm provide a cross sectional view of both angles in the same image (white to white). Three-dimensional scans of the angles provide a unique view of the trabecular meshwork. Corneal thickness and curvature maps are available in the anterior radial scan (Fig. 2.9).

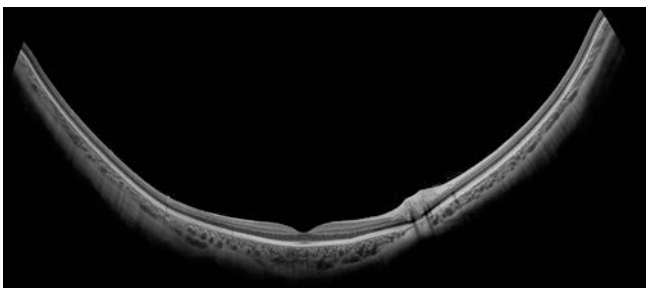

Fig. 2.1 Wide-field SS-OCT of a normal retina demonstrating clear retinal and choroidal detail inclusive of the optic disc, macula and periphery. This image represents a 136° field of view centered on the macula

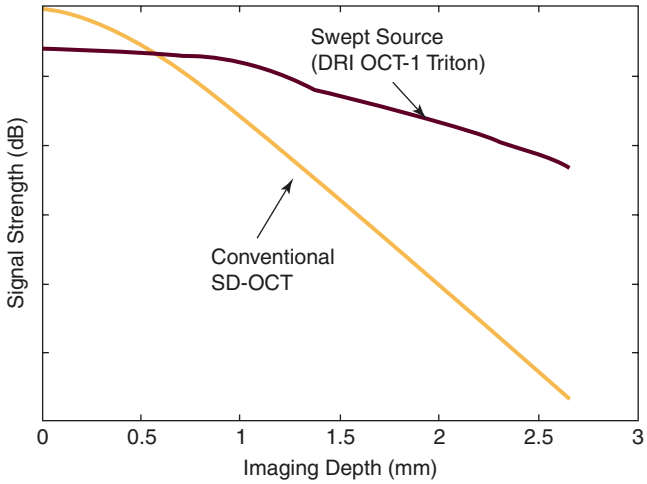

Fig. 2.2 Comparison of sensitivity drop-off between spectral domain and SS-OCT with increasing image depth. There is a significantly greater decrease in sensitivity drop-off with spectral-domain OCT

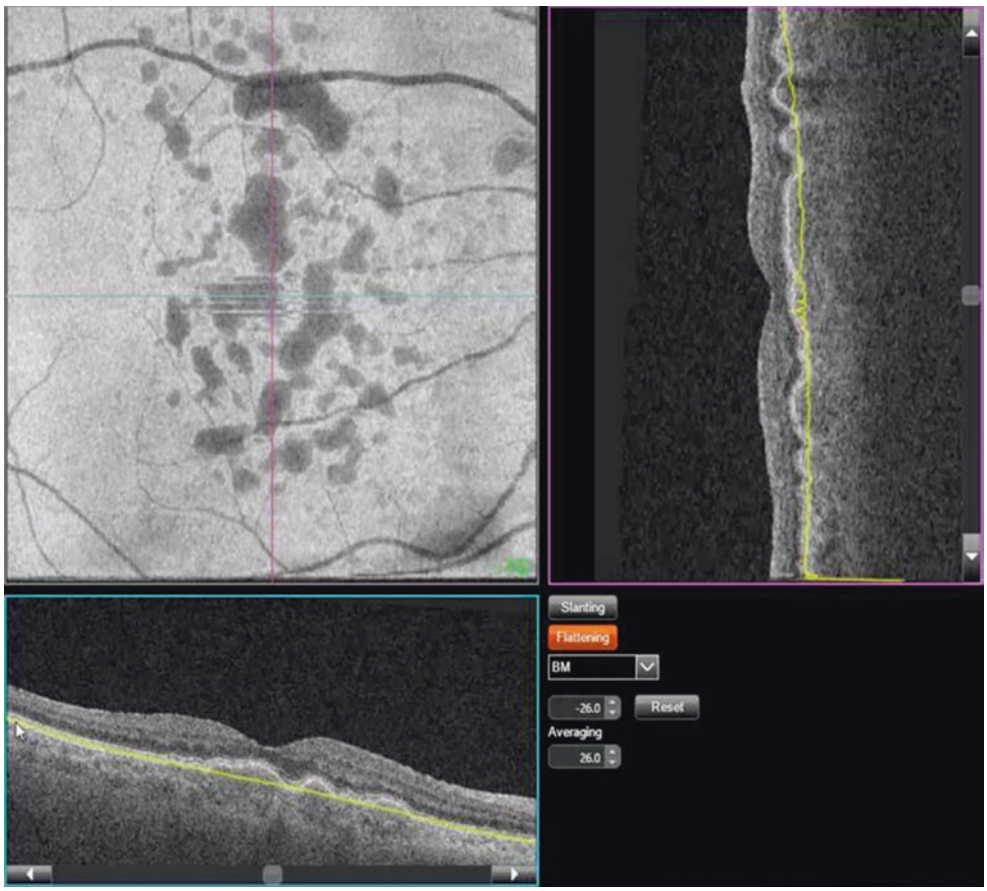

Fig. 2.3. (**a**) *En face* OCT of Dry Age-related Macular Degeneration demonstrating large confluent druse beyond the macula. (**b**) Horizontal segmentation at the level of the retinal pigmented epithelium. (**c**) Vertical segmentation at the level of the retinal pigmented epithelium

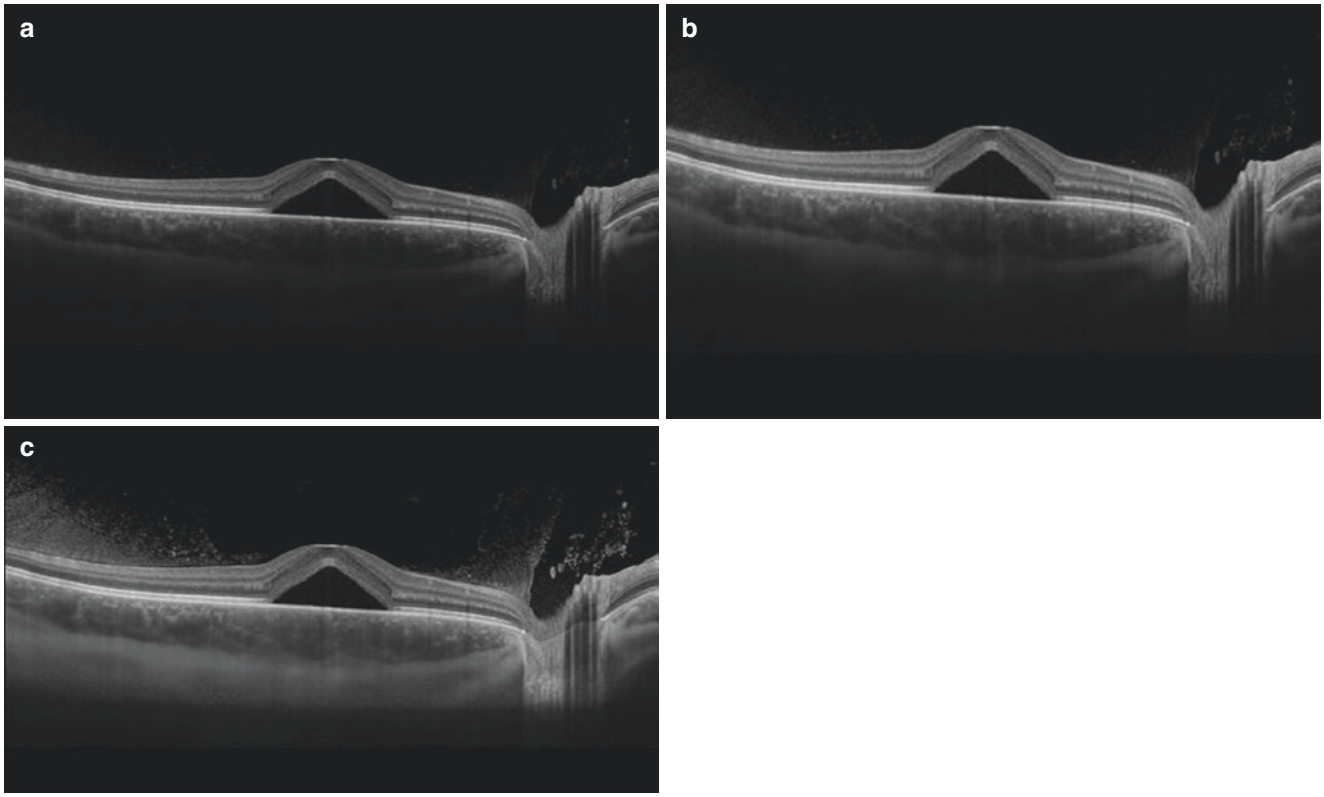

Fig. 2.4 Enhanced vitreous visualization (EVV). (**a**) Demonstrates an eye with acute central serous chorioretinopathy and sub-retinal fluid. In this image there is no vitreous enhancement (EVV "off"). (**b**) The same eye as in (**a**), but with vitreous enhancement turned on its lowest level (+1). (**c**) Demonstrates the same eye in (**a**), but with maximum vitreous enhancement (EVV +5). In this case the choroidal detail is also improved, with clear visualization of the posterior scleral boundary along with the vitreous

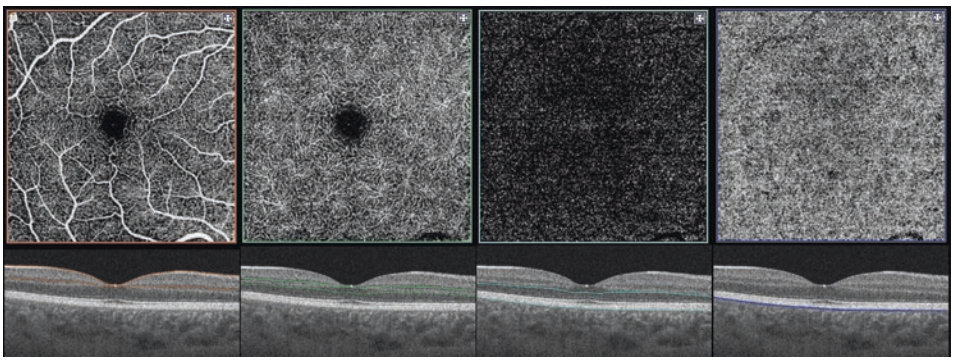

Fig. 2.5 SS-OCT-angiography (4.5 × 4.5 mm) of the normal human retina. (**a**) Superficial capillary plexus. (**b**) Deep capillary plexus. (**c**) Outer retina. (**d**) Choriocapillaris

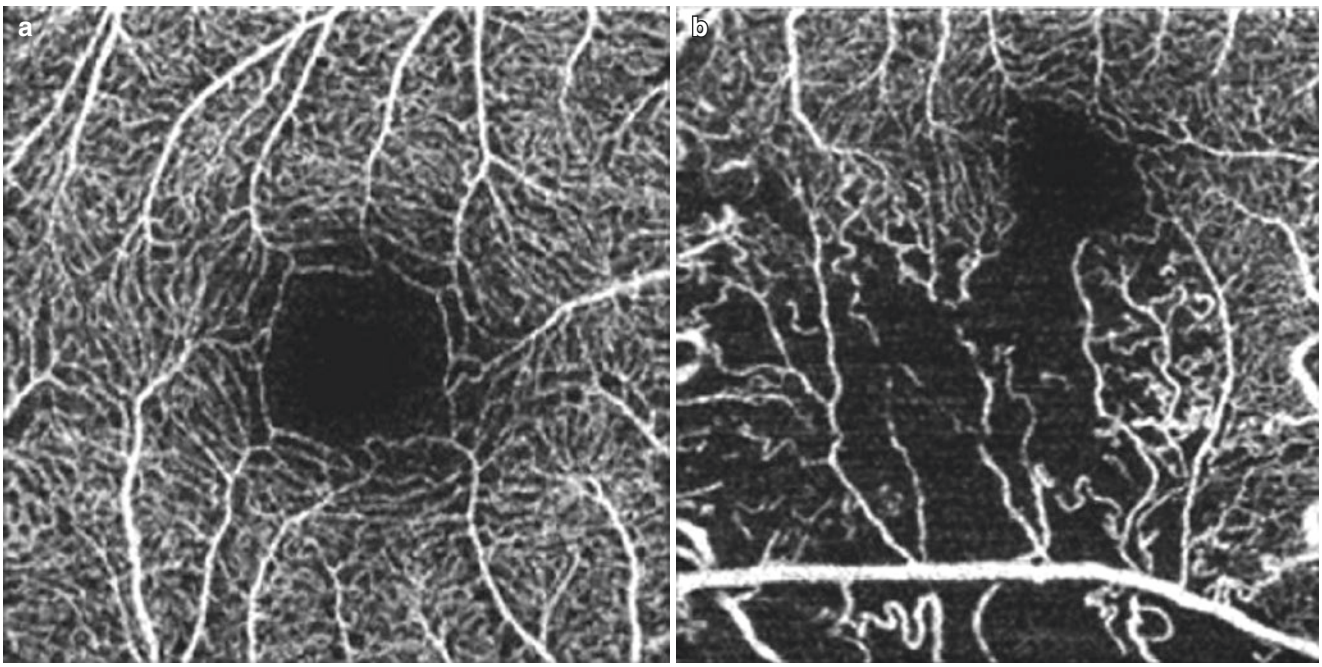

Fig. 2.6 (**a**) OCT Angiography (4.5 × 4.5 mm) of a normal macula demonstrating the superficial capillary, deep capillary plexus, and choriocapillaris combined with a normal foveal avascular zone. (**b**) OCT Angiography of a macula following a branch retinal vein occlusion (BRVO). The areas of reduced flow (non-perfusion) are seen as black with absent vasculature

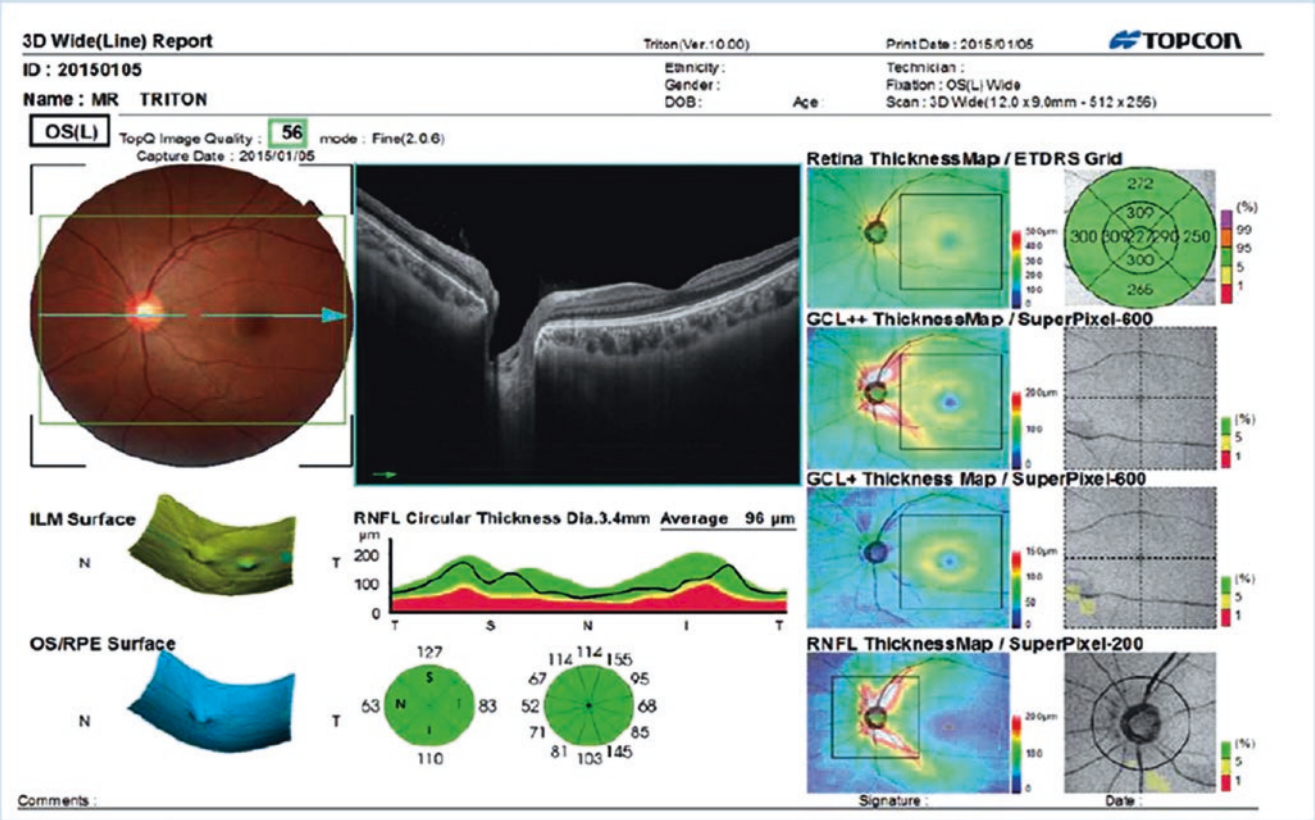

Fig. 2.7 The 12 × 9 wide combination report. There is a high-resolution B scan (highly averaged) shown in the center of the report with the fundus photograph on the left and all thickness maps and deviation maps on the right

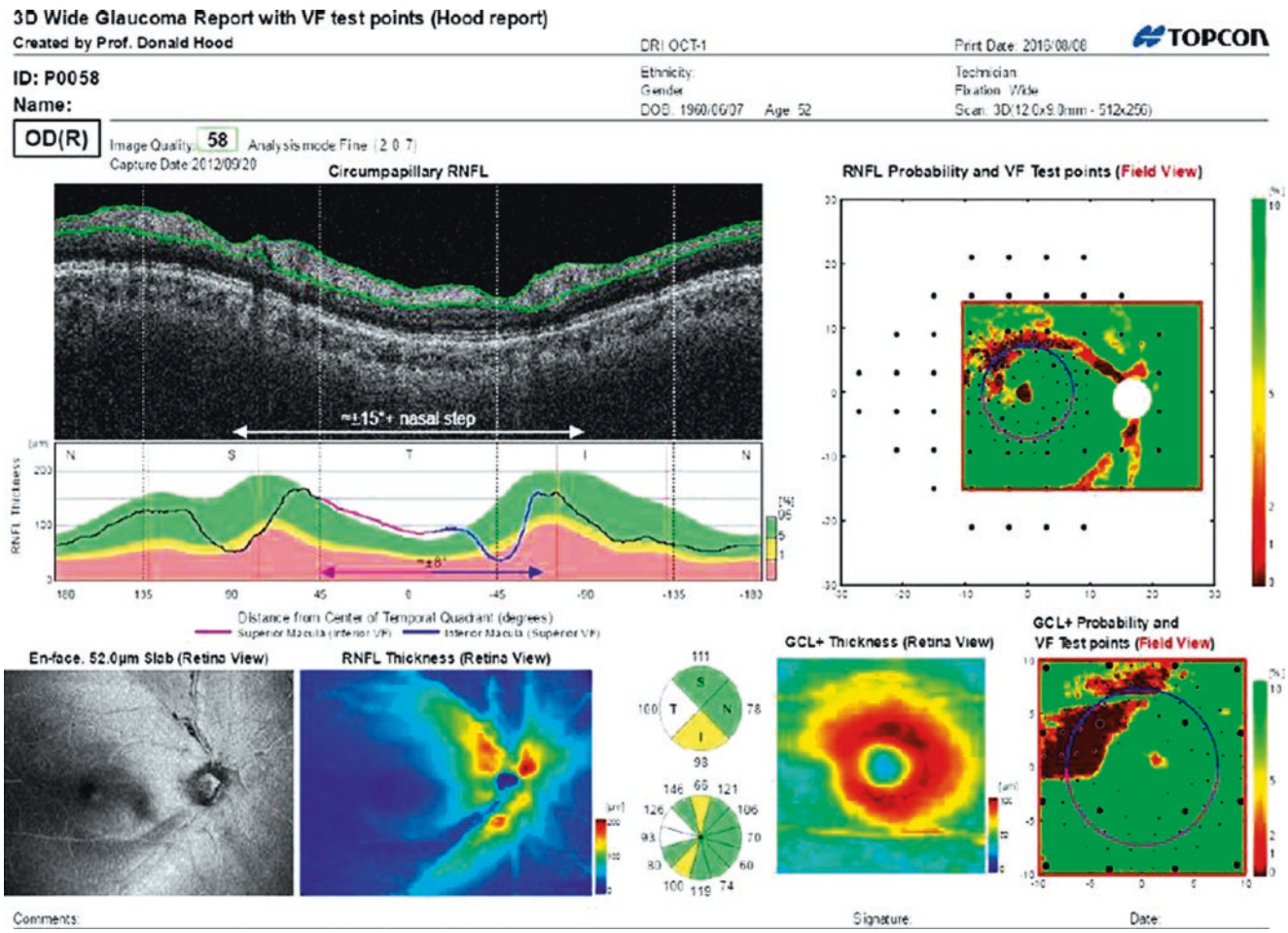

Fig. 2.8 The Hood Report. The peripapillary B-scan and RNFL profile start on the nasal side of the optic disc and move superiorly, temporally, inferiorly, and back to nasal. This highlights the temporal side. The *en face* view and thickness maps at the bottom and the right side show the deviation maps from a visual field perspective with the visual field test location points shown (*Courtesy of* Prof. Donald C. Hood)

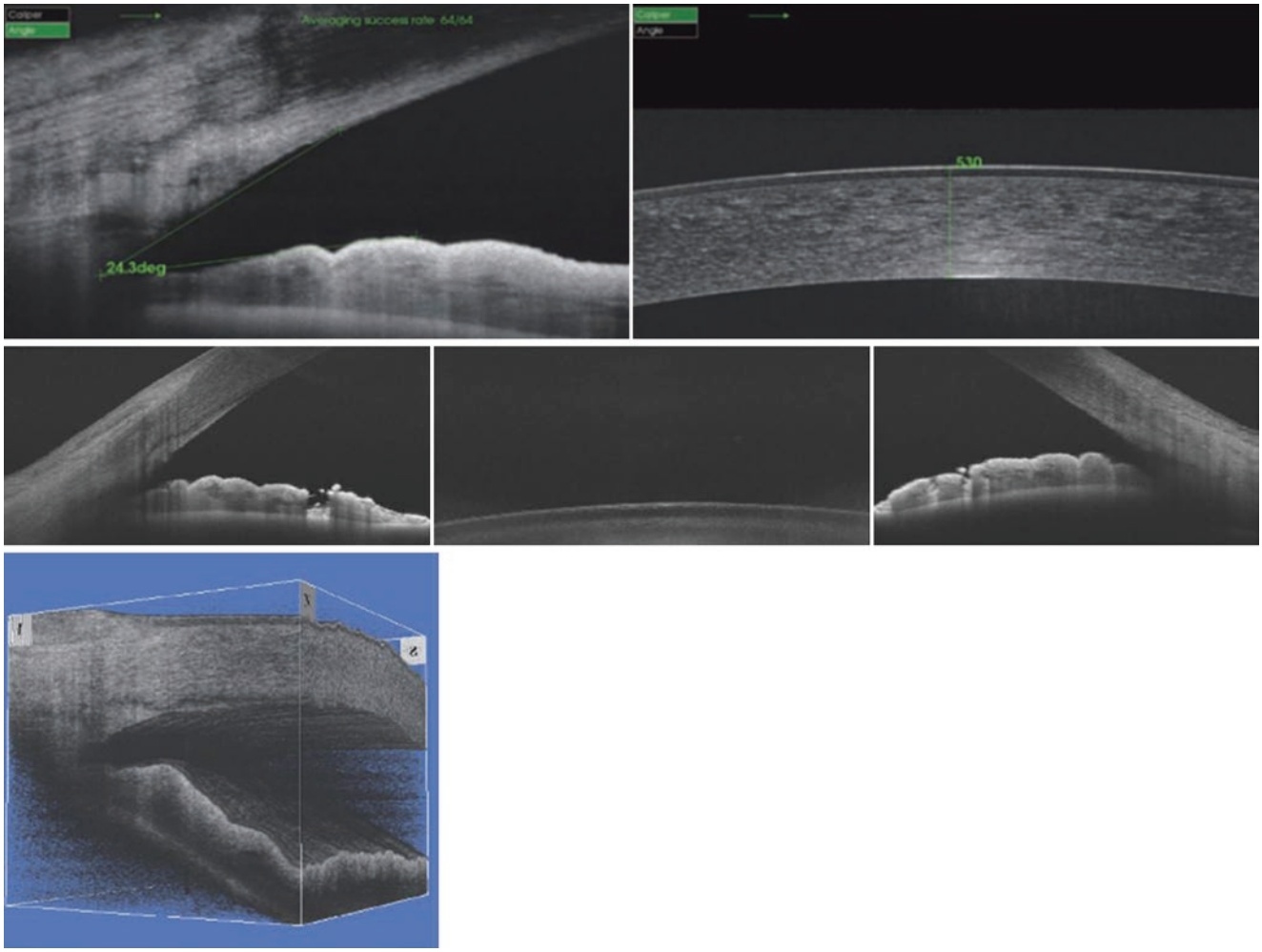

Fig. 2.9 Various anterior segment images from the Triton OCT. Top left is an angle image with manual angle measurement calculation. Top right is the cornea. Middle section is a 16 mm scan showing both angles and the top of the lens. To the right is a 3D scan of the angle

2.1 Interesting Patient Cases

The Triton SS-OCT has many advantages over older OCTs as described above. These advantages have real clinical implications. This section will highlight several patient cases that demonstrate the clinical utility and power of the Triton SS-OCT.

Case 2.1
Fifty-three-year-old male diagnosed with proliferative diabetic retinopathy (PDR). The patient has extensive subhyaloid hemorrhage severely obstructing the view in the fundus photograph. Most spectral domain OCTs would have great difficulty penetrating the blood, which would typically render the OCT images useless. However, the Triton SS-OCT has a 1 μm light source (1050 nm) which enables better penetration through the blood. The OCT images in this case were very high quality, allowing the clear visualization of the macula below (Fig. 2.10). Focal hyper-reflective dots can be seen in the vitreous cavity representing individual red blood cells, and hemorrhage above (*arrowhead*) and below the hyaloid (*arrow*) is seen as thick hyper-reflective material secondary to neovascularization. The retina and choroid behind the hemorrhage can clearly be seen on the OCT.

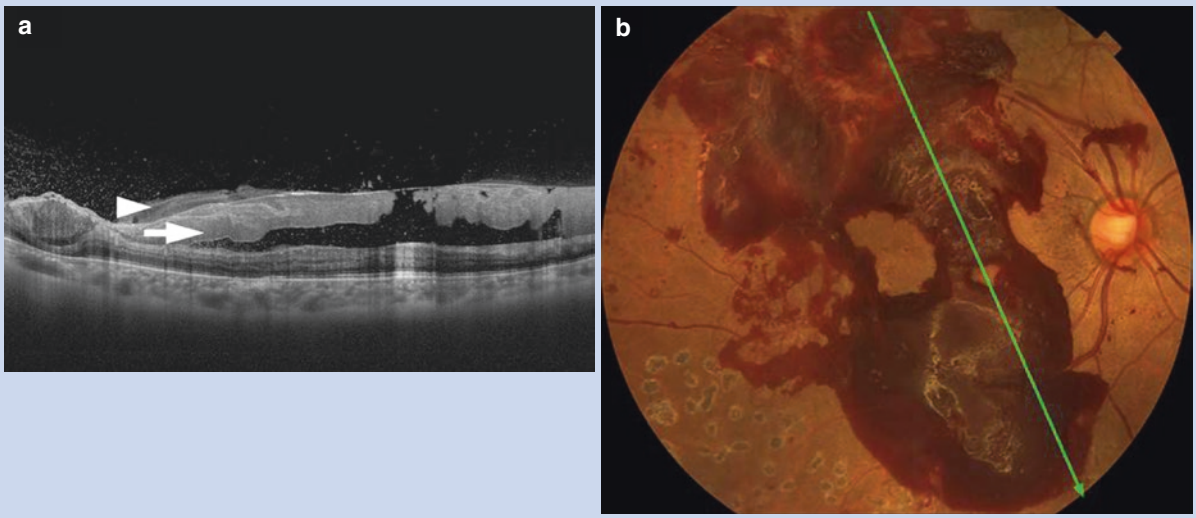

Fig. 2.10 (**a**) SS-OCT (12 mm) through subhyaloid hemorrhage in proliferative diabetic retinopathy. Focal hyper-reflective dots can be seen in the vitreous cavity representing individual red blood cells, hemorrhage above (*arrowhead*) and below the hyaloid (*arrow*) is seen as thick hyper-reflective material can be seen secondary to neovascularization. The retina and choroid behind the hemorrhage can clearly be seen on the OCT. (**b**) Color fundus photograph corresponding to the OCT image in (**a**) demonstrating pre-retinal and subhyaloid hemorrhage without any view to the retina beneath the hemorrhage

Case 2.2

Forty-three-year-old female undergoing a diabetic retinal detachment surgery with silicone oil placement. Similar to the presence of hemorrhage, it is usually very difficult to get a good quality OCT image in this type of patient who has silicone oil in the vitreous. In this case, however, the Triton OCT could penetrate and provide high-quality OCT images revealing an attached retina under oil (Fig. 2.11).

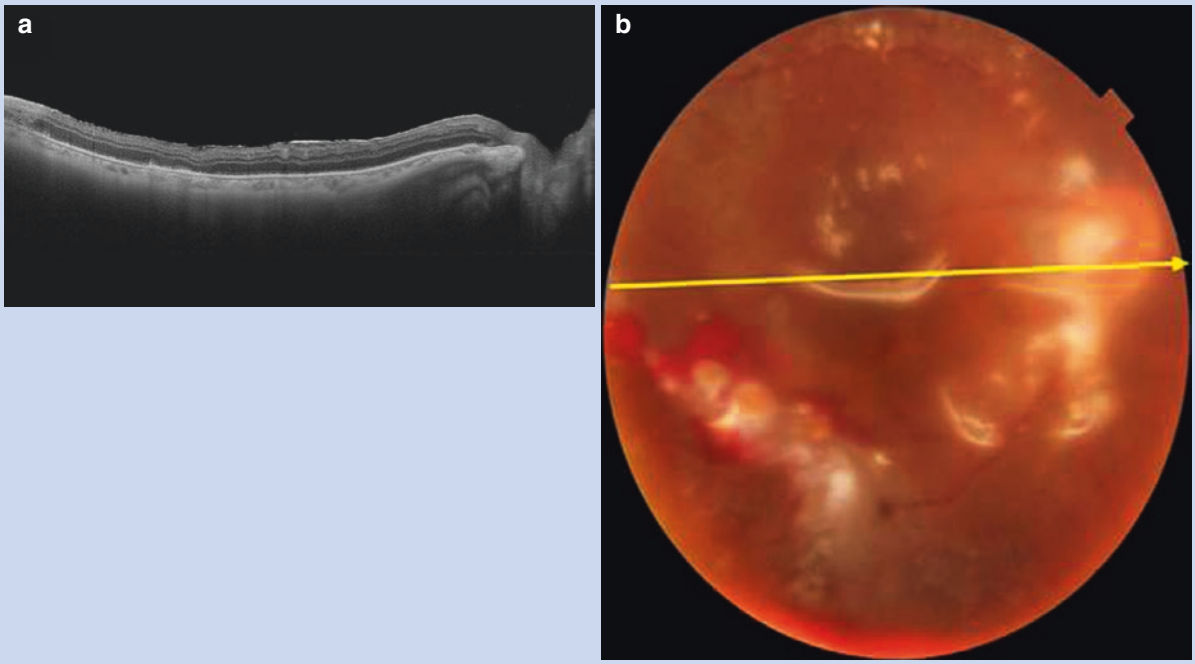

Fig. 2.11 (**a**) Swept source OCT through silicone oil demonstrating clear visualization of all retinal layers in a 12 mm line scan in a region superior to the fovea. (**b**) Color fundus photograph of a silicone oil-filled eye following diabetic retinal detachment surgery. The fundus photograph is unclear and obstructed by hemorrhage and the light reflex from the silicone oil

Case 2.3

Fifty-six-year-old male with a highly myopic eye with an inferior posterior staphyloma (−15 diopters) underwent a pars plana vitrectomy for a myopic macular hole repair. Typically it is difficult to obtain good quality OCT images through the gas in these types of procedures. The Titon OCT, however, was able to penetrate the intravitreal gas and allow for visualization of the macula clearly, revealing an open hole along with the deeper retinal structures, including the sclera and orbital bone (Fig. 2.12).

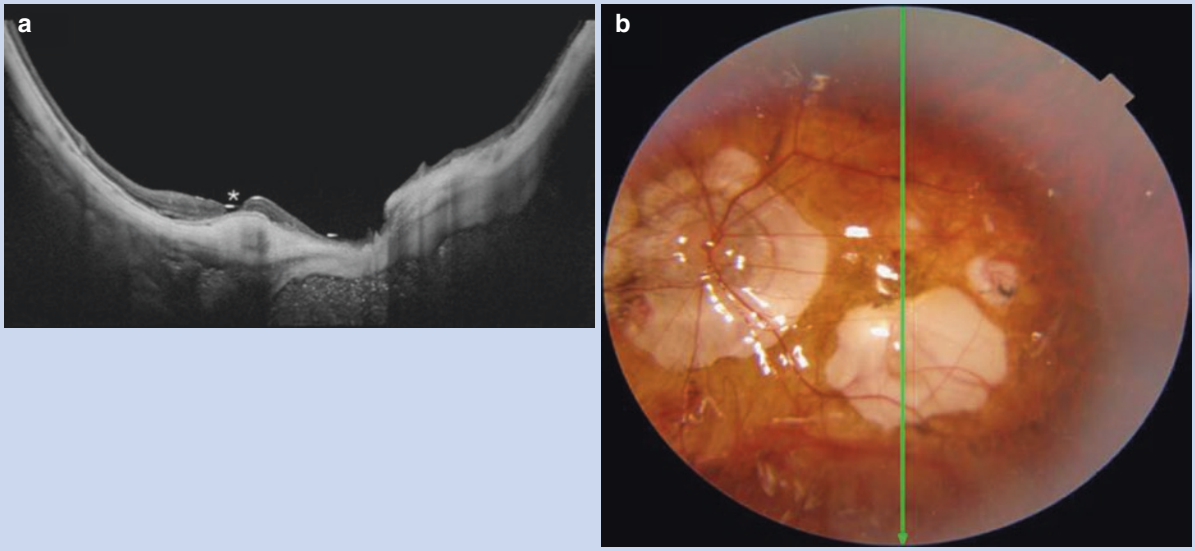

Fig. 2.12 (**a**) Swept source OCT through gas in a myopic eye 1 day following pars plana vitrectomy for a myopic macular hole repair. This 12 mm line scan clearly reveals all retinal layers, including the macular hole which appears open along with the overlying light reflex from the gas bubble (*asterisk*). All retinal layers including the sclera and orbital bone are visible. (**b**) Color fundus photograph of the eye in (**a**) through gas demonstrating a myopic fundus with an inferior posterior staphyloma

Case 2.4

Fifty-eight-year-old female with prior uncomplicated cataract surgery and worsening vision was examined using the Triton OCT using anterior segment imaging. The Triton OCT revealed the presence of cortical material retained behind the intraocular lens (IOL) as hyper-reflective material (*arrowhead*). The IOL can be almost completely be visualized despite the overlying backscattering from the iris above. Furthermore, focal hyper-reflectivities on the IOL representing "glistenings" can be seen in the body of the IOL (Fig. 2.13).

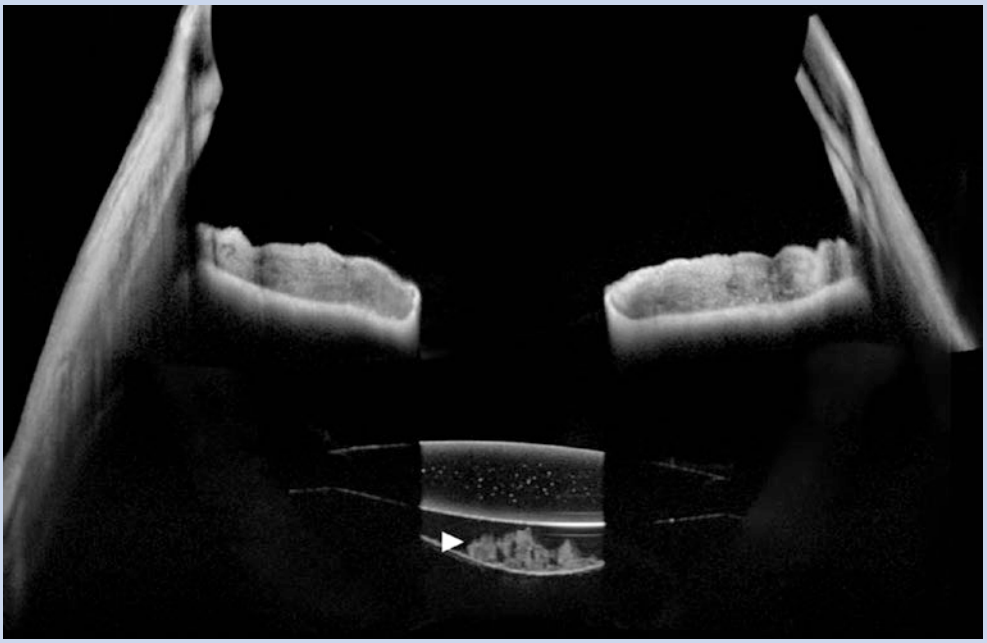

Fig. 2.13 SS-OCT of retained cortical material can be seen behind the intraocular lens (IOL) as hyper-reflective material (*arrowhead*). The IOL can be almost completely visualized despite the overlying backscattering from the iris above. Furthermore, focal hyper-reflectivities on the IOL representing "glistenings" can be seen in the body of the IOL

Conclusion

OCT technology is continuing to evolve at a rapid rate and has become an indispensable clinical tool in ophthalmology. The latest generation of SS-OCT represents a significant advancement in the ability to examine the human eye. The Triton SS-OCT has many clinical advantages over older OCT methods (Spectral Domain or Time Domain). Faster speed, deeper penetration, uniform sensitivity, and ease of use in clinical practice represent a significant advancement in OCT imaging. These advantages combined with new software features such as OCT Angiography imaging, image tracking, and vitreous enhancement, all place swept source imaging and the Triton on the frontier of ophthalmic OCT imaging.

References

1. Huang D, Swanson EA, Lin CP, Schuman JS, Stinson WG, Chang W, et al. Optical coherence tomography. Science. 1991;254:1178–81.
2. Hirata M, Tsujikawa A, Matsumoto A, Hangai M, Ooto S, Yamashiro K, et al. Macular choroidal thickness and volume in normal subjects measured by swept-source optical coherence tomography. Invest Ophthalmol Vis Sci. 2011;52(8):4971–8.
3. Usui S, Ikuno Y, Miki A, Matsushita K, Yasuno Y, Nishida K. Evaluation of the choroidal thickness using high-penetration optical coherence tomography with long wavelength in highly myopic normal-tension glaucoma. Am J Ophthalmol. 2012;153(1):10–6.e1.
4. Usui S, Ikuno Y, Akiba M, Maruko I, Sekiryu T, Nishida K, et al. Circadian changes in subfoveal choroidal thickness and the relationship with circulatory factors in healthy subjects. Invest Ophthalmol Vis Sci. 2012;53(4):2300–7.
5. Ruiz-Moreno JM, Flores-Moreno I, Lugo F, Ruiz-Medrano J, Montero JA, Akiba M. Macular choroidal thickness in normal pediatric population measured by swept-source optical coherence tomography. Invest Ophthalmol Vis Sci. 2013;54(1):353–9.
6. Mansouri K, Weinreb RN. Evaluation of retinal and choroidal thickness by swept source optical coherence tomography: repeatability and assessment of artifacts. Am J Ophthalmol. 2014;157:1022–32.
7. Ruiz-Medrano J, Ruiz-Moreno JM. Macular choroidal thickness profile in a healthy population measured by swept-source optical coherence tomography. Invest Ophthalmol Vis Sci. 2014;55:3532–42.
8. Mansouri K, Medeiros FA, Weinreb RN. Assessment of choroidal thickness and volume during the water drinking test by swept-source optical coherence tomography. Ophthalmology. 2013;120:2508–16.
9. Michalewska Z, Michalewska J, Adelman RA, Zawlslak E, Nawrocki J. Choroidal thickness measured with swept source optical coherence tomography before and after vitrectomy with interal limiting membrane peeling for idiopathic epiretinal membranes. Retina. 2015;35:487–91.
10. Michalewska J, Michalewska Z, Nawrocka Z, Bednarski M, Nawrocki J. Correlation of choroidal thickness and volume measurements with axial length and age using swept-source optical coherence tomography and optical low-coherence reflectometry. BioMed Research Inter. 2014;2014:639160.
11. Zhang C, Tatham AJ, Medeiros FA, Zangwill LM, Yang Z, Weinreb RN. Assessment of choroidal thickness in healthy and glaucomatous eyes using swept source optical coherence tomography. PLoS One. 2014;9(10):e109683.
12. Itakura H, Kishi S, Li D, Akiyama H. Observation of posterior precortical vitreous pocket using swept-source optical coherence tomography. Invest Ophthalmol Vis Sci. 2013;54(5):3102–7.
13. Itakura H, Kishi S. Vitreous changes in high myopia observed by swept-source optical coherence tomography. Invest Ophthalmol Vis Sci. 2014;55:1447–52.
14. Schaal KB, Pang CE, Engelbert M. The premacular bursa's shape revealed in vivo by swept-source optical coherence tomography. Ophthalmology. 2014;121:1020–8.
15. Stanga PE, Sala-Puigdollers A, Caputo S, Jaberansari H, Cien M, Gray J, et al. In vivo imaging of cortical vitreous using 1050 nm swept source deep range imaging optical coherence tomography. Am J Ophthalmol. 2014;157(2):397–404e2.
16. Itakura H, Kishi S, Li D, Akiyama H. En face imaging of posterior precortical vitreous pockets using swept-source optical coherence tomography. Invest Ophthalmol Vis Sci. 2015;56(5):2898–900.
17. Novais EA, Adhi M, Moult EM, Louzada RN, Cole ED, Husvogt L, et al. Choroidal neovascularization analyzed on ultrahigh-speed swept-source optical coherence tomography angiography compared to spectral-domain optical coherence tomography angiography. Am J Ophthalmol. 2016;164:80–8.
18. Hood DC, Raza AS. On improving the use of OCT imaging for detecting glaucomatous damage. Br J Ophthalmol. 2014;98:ii1–9.
19. Hood DC, Raza AS, de Moraes CGV, Liebmann JM, Ritch R. Glaucomatous damage of the macula. Prog Retin Eye Res. 2013;32:1–21.
20. Hood DC, Fortune B, Mavrommatis MA, Reynaud J, Ramachandran R, Ritch R, et al. Details of glaucomatous damage are better seen on OCT en face images than on OCT retinal nerve fiber layer thickness maps. Invest Ophthalmol Vis Sci. 2015;56(11):6208–16.
21. Hood DC, De Cuir N, Mavrommatis MA, Xin D, Muhammad H, Reynaud J, et al. Defects along blood vessels in glaucoma suspects and patients. Invest Ophthalmol Vis Sci. 2016;57(4):1680–6.
22. Hood DC, Raza AS, De Moraes CG, Alhadeff PA, Idiga J, Blumberg DM, et al. Evaluation of a one-page report to aid in detecting glaucomatous damage. Transl Vis Sci Technol. 2014;3(6):8.

Swept Source OCT Angiography in Different Diseases

3

Ricardo Noguera Louzada, Eric M. Moult, Emily Cole, James G. Fujimoto, and Jay S. Duker

Swept source optical coherence tomography angiography (SS-OCTA) devices are the latest OCT technology to become commercially available. These units feature scan rates of 100,000 A-scans per second. In this chapter, the use of an ultra-high speed SS-OCTA prototype device developed at Massachusetts Institute of Technology (Cambridge, MA, USA) and deployed to New England Eye Center, Boston, MA will be discussed. The prototype SS-OCT system has been described previously, so only key attributes are considered for the purposes of this chapter [1]. This device utilizes a vertical-cavity surface-emitting laser (VCSEL) with a light source operating at a 1050 nm wavelength and a scan rate of 400,000 A-scans per second. Images are obtained by acquiring five repeated B-scans from 500 sequentially uniformly spaced locations on the retina, with each B-scan consisting of 500 A-scans. Thus a total of 5 × 500 × 500 A-scans are acquired per SS-OCTA volume with a total acquisition time of approximately 3.8 s. The imaging range is approximately 2.1 mm in tissue, and the axial and transverse resolutions in tissue are approximately 8–9 μm and approximately 15 μm, respectively. A post-processing registration step merges the orthogonally scanned "X-fast" and "Y-fast" volumes to patient motion artifacts [2].

Both hardware and software components of SS-OCTA devices are equally important in the acquisition and generation of high-quality SS-OCTA images, and differences in the appearance of SS-OCTA images from different commercially available devices cannot be solely attributed to wavelength, type of device, or the number of A-scans per second. It is also important to consider whether eye tracking is used, as this may contribute to reduced motion artifact; the prototype does not utilize eye tracking. Finally, there are intrinsic properties of SS-OCTA image processing software that can affect the final appearance of the images, including grayscale, brightness, and image thresholding. Thresholding is a background step that is applied to the SS-OCT signals that are used to generate the SS-OCTA images. It is part of the image processing that occurs before the final SS-OCTA image is displayed to the clinician on the SS-OCTA device. Thresholding is a process that allows "noise" to be differentiated from what can reliably be interpreted as flow.

SS-OCTA images are created by computing the differences between SS-OCT B-scans consecutively acquired from the same retinal location. The contrast in an SS-OCTA image is generated by the movement of the erythrocytes; however, if the velocity of erythrocytes in the vessels is very slow, then the consecutively acquired SS-OCT B-scan will not be sufficiently different for erythrocyte motion to be detected. Thus, SS-OCTA systems have a characteristic "slowest detectable flow," below which erythrocyte flows cannot be detected. The slowest detectable flow is dependent on the interscan time—that is, the time between repeated B-scans. Current interscan times on commercial spectral domain OCT (SD-OCT) devices are approximately 5 ms, while the interscan time on the prototype SS-OCT system used in this chapter is approximately 1.5 ms.

The variable interscan time analysis (VISTA) algorithm works by collecting multiple (>2) repeated B-scans at each

R.N. Louzada
Department of Ophthalmology, Federal University of Goiás, Goiânia, Goiás, Brazil

New England Eye Center, Tufts University School of Medicine, Boston, MA, USA

E. Cole • J.S. Duker (✉)
New England Eye Center, Tufts University School of Medicine, Boston, MA, USA
e-mail: jduker@tuftsmedicalcenter.org

E.M. Moult
Department of Electrical Engineering and Computer Science, and Research Laboratory of Electronics, Massachusetts Institute of Technology, Cambridge, MA, USA

Harvard MIT Department of Health Science and Technology, Cambridge, MA, USA

J.G. Fujimoto
Department of Electrical Engineering and Computer Science, and Research Laboratory of Electronics, Massachusetts Institute of Technology, Cambridge, MA, USA

© Springer International Publishing AG 2017

Z. Michalewska, J. Nawrocki (eds.), *Atlas of Swept Source Optical Coherence Tomography*,
DOI 10.1007/978-3-319-49840-9_3

retinal location and then forming images with different effective interscan times by comparing differently spaced image pairs. By altering the effective interscan time the slowest detectable flow is shifted and different flow speeds can be visualized. Thus VISTA allows for relative flow speeds to be visualized. Because the VISTA requires the acquisition of multiple (>2) repeated B-scans, high-speed imaging is needed [2, 3].

All of the images in this chapter were taken using the SS-OCTA Prototype device developed at Massachusetts Institute of Technology.

3.1 OCT Angiography of Vascular Occlusions

3.1.1 Retina Vein Occlusion

Retinal vein occlusion (RVO) is the second most common retinal vascular disease after diabetic retinopathy. RVO is commonly divided into central retinal vein occlusion (CRVO) and branch retinal vein occlusion (BRVO), and can be associated with macula edema, which affects the central visual acuity. Increased retinal thickness can be caused by the intraretinal cysts as well as serous retinal detachment [4]. Venous occlusion in both BRVO and CRVO may be caused by an intraluminal vascular obstruction, external venous compression, or other extrinsic vascular pathology [5, 6].

Fluorescein angiography (FA) is the most common ancillary test used for imaging the retinal vasculature in vein obstructions and is useful to identify, monitor, and visualize the vascular changes as well as confirm the presence of non-perfusion, neovascularization, and macular edema. The disadvantages of FA include the invasive injection of dye, risk of adverse side effects, length of imaging, and difficulty visualizing structures that may be obscured due to leakage.

SS-OCTA is a depth-resolved imaging modality which allows the evaluation of spatial relationships of fundus vessels and enables detailed *en face* visualization of the superficial and deep retinal vascular plexuses. It can be used to quantify the foveal vascular zone (FAZ) enlargement, capillary non-perfusion appearance, microvascular abnormalities, and vascular congestion. SS-OCTA is also able to analyze arteriovenous anastomoses of the superficial and deep plexus. In ischemic RVO, it is possible to visualize areas of capillary non-perfusion in retina areas using both FA and SS-OCTA. In RVO, it was suggested that the decrease in vascular perfusion is more prominent in the deep retinal capillary plexus (see Figs. 3.1 and 3.2) [6].

In retinal vein occlusions, the ultra-high speed SS-OCTA does not offer a clear advantage over SD-OCTA systems in visualization of the vascular abnormalities of the superficial and deep plexuses. However, long wavelength SS-OCTA is better able to visualize the choriocapillaris and choroidal vessels and ischemic changes that may occur as part of the global ischemia that occurs. Additionally, SS-OCTA can be used to visualize the progression or reperfusion of ischemia over time, as it is an imaging study that can be easily performed at multiple follow-up visits.

Alteration of the retinal contour may occur secondary to macular edema in patients with vein occlusions, which can cause segmentation error in automated segmentation algorithms on commercially available devices. Post-acquisition image processing uses Bruch's membrane, the internal limiting membrane (ILM), or other distinct layer in the chorioretinal anatomy as a reference with respect to which *en face* image planes are segmented [7]. However, manual segmentation and flattening of these prototype images can help reduce segmentation error and better visualize the vasculature in one plane simultaneously without needing to scroll through a three-dimensional volume. Future commercially available SS-OCT systems should include automated flattening software for better visualization of SS-OCTA features.

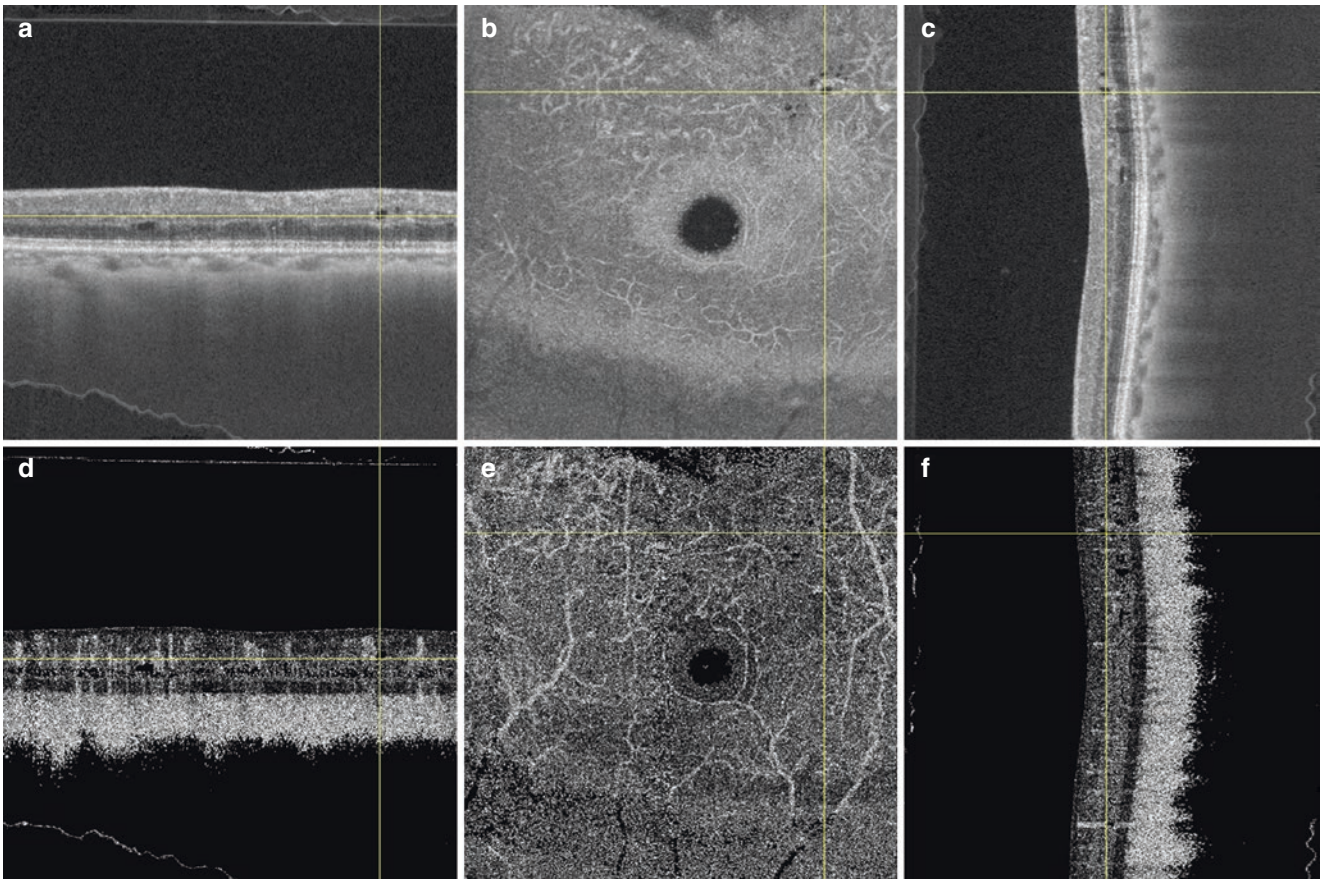

Fig. 3.1 SS-OCTA orthogonal view of branch retina vein occlusion. The left eye of a 61-year-old Caucasian female using the VCSEL SS-OCTA. (**a**) Unflattened structural en face 3 × 3 mm SS-OCT with (**b**), the corresponding 3 × 3 mm X-Fast SS-OCT B-scan, and (**c**), the corresponding 3 × 3 mm Y-Fast OCT B-scan. (**d**) Unflattened structural en face 6 × 6 mm SS-OCT with (**e**) the corresponding 6 × 6 mm X-Fast SS-OCT B-scan and (**f**) corresponding 6 × 6 mm Y-Fast SS-OCT B-scan. The SS-OCTA shows microvascular abnormalities such as areas of capillary non-perfusion, capillary loops, and microaneurysms

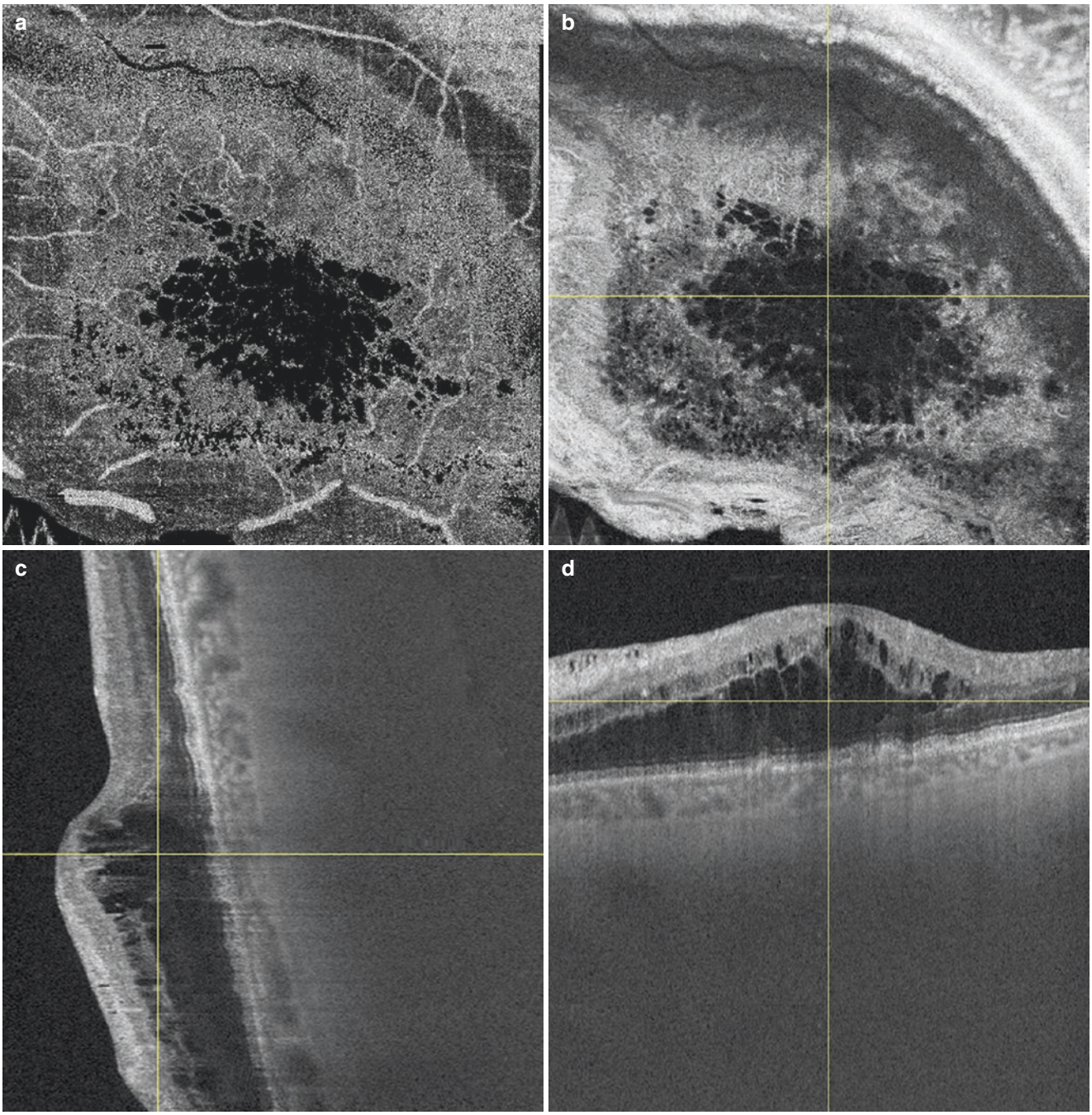

Fig. 3.2 OCTA orthogonal view of macular edema due to central retina vein occlusion (CRVO). The left eye of a 72-year-old Caucasian male using the VCSEL SS-OCTA. (**a**), 3 × 3 mm SS-OCT angiogram and (**b**), the corresponding structural *en face* SS-OCT. (**c**), 3 × 3 mm X-Fast SS-OCT B-scan and (**d**), the corresponding 3 × 3 mm Y-Fast SS-OCT B-scan. The areas of macular edema appear as dark, cystic areas with well-delineated borders

3.1.2 Retinal Artery Occlusion

There are two main forms of retinal artery occlusion: branch retinal artery occlusion (BRAO) and central retinal artery occlusion (CRAO). BRAO occurs when the artery becomes blocked, usually due to an embolus. BRAO is usually the result of embolus that lodges at the bifurcation of a retinal arteriole. In the obstructed area, capillary drop-out due to occlusion of blood flow is evident. Histopathologic studies have shown that in acute BRAO, there is an area of ischemia in the corresponding retinal quadrant, which is followed by inner retinal atrophy in long-standing cases. On SS-OCT, CRAO shows a distinct pattern of increased reflectivity and thickness of the inner retina in the acute phase and a corresponding decrease in reflectivity of the outer layer of the retina, retina pigment epithelium (RPE), and choriocapillaris. Similar to retinal vein occlusions, the ultra-high speed SS-OCTA may not offer a clear advantage over SD-OCTA systems in visualization of the vascular abnormalities of the superficial and deep plexuses, where the most obvious and dramatic changes occur. As well as the SD-OCTA, SS-OCTA of an acute BRAO show an ischemic area (see Fig. 3.3c) in the corresponding retinal quadrant of the branch marked by inner retinal edema at the initial stage followed by atrophy in long-standing cases (see Fig. 3.3).

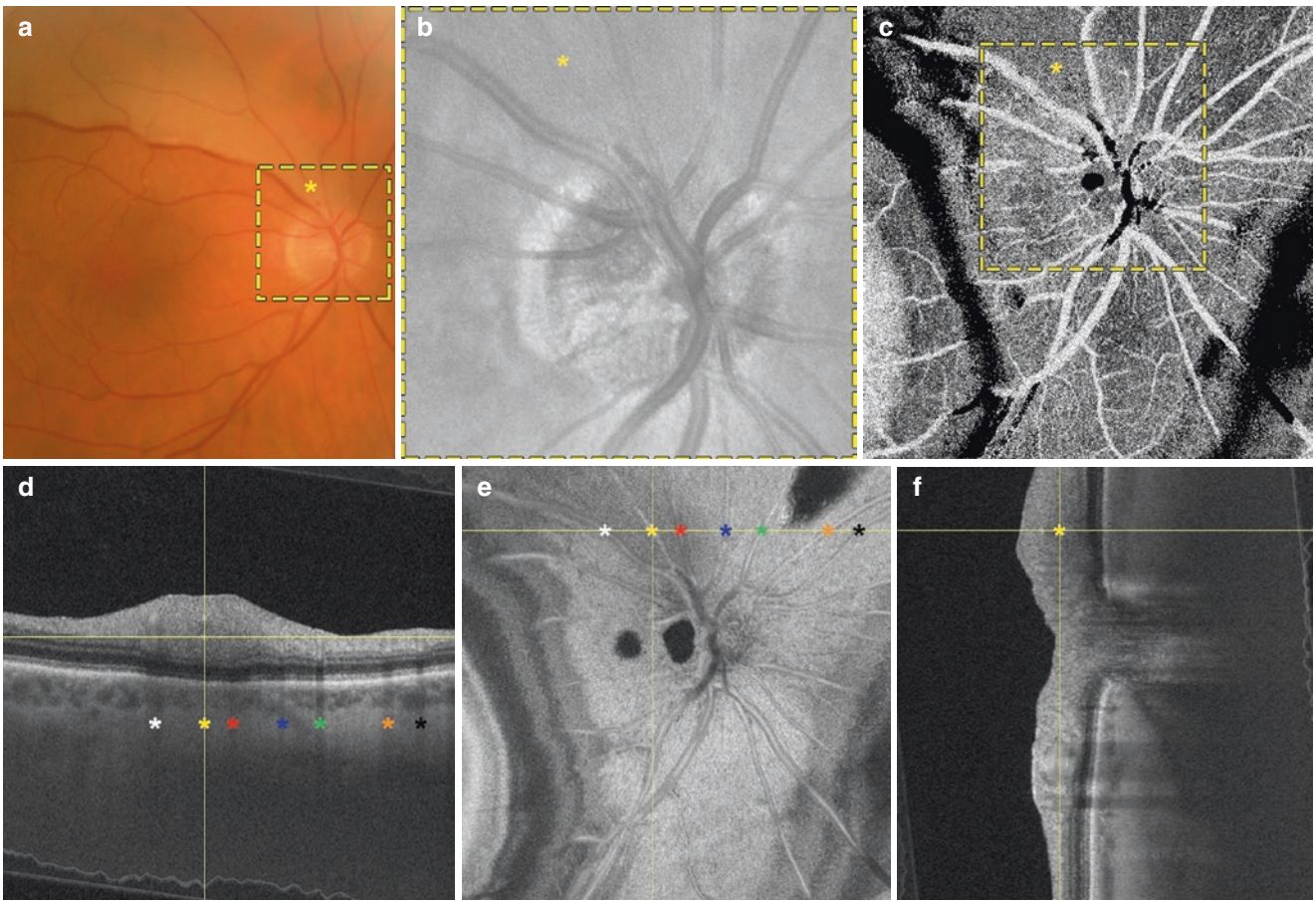

Fig. 3.3 Multimodal image of branch retina artery occlusion (BRAO) with color fundus photo. The right eye of a 70-year-old Caucasian man using the VCSEL SS-OCTA. In the superficial plexus, it is possible to visualize the main superficial retina vessels in the arterial occluded area that lose some, but not all, collateral branches (*asterisk*) after the ischemic event. (**a**) Color fundus photo zoomed in to an approximately 3 × 3 mm area centered at the optic nerve showing RAO (*asterisk*). (**b**) Unflattened structural en face 3 × 3 mm SS-OCT. (**c**) 6 × 6 mm SS-OCTA of the superficial vascular plexus. The *yellow asterisk* corresponds to an occluded vessel that can be faintly seen on the structural *en face* SS-OCT, but not the SS-OCT angiogram. (**d**) Corresponding 6 × 6 mm X-Fast SS-OCT B-scan. The stars mark the corresponding shadowing artifact from the overlying vessels (**e**) unflattened structural *en face* 6 × 6 mm SS-OCT at the level of the RPE. (**f**) Corresponding 6 × 6 mm Y-Fast SS-OCT B-scan

3.2 Non-neovascular Age-Related Macular Degeneration

Dry, or non-neovascular, age-related macular degeneration (AMD) is a progressive chronic disease that is one of the leading causes of irreversible legal blindness in developed countries in adults older than 50 years of age. It is almost always bilateral and primarily affects the macula. There are both genetic and lifestyle risk factors that are related to the development and progression of dry AMD [8, 9].

Drusen, pigmentary changes, and photoreceptor and retina pigment epithelium loss can be observed clinically on fundoscopic examination. Photoreceptor changes can be caused by RPE dysfunction or can be secondary to choriocapillaris loss or both. The RPE provides nutrients to the overlying photoreceptors. RPE changes are the hallmark of late-stage dry AMD, and these areas of atrophy are commonly known as geographic atrophy (GA).

The SS-OCT prototype used in this chapter utilizes a longer wavelength, 1050 nm which has increased penetration through the RPE compared to shorter wavelength, ~840 nm, commercial SD-OCT systems. Depending on the imaging regime, SD-OCT may also suffer from sensitivity roll-off when imaging beneath the RPE. One of the most important advantages of SS-OCT in dry AMD is the enhanced visualization of the choriocapillaris and the ability to visualize of the presence and pattern of ischemia in this layer.

3.2.1 SS-OCTA in Early- and Intermediate-Stage Dry AMD

SS-OCTA enables precise correlation of structural and microvascular changes in the layers of the retina and choroid, which has improved our understanding of this condition and its pathogenesis. Despite limited clinical symptoms in early AMD, it is possible to visualize chorioretinal changes in early-stage AMD on SS-OCT. Drusen presents as hyperreflective material between Bruch's membrane and the RPE. SS-OCTA, with its enhanced visualization of the choroid and choriocapillaris, can help to better visualize the relationship between the RPE, Bruch's membrane, and the choriocapillaris (CC) in the pathogenesis of AMD [10].

By simultaneous visualization of structural and microvascular information on SS-OCTA, it is possible to visualize drusen and observe vascular changes in the choriocapillaris both underneath and surrounding drusen. It has been noted that early dry AMD is associated with focal areas of choriocapillaris loss and a general reduction in choriocapillaris density when compared to age-matched normal controls. It is also possible to visualize the large choroidal vessels that lie below these areas of choriocapillaris loss. These SS-OCTA findings are supported by histopathologic data which have noted that drusen form over areas devoid of capillary lumens and extend into the intercapillary pillars, and that increased drusen density is associated with a reduction in the vascular density of the choriocapillaris [11–13].

3.2.2 SS-OCTA in Advanced Dry AMD

Geographic atrophy (GA) occurs in late-stage AMD and SS-OCTA in this area shows loss of choriocapillaris underlying large areas of atrophy. Figure 3.4 shows that areas of choriocapillaris loss can be correlated to areas of RPE atrophy.

SS-OCTA has been used to show that alterations in the choriocapillaris within the borders of GA tend to be primarily atrophic, while changes in the choriocapillaris beyond the GA borders appear to be mostly areas of impaired flow. When the area of choriocapillaris under the GA is compared to the surrounding normal areas, it is noted that there is considerable loss of flow in the choriocapillaris.

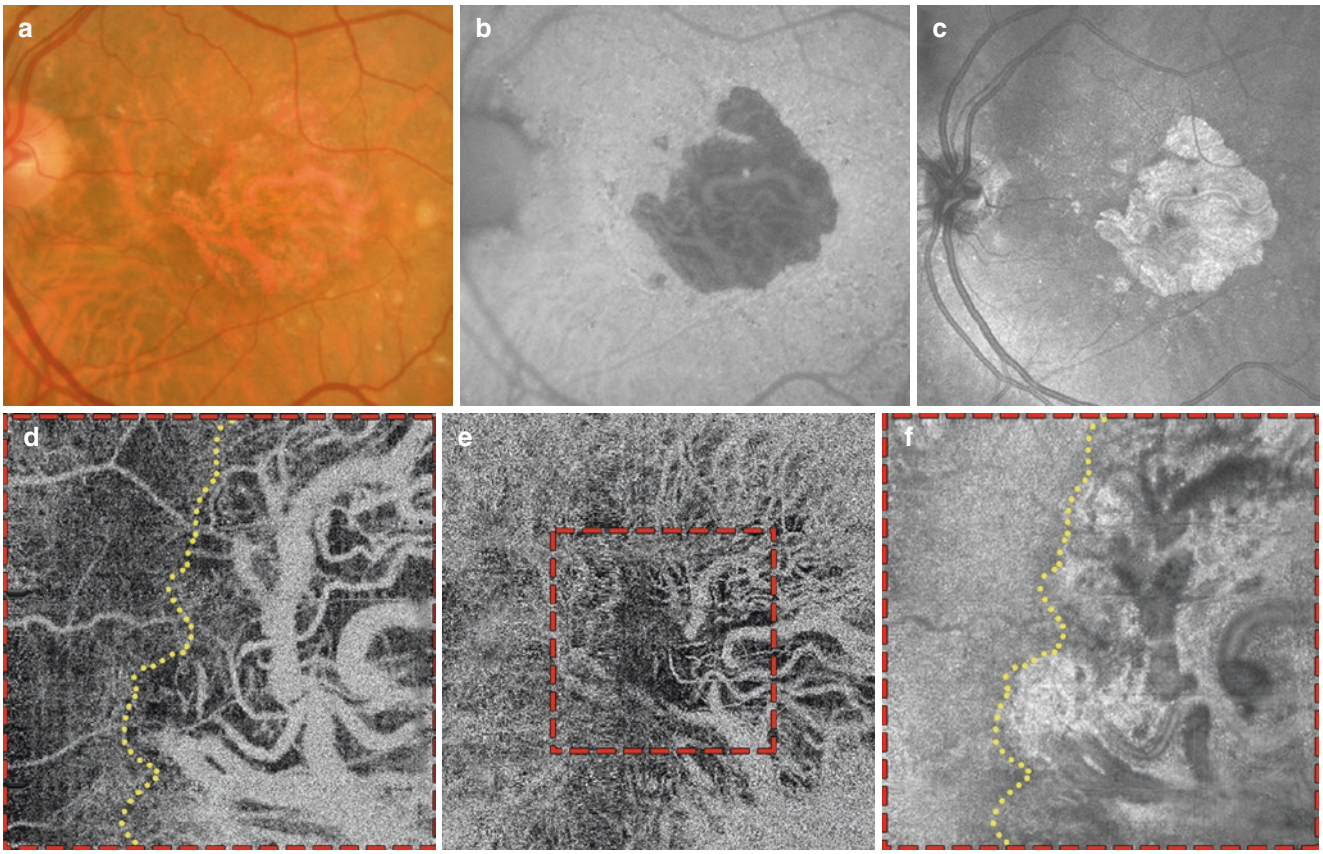

Fig. 3.4 Non-neovascular AMD. SS-OCT angiogram fields of view with color fundus photo. The left eye with geographic atrophy (GA) of a 62-year-old Caucasian man using the VCSEL SS-OCTA. (**a**) Color fundus photo showing the GA. (**b**) Fundus autofluorescence showing the GA. (**c**) Structural *en face* 9 × 9 mm showing the GA. (**d**) The 3 × 3 mm SS-OCTA of the choriocapillaris demonstrates flow impairment in a similar area as the area of RPE atrophy and larger choroidal vessels have been push inward into the area of choriocapillaris atrophy. (**e**, **f**) The 6 × 6 mm SS-OCTA of the choriocapillaris with a *red dotted line* around an approximately 3 × 3 mm area centered at the macula. (**f**) Structural *en face* SS-OCT-B 3 × 3 mm showing the GA

3.3 Central Serous Choroidal Retinopathy

Central serous chorioretinopathy (CSCR) usually affects young or middle-aged healthy individuals and can result in both acute, usually reversible, visual loss or in some cases a chronic decrease in visual acuity. Acute CSCR is caused by the rapid accumulation of subretinal fluid (SRF) in the macular area secondary to a focal leak in the RPE. The chronic form is believed to be due to more diffuse RPE changes located in the macula and is characterized by diffuse RPE leakage on the fluorescein angiography. It may or may not be associated with the presence of SRF. One or more serous retinal detachments of the neurosensory retina can be associated with the concurrent presence of one or more retinal pigment epithelium detachments (RPED) that can be located foveally, subfoveally, and perifoveally. Photoreceptor damage and permanent vision loss can result from persistent SRF [14].

Choroidal neovascularization (CNV) in CSCR is a potential cause of vision loss in the chronic form of the disease. It predominantly occurs in middle-aged to older male patients and is typically unilateral. It can be easily confused with CNV due to wet AMD.

FA and ICGA are considered the gold standard for imaging the retinal and choroidal vasculature. These modalities are dynamic and can visualize dye transit over time, allowing direct visualization of large vessel filling and eventual leakage and/or pooling of dye [15].

3.3.1 SS-OCTA Imaging of CNV Secondary to CSCR

SS-OCTA imaging is an important modality in diagnosing and managing patients with CSCR, particularly for the assessment of CNV in chronic CSCR. CSCR complicated with CNV is less often associated with subretinal hemorrhage compared to wet AMD, which makes it more suitable to be imaged with this technology, as subretinal hemorrhages can cause large areas of signal blockage and poor quality OCTA images. In cases in which hemorrhages are present, however, longer wavelength SS-OCTA will present better signal penetration and may have better visualization of vascular features of CNV compared to other commercially available SD-OCTA devices (see Fig. 3.5).

Structural and microvascular details of CNV and the presence of trunk vessels are more prominent on SS-OCTA compared to FA and ICGA. Trunk vessels are defined as large vessels with multiple branch points coming off a single location and can either be feeding or draining vessels. It is not possible to determine whether they are feeding or draining vessels on OCTA since it is a static study that cannot visualize blood flow over time. The corresponding *en face* SS-OCT is able to detect RPE alterations that are associated with choroidal abnormalities. SS-OCTA (see Fig. 3.6b, c) scans can be helpful to visualize the morphology of vessels at the periphery of the lesion, branching patterns, and vascular anastomoses (see Fig. 3.7) [1, 15].

The decreased signal roll-off and longer wavelength of the SS-OCT technology allow better interpretation of imaging of the choroidal vasculature, which allows for the assessment and diagnosis of co-existing CNV lesions to be detected even if they are non-exudative (see Figs. 3.5, 3.6 and 3.7). It can also better visualize the full extent of the neovascular membrane compared to commercially available SD-OCT devices [1, 7].

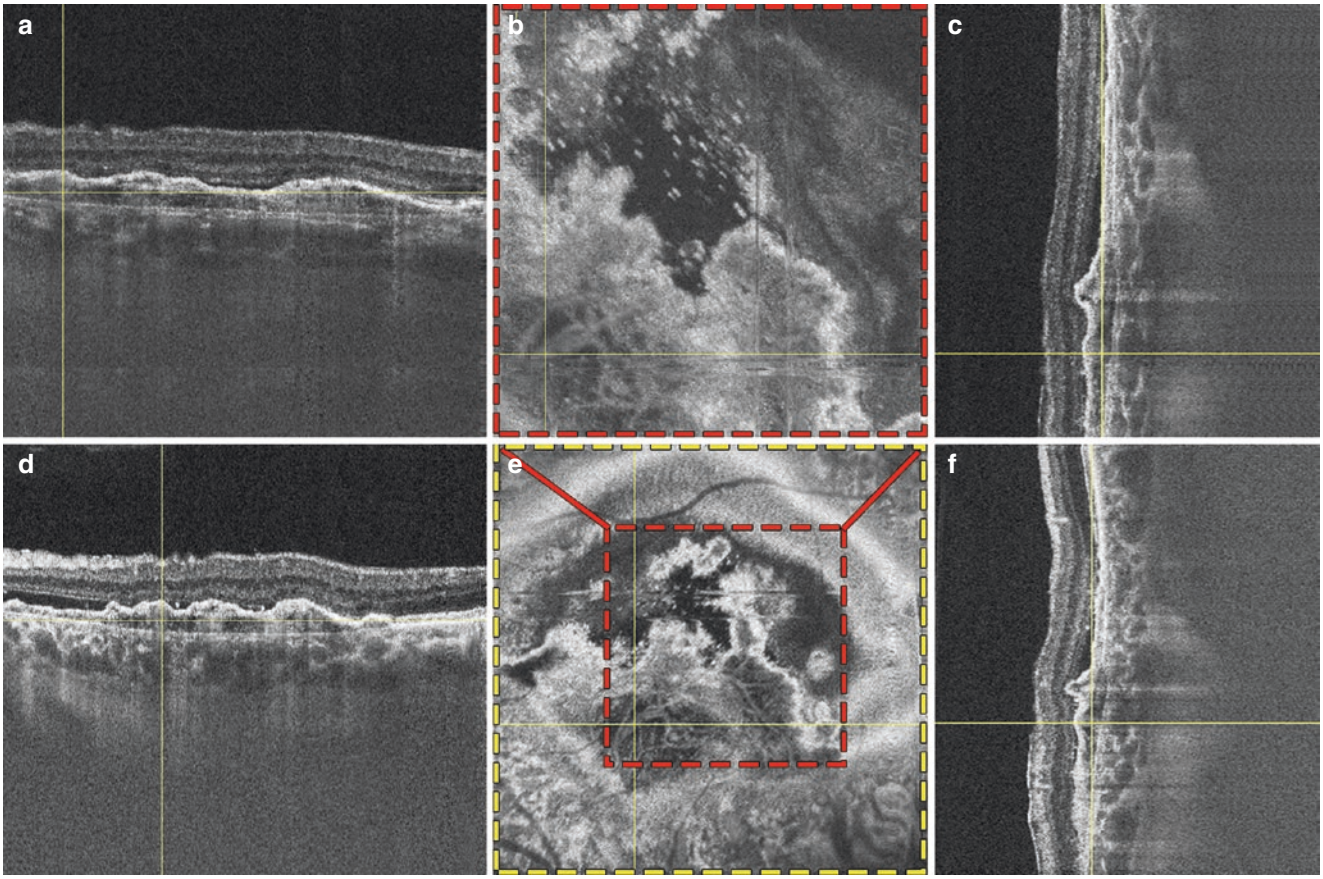

Fig. 3.5 SS-OCTA of type 1 choroidal neovascularization (CNV) in Chronic Central Serous Chorioretinopathy. The left eye of a 71-year-old Caucasian man using the VCSEL SS-OCTA. (**a**) Corresponding 3 × 3 mm X-Fast SS-OCT B-scan. (**b**) Unflattened Structural *en face* 3 × 3 mm SS-OCT at the level of the RPE. (**c**) Corresponding 3 × 3 mm Y-Fast SS-OCT B-scan. (**d**) Corresponding 6 × 6 mm X-Fast SS-OCT B-scan. (**e**) Unflattened Structural *en face* 6 × 6 mm SS-OCT at the level of the RPE. The *red dotted box* is the corresponding 3 × 3 mm. (**f**) Corresponding 6 × 6 mm Y-Fast SS-OCT B-scan

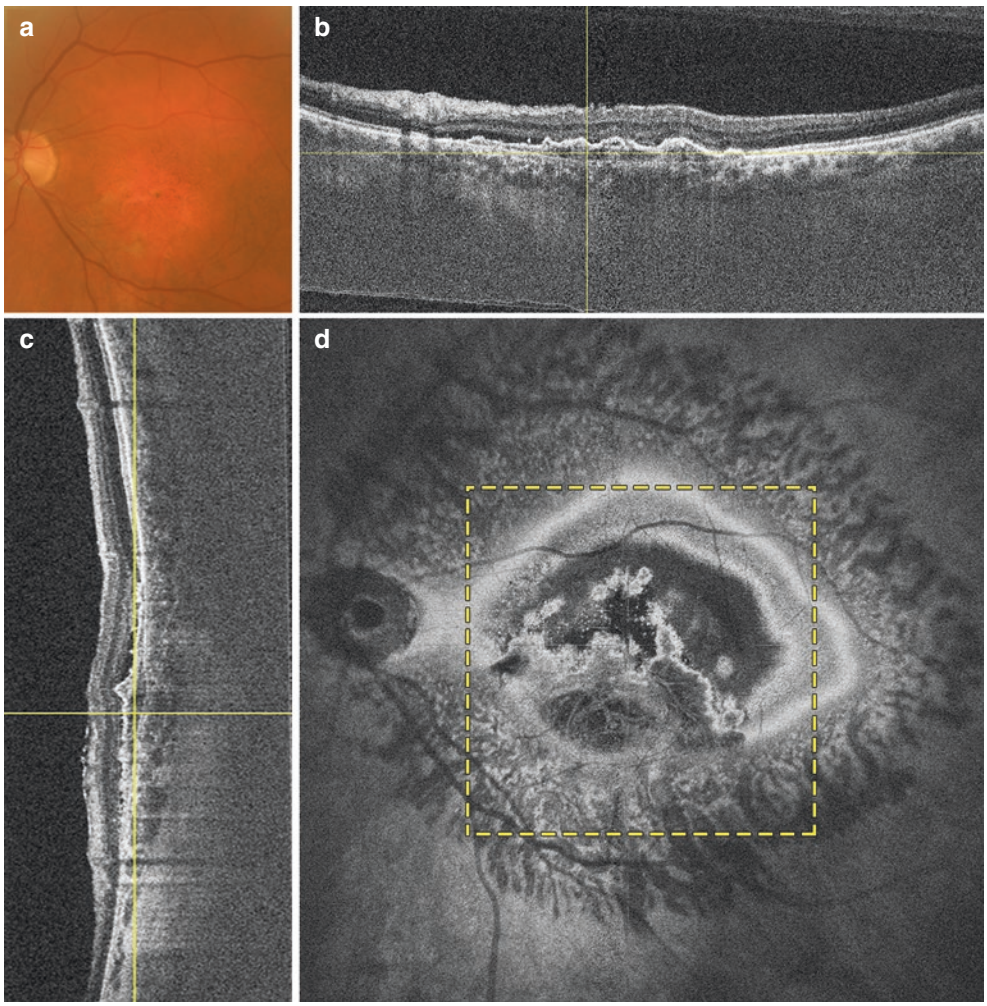

Fig. 3.6 SS-OCTA wide-field view 12 × 12 mm and segmentation layer and color fundus photo in type 1 choroidal neovascularization (CNV) in chronic central serous chorioretinopathy. The left eye of a 71-year-old Caucasian man using the VCSEL SS-OCTA. (**a**) Color fundus photo. (**b**) 12 × 12 mm X-Fast SS-OCT B-scan. (**c**) 12 × 12 mm Y-Fast SS-OCT B-scan. (**d**) Structural *en face* 12 × 12 mm with the *yellow dotted box* corresponding the 6 × 6 mm

Fig. 3.7 SS-OCT angiogram fields of view and segmentation layers. The left eye with type 1 choroidal neovascularization (CNV) in chronic central serous chorioretinopathy of a Caucasian man using the VCSEL SS-OCTA. (**a**) Structural *en face* 3 × 3 mm. (**b**) Color fundus photo. (**c**) Corresponding X-axis SS-OCT B-scan at the cross-section. (**d**) SS-OCTA retina of the choriocapillaris showing the type 1 CNV with the corresponding X-axis SS-OCT B-scan at the cross-section (*yellow horizontal line* in (**e**)). (**f**) SS-OCTA unthresholded of the choriocapillaris showing type 1 CNV with the corresponding X-axis SS-OCT B-scan at the cross-section (the *yellow horizontal line* in (**g**))

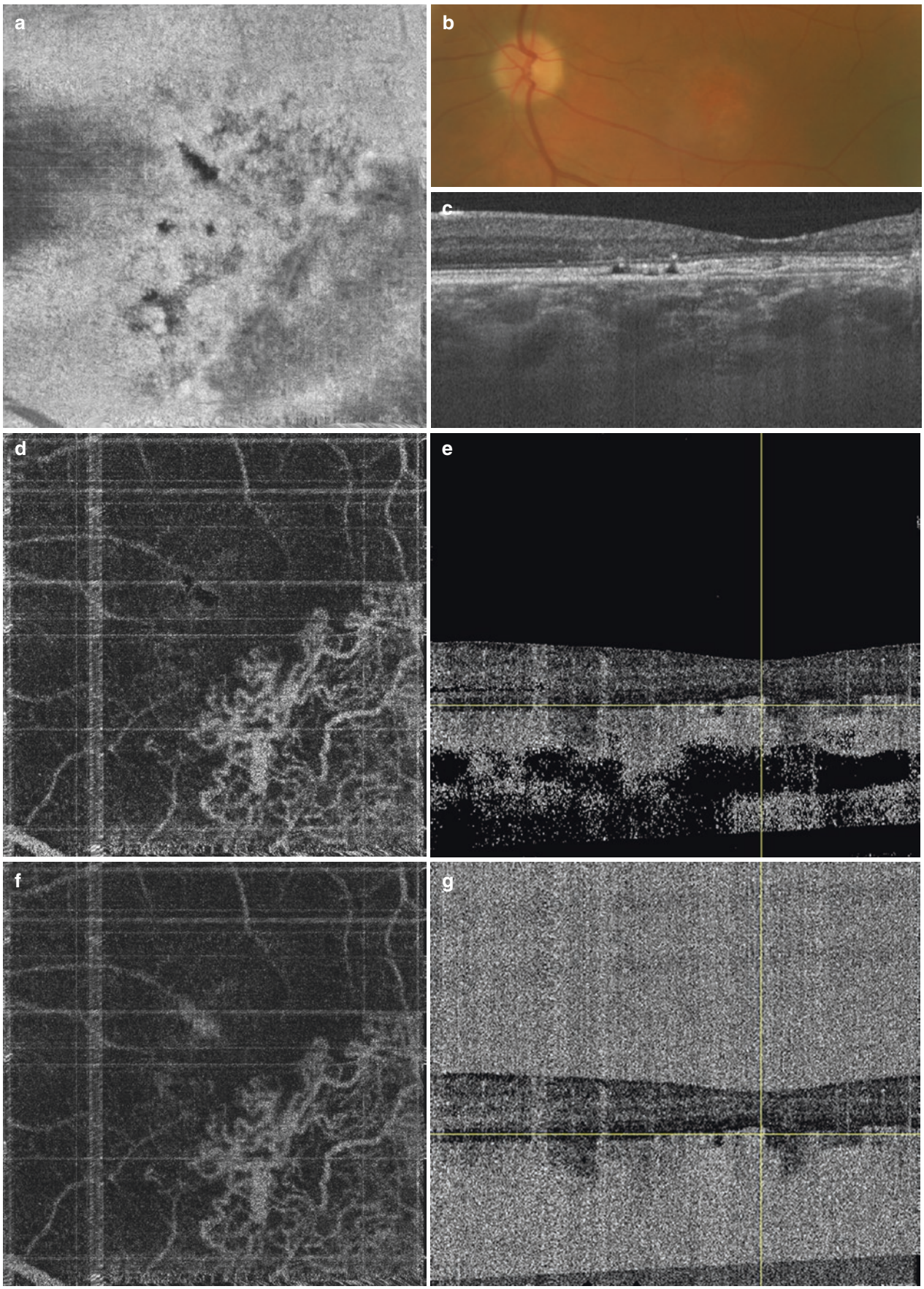
a
b
c
d
e
f
g

3.4 Polypoidal Choroidal Vasculopathy

Polypoidal choroidal vasculopathy (PCV) is characterized by the presence of recurrent serosanguineous PEDs and neurosensory retinal detachments, and is considered a variant form of CNV characterized by the presence of multiple polyps [16]. The vascular abnormalities underlying the disorder in PCV are thought to be a variant of a choroidal neovascular complex, which is composed of a branching vascular network with terminal polypoidal dilatations. ICG is regarded as the gold standard for the diagnosis of the PCV, as it can delineate the presence of single or multiple nodular areas of hyperfluorescence arising from the choroidal circulation with or without an associated branching vascular network. On SS-OCT angiography the increased penetration allows for improved imaging beneath the RPE. The structural *en face* SS-OCT can better visualize the microvascular structure of the polyps due to the longer wavelength with increased choroidal and decreased sensitivity roll-off (see Fig. 3.8) [7, 16].

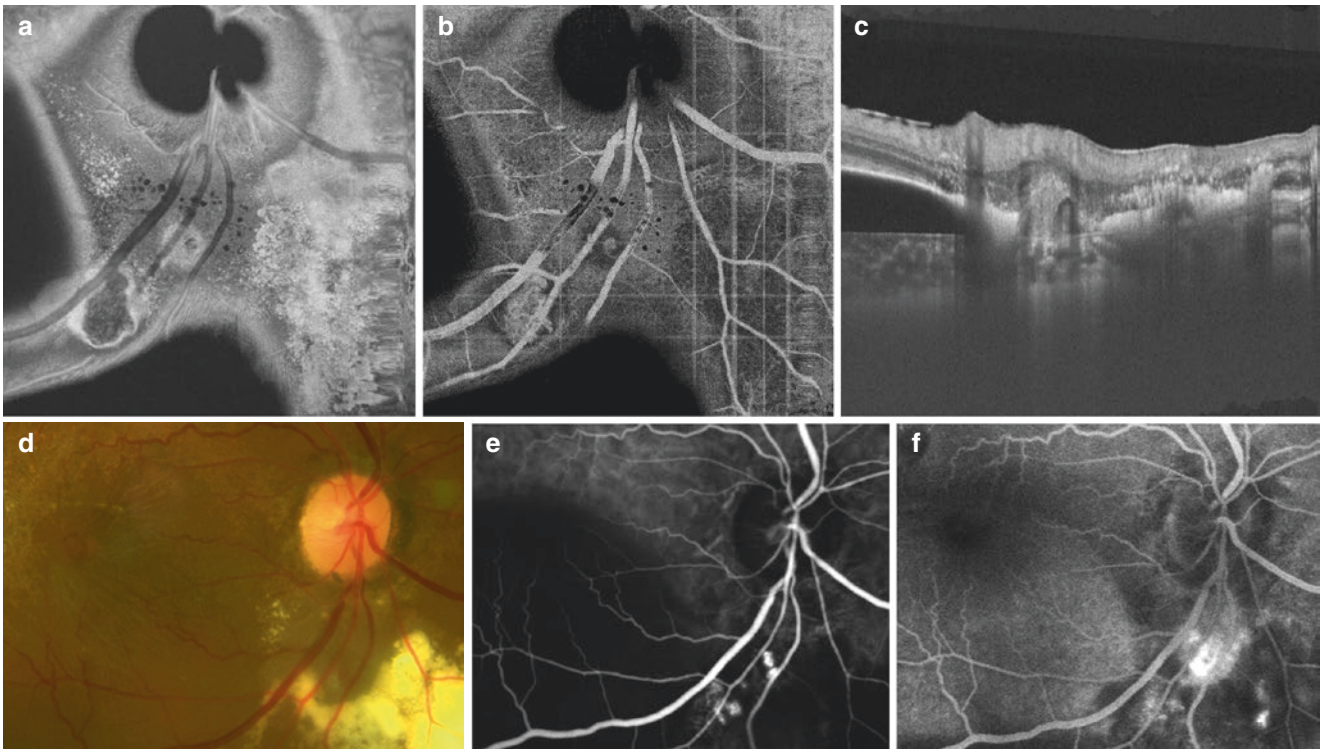

Fig. 3.8 Multimodal image of polypoidal choroidal vasculopathy (PCV). The right eye of a 62-year-old male using the VCSEL SS-OCTA. (**a**) Unflatten structural en face 3 × 3 mm SS-OCT angiogram. (**b**) Unflattened 3 × 3 mm SS-OCTA. (**c**) Corresponding SS-OCT B-scan. (**d**) Color fundus photo. (**e**) Fluorescein angiography. (**f**) Indocyanine green angiography

3.5 SS-OCT Angiography of Choroidal Nevi

Choroidal nevi are flat, benign, pigmented choroidal lesions that are neoplasms of melanocytes in the outer layers of the choroid. OCTA of choroidal nevi does not show blood flow or vascular structures inside the structure, and the choriocapillaris and choroidal vessels cannot be visualized on OCTA. The pigmented lesions cause OCT signal attenuation underneath the lesion, so structures below the RPE and choriocapillaris are difficult to visualize, even using SS-OCTA (see Fig. 3.9). Thicker nevi may obstruct blood flow to the RPE and outer retinal layers and lead to RPE and photoreceptor degeneration. Rarely, CNV can be associated with choroidal nevi [7, 17, 18].

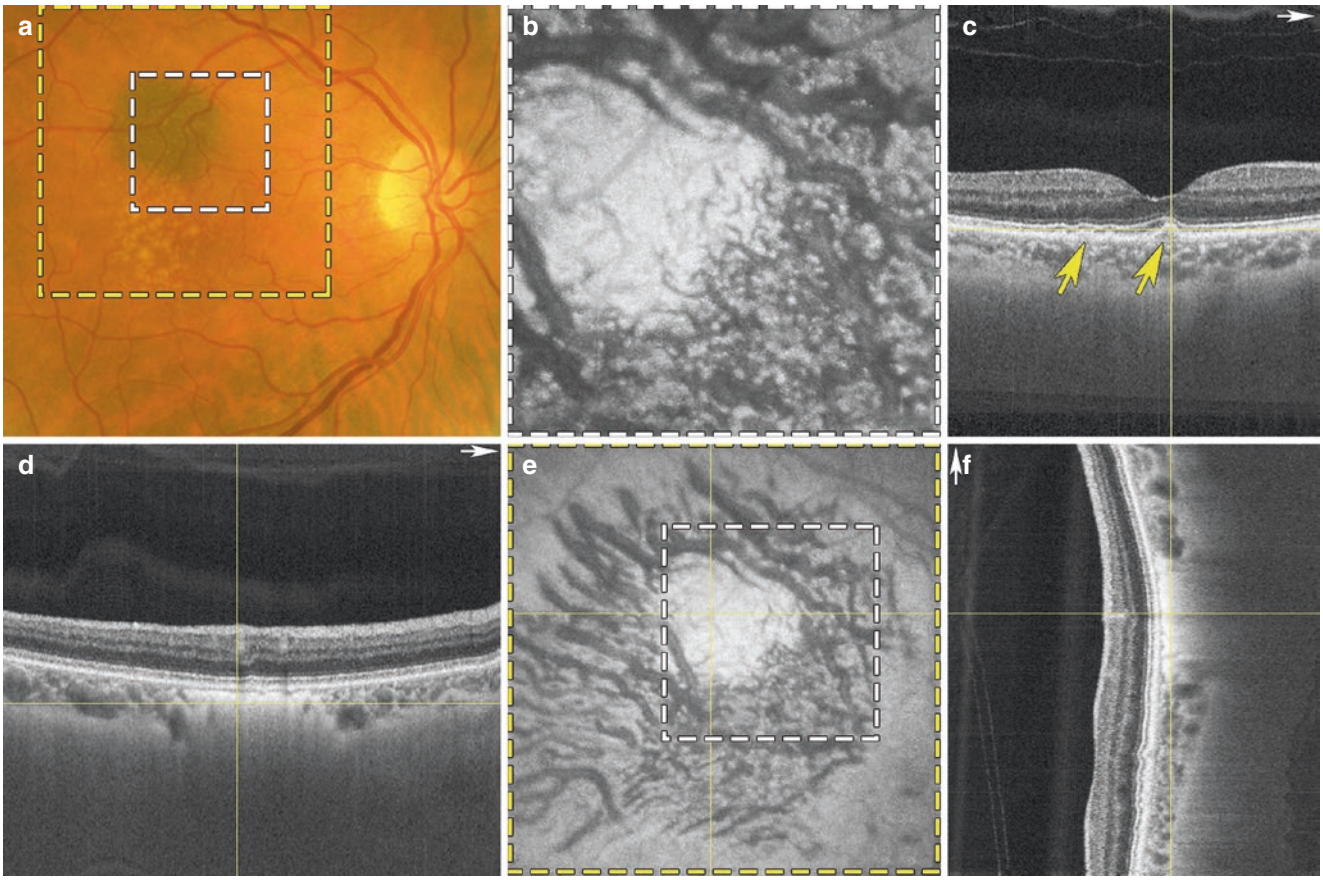

Fig. 3.9 SS-OCT angiogram fields of view and segmentation layers in nevus. The right eye with Choroidal nevi using the VCSEL SS-OCTA. (**a**) Color fundus photo showing the nevus. The *dotted white square* is zoomed in to an approximately 3 × 3 mm area and the *dotted yellow square* is zoomed in to an approximately 6 × 6 mm area centered at the macula. (**b**) Structural *en face* 3 × 3 mm showing the NEVI. (**c**) Corresponding X axis 3 mm SS-OCT B-scan at the cross-section. *Yellow arrows* show drusen surrounded the nevus. (**d**) Corresponding X-axis 6 mm SS-OCT B-scan at the cross-section (*horizontal yellow line* in (**e**)). (**e**) Structural *en face* 6 × 6 mm showing the nevus. The *dotted white square* is zoomed in to an approximately 3 × 3 mm area centered at the macula. (**f**) Corresponding Y-axis 6 mm SS-OCT B-scan at the cross-section demonstrated by the *horizontal yellow line* in (**e**)

Acknowledgments *The authors gratefully acknowledge Eduardo Novais and Mark Lane for assistance with imaging; ByungKun Lee and Chen Lu and Jonathan Liu for developing the swept source technology; Benjamin Potsaid and Alex Cable from Thorlabs; Vijaysekhar Jayaraman from Praevium Research for developing VCSEL laser technology; and Stefan Ploner, Julia Schottenhamml, and Lennart Husvogt for developing the Pipeline and Vista software.*

References

1. Novais EA, Adhi M, Moult EM, Louzada RN, Cole ED, Husvogt L, et al. Choroidal neovascularization analyzed on ultrahigh-speed swept-source optical coherence tomography angiography compared to spectral-domain optical coherence tomography angiography. Am J Ophthalmol. 2016;164:80–8.
2. Kraus MF, Potsaid B, Mayer MA, Bock R, Baumann B, Liu JJ, et al. Motion correction in optical coherence tomography volumes on a per A-scan basis using orthogonal scan patterns. Biomed Opt Express. 2012;3:1182–99.
3. Kraus MF, Liu JJ, Schottenhamml J, Chen CL, Budai A, Branchini L, et al. Quantitative 3D-OCT motion correction with tilt and illumination correction, robust similarity measure and regularization. Biomed Opt Express. 2014;5:2591–613.
4. Ota M, Tsujikawa A, Murakami T, Yamaike N, Sakamoto A, Kotera Y, et al. Foveal photoreceptor layer in eyes with persistent cystoid macular edema associated with branch retinal vein occlusion. Am J Ophthalmol. 2008;145:273–80.
5. Hayreh SS, Zimmerman MB. Fundus changes in branch retinal vein occlusion. Retina. 2015;35:1016–27.
6. Hayreh SS. Classification of central retinal vein occlusion. Ophthalmology. 1983;90:458–74.
7. Ferrara D, Waheed NK, Duker JS. Investigating the choriocapillaris and choroidal vasculature with new optical coherence tomography technologies. Prog Retin Eye Res. 2016;52:130–55. doi:10.1016/j.preteyeres.2015.10.002. Epub 2015 Oct 23
8. Seddon JM, Francis PJ, George S, Schultz DW, Rosner B, Klein ML. Association of CFH Y402H and LOC387715 A69S with progression of age-related macular degeneration. JAMA. 2007;297:1793–800.
9. Shah AR, Williams S, Baumal CR, Rosner B, Duker JS, Seddon JM. Predictors of response to intravitreal anti-vascular endothelial growth factor treatment of age-related macular degeneration. Am J Ophthalmol. 2016;163:154–66.e8.
10. Bhutto I, Lutty G. Understanding age-related macular degeneration (AMD): relationships between the photoreceptor/retinal pigment epithelium/Bruch's membrane/choriocapillaris complex. Mol Asp Med. 2012;33:295–317.
11. Lutty G, Grunwald J, Majji AB, Uyama M, Yoneya S. Changes in choriocapillaris and retinal pigment epithelium in age-related macular degeneration. Mol Vis. 1999;5:35.
12. McLeod DS, Grebe R, Bhutto I, Merges C, Baba T, Lutty GA. Relationship between RPE and choriocapillaris in age-related macular degeneration. Invest Ophthalmol Vis Sci. 2009;50:4982–91.
13. McLeod DS, Taomoto M, Otsuji T, Green WR, Sunness JS, Lutty GA. Quantifying changes in RPE and choroidal vasculature in eyes with age-related macular degeneration. Invest Ophthalmol Vis Sci. 2002;43:1986–93.
14. Spaide RF, Campeas L, Haas A, Yannuzzi LA, Fisher YL, Guyer DR, et al. Central serous chorioretinopathy in younger and older adults. Ophthalmology. 1996;103:2070–9. discussion 9–80
15. Kitaya N, Nagaoka T, Hikichi T, Sugawara R, Fukui K, Ishiko S, et al. Features of abnormal choroidal circulation in central serous chorioretinopathy. Br J Ophthalmol. 2003;87:709–12.
16. Yannuzzi LA, Sorenson J, Spaide RF, Lipson B. Idiopathic polypoidal choroidal vasculopathy (IPCV). Retina. 1990;10:1–8.
17. Callanan DG, Lewis ML, Byrne SF, Gass JD. Choroidal neovascularization associated with choroidal nevi. Arch Ophthalmol. 1993;111:789–94.
18. Shields CL, Mashayekhi A, Materin MA, Luo CK, Marr BP, Demirci H, et al. Optical coherence tomography of choroidal nevus in 120 patients. Retina. 2005;25:243–52.

Healthy Retinal Vasculature

4

Mayss Al-Sheikh and SriniVas R. Sadda

Swept source optical coherence tomography angiography (SS-OCTA) is a noninvasive technique used to compare the movement of blood over multiple B-scans to assess the retinal vasculature at a microscopic level three-dimensionally, without using any intravenous dye.

Previous anatomic studies showed that the retinal vessels were distributed in a superficial plexus, at the border between the ganglion cell layer and the nerve fiber layer, and a deep plexus, containing two layers of small-sized capillaries that bracket the inner nuclear layer [1].

OCT angiography (OCTA) confirmed those histological findings and allowed examination of the vessel plexus in the superficial and deep retinal layers with their different features [2]. The two plexuses that make up the deep capillary plexus may be considered a single "deep" layer; there may, however, be reasons to treat them as two individual layers ("intermediate" and "deep"), as there may be diseases that may affect them selectively (e.g., paracentral acute middle maculopathy versus acute macular neuroretinopathy). This is a topic that requires further study and most commercial OCTA instruments display only superficial and deep layers as a default.

The SS-OCTA examination described herein was performed using a device with a central wavelength of 1050 nm and an A-scan-rate of 100,000 scans per second (DRI OCT Triton, TOPCON). A 3 × 3 × 3 mm macula cube image was acquired, each cube consisting of 320 clusters of four repeated B-scans, each containing 320 A-scans. Tissue resolution was 7 and 20 μm in tissue (axial and transverse).

En face images of the retinal vasculature were generated from the superficial capillary layers (SCL) and deep capillary layers (DCL). The internal limiting membrane was used as the plane of reference. The superficial capillary layer was segmented, starting with the internal limiting membrane, including the ganglion cell layer to the inner boundary at the inner plexiform layer. The deep capillary plexus was segmented from the inner boundary of the inner plexiform layer, including the inner nuclear layer to the outer plexiform layer.

M. Al-Sheikh, MD (✉)
Doheny Image Reading Center, Doheny Eye Institute,
Los Angeles, CA, USA
e-mail: mayss.alsheikh@gmail.com

S.R. Sadda, MD
Department of Ophthalmology, David Geffen School of Medicine,
University of California, Los Angeles, CA, USA

© Springer International Publishing AG 2017

Z. Michalewska, J. Nawrocki (eds.), *Atlas of Swept Source Optical Coherence Tomography*,
DOI 10.1007/978-3-319-49840-9_4

4.1 The Superficial Capillary Layer

The superficial capillary plexus, located in the ganglion cell layer and the nerve fiber layer, is composed of long arterioles and venules that emanate from the superior and inferior vessel arcades. The arterioles and venules are connected by transverse capillaries, forming an interconnecting plexus (see Fig. 4.1). The capillary terminals form a continuous perifoveal ring.

4.2 The Deep Capillary Layer

The deep capillary plexus is located in the inner nuclear layer and external plexiform layer. Former histologic studies have shown this capillary network to consist of two layers bracketing the two borders of the inner nuclear layer. On OCTA with slab segmentation thickness of 30 μm, those two layers can be merged and considered as one deep plexus.

The deep retinal layer shows a polygonal-shaped capillary plexus, radially connected toward the center (see Fig. 4.2). It is believed that the center leads to a vertical interconnecting channel that connects the superficial and deep plexuses.

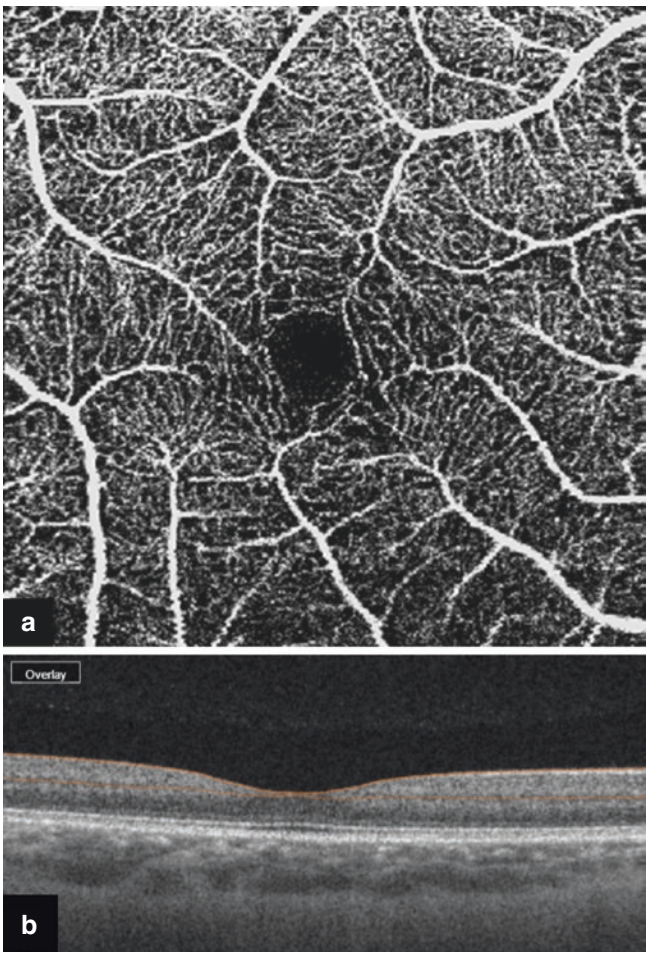

Fig. 4.1 (**a**) A 55 μm thick OCTA C-scan (autosegmented 3 × 3 mm) using the internal limiting membrane (ILM) as a plane of reference. The scan is taken from 2.6 μm underneath the ILM to 15.7 μm below the boundary between inner plexiform layer (IPL) and inner nuclear layer (INL) at the level of the ganglion cell layer (GCL), showing the arterioles and venules originating from the superior and inferior arcades and the transverse connecting capillaries. (**b**) The corresponding B-scan shows the precise segmentation of the superficial capillary layer

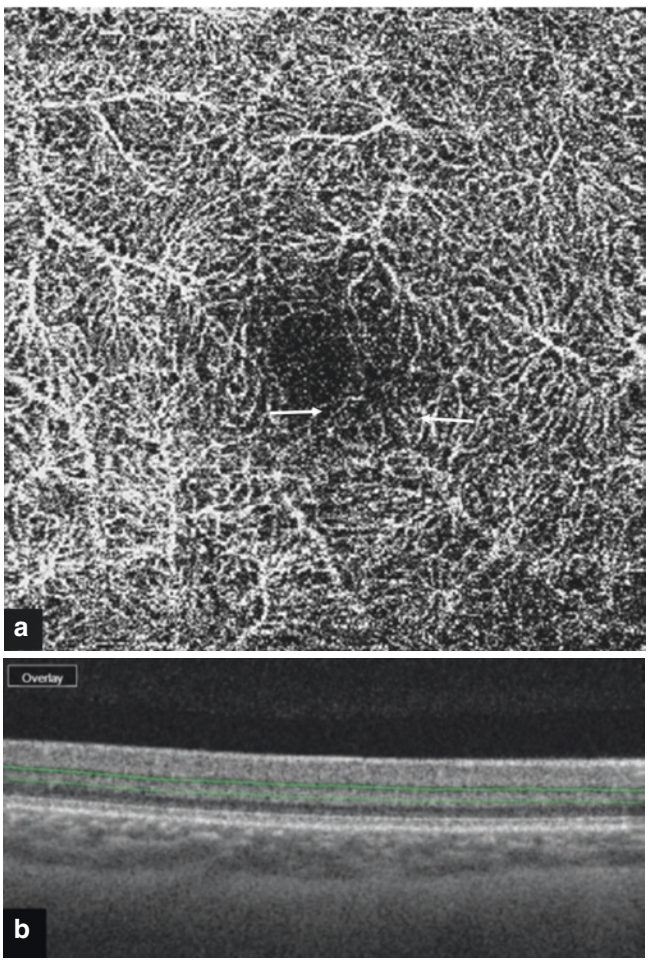

Fig. 4.2 (**a**) A 90 μm thick OCTA C-scan using of the deep capillary layer. The scan is taken from 15.7 μm underneath the inner plexiform layer (IPL)/inner nuclear layer (INL) to 70 μm underneath, at the level of the (INL). Some projection artifact from the superficial capillary layer can be seen (*arrows*). (**b**) The corresponding B-scan shows the precise segmentation of the deep capillary layer

4.3 The Outer Retina

Viewed on OCTA, the outer retina is avascular. Using high resolution SS-OCTA allows visualization of the different layers of the outer retina (see Fig. 4.3). The outer nuclear layer (ONL) and the Henle's fiber layer are localized between the external limiting membrane (ELM) and the outer plexiform layer (OPL). The ONL is relatively hyporeflective, but the Henle's layer may have variable reflectivity depending on the orientation of the light source relative to the plane of the retina at that location. The myoid zone, the next hyperreflective band in the outer retina, extends between the ELM and the ellipsoid zone and represents the myoid fraction of the inner segment of the photoreceptors. The ellipsoid zone is a hyperreflective band representing an interface between inner and outer photoreceptor segments. The outermost hyperreflective band is the interdigitation zone, anterior to the retina pigment epithelium (RPE), representing the contact cylinders composed of the apical processes of the RPE cells and tips of the cone photoreceptor outer segments.

4.4 The Choriocapillaris

The choriocapillaris, which is limited to the inner portion of the choroid, contains small vessels with fenestrated endothelial cells. The choriocapillaris supplies oxygen and other metabolites to the RPE and outer neurosensory retina.

The choroid has the highest blood flow per unit of tissue weight in the human body. The architecture of the choriocapillaris is still controversial. A lobular vasculature was detected in the posterior pole using scanning electron microscopy. Figure 4.4 shows "confluent" flow of the choriocapillaris on SS-OCTA; however the inter-sinusoidal spaces in the macula are likely at the transverse resolution limit of conventional OCT. In addition, using SS-OCTA based on motion as contrast has its limitations specifically for the choriocapillaris. Since this method detects flow velocity within a limited dynamic range, vascular flow in the choriocapillaris that is too slow will not be detected. Therefore, a focal "absence" of choriocapillaris on an OCTA image may be related to slower flow rather than absent flow.

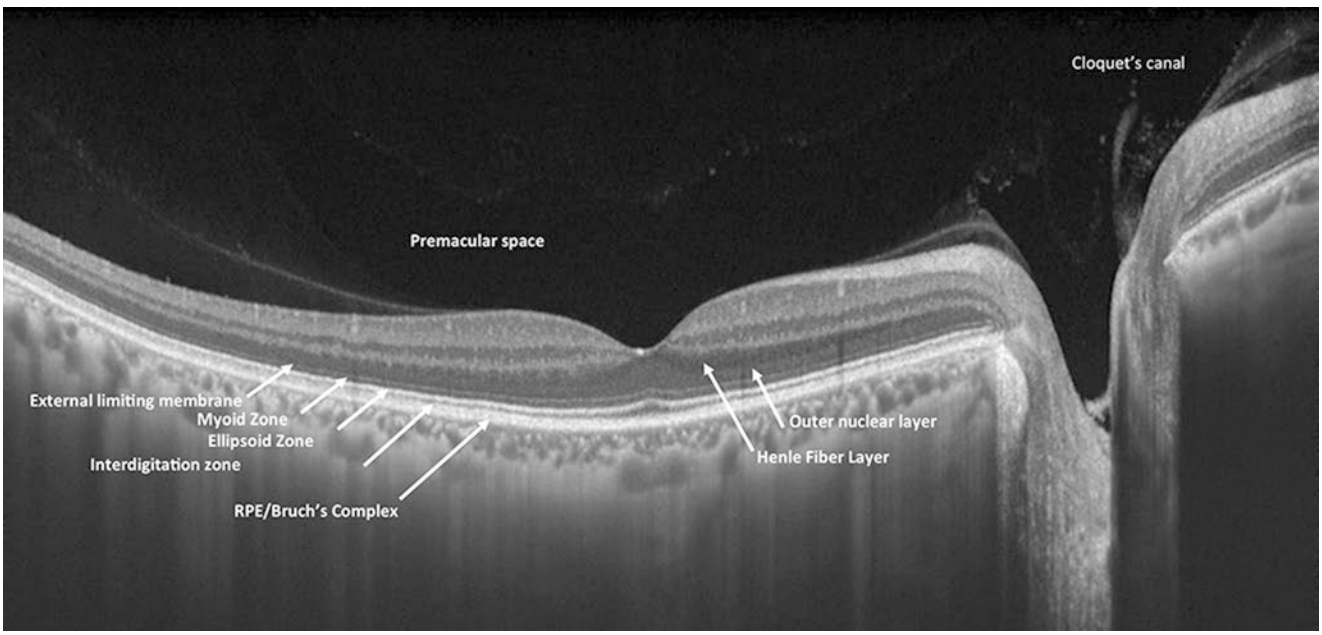

Fig. 4.3 Shows the different layers of the outer retina and vitreous

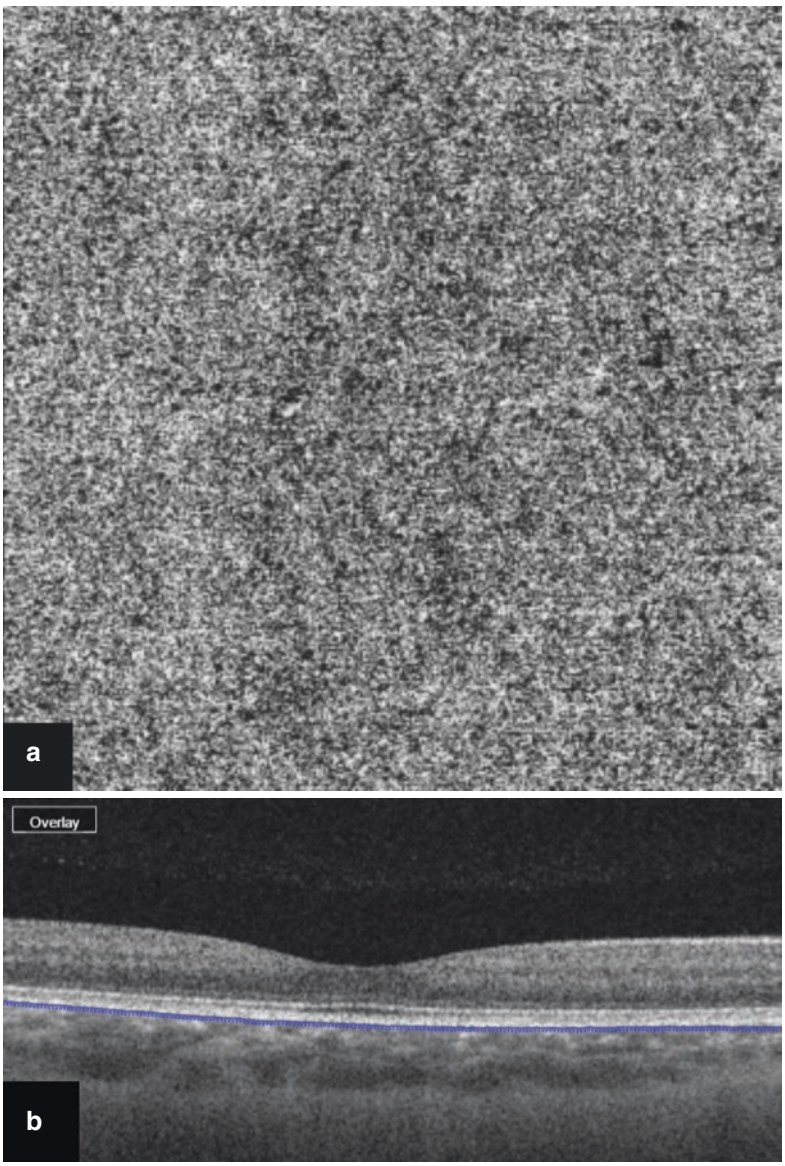

Fig. 4.4 (**a**) A 10 μm thick OCTA scan of the choriocapillaris using the Bruch's membrane as a plane of reference demonstrating the "confluent" flow of the choriocapillaris. (**b**) The corresponding B-scan shows the precise segmentation of the choriocapillaris

4.5 The Vitreous

The vitreous body, which consists of organized collagen fibers and hyaluronic acid, occupies about 80% of the eye volume. Based on the remarkable development of imaging techniques, recent studies have shown detailed observations of the posterior vitreous spaces using SS-OCT with increasing resolution and depth of field. Several optically empty spaces could be identified using SS-OCT [3, 4]. The first space overlies the macula and corresponds to the premacular bursa described by Worst. The second space overlies the optic nerve with a connection to the premacular space. This space corresponds to the previously described area of Martegiani. The anterior and superior extension of the premacular bursa shows a connection to the Cloquet's canal at variable distance from the optic disc (see Fig. 4.3).

References

1. Snodderly DM, Weinhaus RS. Retinal vasculature of the fovea of the squirrel monkey, Saimiri sciureus: three-dimensional architecture, visual screening, and relationships to the neuronal layers. J Comp Neurol. 1990;297:145–63.
2. Spaide RF, Klancnik Jr JM, Cooney MJ. Retinal vascular layers imaged by fluorescein angiography and optical coherence tomography angiography. JAMA Ophthalmol. 2015;133:45–50.
3. Schaal KB, Pang CE, Pozzoni MC, Engelbert M. The premacular bursa's shape revealed in vivo by swept-source optical coherence tomography. Ophthalmology. 2014;121:1020–8.
4. Stanga PE, Sala-Puigdollers A, Caputo S, Jaberansari H, Cien M, Gray J, et al. In vivo imaging of cortical vitreous using 1050-nm swept-source deep range imaging optical coherence tomography. Am J Ophthalmol. 2014;157:397–404.e2.

Swept Source OCT in Pseudodrusen

5

Hideyasu Oh

Pseudodrusen are pathological deposits that locate in the outer retinal layer. Unlike hard drusen and soft drusen, which are normally observed outside the retina pigment epithelium (RPE) layer, pseudodrusen are detected in the photoreceptor layer of the retina on swept source optical coherence tomography (SS-OCT) images. The characteristic morphology of pseudodrusen is that they are often conical, but can be rounded in some cases. They can also be well documented through the use of blue-light fundus photography and infrared scanning ophthalmoscopes. Clinically, pseudodrusen have been reported to be involved in the development of advanced age-related macular degeneration (AMD); detection is therefore crucial in the effort to prevent visual impairment.

5.1 Background

Pseudodrusen were first reported by Mimoun et al. as a yellowish interlacing pattern of macular lesions, and were best observed with blue-light fundus photography [1]. Arnold et al. [2] described the appearance as "reticular pseudodrusen" and proposed that the lesion might arise from the choroid. Subsequently, Schmitz-Valckenberg et al. reported that infrared scanning ophthalmoscopes are capable of effective illustration and diagnosis of the presence of pseudodrusen [3].

5.2 Classification

Based on spectral domain optical coherence tomography (SD-OCT) findings, Zweifel et al. [4] reported that pseudodrusen are subretinal drusenoid deposits, and classified them into three stages during disease progression. Stage 1 is defined as diffuse deposition of granular hyperreflective material between the retinal pigment epithelium and the ellipsoid zone. Stage 2 occurs when the contour of the ellipsoid zone is altered by accumulated material. In stage 3, the material becomes conical in shape and breaks through the ellipsoid zone.

Suzuki et al. recently proposed that pseudodrusen can be classified into three subtypes, based on multimodal fundus imaging [5]. The principal type, "dot pseudodrusen," is characterized as discrete dots on color photography, hyporeflective dots with target configuration on infrared scanning laser ophthalmoscope (IR-SLO), and subretinal accumulation of material with sharp peaks on SS-OCT (Figs. 5.1, 5.2, 5.3, 5.4 and 5.5). The second type, "ribbon pseudodrusen," is manifested as interlocking ribbons on color photography, faint hyporeflective ribbons on IR-SLO, and subretinal accumulation of material forming broad, rounded prominences on SS-OCT (Figs. 5.6, 5.7, 5.8, 5.9, 5.10 and 5.11). The third type, "peripheral pseudodrusen," is rare and has small individual globules on color fundus photography, hyperreflective spots on IR-SLO, and subretinal accumulation of material forming rounded elevations on SS-OCT.

H. Oh, MD, PhD
Department of Ophthalmology, Hyogo Prefectural Amagasaki General Medical Center (AGMC), Amagasaki, Hyogo, Japan
e-mail: hideyasu@kuhp.kyoto-u.ac.jp

© Springer International Publishing AG 2017

Z. Michalewska, J. Nawrocki (eds.), *Atlas of Swept Source Optical Coherence Tomography*,
DOI 10.1007/978-3-319-49840-9_5

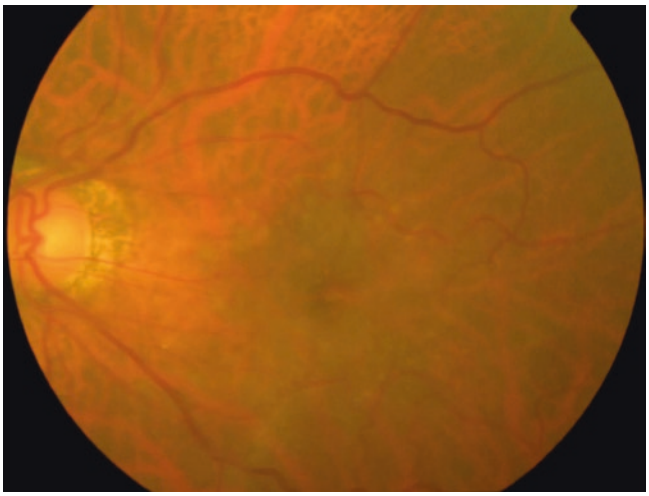

Fig. 5.1 A color fundus photograph of a case of dot pseudodrusen. A few pseudodrusen were documented

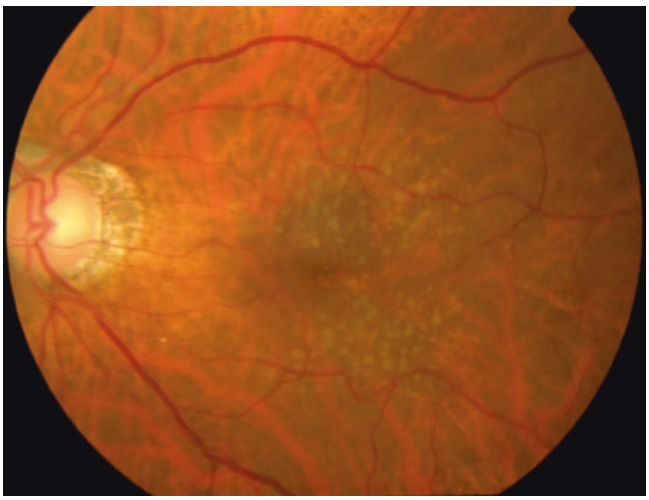

Fig. 5.2 One year later in the same eye, increased pseudodrusen were observed

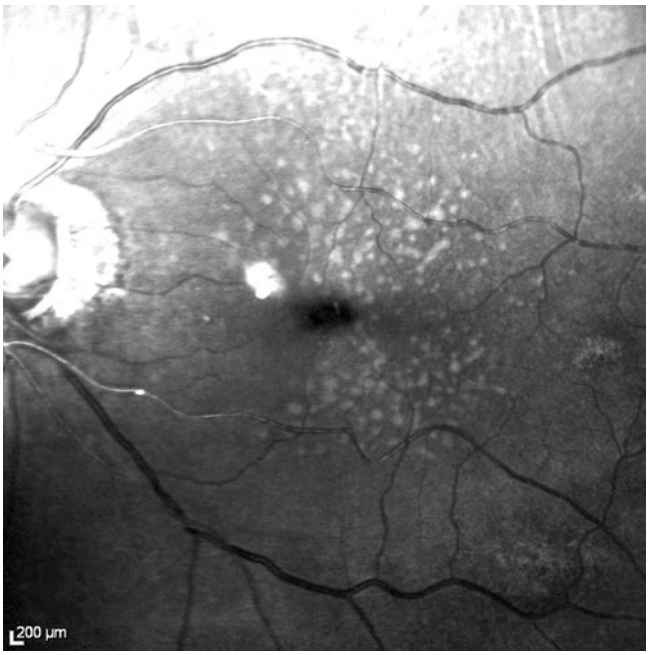

Fig. 5.3 Blue reflectance SLO image. The contour of individual pseudodrusen were clearly defined

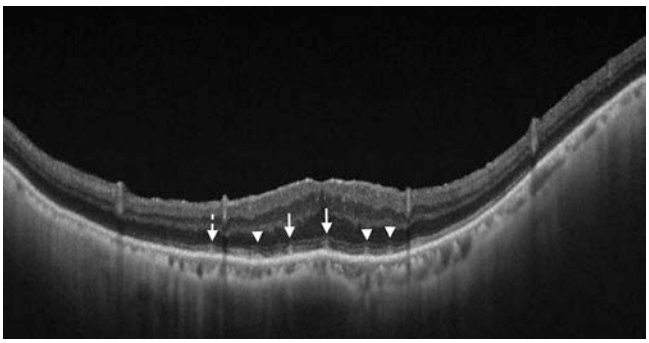

Fig. 5.4 SS-OCT image. Triangular or rounded hyperreflective deposits located in the outer retina. Note that the different stages of pseudodrusen were detected in this single scan image. *Dashed arrow*, *arrow heads*, and *arrows* indicate stage 1, 2, and 3 pseudodrusen respectively, according to the classification of Zweifel et al.

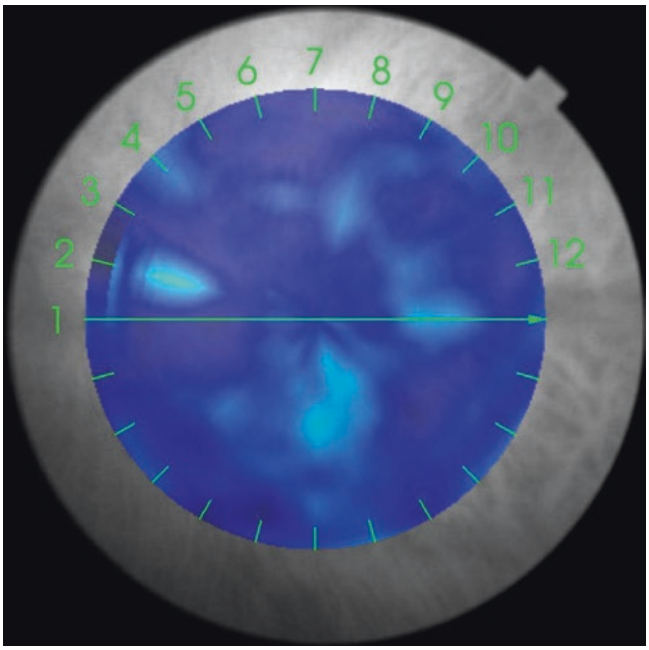

Fig. 5.5 A color-coded choroidal thickness map created from SS-OCT radial scans. Note that most parts of the macula are occupied with thin choroid

5.3 Clinical Implications

A prospective cohort study of subjects with unilateral choroidal neovascularization (CNV) and large soft drusen found that their fellow eyes with pseudodrusen at baseline have higher incidence of developing advanced AMD after 3 years of follow-up, as compared to those without pseudodrusen at baseline [6] (Figs. 5.6, 5.7, 5.8, 5.9, 5.10 and 5.11).

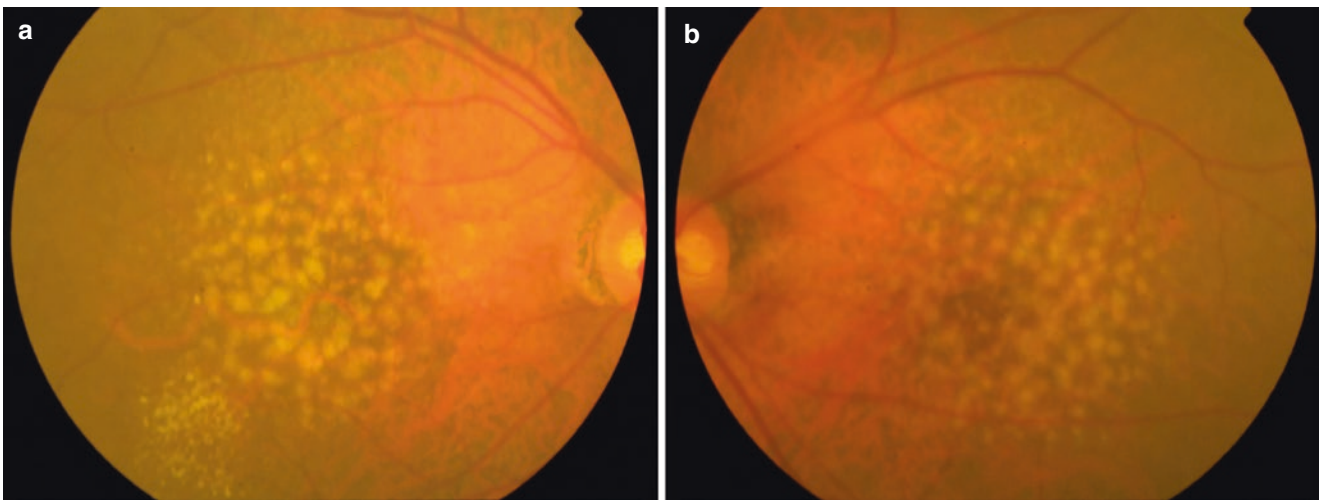

Fig. 5.6 Color fundus photographs of a case of a combination of ribbon and dot pseudodrusen ((**a**), right eye; (**b**), left eye)

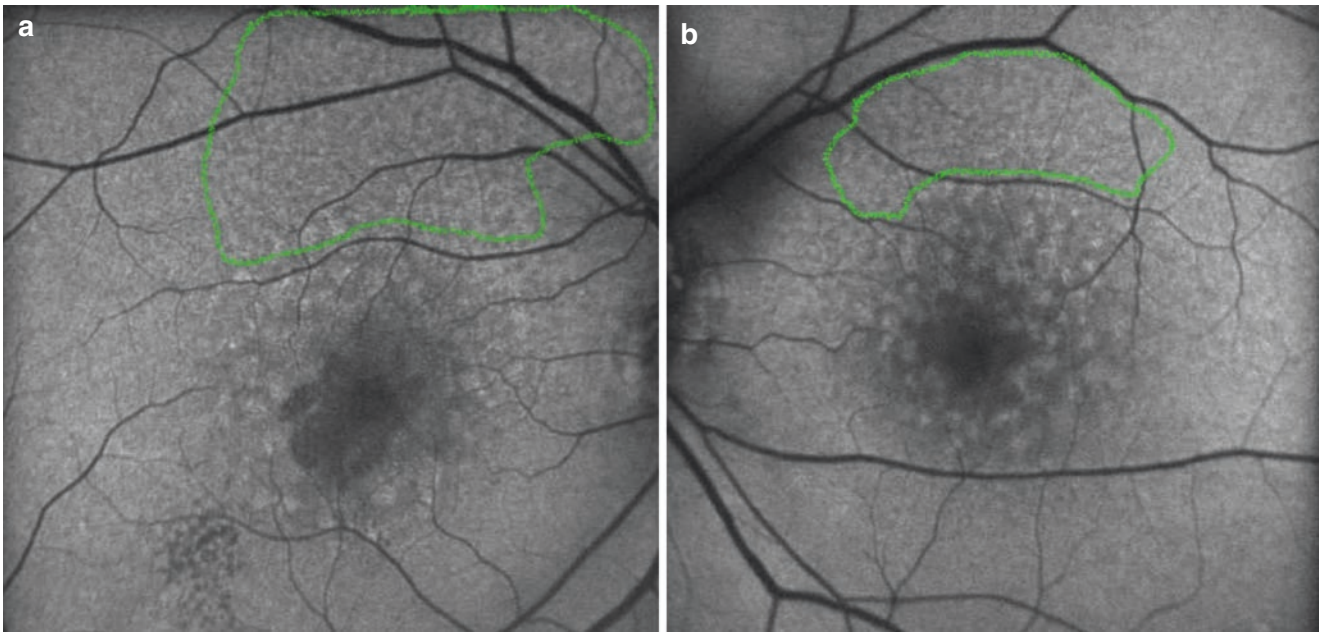

Fig. 5.7 Fundus autofluorescence images ((**a**), right eye; (**b**), left eye). A combination of ribbon and dot pseudodrusen exhibit hyporeflectivity (area within the *line*)

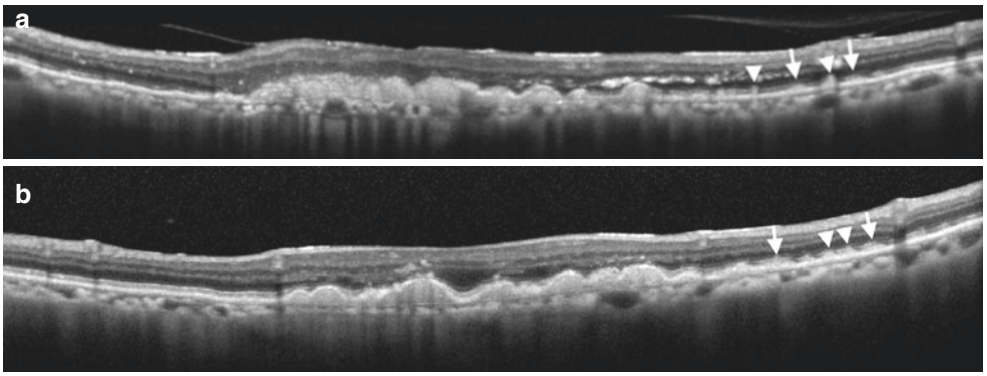

Fig. 5.8 Spectral domain OCT images ((**a**), right eye; (**b**); left eye). *Arrows* and *arrowheads* indicate ribbon and dot pseudodrusen, respectively

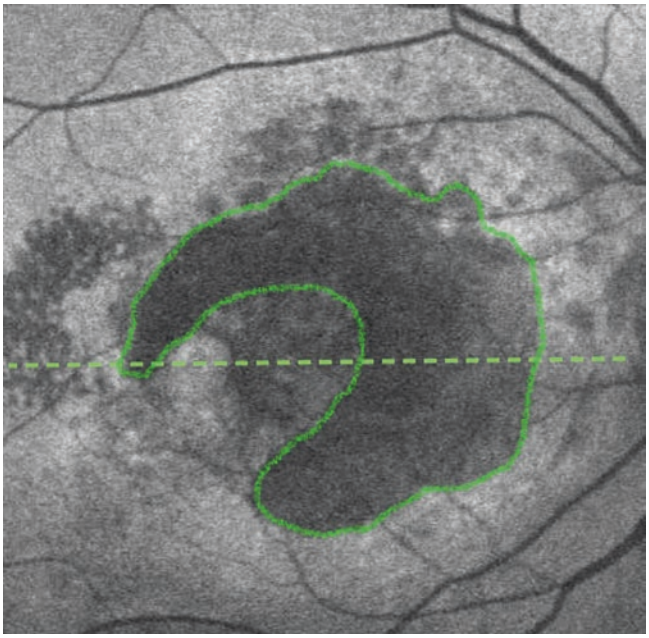

Fig. 5.9 Four years after the initial visit, the right eye developed choroidal neovascularization and an RPE tear. The fundus autofluorescence image shows the retina with denuded RPE due to an RPE tear (area within the *line*). The dashed line indicates the scan line in Fig. 5.11a

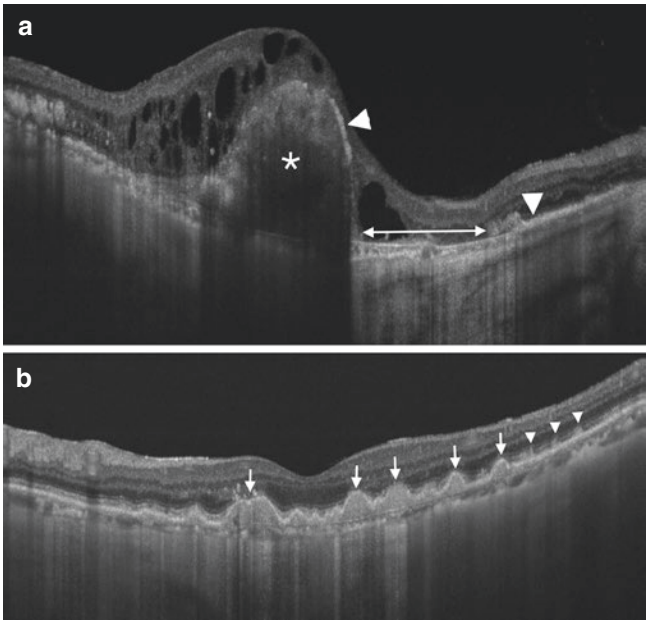

Fig. 5.11 SS-OCT images ((**a**), right eye; (**b**), left eye). (**a**) RPE layer (*arrowheads*), rolled RPE (*asterisk*), and area with denuded RPE (*double-headed arrow*). (**b**) Dot pseudodrusen (*arrowheads*) and drusen (*arrows*). Note that the choroidal thickness of both eyes is extremely thin

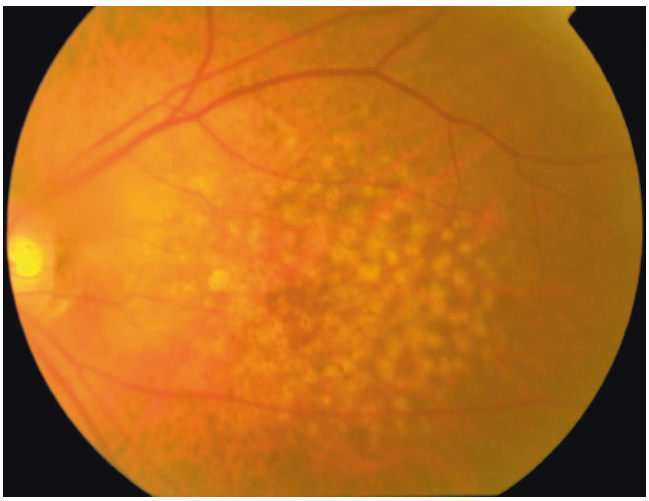

Fig. 5.10 Color fundus photograph of the left eye recorded at the same visit as in Fig. 5.9. No remarkable changes were detected

5.4 Choroidal Correlations

Grewal et al. recently reported that pseudodrusen are more likely to be located in the immediate proximity of the choroidal vessels when compared to the remaining control lesions [7]. By using a choroidal thickness/volume map created from 3D raster SS-OCT scans, Ueda-Arakawa et al. found that eyes with pseudodrusen commonly have a thin choroid regardless of choroidal neovascularization/geographic atrophy. They also reported that the area of choroidal vasculature is significantly reduced in eyes with pseudodrusen [8].

References

1. Mimoun G, Soubrane G, Coscas G. Macular drusen. J Fr Ophtalmol. 1990;13:511–30.
2. Arnold JJ, Sarks SH, Killingsworth MC, Sarks JP. Reticular pseudodrusen: a risk factor in age-related maculopathy. Retina. 1995;15:183–91.
3. Schmitz-Valckenberg S, Alten F, Steinberg JS, Jaffe GJ, Fleckenstein M, Mukesh BN, et al. Reticular drusen associated with geographic atrophy in age-related macular degeneration. Invest Ophthalmol Vis Sci. 2011;52:5009–15.
4. Zweifel SA, Spaide RF, Curcio CA, Malek G, Imamura Y. Reticular pseudodrusen are subretinal drusenoid deposits. Ophthalmol. 2010;117:303–12.e1.
5. Suzuki M, Sato T, Spaide RF. Pseudodrusen subtypes as delineated by multimodal imaging of the fundus. Am J Ophthalmol. 2014;157:1005–12.
6. Pumariega NM, Smith T, Sohrab M, LeTien V, Souied EH. A prospective study of reticular macular disease. Ophthalmol. 2011;118:1619–25.
7. Grewal DS, Chou J, Rollins SD, Fawzi AA. A pilot quantitative study of topographic correlation between reticular pseudodrusen and the choroidal vasculature using en face optical coherence tomography. PLoS One. 2014;9(3):e92841. doi:10.1371/journal.pone.0092841.
8. Ueda-Arakawa N, Ooto S, Ellabban AA, Takahashi A, Oishi A, Tamura H, et al. Macular choroidal thickness and volume of eyes with reticular pseudodrusen using swept-source optical coherence tomography. Am J Ophthalmol. 2014;157:994–1004.

En Face Swept Source OCT Study of Neovascular Age-Related Macular Degeneration

6

Ignacio Flores-Moreno, Luis Arias-Barquet, Jorge Ruiz-Medrano, José M. Ruiz-Moreno, and Josep M. Caminal

Swept source optical coherence tomography (SS-OCT) *en face* mode provides a coronal view of the posterior segment at different depths. This mode provided a way to explore the fundus similar to that of a routine slit-lamp examination, or traditional fundus photographs or angiography. It supplies more information than conventional cross-sectional imaging, allowing the physician to make a rapid diagnosis across the macula with a full macular view at different depths, which gives a three-dimensional perspective. When B-scan and *en face* mode are used together, they may provide additional anatomic insight into diseases in a non-invasive manner.

En face images are obtained after an automatic flattening at the desired depth, usually at the retinal pigment epithelium (RPE)—Bruch's membrane layers, using a three-dimensional volumetric scan. This segmentation provides better quality images due to the correction of the concavity of the eye, tilted tomography scans, anatomic distortions due to retinal edema, subretinal fibrosis, retinal pigment epithelium detachment, or choroidal excavation.

6.1 *En Face* OCT in Neovascular Age-Related Macular Degeneration

Our research group, studying neovascular age-related macular degeneration (nvAMD), has described the features of the RPE and the choroid and compared them with fluorescein angiography (FA) and/or indocyanine green angiography (ICGA) findings [1]. The investigators examined fundus photographs, areas of fluid leakage in early and late frames of FA and hyperfluorescent plaques, hot spots and polyps in early and late frames of ICGA, and *en face* SS-OCT images from 38 eyes with nvAMD including types 1, 2, and 3 of the new OCT-based nvAMD classification [2]. The choroid plays an important role in the etiology and physiopathology of types 1 (Fig. 6.1) and 2 (Fig. 6.2) and in the late stages of type 3.

RPE *en face* images revealed pathologic alterations in all the studied eyes. Changes in the RPE were classified into two groups: group 1, related to the neovascular lesion or group 2, surrounding the neovascular lesion. The extent of the neovascularization was determined using a multimodal imaging study, including FA, ICGA, and SS-OCT images. All the eyes had RPE defects within the neovascular area, and most of them (76%) showed a hyporeflective lesion. Forty-seven percent of the eyes had a defect surrounding the neovascular lesion, which was hyperreflective in 39% and hyporeflective in 61% of the cases. All the eyes showed changes in the choriocapillaris in *en face* imaging, and nearly 50% of them presented hyperreflective or hyporeflective alterations. The normal capillary pattern was interrupted at the neovascularization area in all the cases, considering the choriocapillaris the layer just behind the RPE.

Sattler and Haller's layers showed no changes in a few eyes corresponding to early (Fig. 6.3) and small neovascular membranes as determined by FA with minimal retinal anatomic distortion on B-scan SS-OCT and type 3 choroidal neovascularization (CNV). The rest of the patients showed mostly hyperreflective changes at these layers. No differences were found between the neovascular complex area, horizontal and vertical diameters, measured by *en face* SS-OCT and FA [1].

I. Flores-Moreno, MD, PhD
Clínico San Carlos University Hospital, Madrid, Spain

Bellvitge University Hospital, Hospitalet de Llobregat, Barcelona, Spain

L. Arias-Barquet, MD, PhD • J.M. Caminal, MD, PhD
Bellvitge University Hospital, Hospitalet de Llobregat, Barcelona, Spain

J. Ruiz-Medrano, MD (✉)
Clínico San Carlos University Hospital, Madrid, Spain
e-mail: jorge.ruizmedrano@gmail.com

J.M. Ruiz-Moreno, MD, PhD
Castilla La Mancha University,
Albacete, Spain

© Springer International Publishing AG 2017

Z. Michalewska, J. Nawrocki (eds.), *Atlas of Swept Source Optical Coherence Tomography*,
DOI 10.1007/978-3-319-49840-9_6

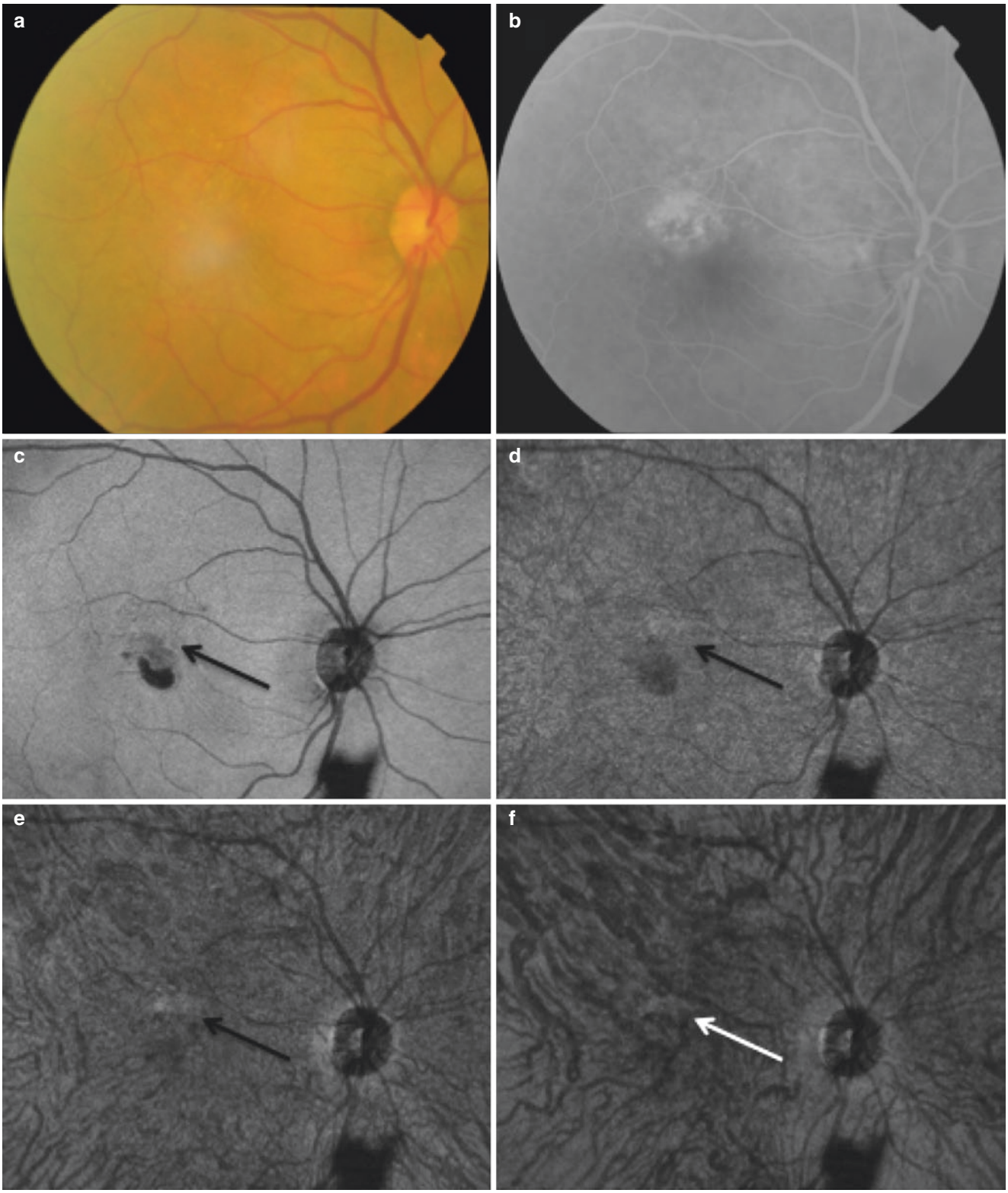

Fig. 6.1 Neovascularization type 1 *en face* SS-OCT. An 80-year-old male diagnosed with neovascularization type 1 in his right eye. In the fundus photograph, changes in retinal pigment epithelium (RPE) and subretinal fluid, superior to the fovea, are shown (**a**) and choroidal neovascularization is confirmed in fluorescein angiography (**b**). At the level of RPE (**c**), *en face* scan shows a granulate hyperreflective area just above a dark area that corresponds with a RPE detachment associated to the neovascular complex. A hyperreflective area represents the neovascular lesion in choriocapillaris (**d**), Sattler's (**e**), and Haller's layers (**f**) level

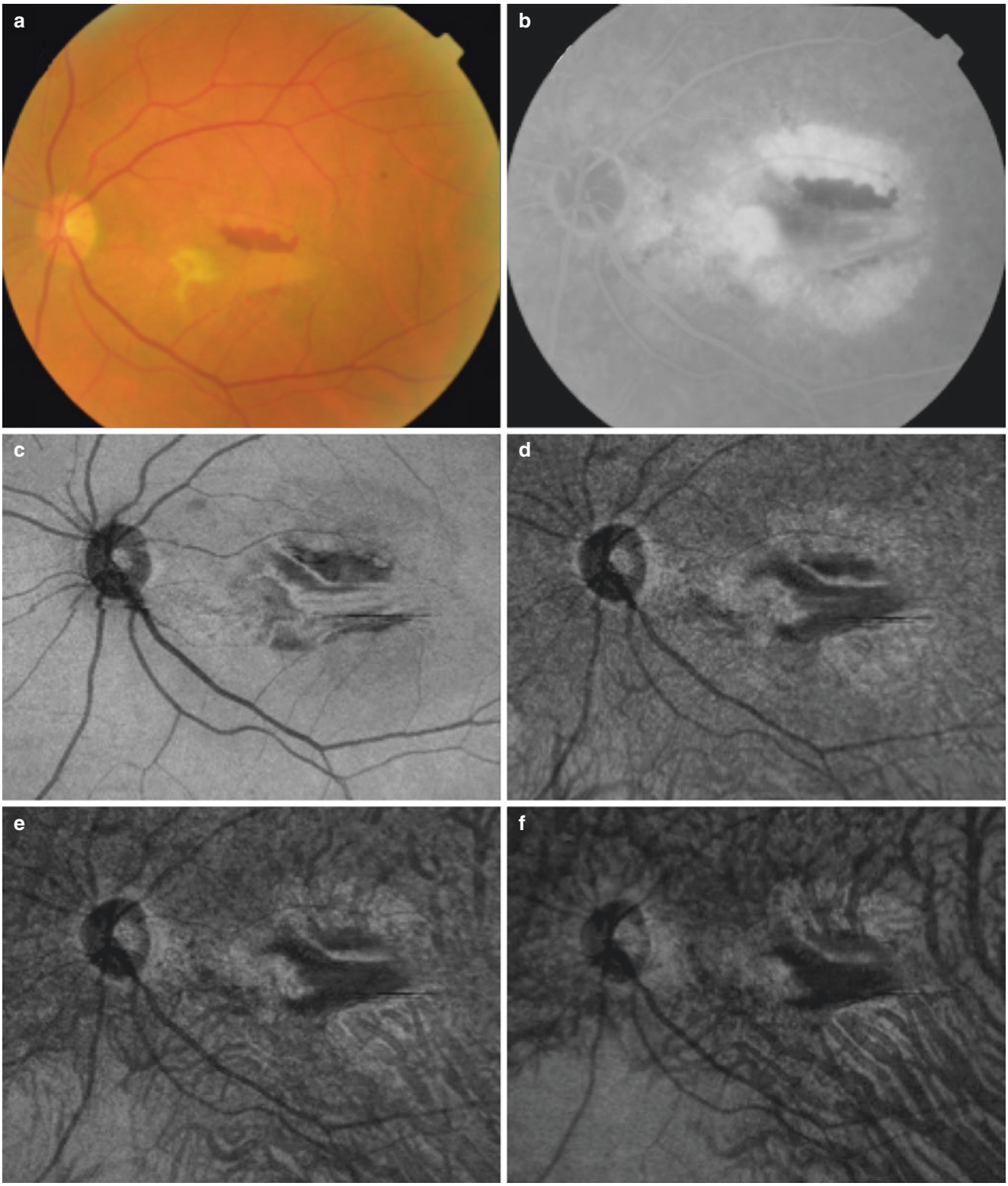

Fig. 6.2 Neovascularization type 2 *en face* SS-OCT. An 81-year-old female diagnosed with neovascularization type 2 in the left eye. A neovascular membrane associated with a subretinal fibrotic area with a macular hemorrhage is observed in fundus photograph (**a**). Fluorescein angiography confirms the neovascular complex with an extensive macular area of leakage (**b**). *En face* SS-OCT at retinal pigment epithelium (RPE) level shows hyporeflective changes corresponding with the area of leakage and a darker area corresponding with the macular hemorrhage (**c**). The corresponding areas of the neovascular complex in choriocapillaris (**d**), Sattler's (**e**), and Haller's (**f**) are seen with hyperreflective changes

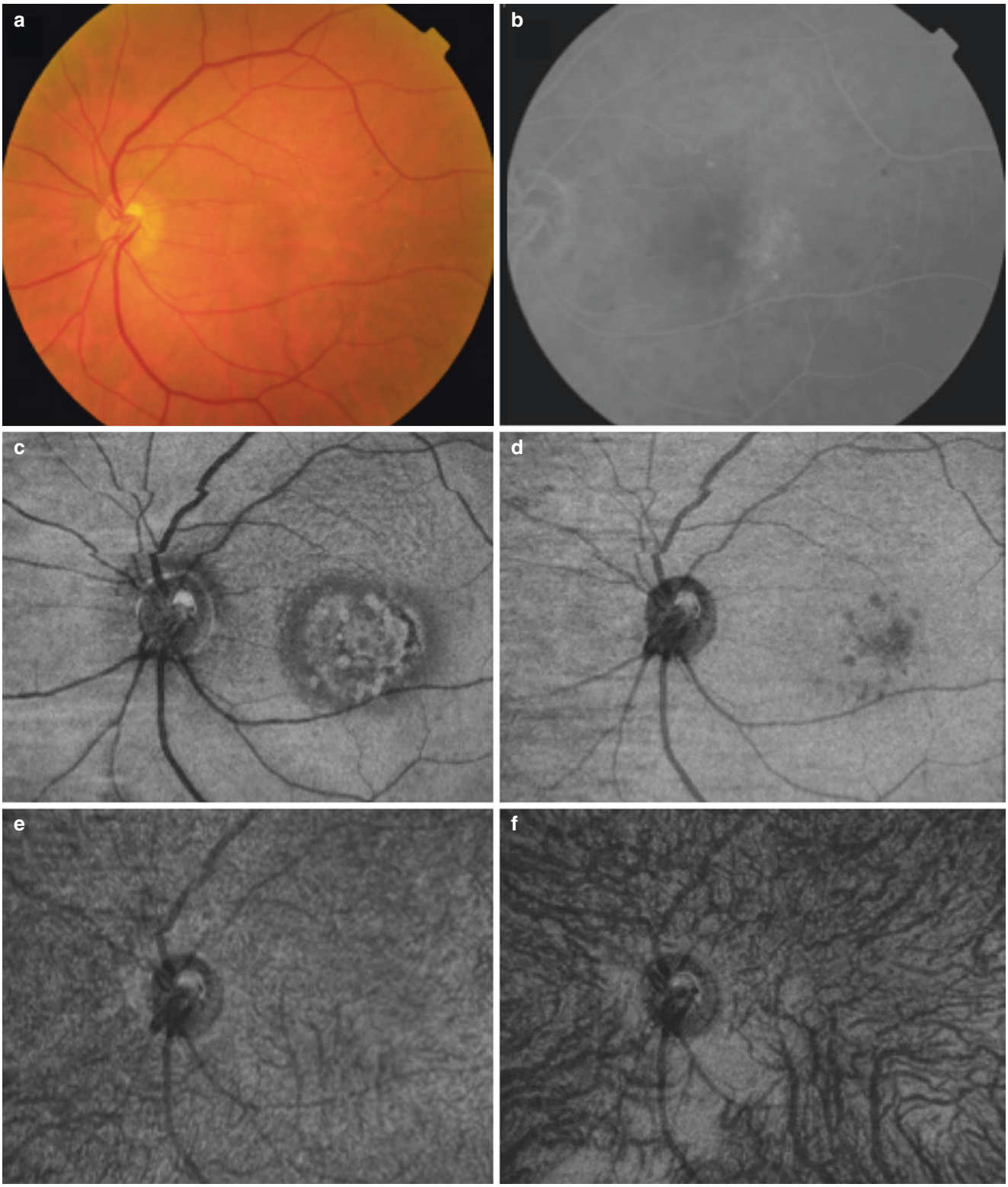

Fig. 6.3 *En face* SS-OCT in neovascular AMD. A recently diagnosed neovascular AMD with subtle changes is shown in fundus photograph (**a**). A neovascular complex is confirmed in fluorescein angiography, with most of the leakage temporal in the macular area (**b**). *En face* SS-OCT at retinal pigment epithelium level shows mottled hyperreflective changes at the foveal and perifoveal area, with a surrounding hyporeflective halo (**c**). The choriocapillaris level presents mottled hyporeflective changes at the center of the macula (**d**). No changes in the vascular patter of deeper layers are present in this patient (**e**, **f**)

6.2 SS-OCT Angiography in Neovascular Age-Related Macular Degeneration

SS-OCTA is a new technology that visualizes vasculature using motion contrast, without using exogenous dyes [3]. Repeated scanning at the same location detects moving tissue, which the device converts into an SS-OCT signal, and, simply, everything that the device detects as moving is translated in blood flow [3].

Type 1 neovascularization in AMD has been studied with SS-OCTA [4]. Two distinct forms were identified in 76% of the eyes studied. The most frequent pattern was the "medusa" form, which was defined as a neovascular membrane in which the vessels branched in all directions from the center of the lesion. The "seafan" form corresponds with a membrane that 90% of the lesion radiates from one side. Seventy-eight percent of the "medusa" form and 57% of the "seafan" form had a visible feeder vessel (Figs. 6.4, 6.5 and 6.6) [4].

Type 3 lesions have also been described using SS-OCTA. Twenty-nine eyes diagnosed with type 3 neovascularization in AMD were studied. Only 34% of the membranes could be detected using SS-OCTA, but these comprised 63% of the lesions that were active at the moment of the study. The neovascular complexes appeared as small tufts of bright, high-flow minuscule vessels with curvilinear morphology in the outer retinal layers [5]. Neovascular complex in retinal angiomatous proliferation are usually very small, even to perfectly delimited, in AF, so SS-OCTA could be a promising technique for this entity.

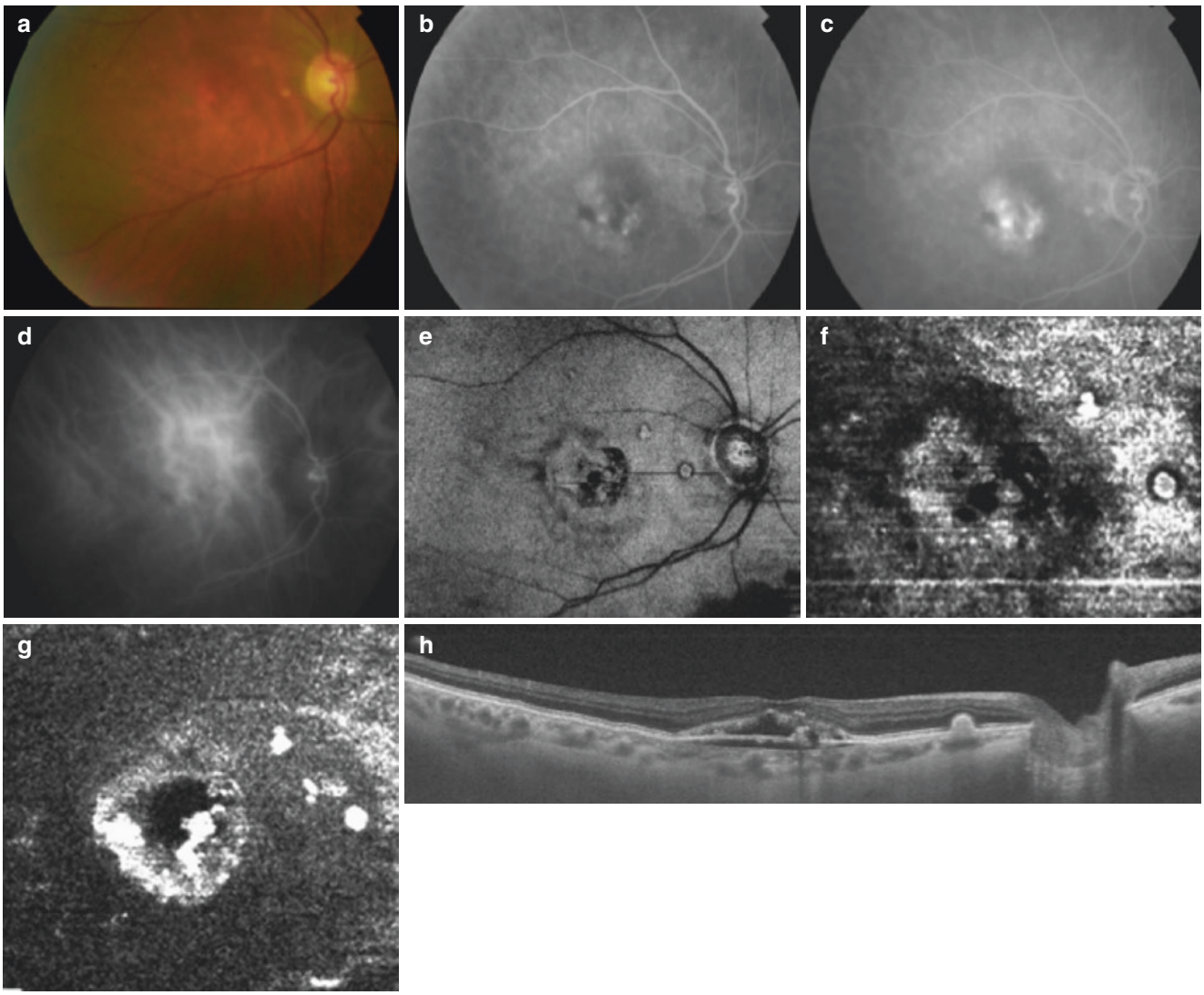

Fig. 6.4 *En face* and SS-OCTA in neovascular AMD. Fundus photograph (**a**), early frames (**b**), and late frames of fluorescein angiography (**c**) show a classic neovascular lesion in the right eye of this patient. Indocyanine green angiography doesn't show any abnormality (**d**). *En face* SS-OCT scan at retinal pigment epithelium (RPE) level shows hyporeflective changes at the neovascular complex level and also at the fibrovascular RPE detachment level (**e**). Drusenoid RPE detachment at the papillomacular bundle is presented hyperreflective in the *en face* scan (**e**). SS-OCTA shows a hyperreflective lesion corresponding to the neovascular complex at the superficial retinal capillary plexus (**f**) and deep retinal plexus (**g**). B-scan SS-OCT shows subretinal fluid, with shaggy photoreceptors and a flat RPE detachment (**h**)

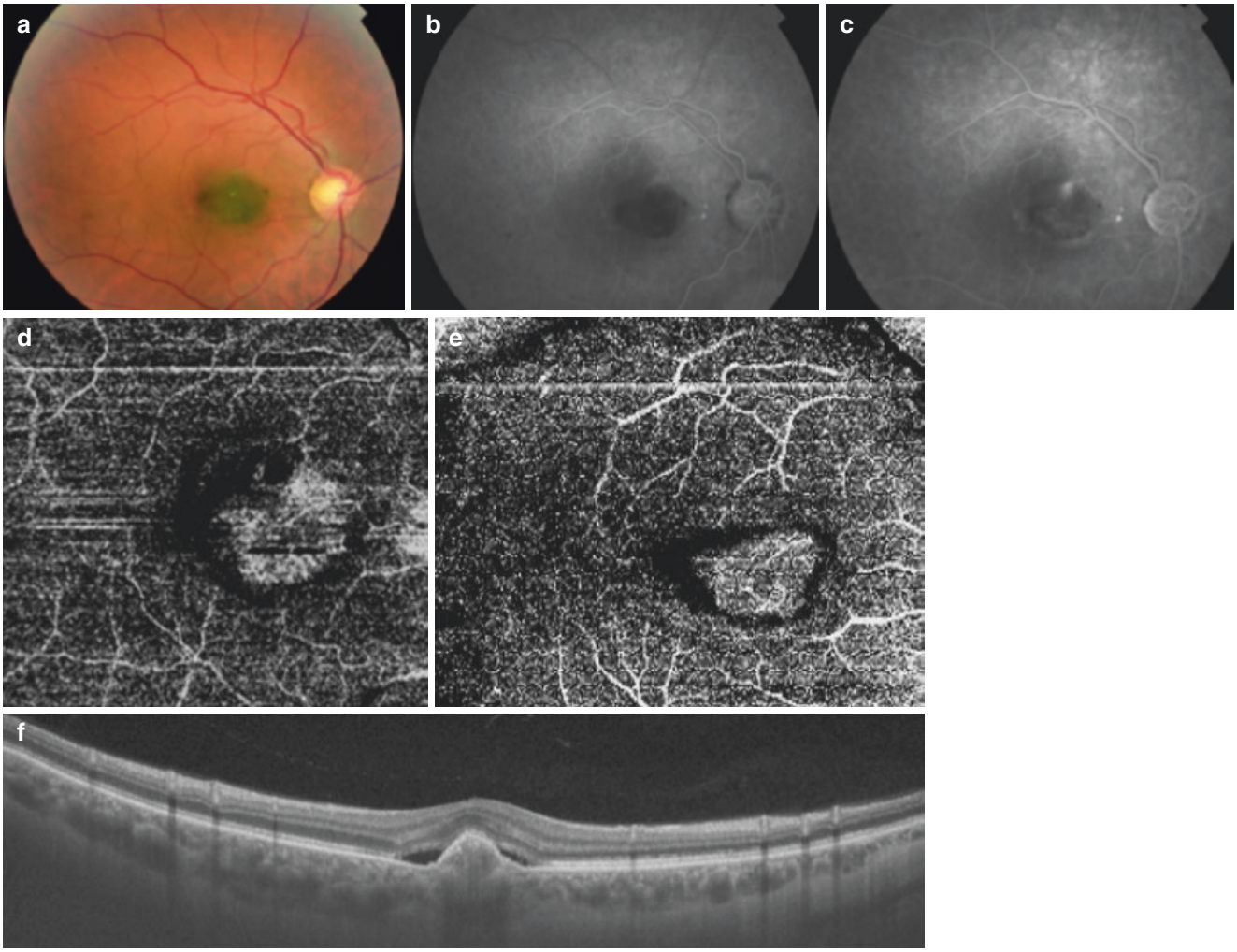

Fig. 6.5 SS-OCTA in neovascular AMD. A pigmented lesion is shown in this patient (**a**), who complains of a decrease in visual acuity. Neovascular AMD is confirmed in early (**b**) and late frames (**c**) of fluorescein angiography. The neovascular membrane is clearly defined at the superficial (**d**) and deep retinal capillary plexus (**e**) in the SS-OCTA images. B-scan SS-OCT shows subretinal fluid at both sides of a subfoveal retinal pigment epithelium detachment (**f**)

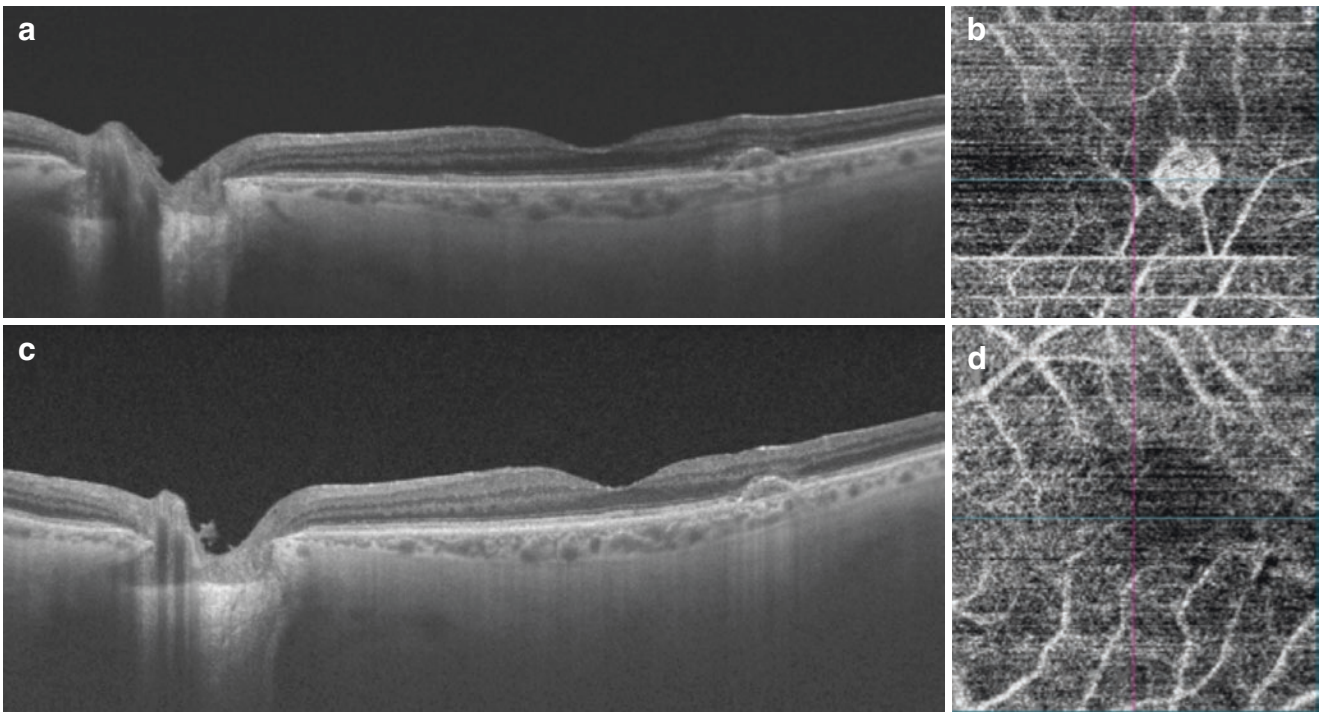

Fig. 6.6 SS-OCTA after aflibercept treatment in neovascular AMD. An extrafoveal fibrovascular pigment epithelium detachment (DEP) with some subretinal fluid is defined in the B-scan, secondary to neovascular AMD (**a**). SS-OCTA shows a neovascular complex in the deep retinal capillary plexus, with a clear afferent vessel (**b**). After one single aflibercept intravitreal injection, B-scan shows no changes in the DEP but a decrease of subretinal fluid (**c**). The neovascular complex has disappeared in the SS-OCTA image (**d**)

Conclusions

En face SS-OCT is a rapid, non-invasive, high-resolution, promising technology that allows a complementary study of nvAMD. RPE and choriocapillaris layers are affected early in nvAMD (including early stages of retinal angiomatous proliferation), and changes in the large and medium choroidal vessels are detected in well-established lesions. There is a correlation between angiography and en face SS-OCT images in neovascular AMD.

AMD study through SS-OCTA is the next step in imaging to visualize retinal and choroidal vessels and neovascular complex. This new technology will allow us a new perspective in nvAMD.

References

1. Flores-Moreno I, Arias-Barquet L, Rubio-Caso MJ, Ruiz-Moreno JM, Duker JS, Caminal JM. En face swept-source optical coherence tomography in neovascular age-related macular degeneration. Br J Ophthalmol. 2015;99:1260–7.
2. Freund KB, Zweifel SA, Engelbert M. Do we need a new classification for choroidal neovascularization in age-related macular. Retina. 2010;30:1333–49.
3. Spaide RF, Fujimoto JG, Waheed NK. Optical coherence tomography angiography. Retina. 2015;35:2161–2.
4. Kuehlewein L, Bansal M, Lenis TL, Iafe NA, Sadda SR, Bonini Filho MA, et al. Optical coherence tomography angiography of type 1 neovascularization in age-related macular degeneration. Am J Ophthalmol. 2015;160:739–48.
5. Kuehlewein L, Dansingani KK, de Carlo TE, Bonini Filho MA, Iafe NA, Lenis TL, et al. Optical coherence tomography angiography of type 3 neovascularization secondary to age-related macular degeneration. Retina. 2015;35:2229–35.

Neovascular Age-Related Macular Degeneration Studied with Swept Source OCT

7

Ignacio Flores-Moreno, Luis Arias-Barquet, Jorge Ruiz-Medrano, José M. Ruiz-Moreno, and Josep M. Caminal

Age-related macular degeneration (AMD) is a chronic degenerative disease that affects the central retina and is one of the most important causes of blindness in the world and the most frequent cause of irreversible legal blindness among people aged 50 or older in the developed countries [1]. 1.5% of Spain's population (about 680,000 people) are affected by this disease, whereas in the United States the prevalence is around 6.5% in people aged 40 and older, affecting more than eight million people [2]. These figures are surely going to increase due to the exponential growth and aging of world population, with an estimated 288 million people suffering from the disease in 25 years' time [3, 4].

AMD is reported to reduce the quality of life and to cause a loss of independence in daily activities of patients who are affected [5]. Several risk factors have been related to this disease, including age, gender, diet, smoking, cardiovascular diseases, obesity, hypertension and hypercholesterolemia among others, while a certain genetic predisposition has also been suggested [1, 6–11].

Degenerative macular changes have been typically classified into dry or wet AMD. Both these forms can cause visual acuity (VA) loss. This loss is usually progressive among patients who show the dry form, and drusen, hyper, or hypopigmentation of retinal pigment epithelium (RPE) are the usual ophthalmoscopic findings. On the other hand, patients suffering from wet (or exudative) AMD may attend with sudden VA loss caused by fluid leaks or hemorrhage from choroidal neovascularization (CNV).

Optical coherence tomography (OCT) is a useful imaging tool for the diagnosis and characterization of patients with AMD, and it has grown to be close to indispensable to correct treatment follow-up [12]. Longer-wavelength, swept source OCT (SS-OCT) is an innovative technology available for OCT imaging that further improves choroidal imaging compared to previous devices [13–19]. SS-OCT can perform image averaging of up to 96 B-scans at each location with an exploration time of 1 s [20].

7.1 Classification of AMD

Using a modified Delphi technique, a committee of experts in the field worked on a new classification system and terminology for AMD in 2013. They took into account lesions within two disk diameters of the foveal center in patients aged 55 and older [21, 22].

- Patients with no signs of retinal aging: No drusen or RPE alterations. AMD-related findings include hypo/hyperpigmentation along medium or large drusen, which cannot be associated with any other known retinal disease.
- Normal aging changes: Only small drusen (<63 μm), called drupelets to avoid confusion with larger drusen. These patients only show a 0.5% 5-year risk of developing late forms of AMD.
- Early AMD: Patients showing medium drusen (63–125 μm) without pigmentary abnormalities.
- Intermediate AMD: Medium drusen in the context of RPE alterations or large drusen (>125 μm). Highest intermediate AMD risk group shows a 50% five-year risk of advancing to late AMD.
- Late AMD: Persons with lesions associated with neovascular AMD or geographic atrophy (GA).

I. Flores-Moreno, MD, PhD
Clinico San Carlos University Hospital, Madrid, Spain

Bellvitge University Hospital, Hospitalet de Llobregat, Barcelona, Spain

L. Arias-Barquet, MD, PhD • J.M. Caminal, MD, PhD
Bellvitge University Hospital, Hospitalet de Llobregat, Barcelona, Spain

J. Ruiz-Medrano, MD (✉)
Clinico San Carlos University Hospital, Madrid, Spain
e-mail: jorge.ruizmedrano@gmail.com

J.M. Ruiz-Moreno, MD, PhD
Castilla-La Mancha University, Albacete, Spain

© Springer International Publishing AG 2017

Z. Michalewska, J. Nawrocki (eds.), *Atlas of Swept Source Optical Coherence Tomography*,
DOI 10.1007/978-3-319-49840-9_7

7.2 Early and Intermediate AMD

Several types of drusen have been described and related to different rates of progression to advanced forms of AMD. They are identified as small white-yellowish lesions, usually located at the posterior pole, that become more diffuse as their size increases. On SS-OCT B-scans they are seen as rounded deposits located between Bruch's membrane and the RPE [23]. Drusen margins are clearly visible on SS-OCT images in the case of hard or small drusen, and more difficult to identify in the case of larger, soft drusen (see Figs. 7.1 and 7.2).

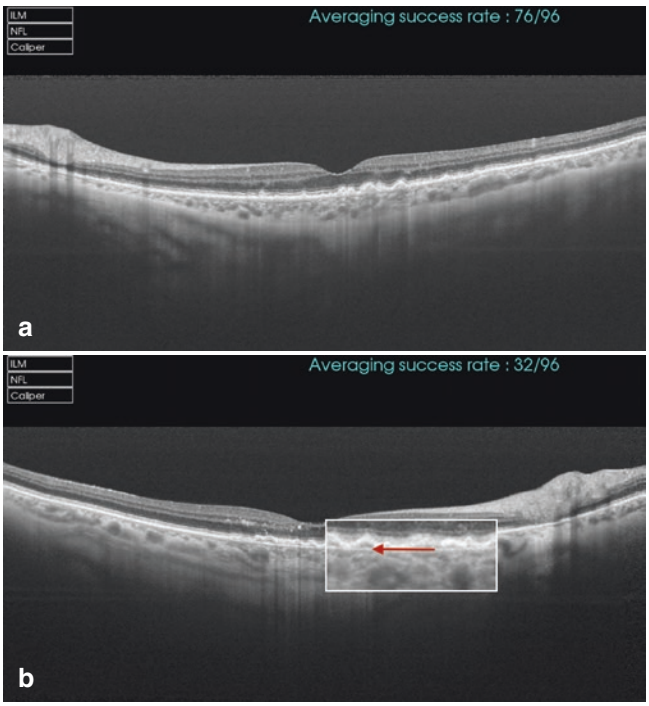

Fig. 7.1 SS-OCT B-scan of a patient with early age-related macular degeneration. Hard drusen are extracellular deposits located in the space between the elevated RPE and Bruch's membrane. The protrusions of the RPE into the retina on SS-OCT appear as well-defined and usually smaller than a retinal vein's width (<63 μm). The contents are sometimes moderately reflective (**a**). Longer-wavelength, SS-OCT allow for higher tissue penetration with image-quality loss, which allows us to see below the RPE. In the image, clearly defined Bruch's membrane (*red arrow*) (**b**)

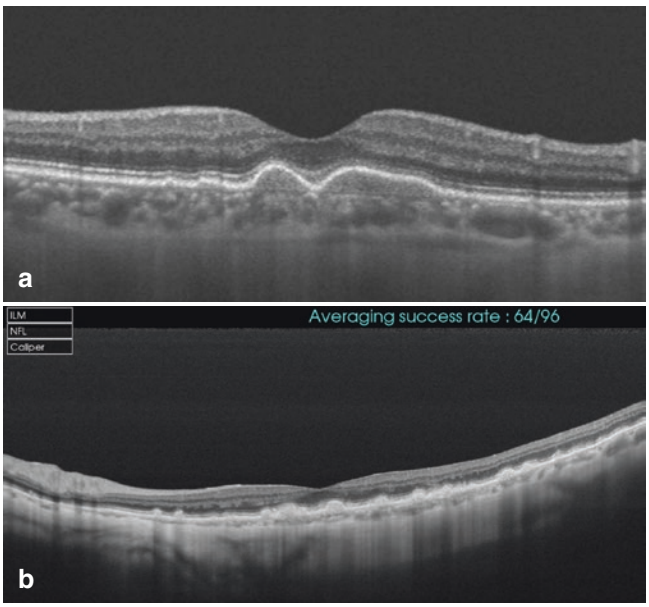

Fig. 7.2 SS-OCT B-scan of a patient with intermediate age-related macular degeneration. Soft drusen contents are sometimes moderately reflective and sometimes barely reflective at all (**a**). Margins are more difficult to identify than in the case of hard drusen (**b**), and separation between RPE and Bruch's membrane becomes clearer

7.2.1 Basal Laminar Drusen (Cuticular Drusen)

Basal laminar drusen appear as multiple small yellow lesions in the macular area, growing from the Bruch's membrane showing a continuous nodular display. They tend to appear in relatively young adults. Pseudovitelliform macular detachments have been related to this type of drusen. On OCT B-scans they show a particular pattern that Leng et al. described as sawtooth pattern [24]. These authors also state the RPE overlying these lesions may suffer modifications leading to attenuation or increase of the OCT signal of the tissues below, depending on the damage or thickening of the RPE (see Fig. 7.3) [24].

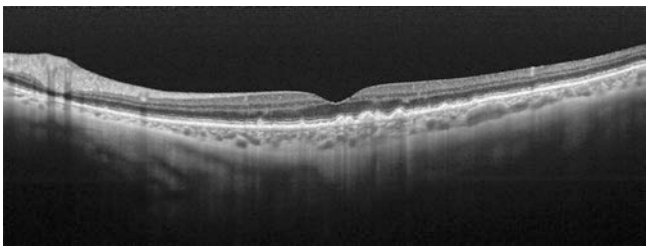

Fig. 7.3 Cuticular drusen. As is the case with typical drusen, these drusen are located beneath the RPE. Cuticular drusen are thought to damage the RPE cells as a result of steep protrusion of drusen into it. These damaged sites exhibit window defects. In typical cases, small, steep protrusions in the RPE known, as "sawtooth," are visible on SS-OCT

7.2.2 Reticular Pseudodrusen

Reticular pseudodrusen (RPD), easier to identify at first using blue light [25, 26], were described by Arnold and colleagues as a yellowish interlacing network of oval-shaped or roundish lesions, with a diameter of 125–250 mm, which were seen in red-free fundus photography and infrared scanning-laser ophthalmoscopy [27]. RPD have been associated with a higher likelihood of developing neovascular AMD and GA [28, 29]. RPD have been associated with choroidal vascular abnormalities such as the loss of the inner and middle layers of the choroid, subsequently leading to fibrous replacement of choroidal stroma [30]. On SS-OCT they are seen as subretinal accumulation of material typically forming sharp peaks or broader, rounder elevations (see Fig. 7.4) [31].

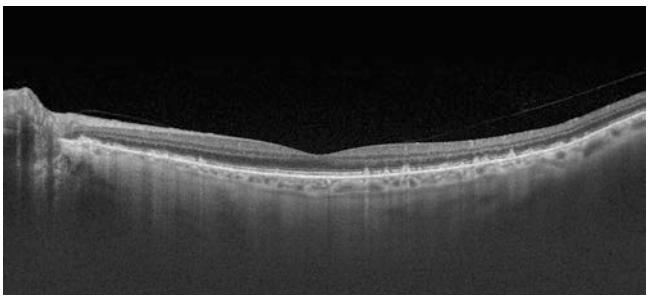

Fig. 7.4 SS-OCT B-scan of a patient showing reticular pseudodrusen (RPD). RPD are seen as triangular highly reflective deposits on the apical side of RPE, which differs from typical drusen location. RPD are a risk factor of progression to late AMD and for the development of retinal angiomatous proliferation

7.2.3 Pigment Epithelium Detachment (PED)

Pigment epithelium detachment (PED) may appear in the absence of clinically or angiographically detectable CNV. They can be well-defined and contain only serous material. OCT imaging shows a clear detachment between Bruch's membrane and the RPE, creating an optically empty space. It may also reveal neurosensory retinal detachments that do not necessarily mean there is a CNV present (see Fig. 7.5) [32]. On the other hand, patients may show PED of reflective contents as soft drusen coalesce and grow, forming drusenoid PED. Type I CNV typically grow below the RPE and can lead to a clear detachment between RPE and Bruch's membrane of irregular hyperreflective content representing fibrovascular tissue (see Fig. 7.6). RPE tears can develop between detached and attached RPE if tangential forces are strong enough. They may appear spontaneously or after laser photocoagulation, photodynamic therapy, or anti-VEGF (vascular endothelial growth factor) intravitreal injections. Age and size of the PED are risk factors for presenting a RPE tear (see Fig. 7.7).

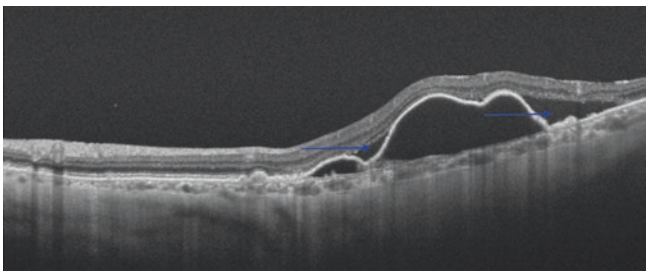

Fig. 7.5 Serous pigment epithelium detachment. The contents of the PED are optically empty and no CNV reflectivity is appreciated. The presence of subretinal fluid (*blue arrows*) is not necessarily linked to the existence of choroidal neovascularization

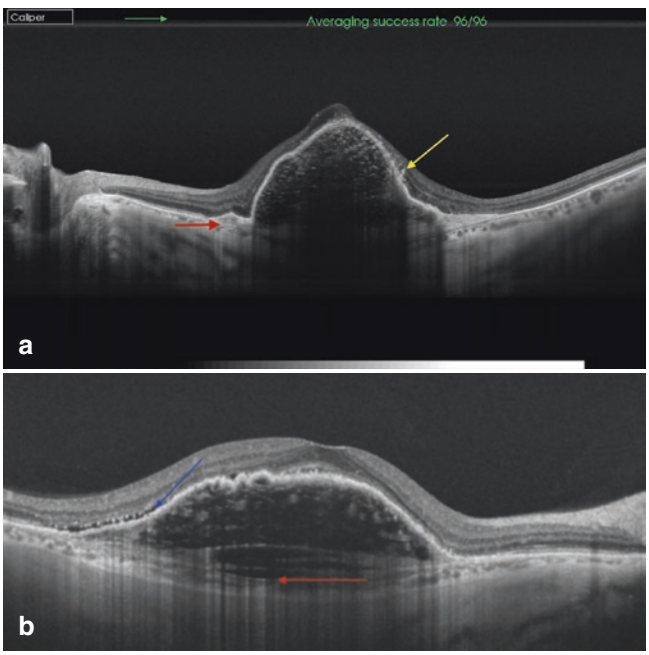

Fig. 7.6 SS-OCT B-scan of a patient showing a massive fibrovascular PED. Bruch's membrane can be clearly seen (*red arrows*). Migrating RPE cells are seen within the sensory retina (*yellow arrow*) (**a**). Subretinal fluid is a frequent finding in the context of fibrovascular PED (*blue arrow*) (**b**)

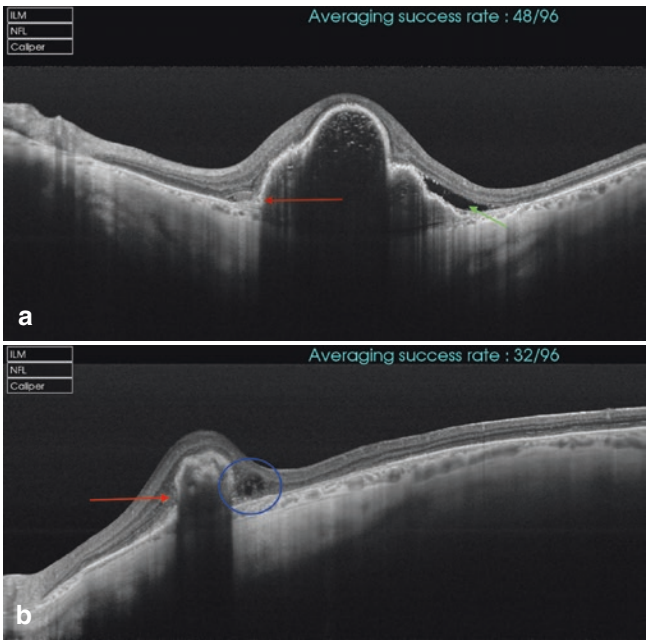

Fig. 7.7 When tangential forces are strong enough, the RPE can suffer a tear (*red arrows*), leading to a neovascular growth over it and under the neurosensory retina, and visual acuity loss. RPE tear and subretinal fluid (*green arrow*) (**a**). RPE tear with intraretinal fluid (*blue circle*) (**b**)

7.3 Late AMD

7.3.1 Neovascular AMD

Neovascular AMD is defined by the presence of a choroid neovascularization leading to hemorrhagic or serous complications for patients suffering from this disease. It was classically subcategorized based on fluorescein angiography findings in the original classification by Donald Gass [33], but the advent of new technologies like spectral domain OCT (SD-OCT) led Freund and colleagues to propose a new classification of neovascular AMD based on the location of the CNV in relation to the RPE [34]. The subtype of CNV and its nature are key factors to therapeutic decisions, response, and visual prognosis [22, 34].

7.3.1.1 Type 1

In Type 1, CNV are located underneath the RPE without infiltration of the subretinal space. This kind of CNV was previously classified as *occult* under Gass' system (see Fig. 7.8). Theories state its pathogenesis is based on a compensatory response to the hypoxia suffered by the external neurosensory retina, inducing pathological modifications and increasing the size of choroidal vessels [35]. If this is true, destroying theses CNV complexes could be potentially harmful to an already compromised retina leading to RPE atrophies and VA loss. Type 1 CNV shows better visual prognosis than other types of CNV. Maduration of choroid vessels forming the CNV may lead to the appearance of polypoidal dilations leading to polypoidal choroidal vasculopathy (PCV) (see Fig. 7.9) [36].

7.3.1.2 Type 2

In Type 2, the CNV complex is located above the RPE in the subretinal space. It matches the previously classified *classic* CNVs (see Fig. 7.10). Type 2 CNV damages the RPE and alters the ellipsoid line, so the loss of the external blood-retinal barrier leads to much more frequent recurrence. On the other hand, they show better response to treatment. It is the most common type of CNV in patients with fewer diffuse lesions of the RPE and more focused on the macula like pathological myopia, lacquer cracks, and inner punctate choroidopathy. SS-OCT images may show spirals or tubulations of the external retina (see Fig. 7.11). Tubulations are structures encircled by a moderately reflective ring first described by Freund et al. in adjacent areas to atrophic retina, between the CNV and outer plexiform layer.

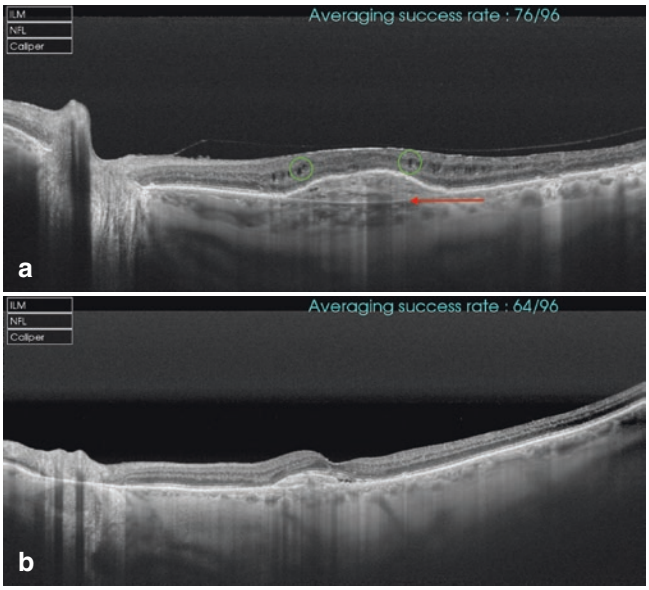

Fig. 7.8 SS-OCT of the left eye of a patient suffering from type 1 choroidal neovascularization. CNV is confined to the space between RPE and Bruch's membrane and B-scans reveal an RPE elevation showing hyperreflectivity of the subretinal space due to exudation and hemorrhage, along with intraretinal cysts (*green circles*). Thanks to its deeper penetration, this device allows a clear visualization of Bruch's membrane (a straight, highly reflective line indicated by *red arrow*) despite the high density of the CNV tissue (**a**). B-scan of left eye of another patient showing a type 1 CNV that exhibits moderate reflectivity and is located below the RPE (**b**)

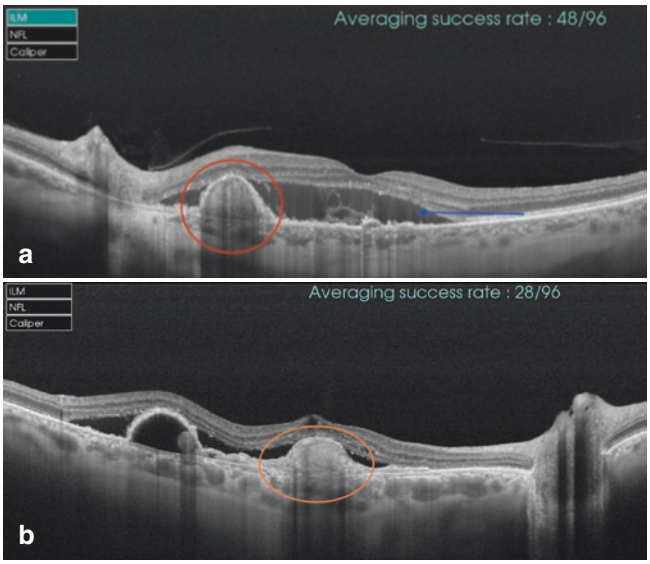

Fig. 7.9 SS-OCT B-scan of the left eye of a patient diagnosed of polypoidal choroidal vasculopathy. Note the polypoidal lesion nasally to the fovea (*red circle*), detaching RPE and Bruch's membrane. A *double layer sign* describes the parallel appearance of the detached RPE line and this bold line derived from the complex. These kinds of lesions induce the appearance of neurosensory retinal detachments due to the accumulation of subretinal fluid (*blue arrow*) (**a**). Moderately reflective contents suggest the presence of fibrovascular tissue (*orange circle*) (**b**)

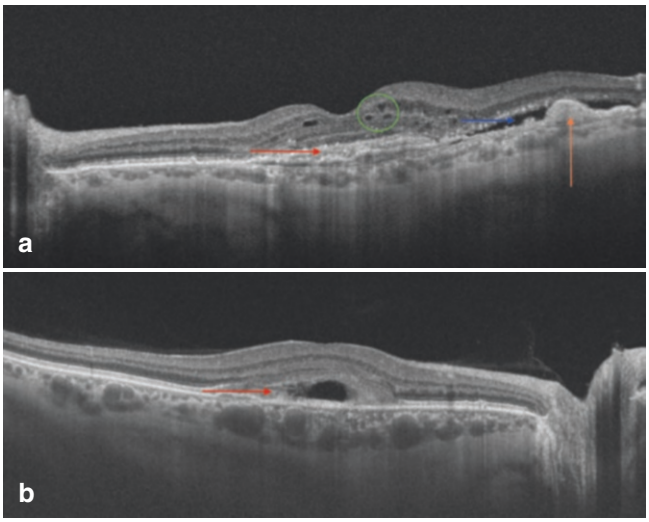

Fig. 7.10 SS-OCT B-scan of a type 2 CNV. These lesions are located between the RPE and the neurosensory retina (*red arrow*). Intraretinal cysts (*green circle*), subretinal fluid (*blue arrow*) and fibrovascular RPE detachments (*orange arrow*) are also shown. Another case of type 2 CNV, above the RPE (*red arrow*) (**b**). SS-OCT horizontal scan of the right eye: CME accompanied by a large foveal cystoid space (*asterisk*) exists over the entire macular area. The RPE line is seen over almost the entire length and appears flat on this scan. There are highly reflective clumps above the RPE, which are due to CNV and fibrin

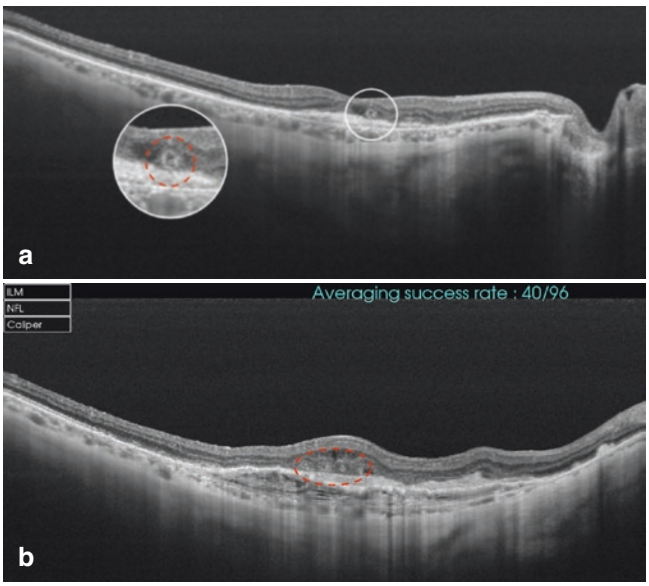

Fig. 7.11 SS-OCT images may show spirals or tubulations of the external retina (**a**, *red dashed circle*). Tubulations are structures encircled by a moderately reflective ring, first described by Freund et al. [34], in adjacent areas to atrophic retina, between the CNV and outer plexiform layer (**b**)

7.3.1.3 Type 3

Late-stage CNVs tend to form retinal-choroidal anastomosis (RCA) as choroidal vessels penetrate the retina and communicate with retinal circulation [37, 38]. This process also takes place the other way around in some patients with AMD, where retinal capillaries grow deep through the retina and connect with choroidal circulation, forming a CNV complex that Yannuzzi et al. called "retinal angiomatous proliferation" (RAP), which is typically extrafoveal [39] (Fig. 7.12). It is usually bilateral and appears in areas with photoreceptor damage, so VA response to treatment may not be good. As these lesions evolve, they become more resistant to intravitreal treatments.

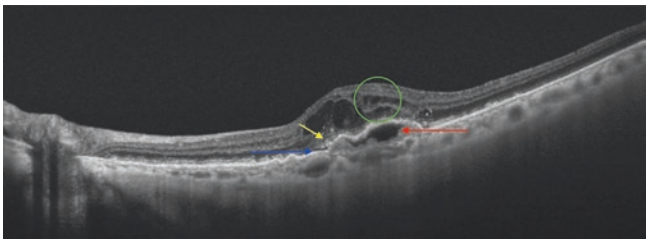

Fig. 7.12 Retinal angiomatous proliferation. Typical tomographic findings include cystic macular edema (*green circle*), serous or fibrovascular PED (*red arrow*) and subretinal fluid (*blue arrow*). In some cases, intraretinal neovascularization can be seen as a focal hyperreflective spot (*yellow arrow*)

7.3.2 Geographic Atrophy

Geographic atrophy (GA) is the term used to describe areas showing loss of RPE and choriocapillaris of at least 175 μm, which can follow pigment alterations, large drusen regression, RPE detachments, CNV, etc. It usually appears in the center of the macula. It is not uncommon to see choroid vessels through the atrophic RPE and retina. SS-OCT images of GA show findings such as loss of the RPE with the subsequent choroidal signal enhancement and atrophy of the sensory retina (see Fig. 7.13). Chronic patients tend to show cystic changes of the retina, which should not be confused with exudation. Despite these findings, fundus autofluorescence (FAF) is the most useful tool for follow-up with these patients.

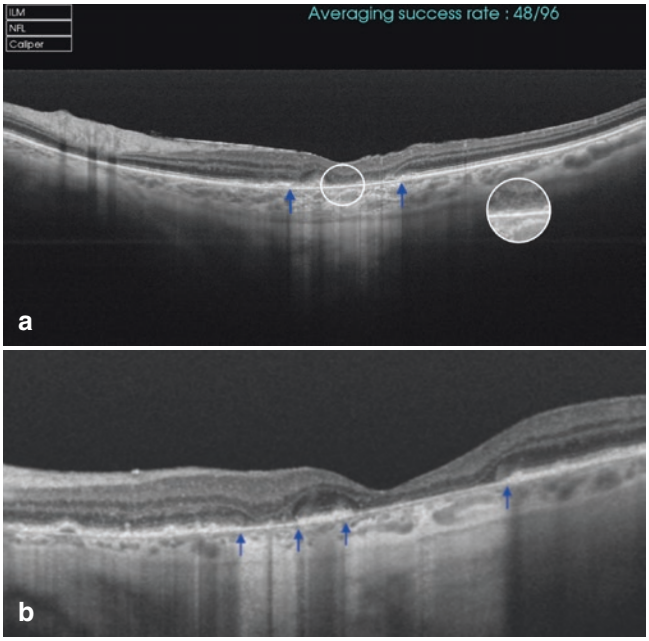

Fig. 7.13 Examples of cases of geographic atrophy. RPE, external limiting membrane, and photoreceptors have completely disappeared in the atrophic area, with a clear reduction of the outer nuclear layer as well (**a**, *close-up*). As a result of the RPE defects, choroidal signal is enhanced (**a**, **b**, *between blue arrows*)

References

1. Lim LS, Mitchell P, Seddon JM, Holz FG, Wong TY. Age-related macular degeneration. Lancet. 2012;379:1728–38.
2. Klein R, Chou C-F, Klein BEK, Zhang X, Meuer SM, Saaddine JB. Prevalence of age-related macular degeneration in the US population. Arch Ophthalmol. 2011;129:75–80.
3. Reibaldi M, Longo A, Pulvirenti A, Avitabile T, Russo A, Cillino S, et al. Geo-epidemiology of age-related macular degeneration: new clues into the pathogenesis. Am J Ophthalmol. 2016;161:78–93.
4. Wong WL, Su X, Li X, Cheung CM, Klein R, Cheng CY, et al. Global prevalence of age-related macular degeneration and disease burden projection for 2020 and 2040: a systematic review and meta-analysis. Lancet Glob Health. 2014;2:e106–16.
5. Miskala PH, Bass EB, Bressler NM, Childs AL, Hawkins BS, Mangione CM, et al. Surgery for subfoveal choroidal neovascularization in age-related macular degeneration: quality-of-life findings: SST report no. 12. Ophthalmology. 2004;111:1981–92.
6. Seddon JM, Willett WC, Speizer FE, Hankinson SE. A prospective study of cigarette smoking and age-related macular degeneration in women. JAMA. 1996;276:1141–6.
7. Cho E, Seddon JM, Rosner B, Willett WC, Hankinson SE. Prospective study of intake of fruits, vegetables, vitamins, and carotenoids and risk of age-related maculopathy. Arch Ophthalmol. 2004;122:883–92.
8. Johnson LV, Leitner WP, Staples MK, Anderson DH. Complement activation and inflammatory processes in Drusen formation and age related macular degeneration. Exp Eye Res. 2001;73:887–96.
9. Anderson DH, Mullins RF, Hageman GS, Johnson LV. A role for local inflammation in the formation of drusen in the aging eye. Am J Ophthalmol. 2002;134:411–31.
10. Tomany SC, Wang JJ, Van Leeuwen R, Klein R, Mitchell P, Vingerling JR, et al. Risk factors for incident age-related macular degeneration: pooled findings from 3 continents. Ophthalmology. 2004;111:1280–7.
11. Seddon JM, Cote J, Page WF, Aggen SH, Neale MC. The US twin study of age-related macular degeneration: relative roles of genetic and environmental influences. Arch Ophthalmol. 2005;123:321–7.
12. Hee MR, Baumal CR, Puliafito CA, Duker JS, Reichel E, Wilkins JR, et al. Optical coherence tomography of age-related macular degeneration and choroidal neovascularization. Ophthalmology. 1996;103:1260–70.
13. Spaide R, Koizumi H, Pozzoni M. Enhanced depth imaging spectral-domain optical coherence tomography. Am J Ophthalmol. 2008;146:496–500.
14. Fleckner MR, Hochman MA, Buzney SM, Weiter JJ, Tolentino FI, Khadem JJ. Complications of surgery for subfoveal choroidal neovascularization. Int Ophthalmol Clin. 2000;40:201–14.
15. Margolis R, Spaide RF. A pilot study of enhanced depth imaging optical coherence tomography of the choroid in normal eyes. Am J Ophthalmol. 2009;147:811–5.
16. Huber R, Adler D, Srinivasan VJ, Fujimoto JG. Fourier domain mode locking at 1050 nm for ultra-high-speed optical coherence tomography of the human retina at 236,000 axial scans per second. Opt Lett. 2007;32:2049–51.
17. Copete S, Flores-Moreno I, Montero JA, Duker JS, Ruiz-Moreno JM. Direct comparison of spectral-domain and swept-source OCT in the measurement of choroidal thickness in normal eyes. Br J Ophthalmol. 2014;98:334–8.
18. Ruiz-Moreno JM, Flores-Moreno I, Lugo F, Ruiz-Medrano J, Montero JA, Akiba M. Macular choroidal thickness in normal pediatric population measured by swept-source optical coherence tomography. Invest Ophthalmol Vis Sci. 2012;54:353–9.
19. Ruiz-Medrano J, Flores-Moreno I, Peña-García P, Montero JA, Duker JS, Ruiz-Moreno JM. Macular choroidal thickness profile in a healthy population measured by swept-source optical coherence tomography. Invest Ophthalmol Vis Sci. 2014;55:3532–42.
20. Ikuno Y, Maruko I, Yasuno Y, Miura M, Sekiryu T, Nishida K, et al. Reproducibility of retinal and choroidal thickness measurements in enhanced depth imaging and high-penetration optical coherence tomography. Invest Ophthalmol Vis Sci. 2011;51:5536–40.
21. Ferris 3rd FL, Wilkinson CP, Bird A, Chakravarthy U, Chew E, Csaky K, et al. Clinical classification of age-related macular degeneration. Ophthalmology. 2013;120:844–51.
22. Ruiz-Moreno JM, Arias L, Armada-Maresca F, Boixadera-Espax A, Garcia-Layana A, Gomez-Ulla F, et al. Tratamiento de La degeneracion macular asociada a la edad (DMAE) exudativa y atrofica. Sociedad Española de Retina y Vitreo; Madrid; March 6–7, 2009.
23. Spaide RF, Curcio CA. Drusen characterization with multimodal imaging. Retina. 2010;30:1441–54.
24. Leng T, Rosenfeld PJ, Gregori G, Puliafito CA, Punjabi OS. Spectral domain optical coherence tomography characteristics of cuticular drusen. Retina. 2009;29:988–93.
25. Klein R, Davis MD, Magli YL, Segal P, Klein BE, Hubbard L. The Wisconsin age-related maculopathy grading system. Ophthalmology. 1991;98:1128–34.
26. Mimoun G, Soubrane G, Coscas G. Macular drusen. J Fr Ophtalmol. 1990;13:511–30.
27. Arnold JJ, Sarks SH, Killingsworth MC, Sarks JP. Reticular pseudodrusen. A risk factor in age-related maculopathy. Retina. 1995;15:183–91.
28. Cohen SY, Dubois L, Tadayoni R, Delahaye-Mazza C, Debibie C, Quentel G. Prevalence of reticular pseudodrusen in age-related macular degeneration with newly diagnosed choroidal neovascularisation. Br J Ophthalmol. 2007;91:354–9.
29. Smith RT, Chan JK, Busuoic M, Sivagnanavel V, Bird AC, Chong NV. Autofluorescence characteristics of early, atrophic, and high-risk fellow eyes in age-related macular degeneration. Invest Ophthalmol Vis Sci. 2006;47:5495–504.
30. Garg A, Oll M, Yzer S, Chang S, Barile GR, Merriam JC, et al. Reticular pseudodrusen in early age-related macular degeneration are associated with choroidal thinning. Invest Ophthalmol Vis Sci. 2013;54:7075–81.
31. Suzuki M, Sato T, Spaide RF. Pseudodrusen subtypes as delineated by multimodal imaging of the fundus. Am J Ophthalmol. 2014;157:1005–12.
32. Kuehlewein L, Bansal M, Lenis TL, Iafe NA, Sadda SR, Bonini Filho MA, et al. Optical coherence tomography angiography of type 1 neovascularization in age-related macular degeneration. Am J Ophthalmol. 2015;160:739–48.
33. Gass JD. Biomicroscopic and histopathologic considerations regarding the feasibility of surgical excision of subfoveal neovascular membranes. Am J Ophthalmol. 1994;118:285–98.
34. Freund KB, Zweifel SA, Engelbert M. Do we need a new classification for choroidal neovascularization in age-related macular degeneration? Retina. 2010;30:1333–49.
35. Grossniklaus HE, Green WR. Choroidal neovascularization. Am J Ophthalmol. 2004;137:496–503.
36. Sato T, Kishi S, Watanabe G, Matsumoto H, Mukai R. Tomographic features of branching vascular networks in polypoidal choroidal vasculopathy. Retina. 2007;27:589–94.
37. Green WR, Gass JD. Senile disciform degeneration of the macula. Retinal arterialization of the fibrous plaque demonstrated clinically and histopathologically. Arch Ophthalmol. 1971;86:487–94.
38. Green WR, Enger C. Age-related macular degeneration histopathologic studies. The 1992 Lorenz E. Zimmerman Lecture. Ophthalmology. 1993;100:1519–35.
39. Yannuzzi LA, Negrão S, Iida T, Carvalho C, Rodriguez-Coleman H, Slakter J, et al. Retinal angiomatous proliferation in age-related macular degeneration. Retina. 2001;21:416–34.

Pathological Myopia

8

Atsushi Maeda, Takafumi Hirashima, and Hideyasu Oh

Pathologic myopia is one of the major causes of visual impairment worldwide, the prevalence of which has been reported to be about 1% of the population [1–5]. The visual loss is mainly caused by pathological structural changes, such as lacquer crack formation, posterior staphyloma, thinning of the retina, choroid and sclera, retinal schisis, deformation of the optic disc area, and choroidal neovascularization (CNV) [6–9]. Optical coherence tomography (OCT) is very efficient in non-invasive detection of these myopic lesions. The newer generation of OCT, swept source OCT (SS-OCT), has an increased depth of imaging and also a higher speed of scanning, which has made it one of the most useful imaging devices for characterizing pathologic myopia [10–12].

A. Maeda, MD • T. Hirashima, MD • H. Oh, MD, PhD (✉)
Department of Ophthalmology, Hyogo Prefectural Amagasaki General Medical Center (AGMC), Amagasaki, Hyogo, Japan
e-mail: hideyasu@kuhp.kyoto-u.ac.jp

© Springer International Publishing AG 2017
Z. Michalewska, J. Nawrocki (eds.), *Atlas of Swept Source Optical Coherence Tomography*,
DOI 10.1007/978-3-319-49840-9_8

8.1 Posterior Staphyloma

Staphyloma is a local deviation in curvature of the posterior portion of the eyeball in highly myopic cases [13]. The staphylomas were classified into ten different types, mainly by way of slit-lamp biomicroscopy [14], which has been newly classified into six types by way of both wide-field fundus imaging and 3D–MRI [15]: (1) wide macular staphyloma; (2) narrow macular staphyloma; (3) peripapillary staphyloma (4) nasal staphyloma; (5) inferior staphyloma; and (6) other types of staphyloma. The OCT features of staphyloma are an excessive curve and tilt of the retina and a thinning of the choroid (Fig. 8.1).

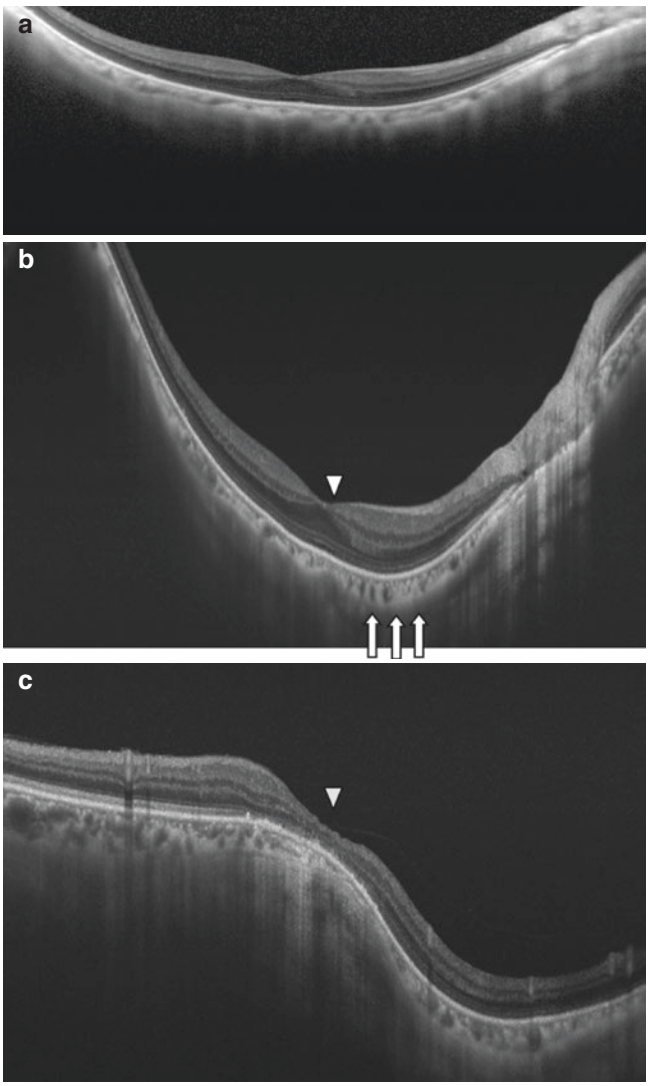

Fig. 8.1 (**a**) Image of wide macular staphyloma in high myopia by spectral-domain OCT. The chorioretinal curvature is not well-delineated. (**b**) Image of wide macular staphyloma from the same patient as (**a**) by swept source OCT. The whole posterior pole area is documented and the central fovea is on the slope (*arrowhead*). The detail structure of the thin choroid is also visualized well (*arrows*). (**c**) SS-OCT image of inferior staphyloma. Note that the central fovea is at the upper edge of staphyloma (*arrowhead*) and the ellipsoid zone line is disrupted

8.2 Myopic Traction Maculopathy

Myopic traction maculopathy (MTM), including retinal schisis (RS) and macular hole retinal detachment (MHRD), is a pathologic myopia-related complication caused by some mechanisms with traction as a common pathway. The diagnosis of MTM by slit-lamp biomicroscopy was very difficult [16, 17]. The introduction of OCT enables one to detect the specific structural features of MTM in detail [6, 16, 18].

8.2.1 Retinal Schisis

Retinal Schisis, also called myopic foveoschisis, is one of the pathological conditions of MTM and is estimated to affect between 9 and 34% of highly myopic eyes with posterior staphyloma [6, 18, 19]. The SS-OCT findings of RS include foveal detachment, lamellar macular holes, macular epiretinal membrane, and vitreoretinal traction (Fig. 8.2).

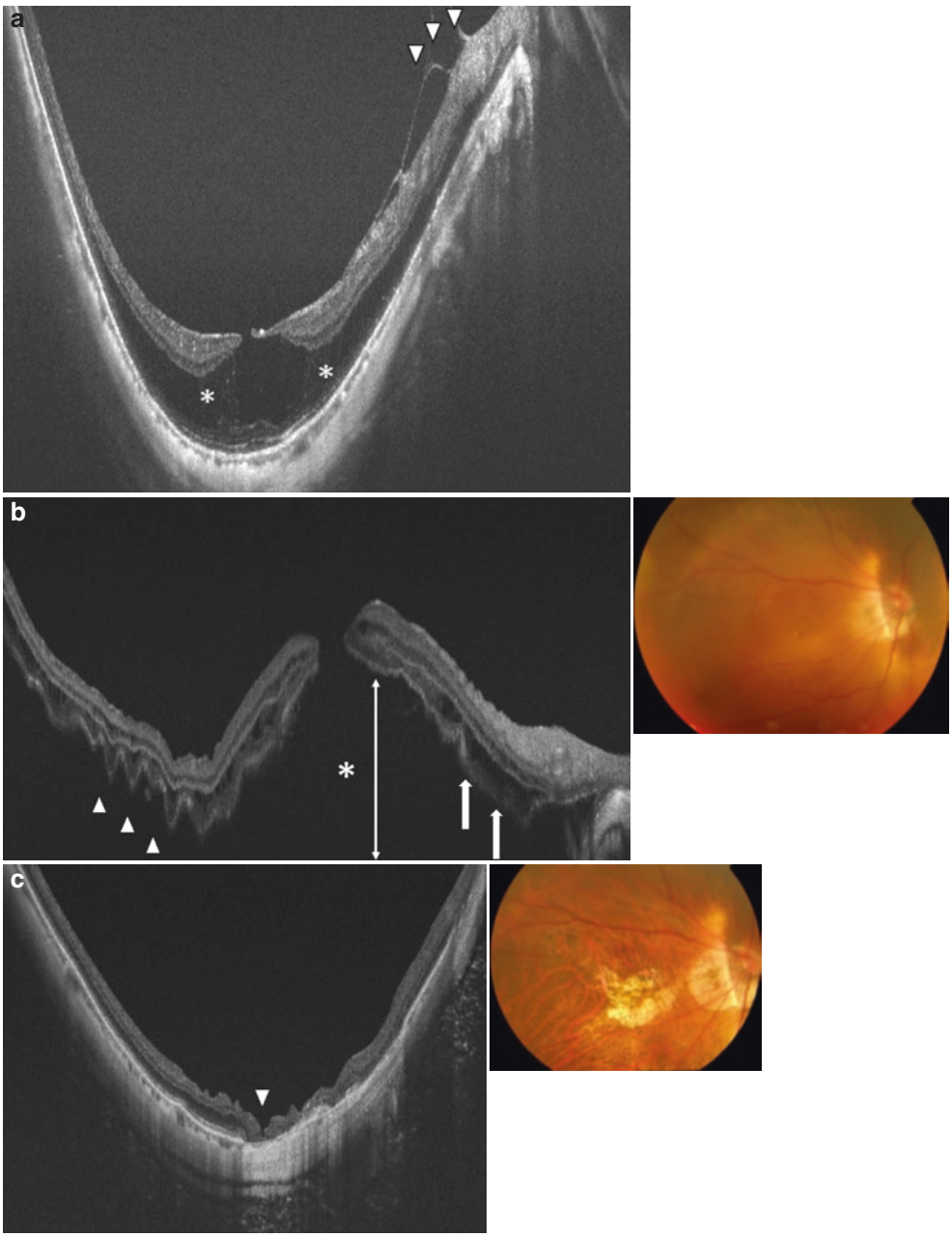

Fig. 8.2 (**a**) SS-OCT image shows outer retinal schisis (*asterisks*) and vitreoretinal traction (*arrowheads*). (**b**) Preoperative SS-OCT image shows outer retinal schisis (*arrows*), waving of the outer retina (*arrowheads*), and foveal detachment with a macular hole. The retinal pigment epithelium layer could not be included due to the excessive height of retinal detachment (*asterisk*). (**c**) SS-OCT image at 1 month after vitrectomy with inverted ILM flap technique shows reattachment of the retina. Note that a thin tissue is observed in the foveal center and thus the macular hole is closed (*arrowhead*). (**d**) Preoperative SS-OCT image shows a full thickness macular hole (*arrowhead*) with an epiretinal membrane, retinal schisis (*arrow*) and retinal detachment. (**e**) SS-OCT image at 2 years after vitrectomy with conventional ILM peeling shows reattachment of the retina (*arrowhead*). An ellipsoid zone at central fovea is visible (*arrowhead*)

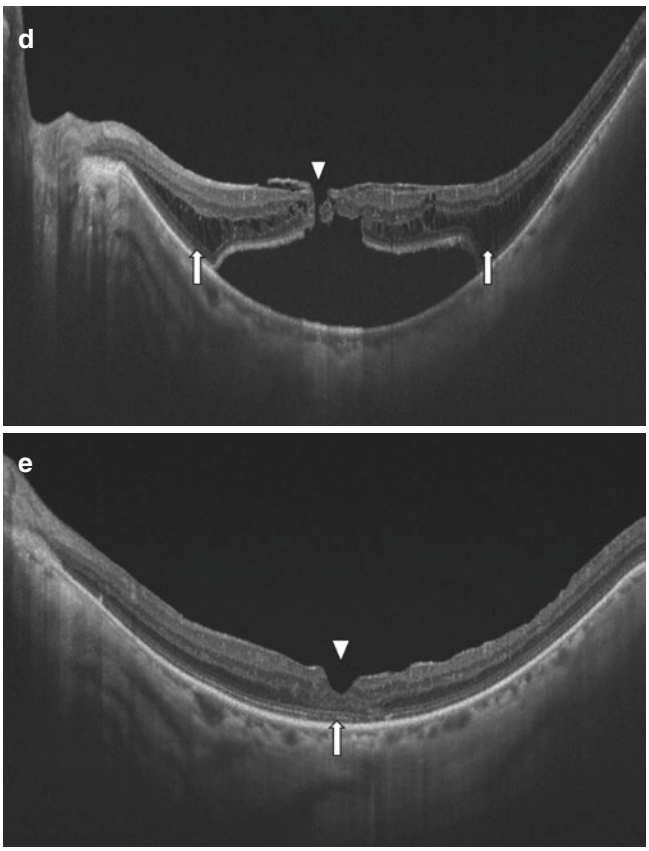

Fig. 8.2 (continued)

8.2.2 Macular Hole Retinal Detachment

Macular hole retinal detachment is considered to be the final stage of progressive MTM. MHRD occurs almost exclusively in high myopes and causes severe visual impairments. The main causative factors of MHRD are both anteroposterior and tangential tractions in the macula area, which is potentially accelerated by the progression of posterior staphyloma [18, 20].

Vitrectomy with gas endotamponade is currently the first-line treatment [21]. Various techniques, such as using silicon oil tamponade, laser around macular hole (MH), internal limiting membrane (ILM) peeling, and inverted ILM flap technique, have been reported [22, 23]. Some studies have shown better anatomic results with ILM peeling since this guarantees complete removal of epiretinal tractions and a more flexible retina [24, 25]. However, the success rate of surgery for MHRD is lower than that of conventional rhegmatogenous retinal detachment, and revisions are sometimes required [22] (Fig. 8.2).

8.3 Choroidal Neovascularization

Myopic CNV often causes severe visual impairment [26]. Myopic CNV is sometimes associated with subretinal dark pigment migration or hemorrhage and develops into chorioretinal atrophy [27]. It has been reported that 13% of eyes with lacquer cracks develop myopic CNV, and the high myopic eyes with lacquer cracks have less choroidal thickness than those without lacquer cracks [8, 28]. Similarly, high myopic eyes with CNV might have less choroidal thickness than those without CNV [29]. Intravitreal anti-VEGF therapy is widely accepted as a first-line treatment of myopic CNV, and recent studies have demonstrated beneficial visual outcomes (Fig. 8.3) [30–32].

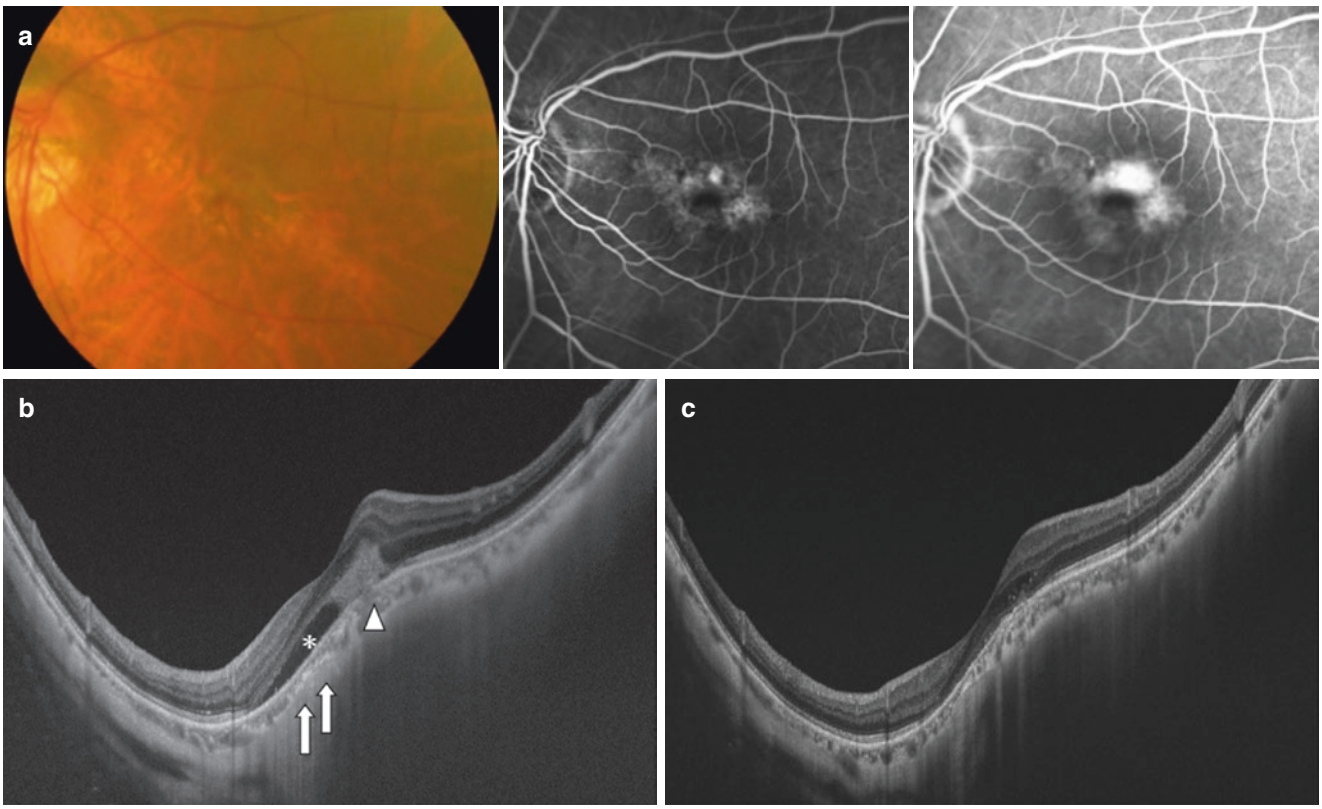

Fig. 8.3 (**a**) Fluorescent fundus angiography of myopic CNV. The leakage is observed at the site of the disruption of retinal pigment epithelium documented in (**b**). (**b**) SS-OCT image shows the subretinal fluid (*asterisk*), subretinal hemorrhage, disruption of retinal pigment epithelium (*arrowhead*), and the thin choroidal thickness (*arrow*). (**c**) SS-OCT image at 1 month after intravitreal ranibizumab injection shows the regression of CNV and resolution of subretinal fluid

8.4 Intrachoroidal Cavitation

Intrachoroidal cavitation (ICC) is a yellow-orange peripapillary area at the inferior border of the myopic conus. Prior to the introduction of OCT, this lesion was described as a peripapillary detachment in pathologic myopia (PDPM) [33]. The main OCT feature of ICC is a large intrachoroidal hyporeflective space (Fig. 8.4) [34].

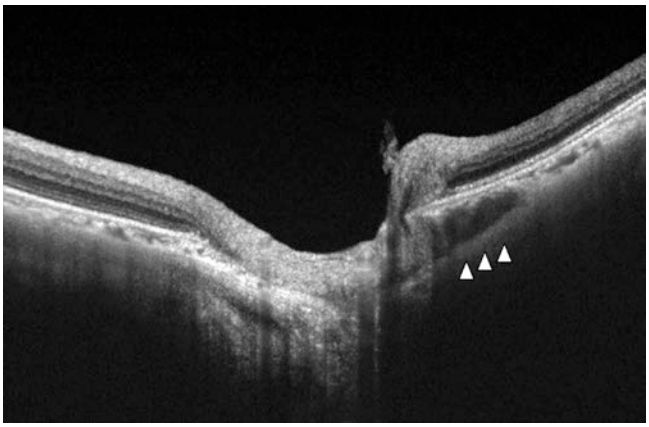

Fig. 8.4 A large intrachoroidal hyporeflective space is observed adjacent to the optic nerve (*arrowheads*)

8.5 Dome-Shaped Macula

Dome-shaped macula (DSM) is first described as an anterior protrusion of the macula in high myopia with posterior staphyloma [35]. DSM sometimes can cause visual impairment due to associated myopic CNV or serous macular detachment (Fig. 8.5) [36].

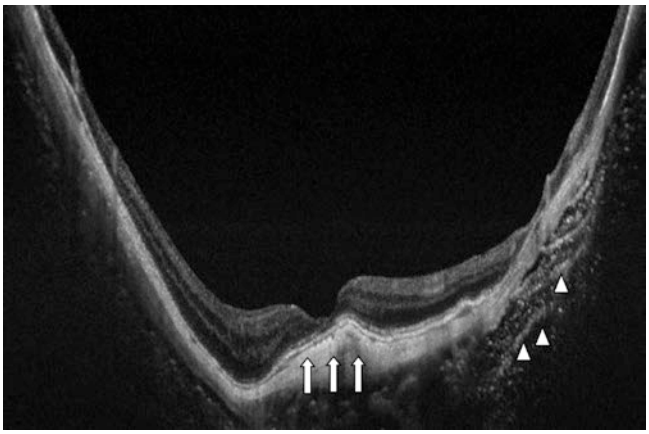

Fig. 8.5 SS-OCT image shows an anterior protrusion of the macula with posterior staphyloma (*arrows*). The sclera is observed as a highly reflective tissue (*arrows*) outside of the very thin choroid. The fibers of Tenon's capsule are also well observed (*arrowheads*)

References

1. Green JS, Bear JC, Johnson GJ. The burden of genetically determined eye disease. Br J Ophthalmol. 1986;70:696–9.
2. Krumpaszky HG, Lüdtke R, Mickler A, Klauss V, Selbmann HK. Blindness incidence in Germany. A population-based study from Wurttemberg-Hohenzollern. Ophthalmologica. 1999;213:176–82.
3. Munier A, Gunning T, Kenny D, O'Keefe M. Causes of blindness in the adult population of the Republic of Ireland. Br J Ophthalmol. 1998;82:630–3.
4. Cotter SA, Varma R, Ying-Lai M, Azen SP, Klein R. Causes of low vision and blindness in adult Latinos: the Los Angeles Latino Eye Study. Ophthalmology. 2006;113:1574–82.
5. Vongphanit J, Mitchell P, Wang JJ. Prevalence and progression of myopic retinopathy in an older population. Ophthalmology. 2002;109:704–11.
6. Takano M, Kishi S. Foveal retinoschisis and retinal detachment in severely myopic eyes with posterior staphyloma. Am J Ophthalmol. 1999;128:472–6.
7. Ohno-Matsui K, Shimada N, Yasuzumi K, Hayashi K, Yoshida T, Kojima A, et al. Long-term development of significant visual field defects in highly myopic eyes. Am J Ophthalmol. 2011;152:256–65.
8. Hayashi K, Ohno-Matsui K, Shimada N, Moriyama M, Kojima A, Hayashi W, et al. Long-term pattern of progression of myopic maculopathy: a natural history study. Ophthalmology. 2010;117:1595–611.
9. Curtin BJ. Basic science and clinical management. In: Curtin BJ, editor. The myopias. New York: Harper and Row; 1985.
10. Fujiwara T, Imamura Y, Margolis R, Slakter JS, Spaide RF. Enhanced depth imaging optical coherence tomography of the choroid in highly myopic eyes. Am J Ophthalmol. 2009;148:445–50.
11. Ohno-Matsui K, Akiba M, Moriyama M, Ishibashi T, Tokoro T, Spaide RF. Imaging the retrobulbar subarachnoid space around the optic nerve by swept source optical coherence tomography in eyes with pathologic myopia. Invest Ophthalmol Vis Sci. 2011;52:9644–50.
12. Zhou M, Wang W, Ding X, Huang W, Chen S, Laties AM, et al. Choroidal thickness in fellow eyes of patients with acute primary angle-closure measured by enhanced depth imaging spectral-domain optical coherence tomography. Invest Ophthalmol Vis Sci. 2013;54:1971–8.
13. Spaide RF. Staphyloma: part 1. In: Spaide RF, Ohno-Matsui K, Yannuzzi LA, editors. Pathologic myopia. New York: Springer; 2013.
14. Curtin BJ. The posterior staphyloma of pathologic myopia. Trans Am Ophthalmol Soc. 1977;75:67–86.
15. Ohno-Matsui K. Proposed classification of posterior staphylomas based on analyses of eye shape by three-dimentional magnetic resonance imaging and wide-field fundus imaging. Ophthalmology. 2014;121:1798–809.
16. Sayanagi K, Morimoto Y, Ikuno Y, Tano Y. Spectral-domain optical coherence tomographic findings in myopic foveoschisis. Retina. 2010;30(4):623–8.
17. Benhamou N, Massin P, Haouchine B, Erginay A, Gaudric A. Macular retinoschisis in highly myopic eyes. Am J Ophthalmol. 2002;133(6):794–800.
18. Panozzo G, Mercanti A. Optical coherence tomography findings in myopic traction maculopathy. Arch Ophthalmol. 2004;122(10):1455–60.
19. Baba T, Ohno-Matsui K, Futagami S, Yoshida T, Yasuzumi K, Kojima A, et al. Prevalence and characteristics of foveal retinal detachment without macular hole in high myopia. Am J Ophthalmol. 2003;135(3):338–42.
20. Mitry D, Zambarakji H. Recent trends in the management of maculopathy secondary to pathological myopia. Graefes Arch Clin Exp Ophthalmol. 2012;250:3–13.
21. Gonvers M, Machemer R. A new approach to treating retinal detachment with macular hole. Am J Ophthalmol. 1982;94:468–72.
22. Ortisi E, Avitabile T, Bonfiglio V. Surgical management of retinal detachment because of macular hole in highly myopic eyes. Retina. 2012;32:1074–8.
23. Kuriyama S, Hayashi H, Jingami Y, Kuramoto N, Akita J, Matsumoto M. Efficacy of inverted internal limiting membrane flap technique for the treatment of macular hole in high myopia. Am J Ophthalmol. 2013;156:125–31.
24. Kadonosono K, Yazawa F, Itoh N, Uchio E, Nakamura S, Akura J, et al. Treatment of retinal detachment resulting from myopic macular hole with internal limiting membrane removal. Am J Ophthalmol. 2001;131:203–7.
25. Ichibe M, Yoshizaka T, Murakami K, Ohta M, Oya Y, Yamamoto S, et al. Surgical management of retinal detachment associated with myopic macular hole: anatomic and functional status of the macula. Am J Ophthalmol. 2003;136:277–84.
26. Curtin BJ, Karlin DB. Axial length measurements and fundus changes of the myopic eye. Am J Ophthalmol. 1971;71:42–53.
27. Yoshida T, Ohno-Matsui K, Yasuzumi K, Kojima A, Shimada N, Futagami S, et al. Myopic choroidal neovascularization: a 10-year follow-up. Ophthalmology. 2003;110:1297–305.
28. Wang NK, Lai CC, Chou CL, Chen YP, Chuang LH, Chao AN, et al. Choroidal thickness and biometric markers for the screening of lacquer cracks in patients with high myopia. PLoS One. 2013;8(1):e53660.
29. El Matri L, Bouladi M, Chebil A, Kort F, Largueche L, Mghaieth F. Macular choroidal thickness assessment with SD-OCT in high myopia with or without choroidal neovascularization. J Fr Ophtalmol. 2013;36:687–92.
30. Lai TY, Luk FO, Lee GK, Lam DS. Long-term outcome of intravitreal anti-vascular endothelial growth factor therapy with bevacizumab or ranibizumab as primary treatment for subfoveal myopic choroidal neovascularization. Eye (Lond). 2012;26:1004–11.
31. Tufail A, Patel PJ, Sivaprasad S, Amoaku W, Browning AC, Cole M, et al. Ranibizumab for the treatment of choroidal neovascularisation secondary to pathological myopia: interim analysis of the REPAIR study. Eye (Lond). 2013;27:709–15.
32. Wolf S, Balciuniene VJ, Laganovska G, Menchini U. Ohno-Matsui K5, Sharma T, et al. RADIANCE: A randomized controlled study of ranibizumab in patients with choroidal neovascularization secondary to pathologic myopia. Ophthalmology. 2014;121(3):682–92.
33. Freund KB, Ciardella AP, Yannuzzi LA, Pece A, Goldbaum M, Kokame GT, et al. Peripapillary detachment in pathologic myopia. Arch Ophthalmol. 2003;121(2):197–204.
34. Toranzo J, Cohen SY, Erginay A, Gaudric A. Peripapillary intrachoroidal cavitation in myopia. Am J Ophthalmol. 2005;140(4):731–2.
35. Gaucher D, Erginay A, Lecleire-Collet A, Haouchine B, Puech M, Cohen SY, et al. Dome-shaped macula in eyes with myopic posterior staphyloma. Am J Ophthalmol. 2008;145(5):909–14.
36. Imamura Y, Iida T, Maruko I, Zweifel SA, Spaide RF. Enhanced depth imaging optical coherence tomography of the sclera in dome-shaped macula. Am J Ophthalmol. 2011;151(2):297–302.

Vitreomacular Traction Syndrome

9

Zofia Michalewska and Jerzy Nawrocki

Swept source OCT (SS-OCT) seems to be an ideal tool to evaluate vitreomacular traction (VMT) syndrome as it enables simultaneous visualization of the vitreous, retina, and choroid on wide-field 12 mm scans.

9.1 Classification of VMT

Idiopathic VMT syndrome was previously described by Gass as a foveaolar yellow spot or ring, loss of foveal depression without vitreofoveal separation.

Some authors have also suggested that focal vitreomacular traction (<1500 μm) is more likely to spontaneously detach than broad attachment (>1500 μm) (Fig. 9.1) [1]. Those eyes are also more likely to develop greater postoperative visual improvement [2].

Bottós et al. classified incomplete detachment of vitreomacular traction as either V-shaped or J-shaped (Fig. 9.1). A high correlation was found between V-shaped and focal vitreomacular traction and between broad and J-shaped vitreomacular traction [3].

Eyes with V-shaped focal attachment are more likely to develop macular edema, full thickness macular hole, and fovea detachment. On the other hand, epiretinal membranes more often coexisted with broad, J-shaped adhesions.

Recently the vitreomacular traction study group differentiated vitreomacular adhesion from vitreomacular traction syndrome. Vitreomacular adhesion does not present morphologic changes in the retina (Fig. 9.2).

Z. Michalewska, MD, PhD (✉) • J. Nawrocki, MD, PhD
Jasne Blonia Ophthalmic Clinic, Lodz, Poland
e-mail: zosia_n@yahoo.com; jerzy_n@poczta.onet.pl

© Springer International Publishing AG 2017

Z. Michalewska, J. Nawrocki (eds.), *Atlas of Swept Source Optical Coherence Tomography*,
DOI 10.1007/978-3-319-49840-9_9

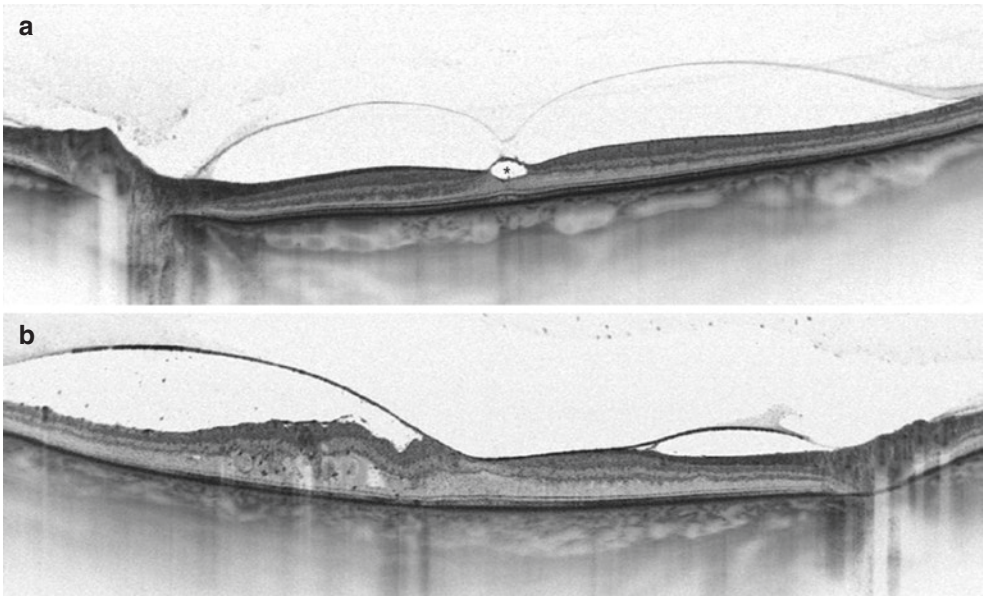

Fig. 9.1 (**a**), Focal idiopathic vitreomacular traction. V-shaped. (**b**) Broad vitreomacular traction in a patient with non-proliferative diabetic retinopathy. J-shaped

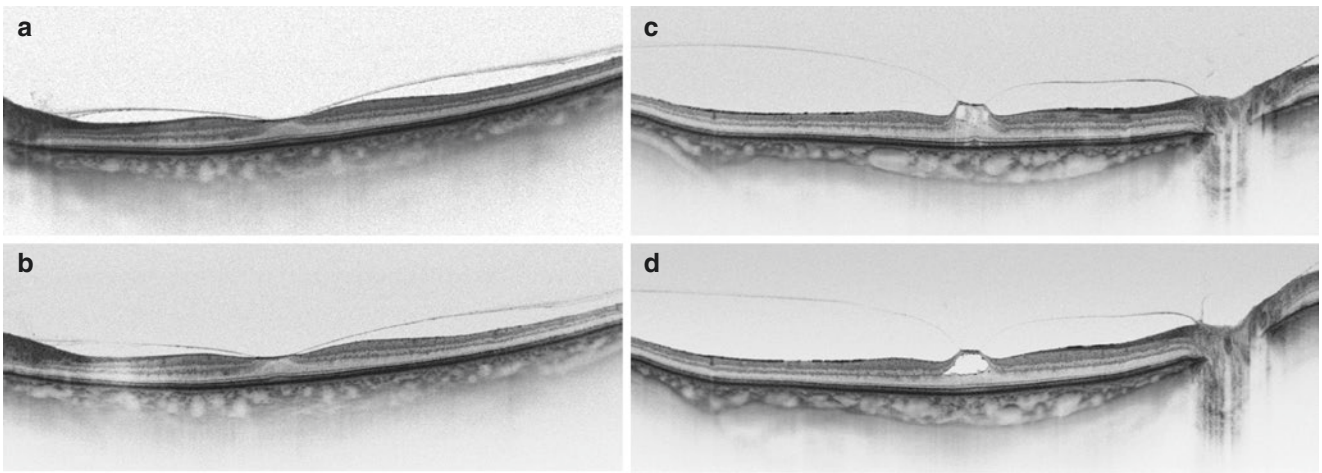

Fig. 9.2 (**a**, **b**) Vitreomacular adhesion in an 80-year-old woman. (**a**) Fovea contour and retina morphology is undisturbed. The outer choroidoscleral boundary is regular. Visual acuity is 1.0 Snellen. (**b**) One year later, vitreomacular adhesion in the same patient. Slight elevation of the fovea contour is visible. Visual acuity is unchanged, 1.0 Snellen. (**c**, **d**) Vitreomacular traction syndrome in a 79-year-old woman. (**c**) Focal vitreomacular traction with elevation of the fovea contour. Cystoid spaces in the inner retinal layers are visible. Slight elevation of the photoreceptor layer and external limiting membrane may be observed. Nuclear and plexiform layers are elevated. The outer choroidoscleral boundary is irregular. Visual acuity is 0.5 Snellen. (**d**) Vitreomacular traction in the same patient eight months later. The cystoid spaces regrouped into one large space. None of the retinal layers are now elevated. Visual acuity decreased to 0.3 Snellen

9.2 Clinical Appearance

Three-dimensional scanning enhances our knowledge of vitreomacular traction syndrome (Figs. 9.3, 9.4, and 9.5). SS-OCT enables simultaneous high quality three-dimensional visualization of the vitreous, retina, and choroid. Vitreomacular traction should always be regarded as a three-dimensional disease. Many adhesion points between the vitreous and retina exist, besides that seen in the foveola on the central B-scan. The adhesion between retina and vitreous is usually strongest 1500 µm around the fovea [4], at the optic nerve, and along retinal vessels. Three-dimensional imaging might thus facilitate surgical planning, as it reveals multiple traction sites besides the fovea. In the natural course of the disease it is possible that the central traction is relieved, but it persists in the proximity to retinal vessels.

Many morphological changes of the fovea might be observed in SS-OCT. Cystoid spaces in the inner retinal layers are visible in most eyes (Fig. 9.1a [*star*]). The photoreceptor layer and external limiting membrane might remain intact in the presence of an inner cystoid space despite existing traction. Thus inner cystoid spaces are not always symptomatic. They might progress over time. If multiple cystoid spaces are present in the inner retinal layers, they tend to group into one larger cystoid space (Fig. 9.2c, d). Less frequent, outer retina cystoid spaces may be visible (Fig. 9.6, upper left [*star*]). If an elevation of the photoreceptor layer coexists with an outer lamellar macular hole, it is highly probable that this appearance will progress to full thickness macular hole (Fig. 9.6) [5]. If vitreomacular traction is released (spontaneously or after treatment), cystoid spaces decrease in size and later disappear (Fig. 9.7).

Epiretinal membranes might coexist with vitreomacular traction syndrome in about 25–83% of eyes (Fig. 9.7) [1, 6, 7]. Spontaneous resolution of eyes with coexisting epiretinal membranes and vitreomacular traction syndrome is less likely, but possible in very rare cases.

Photoreceptor and external limiting membrane defects develop during follow-up of vitreomacular traction syndrome in more than 60% of cases (Fig. 11.1b) [1]. They are associated with decreased visual acuity and metamorphopsia.

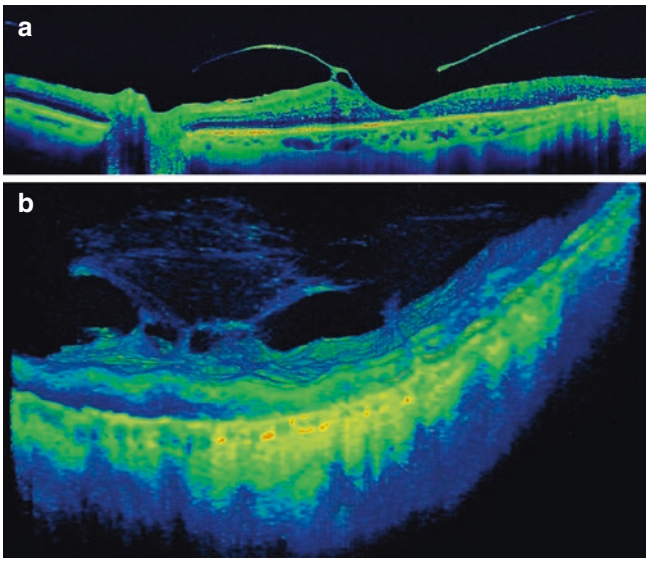

Fig. 9.3 (**a**) Focal vitreomacular traction on SS-OCT. Visual acuity is 0.15. (**b**) Three-dimensional image of the same patient. Multiple adhesion points between the vitreous and fovea are visible

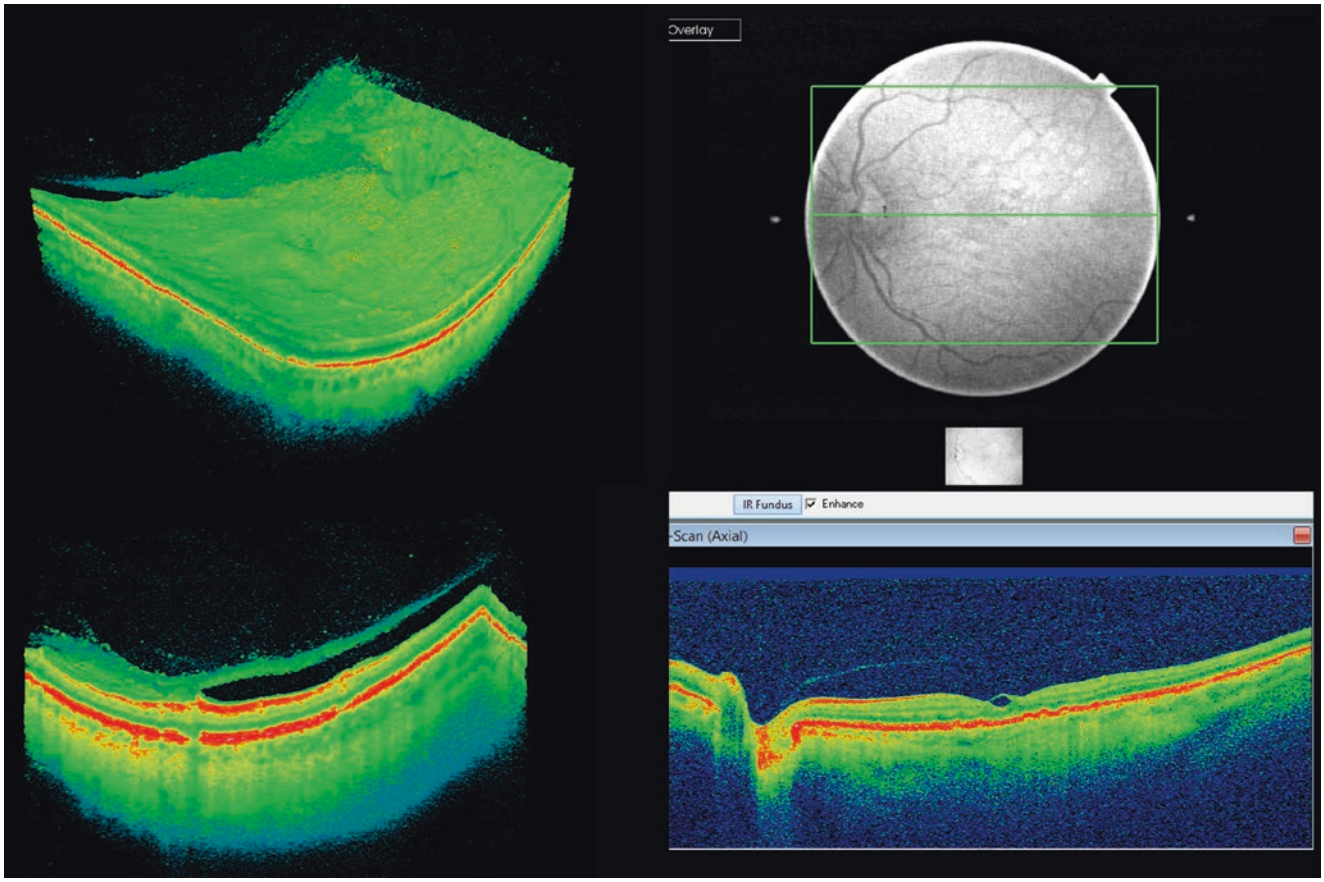

Fig. 9.4 Three-dimensional imaging of vitreomacular traction syndrome

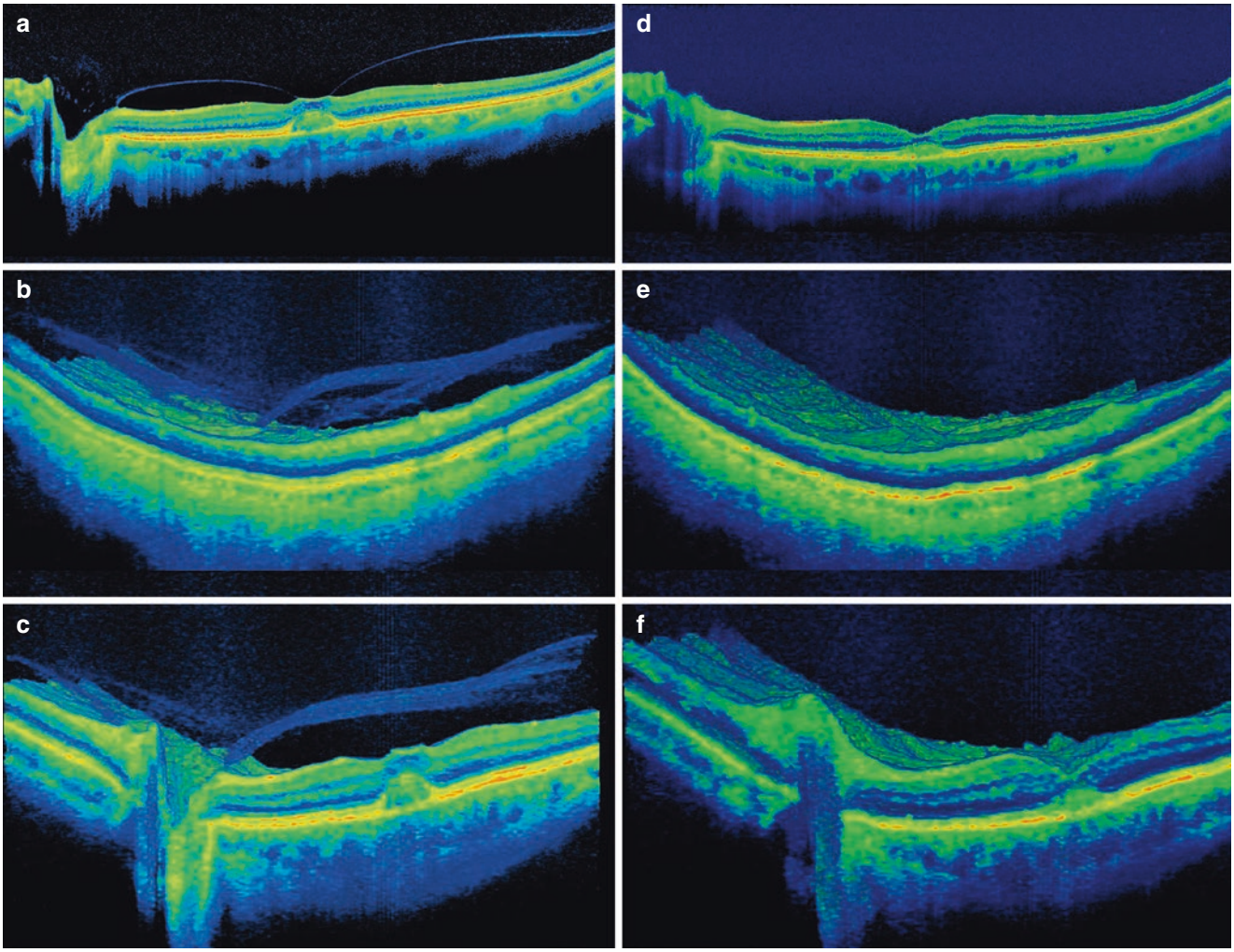

Fig. 9.5 (**a**) B-scan of focal vitreoretinal traction syndrome. Visual acuity is 0.16. (**b**) Three-dimensional SS-OCT scan. Multiple traction sites are visible. (**c**) Cross-section through the fovea in the three-dimensional scan. Traction on the fovea and optic nerve is visible. (**d**) B-scan shows normalization of the fovea contour 6 months after surgery. Visual acuity is 0.8. (**e**) Three-dimensional SS-OCT without any visible traction after surgery. (**f**) Cross-section through the fovea in the three-dimensional scan after surgery

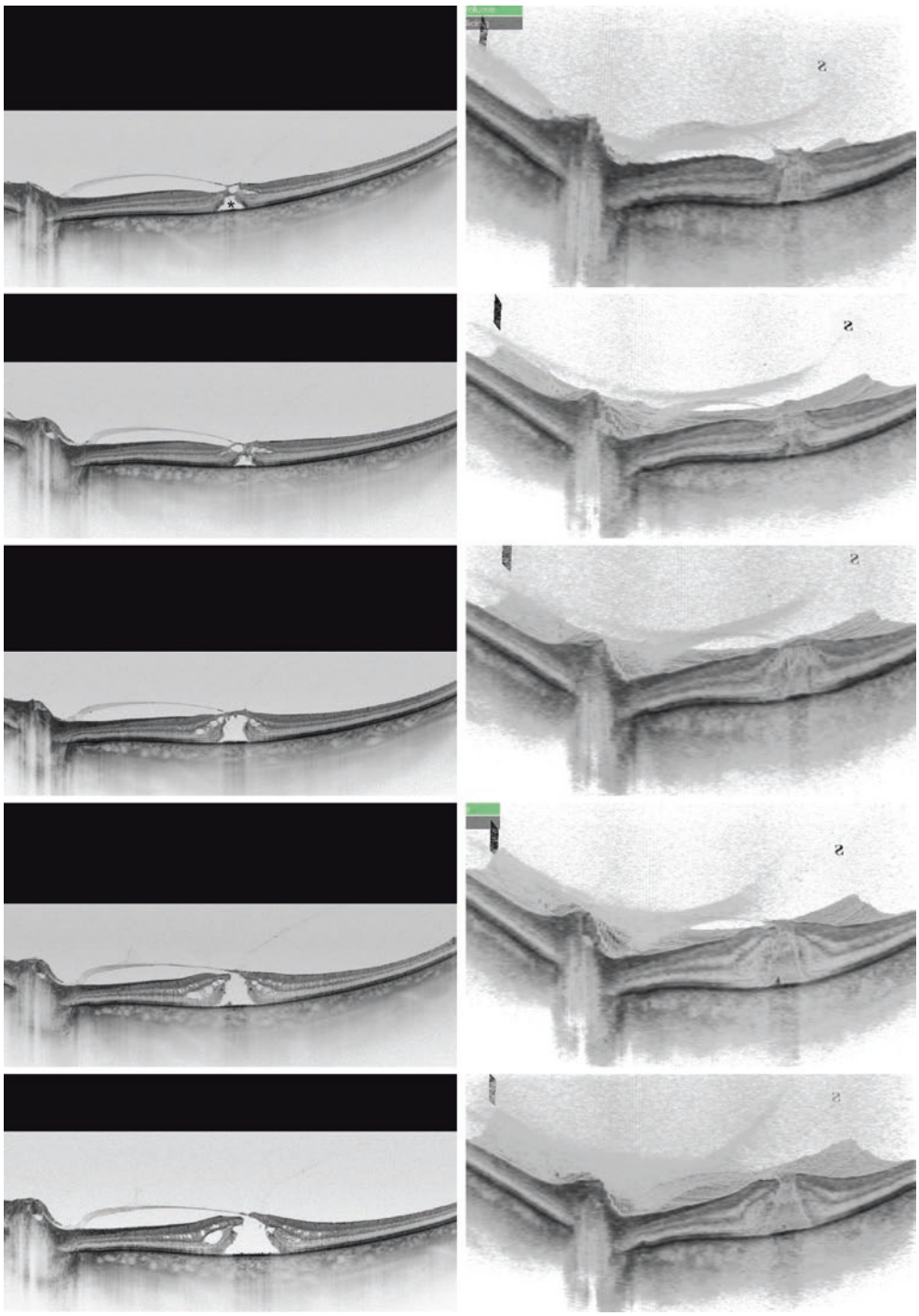

Fig. 9.6 Vitreomacular traction syndrome progressing to a full thickness macular hole. The B-scans, shown on the left, and three-dimensional scans, on the right, were taken at monthly intervals from October 2013 to March 2014. Visual acuity decreased from 0.4 to 0.2 Snellen in the course of this disease

Fig. 9.6 (continued)

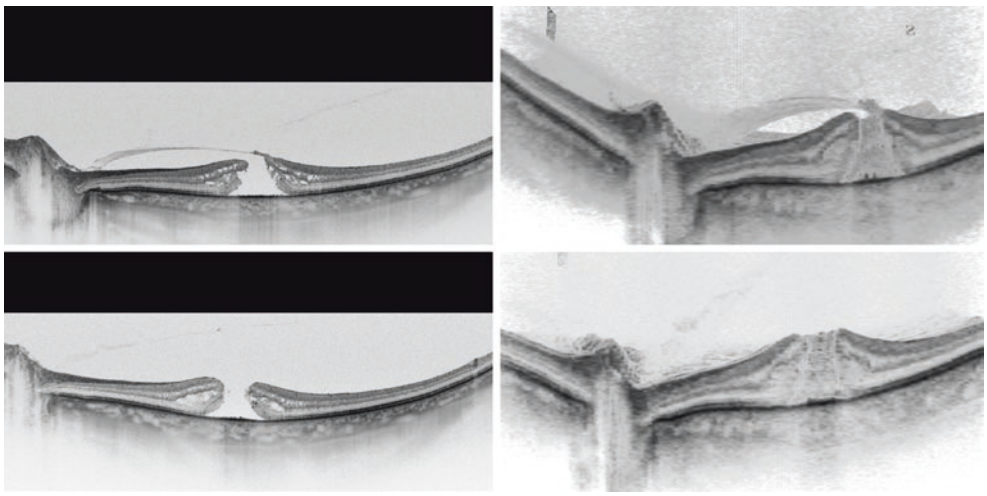

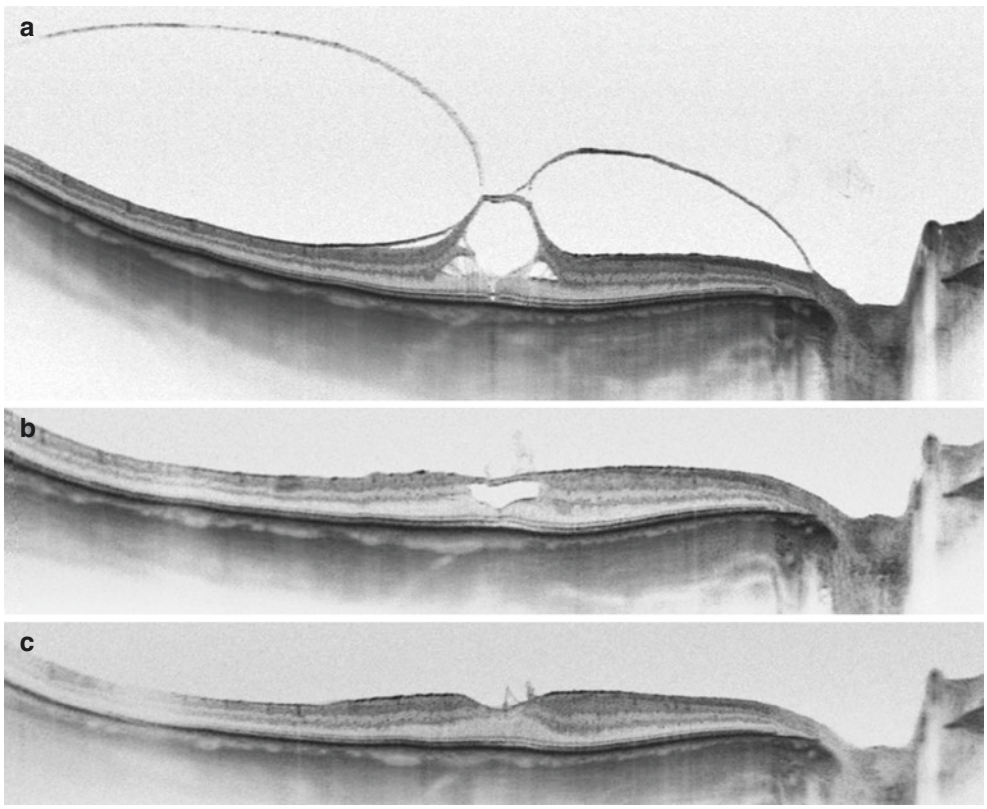

Fig. 9.7 Vitreomacular traction syndrome with epiretinal membrane in a 78-year-old woman. (**a**) Before surgery. Visual acuity is 0.2 Snellen. (**b**) One month after surgery. Visual acuity is 0.2 Snellen. (**c**) Eighteen months after surgery. Fovea contour and retina layers completely normalized. Visual acuity improved to 0.32 Snellen

9.3 The Natural Course of Idiopathic VMT

There are only a few studies describing the natural course of vitreomacular traction. In our series of 130 eyes observed for 24 months, only 20 required surgery (Michalewska et al. unpublished data). Most eyes resolve spontaneously with good final visual acuity (Fig. 9.8). In some cases, however, vitreomacular traction may be a very dynamic disease and may lead to development of full thickness macular holes (Figs. 9.6 and 11.1), lamellar macular holes or epiretinal membranes.

Earlier spectral domain OCT (SD-OCT) studies reported that spontaneous resolution of vitreomacular traction is more probable in eyes with a smaller adhesion area between the vitreous and retina.

We confirmed with multivariate analysis (Michalewska et al. unpublished data) that two factors are independently associated with progression or resolution of vitreomacular traction syndrome: phacoemulsification ($p = 0.02$) and observation time ($p = 0.03$). Unfortunately, it is impossible to predict which vitreomacular traction will progress and which will resolve spontaneously. The only described morphological criterion of progression is the elevation of the photoreceptor layer. If such an elevation exists, it is highly probable that a full-thickness macular hole will develop [5].

Choroidal thickness measurements are possible with SS-OCT. In a group of 27 eyes evaluated for 24 months with SS-OCT we confirmed that choroidal thickness decreases in eyes in which vitreomacular traction is spontaneously relieved (Michalewska et al. unpublished data).

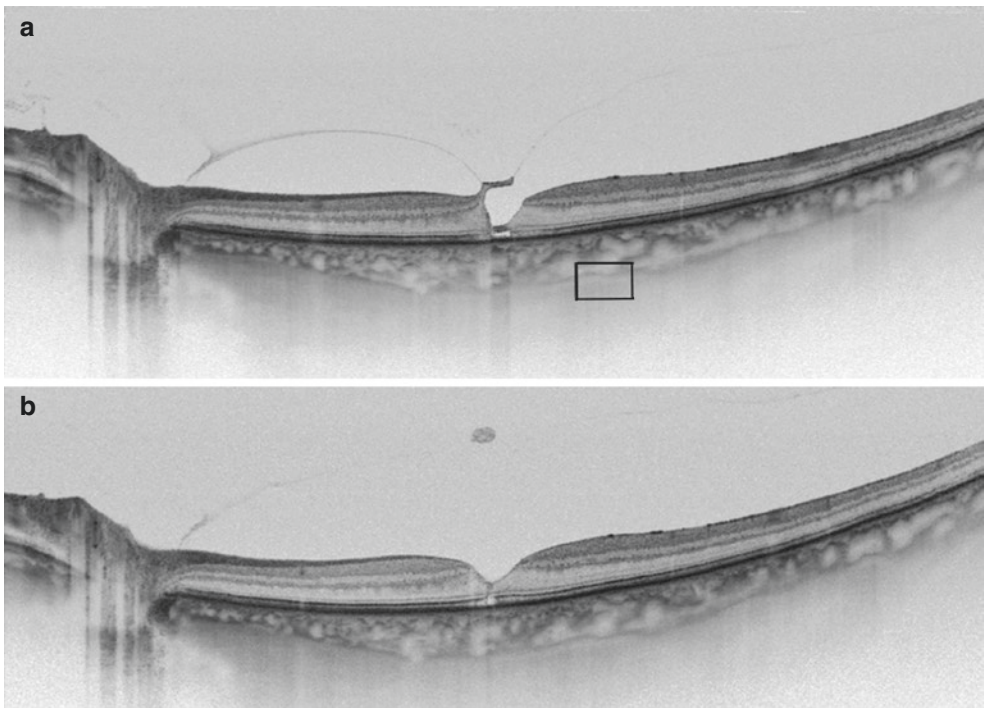

Fig. 9.8 (**a**) Vitreomacular traction syndrome in a 64-year-old woman. Visual acuity is 0.8. Suprachoroidal layer is visible. (**b**) Spontaneous release of traction. Visual acuity is 0.8. Suprachoroidal layer remained visible

9.4 Treatment

Symptomatic vitreomacular traction may be treated with either intravitreal injection of gas, ocriplasmin, or vitrectomy (Figs. 9.7 and 9.9). Vitreomacular adhesion resolves in about one-quarter of ocriplasmin-treated eyes [8], which makes this technique less efficient than vitrectomy. Even if injections are considered to be less invasive than surgery, about 68% of ocriplasmin-treated patients developed minor adverse events, such as conjunctival hemorrhage or floaters. A small case series reported release of traction in about 55% of cases after intrevitreal gas injection [9]. The lack of randomized studies on this topic make specific treatment recommendations difficult. Earlier SD-OCT studies reported that the outer foveal thickness (the distance between the external limiting membrane and the retinal pigment epithelium) is the sole factor confirmed by multivariate analysis to be correlated with visual acuity 12 months after surgery for vitreomacular traction syndrome [10]. The exact timing for treatment still remains a topic of controversy. It must be taken into consideration that according to recent reports, three years after vitrectomy only about 30% of patients have experienced full restoration of the IS/OS junction [11], whereas just 1 year after vitrectomy for full-thickness macular hole, full restoration occurred in 70% of cases [12]. This is perhaps surprising, as most would assume vitreomacular traction as a less severe disease than an impending macular hole (Figs. 9.7 and 9.9).

Another vitreomacular interface disease in which we do not achieve full normalization of the fovea morphology is idiopathic epiretinal membrane. The histopathology of epiretinal membranes and vitreomacular traction is similar. In both entities, fibrous astrocytes, myofibroblasts, and fibrocytes have been observed [13–17]. Assuming that epiretinal membranes occur mostly in eyes with posterior hyaloid detachment, Koizumi and coworkers hypothesized that hyperreflective placoid areas noted in vitreomacular traction syndrome may represent fibrocellular proliferation extending the posterior vitreous. It was also previously reported that posterior vitreous detachment creates dehiscence in the internal limiting membrane through which cells migrate and proliferate on the retinal surface [18]. This may be additionally stimulated by vitreous cortical remnants [6, 19]. Summarizing, there seems to be a correlation between the development of vitreomacular traction syndrome and epiretinal membranes, which requires further study. These entities may also coexist (Fig. 9.7).

Owing to its increased wavelength, SS-OCT enables us to simultaneously visualize the vitreous, retina, and choroid. Below the choroid, the suprachoroidal layer is visible. The suprachoroidal layer is situated on the outer choroidoscleral boundary (CSB). It consists of two lines, the inner hyperreflective and an outer hyperreflective line corresponding to the suprachoroidal space [20]. Earlier reports suggest that the suprachoroidal layer is more often visible in vitreomacular traction syndrome than in other vitreoretinal interface diseases [20–22] (Fig. 9.8 [*box*]). The meaning of this finding is still not completely clear. Probably, dynamic prolonged traction exerts some forces through the retina onto the choroid and broadens the suprachoroidal space slightly.

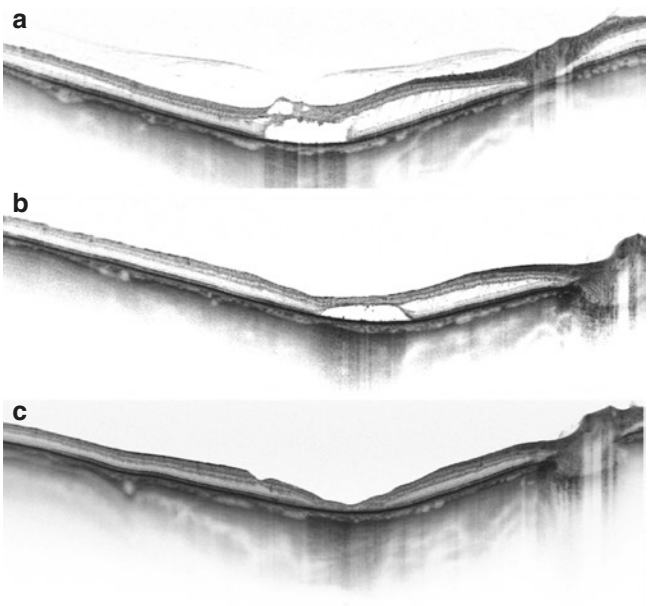

Fig. 9.9 (**a**) Vitreomacular traction syndrome with focal neurosensory retinal detachment. (**b**) SS-OCT after vitrectomy. Defect in the outer retinal layers is visible. (**c**) Six months after surgery. Retina is attached, but defects in the photoreceptor layer are still visible

9.5 Swept Source OCT Angiography

Swept Source OCT Angiography (SS-OCTA) is a technique that derived from *en face* optical coherence tomography. A detailed assessment of the retinal and choroidal circulation is achievable with this method. Moving objects, i.e., erythrocytes, are hyperreflective in SS-OCTA images, while non-moving objects are hyporeflective. This enables the visualization of retinal vessels with persistent flow. As this technique is derived from SS-OCT, it is possible to observe flow at different levels and in all retinal and choroidal layers. Retinal vessels are localized at two levels. The superficial plexus is localized at the level of the retinal nerve fiber layer and is also possible to visualize with fluorescein angiography. The deep retinal plexus is localized at the level of the outer plexiform layer, and could not be identified before the era of SS-OCTA.

Superficial retinal vessels in idiopathic vitreomacular traction syndrome are unchanged (Fig. 9.10, top left). However, in the deep retinal plexus the flow may seem altered (Fig. 9.11, top middle left) when compared to a healthy eye (Fig. 9.12). We note that in the deep retinal plexus, the fovea avascular zone is slightly irregular and wider when compared to a healthy eye. Additionally, deep retinal vessels seem more irregular.

The status of retinal vessels, especially in the deep retinal layers, depends on the severity of VMT. If the pathology is moderate and traction does not cause substantial changes in the fovea morphology, layer segmentation is correct in SS-OCTA and particular retinal layers do not differ much from a healthy subject. If, however, traction severely distorts the foveola, causing an outer macular hole, artifacts are visible (Fig. 9.11). If an outer lamellar macular hole is present, we observe a hyperreflective circle at the level of the choriocapillaries. This circle is an artifact. The laser beam in optical coherence tomography is partially reflected and partially scattered by tissue. If, as in the example of an outer lamellar macular hole, there is a lack of tissue, more laser light arrives to the center of the foveola at the level of the choriocapillaries, and therefore more light is reflected back to the sensor; the resultant "brightness" is an artifact and does not, in this instance, correspond to increased flow. An additional explanation on how such artifacts are created is provided in Chapter 11.

Vitreomacular traction may be idiopathic or coexist with multiple retinal diseases, such as choroidal neovascularization, macular edema in diabetes, or vein occlusion, etc. SS-OCTA without dye might enable us to make a precise diagnosis in those difficult cases. In Fig. 9.13 we notice the development of choroidal neovascularization. The neovascular membrane is presented at the level of the normally avascular retinal pigment epithelium.

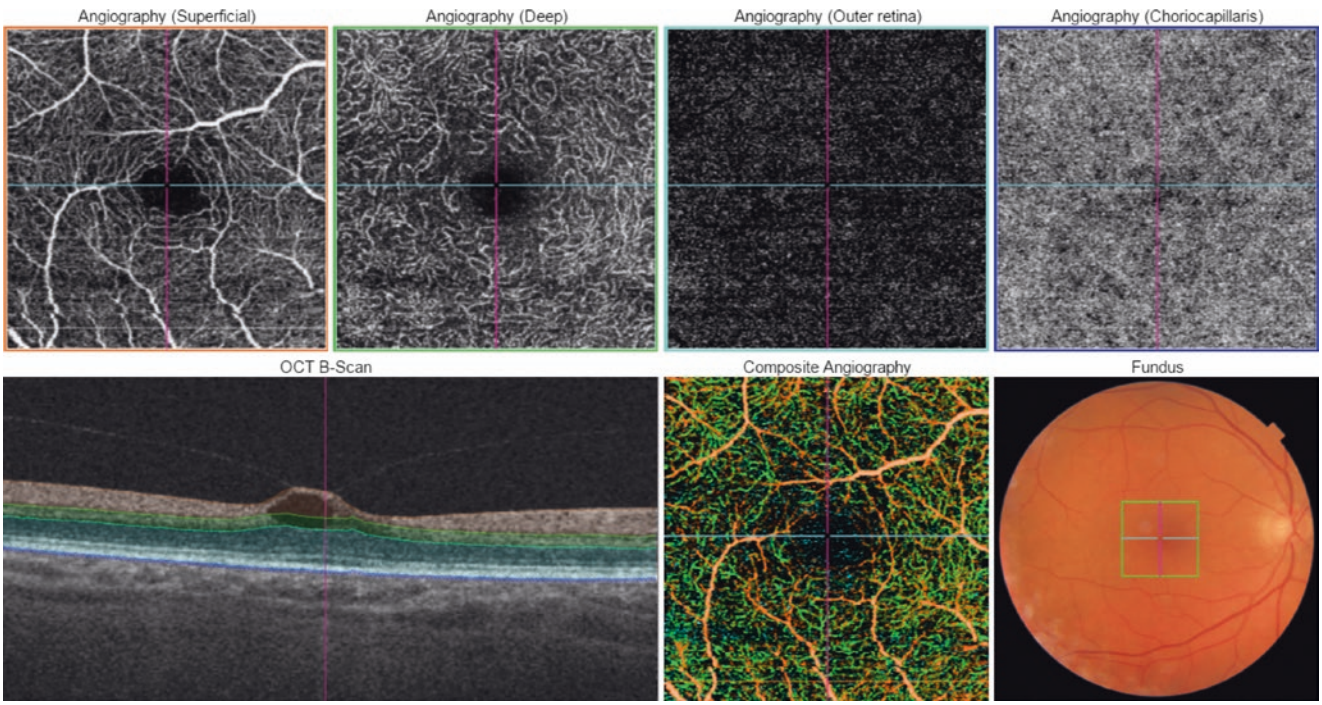

Fig. 9.10 SS-OCTA of an eye with idiopathic vitreomacular traction. The *orange box* (*Angiography [Superficial]*) shows the superficial retinal vessels. The *green box* (*Angiography [Deep]*) shows the deep retinal plexus. Vessels are less packed than in a healthy eye. The foveal avascular zone seems slightly enlarged when compared to a healthy eye. The *light blue box* (*Angiography [Outer retina]*) shows the avascular zone. The *dark blue box* (*Angiography [Choriocapillaris]*) shows the Choriocapillaries. Lower middle (*Composite Angiography*)-SS-OCTA with all layers distinguished by particular colors in one image. Lower right, Fundus photo

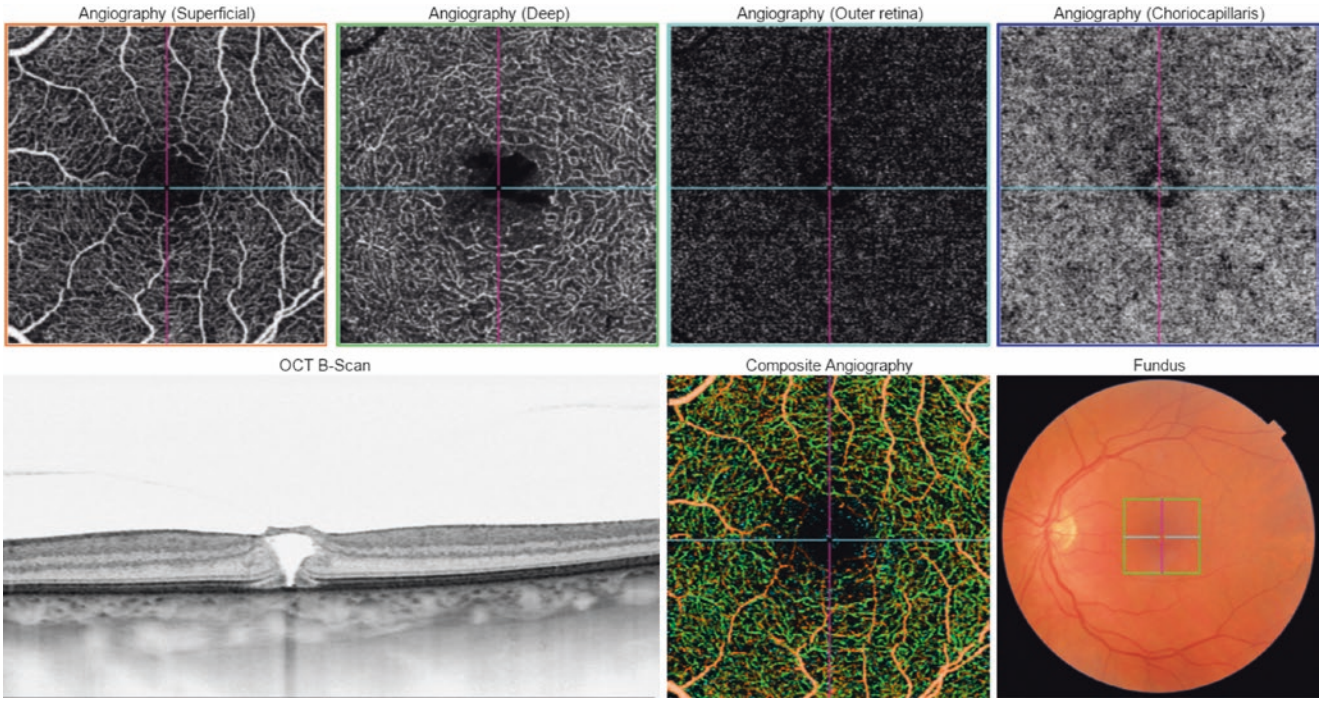

Fig. 9.11 SS-OCTA of an eye with idiopathic vitreomacular traction. *Orange box*, superficial retinal vessels. *Green box*, deep retinal plexus, vessels are less packed than in a healthy eye. The foveal avascular zone seems slightly enlarged when compared to a healthy eye. *Light Blue box*, avascular zone. *Dark blue box*, Choriocapillaries

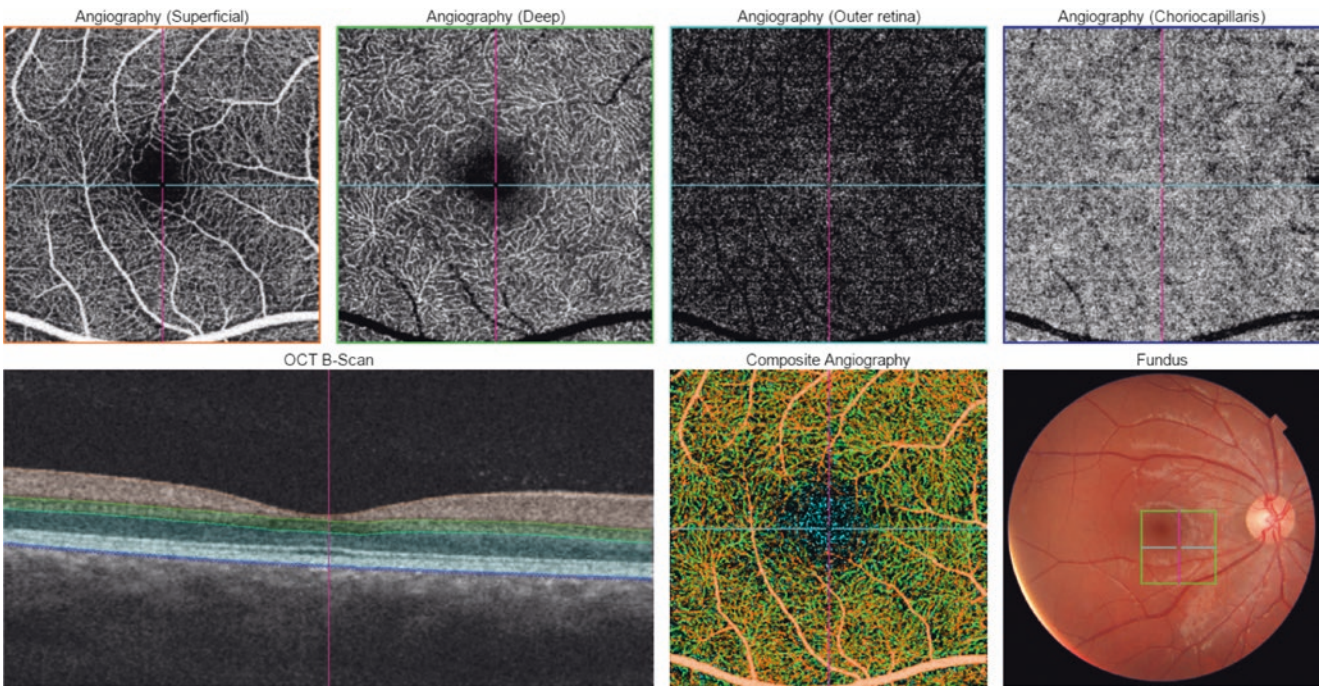

Fig. 9.12 SS-OCTA of a healthy eye. Orange box, superficial retinal vessels. *Green box*, deep retinal plexus. *Light blue box*, avascular zone. *Dark blue box*, Choriocapillaries. Lower left, SS-OCT B-Scan. Lower middle (*Composite Angiography*), SS-OCTA with all layers distinguished by particular colors in one image. Lower right, Fundus photo

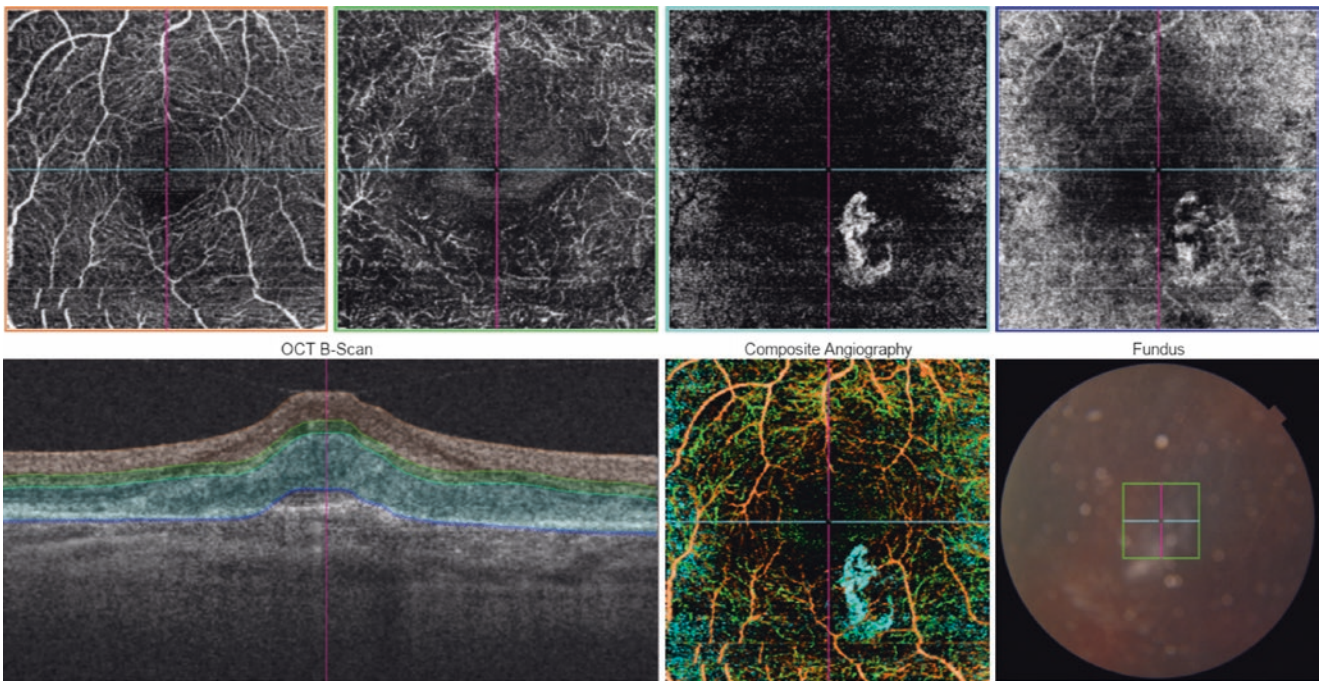

Fig. 9.13 SS-OCTA of an eye with vitreomacular traction and central neovascularization. *Orange box*, superficial retinal vessels. *Green box*, deep retinal plexus. *Light blue box*, avascular zone. Pathological vessels are visible. *Dark blue box*, Choriocapillaries, pathological vessels are visible in this case. Lower left, The SS-OCT B-Scan shows the VMT and subretinal neovascular membrane. Lower middle (*Composite Angiography*), SS-OCTA with all layers distinguished by particular colors in one image. Lower right, Fundus photo

References

1. Odrobina D, Michalewska Z, Michalewski J, Dzięgielewski K, Nawrocki J. Long-term evaluation of vitreomacular traction disorder in spectral-domain optical coherence tomography. Retina. 2011;31:324–31.
2. Bottos J, Elizalde J, Rodrigues EB, Farah M, Maia M. Vitreomacular traction syndrome: postoperative functional and anatomic outcomes. Ophthalmic Surg Lasers Imaging Retina. 2015;46:235–42.
3. Bottós J, Elizalde J, Rodrigues EB, Farah M, Maia M. Classifications of vitreomacular traction syndrome: diameter vs morphology. Eye (Lond). 2014;28:1107–12.
4. Kishi S, Demaria C, Shimizu K. Vitreous cortex remnants at the fovea after spontaneous vitreous detachment. Int Ophthalmol. 1986;9:253–60.
5. Michalewska Z, Michalewski J, Sikorski BL, Kałuzny JJ, Wojtkowski M, Adelman RA, et al. A study of macular hole formation by serial spectral optical coherence tomography. Clin Exp Ophthalmol. 2009;37:373–83.
6. Koizumi R, Spaide RF, Fisher YL, Freund KB, Klancnik Jr JM, Yannuzzi LA. Three-dimensional evaluation of vitreomacular traction and epiretinal membrane using spectral-domain optical coherence tomography. Am J Ophthalmol. 2008;145:509–17.
7. Gandorfer A, Rohleder M, Kampik A. Epiretinal pathology of vitreomacular traction syndrome. Br J Ophthalmol. 2002;86:902–9.
8. Stalmans P, Benz MS, Gandorfer A, Kampik A, Girach A, Pakola S, et al. Enzymatic vitreolysis with ocriplasmin for vitreomacular traction and macular holes. N Engl J Med. 2012;367:606–15.
9. Day S, Martinez JA, Nixon PA, Levitan M, Dooner JW, Wong RW, et al. Intravitreal sulfur hexafluoride injection for the treatment of vitreomacular traction syndrome. Retina. 2016;36:733–7.
10. Ichiyama Y, Kawamura H, Fujikawa M, Sawada O, Saishin Y, Ohji M. Photoreceptor outer segment length and outer foveal thickness as factors associated with visual outcome after vitrectomy for vitreomacular traction syndrome. Retina. 2016;36:1707–12. [Epub ahead of print]
11. Lee EK, Heo JW, Yu HG, Chung H. Recovery of foveal photoreceptor integrity after vitrectomy in eyes with an impending macular hole with vitreomacular traction syndrome. Retina. 2015;36(8):1454–62. [Epub ahead of print]
12. Michalewska Z, Michalewski J, Nawrocki J. Continuous changes in macular morphology after macular hole closure visualized with spectral optical coherence tomography. Graefes Arch Clin Exp Ophthalmol. 2010;248:1249–55.
13. Gastaud P, Betis F, Rouhette H, Hofman P. Ultrastructural findings of epimacular membrane and detached posterior hyaloid in vitreomacular traction syndrome. J Fr Ophtalmol. 2000;23:587–93.
14. Smiddy WE, Green WR, Michels RG, de la Cruz Z. Ultra-structural studies of vitreomacular traction syndrome. Am J Ophthalmol. 1989;107:177–85.
15. Shinoda K, Hirakata A, Hida T, Yamaguchi Y, Fukuda M, Maekawa S, et al. Ultrastructural and immunohistochemical findings in five patients with vitreo-macular traction syndrome. Retina. 2000;20:289–93.
16. Kampik A, Kenyon KR, Michels RG, Green WR, de la Cruz ZC. Epiretinal and vitreous membranes. Comparative study of 56 cases. Arch Ophthalmol. 1981;99:1445–54.
17. Smiddy WE, Maguire AM, Green WR, Michels RG, de la Cruz Z, Enger C, et al. Idiopathic epiretinal membranes. Ultrastructural characteristics and clinicopathologic correlation. Ophthalmology. 1989;96:811–20. discussion 821
18. Clarkson JG, Green WR, Massof D. A histopathologic review of 168 cases of preretinal membrane. Am J Ophthalmol. 1977;84:1–17.
19. Kishi S, Shimizu K. Oval defect in detached posterior hyaloid membrane in idiopathic preretinal macular fibrosis. Am J Ophthalmol. 1994;118:451–6.
20. Michalewska Z, Michalewski J, Nawrocka Z, Dulczewska-Cichecka K, Nawrocki J. Suprachoroidal layer and suprachoroidal space delineating the outer margin of the choroid in swept-source optical coherence tomography. Retina. 2015;35:244–9.
21. Michalewska Z, Michalewski J, Nawrocka Z, Dulczewska-Cichecka K, Nawrocki J. The outer choroidoscleral boundary in full-thickness macular holes before and after surgery-a swept-source OCT study. Graefes Arch Clin Exp Ophthalmol. 2015;253:2087–93.
22. Michalewska Z, Michalewski J, Ornafel-Sagan K, Nawrocki J. Swept-source optical coherence tomography correlations between retina and choroid before and after vitrectomy for epiretinal membranes. Am J Ophthalmol. 2016;165:100–7.

Epiretinal Membranes

10

Zofia Michalewska and Jerzy Nawrocki

Epiretinal membranes are thin fibrovascular structures localized at the inner retinal surface.

Studies based in Spectral Domain OCT (SD-OCT) report a much higher frequency of epiretinal membranes in the population than earlier fundus photography based studies (34% vs. 10.9%) [1, 2].

Most early idiopathic epiretinal membranes stay asymptomatic. In the course of the disease, metamorphopsia, micropsia, and decreased visual acuity are noted. Progression of the disease is very slow, about one or two Snellen lines every 5 years [3].

10.1 Classification

Before the OCT era, epiretinal membranes were classified during the fundus examination according to retinal wrinkling (Table 10.1). In OCT, an epiretinal membrane may be visualized either as a thin hyperreflective structure situated inner to the internal limiting membrane (ILM) and visibly separated from it (typical membranes, tractional membranes), or as a hyperreflective line with a moderately reflective structure filling the space between the line and retinal nerve fiber layer (atypical membranes, dense membranes, thickened membranes, lamellar hole-associated epiretinal proliferation) (Fig. 10.1) [4–6]. Atypical membranes were reported to correspond to thickened posterior hyaloid with embedded epiretinal cells [7]. Immunohistological studies suggested atypical membranes (mostly negative for alpha-smooth muscle protein) produce less tractional forces on the retina than typical, tractional membranes. However, the natural history is similar in both appearances of epiretinal membranes [8].

In epiretinal membrane cases, we recently confirmed that a preoperative decrease in visual acuity is associated with progressing deformation of the plexiform layers (Fig. 10.2) [9]. Photoreceptor defects and central retinal thickness were also confirmed by many studies to be associated with visual acuity, but their progression during the follow up was not often observed.

Epiretinal membranes may either precisely adhere to the inner retinal layers (Fig. 10.3a) or have many junction spots (Fig. 10.3b). It was proposed that in eyes in which there are many adhesion spots between the epiretinal membrane and retina, the epiretinal membrane may be easier to peel [10]. All data acquired with SD-OCT have been confirmed with Swept Source OCT (SS-OCT).

Z. Michalewska, MD, PhD (✉) • J. Nawrocki, MD, PhD
Jasne Blonia Ophthalmic Clinic, Lodz, Poland
e-mail: zosia_n@yahoo.com; jerzy_n@poczta.onet.pl

© Springer International Publishing AG 2017

Z. Michalewska, J. Nawrocki (eds.), *Atlas of Swept Source Optical Coherence Tomography*,
DOI 10.1007/978-3-319-49840-9_10

Table 10.1 ERM and macular hole classification guides

Gass classification of ERM	Grade 0: Cellophane Maculopathy-translucent with no distortion of retina; cellophane light reflex
	Grade 1: Crinkled Cellophane Maculopathy-irregular retinal folds and light reflex, radiating retinal folds; visual acuity >20/40, ±metamorphopsia, insidious onset
	Grade 2: Macular Pucker-grayish membrane; marked retinal crinkling and puckering of macula; PVD in 90%; may see edema, retinal heme, CWS, SRD, and leakage viewed by FA; VA 20/200 or less, insidious to sudden onset, usually with metamorphopsia
OCT classification of ERM (Fig. 10.1)	Typical membranes (tractional membranes): In OCT thin hyperreflective structure situated inner to the internal limiting membrane and visibly separated from it
	Atypical membranes (dense membranes, thickened membranes, lamellar hole–associated epiretinal proliferation): in OCT hyperreflective line and moderately reflective structure filling the space between the line and retinal nerve fiber layer
Etiopathogenetic classification of ERM and non-full-thickness macular holes	Idiopathic (Figs. 10.5 and 10.6)
	Secondary (vascular diseases, retinal detachment, age related macular degeneration) (Fig. 10.7)
Morphologic classification of non-full-thickness macular holes SD-OCT (Fig. 10.5)	Macular pseudoholes
	Paralamellar macular holes
	Pseudoholes with a lamellar defect
	Lamellar macular holes

CWS cotton wool spot, *ERM* epiretinal membranes, *FA* fluorescein angiography, *PVD* posterior vitreous detachment, *OCT* optical coherence tomography, *SRD* serous retinal detachment, *SD-OCT* spectral domain optical coherence tomography, *VA* visual acuity

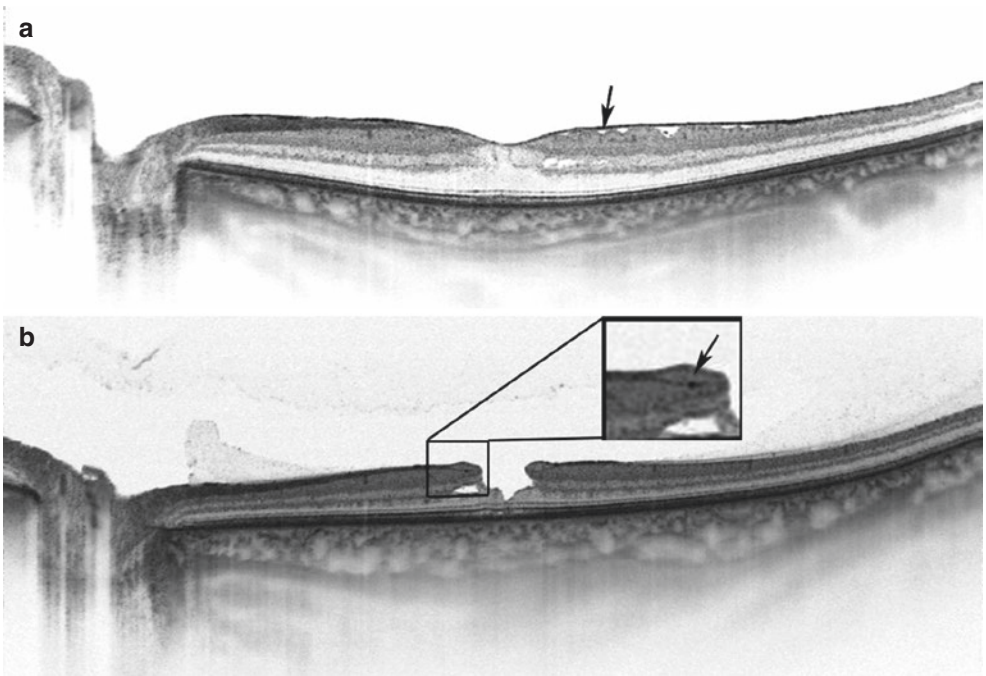

Fig. 10.1 (**a**) Typical: tractional epiretinal membrane (thin hyperreflective structure situated inner to the internal limiting membrane and visibly separated from it (*arrow*). **(b)** Atypical: dense epiretinal membrane (hyperreflective line and moderately reflective structure filling the space between the line and retinal nerve fiber layer [*arrow*])

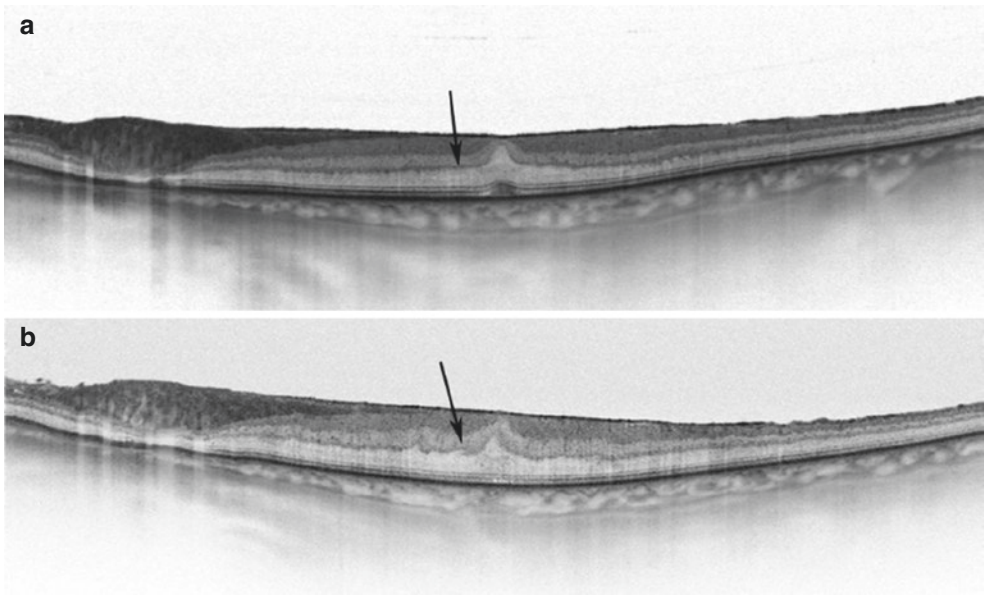

Fig. 10.2 Epiretinal membranes in a 67-year-old woman. (**a**) Initial visit. Visual acuity is 1.0 Snellen. An epiretinal membrane is visible. Slight deformation of the outer plexiform layer in the form of hyperreflective striae is visible (*arrow*). (**b**) One year later. Visual acuity is 0.5 Snellen. No new photoreceptor defects were noted. The outer plexiform layer is wavy (*arrow*)

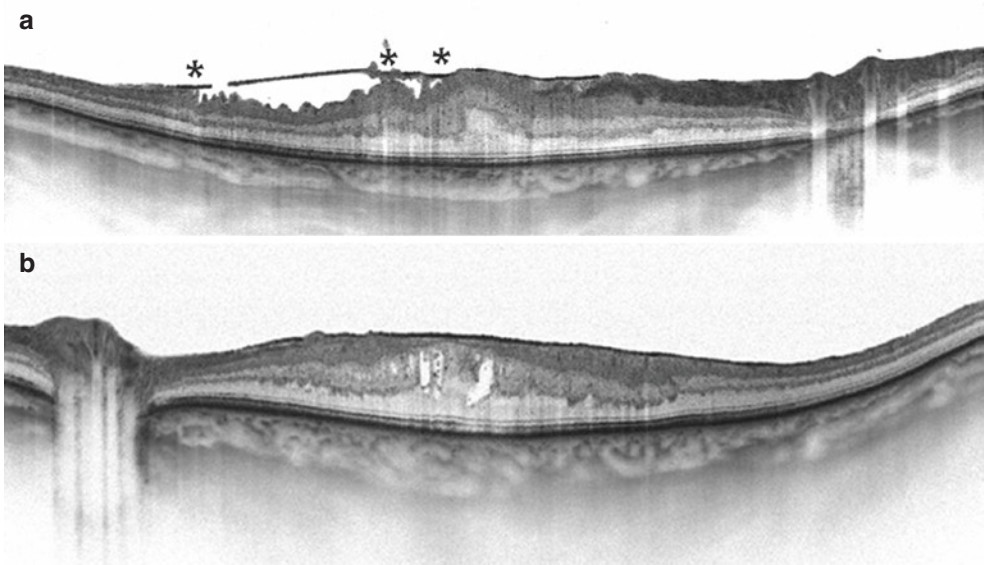

Fig. 10.3 (**a**) Epiretinal membrane with multiple adhesion spots to the retina (*black stars*) in a 68-year-old man. Visual acuity was 0.15. His final visual acuity one year after phacoemulsification combined with vitrectomy with epiretinal membranes removal and ILM peeling was 0.5. (**b**) Epiretinal membrane flat adhering to the retinal surface in a 72-year-old man. Visual acuity 0.1. His final visual acuity one year after phacoemulsification combined with vitrectomy with epiretinal membranes removal and ILM peeling was 0.3

10.2 Epiretinal Membranes Alter the Choroid

SS-OCT enables simultaneous visualization of the vitreous, retina, and choroid, and therefore may add a lot to our understanding of the pathomechanism of visual acuity loss associated with the epiretinal membrane.

Choroidal thickness has a very high intra-individual variability. It decreases in glaucoma or in nicotine abuse, and with age and refractive error [11]. It also depends on systemic vascular disease and caffeine or "energy drink" uptake. To make the measurements as reliable as possible, and thus useful for comparisons, they should be acquired at exactly the same time of the day. However, all choroidal thickness measurements should be evaluated very carefully. There is some primary data suggesting that choroidal thickness might slightly decrease three to 6 months after vitrectomy with ILM peeling for epiretinal membranes, which is not the case if vitrectomy is performed for other macular diseases [12]. The mechanism is not completely clear. It may be that choroidal thickness is slightly increased in the presence of epiretinal membranes and returns to normal values after surgery. It is not likely that vitrectomy causes choroidal thinning, as it was not confirmed for other diseases such as macular holes [13]. Thinning is not progressive, and was observed only three to 6 months after surgery. It must be considered, however, that those changes are very subtle.

A new finding observed with SS-OCT is that it is possible to visualize two lines at the choroidoscleral boundary, an upper, hyperreflective line and a lower, hyporeflective line. Together, the lines delineate the suprachoroidal layer (Fig. 10.4) [14]. The suprachoroidal layer is approximately 10–15 μm thick and is situated on the outer choroidoscleral boundary (CSB). It consists of five to ten layers of giant melanocytes interspersed between flattened processes of fibroblastic cells. As this layer was only recently recognized, little is known about its meaning. In idiopathic epiretinal membranes three factors were recognized, by multiple regression analysis, as being independently associated with the visibility of the suprachoroidal layer. First, this layer is more often visible in eyes with epiretinal membranes in which the outer plexiform layer forms waves on its outer surface, when compared to eyes with solely hyperreflective striae at the outer surface of the outer plexiform layer (Fig. 10.2). Second, it is associated with multiple adhesion points to the retina, and third, it correlates with central retinal thickness before surgery [13]. This might suggest that the suprachoroidal layer is more often visible in eyes with more prominent vitreoretinal traction and tangential traction between the epiretinal membrane and the retina.

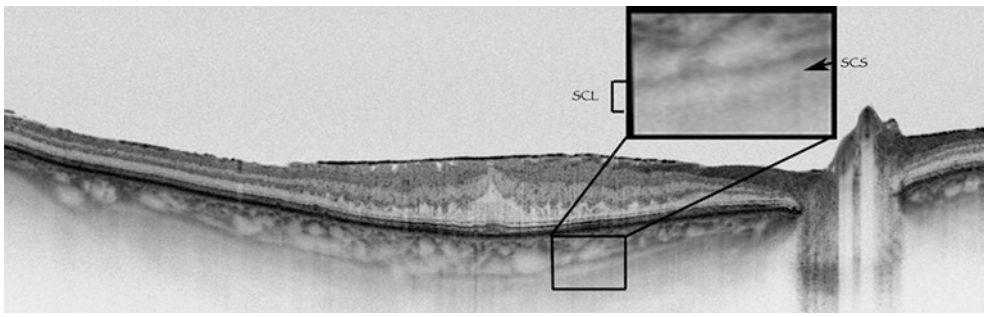

Fig. 10.4 Suprachoroidal layer (*SCL*) and suprachoroidal space (*SCS*) (*enlarged box*) visible in an eye with idiopathic epiretinal membrane

10.2.1 Epiretinal Membranes and Non-Full-Thickness Macular Holes

Since epiretinal membranes are reported to be present in most, if not in all, cases of non-full-thickness macular holes, they also need to be mentioned in this chapter [7, 15]. Before and early in the history of OCT two types of non-full-thickness macular holes were distinguished: macular pseudoholes (Fig. 10.5a) and lamellar macular holes (Fig. 10.6). Originally, lamellar macular holes were described by Gass, in 1975, as an abortive process of full-thickness macular hole-formation resulting from the de-roofing of cystoid macular edema, and macular pseudoholes were described as attributable to centripetal contraction of epiretinal membranes [16]. New developments in retinal imaging enabled a new classification to be proposed (Table 10.1).

Therapeutical options and prognosis depend more on the etiopathogenesis than on the morphology of non-full-thickness macular holes. Thus, in idiopathic cases, surgery may be considered, while in secondary cases it is contraindicated, as the prognosis is poor. We have observed that macular pseudoholes may spontaneously develop to lamellar macular holes, suggesting that both morphological types might be different forms of the same disease [17]. The higher resolution of SD-OCT has also enabled additional morphological variants of non-full-thickness macular holes to be distinguished: macular pseudoholes, paralamellar macular holes, pseudoholes with a lamellar defect and lamellar macular holes (Fig. 10.5). Vitrectomy is thus indicated in all morphological types of symptomatic idiopathic eyes with non-full-thickness macular holes. In idiopathic non-full-thickness macular holes, visual acuity corresponds to photoreceptor defects and external limiting membrane defects. Little data exist on the role of the choroid in non-full-thickness macular holes. Primary data suggest that the choroid is thinner in secondary epiretinal membranes when compared to idiopathic cases. In most healthy eyes, the outer choroidoscleral boundary is regular and follows the natural shape of the globe, whereas in many diseases of the fovea, this regularity is impaired. The frequency of irregular choroidoscleral boundary in non-full-thickness macular holes differs from 25 to 90% between studies. Such irregularities of the outer choroidoscleral boundary are also frequent in eyes with idiopathic epiretinal membrane without a non-full-thickness defect (Fig. 10.6) [14]. The irregularities might be due to the increased diameter of several choroidal vessels while others remain unchanged or thinned [12].

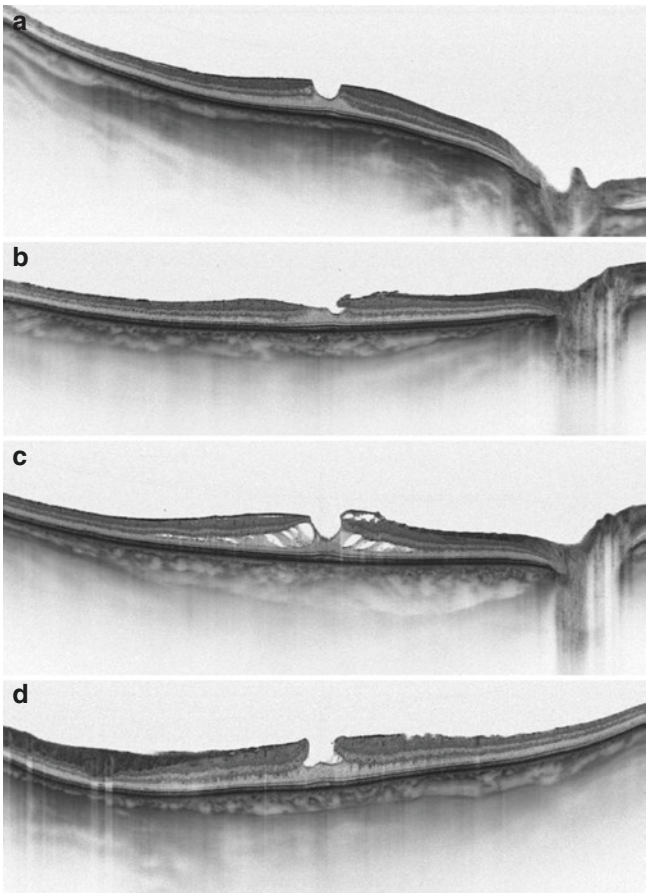

Fig. 10.5 Morphologic classification of non-full-thickness macular holes. (**a**) Macular pseudohole. (**b**) Paralamellar macular hole. (**c**) Pseudohole with lamellar defect. (**d**) Lamellar macular hole

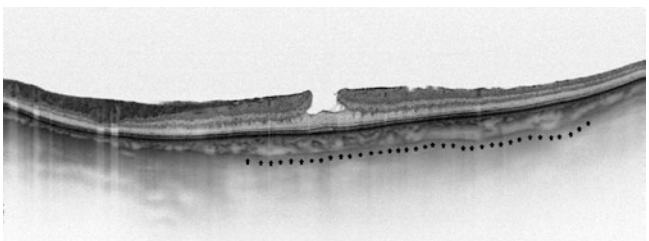

Fig. 10.6 Irregular choroidoscleral boundary in lamellar macular hole with tractional epiretinal membrane (*arrows*)

10.2.2 Epiretinal Membranes and Non-Full-Thickness Macular Holes Secondary to Retinal Diseases

Epiretinal membranes might be classified as either idiopathic or secondary to other retinal diseases, including vascular diseases, neovascular age-related macular degeneration (AMD), diabetic retinopathy, and retinal detachment (Fig. 10.7).

In general, secondary cases of epiretinal membranes or non-full-thickness macular holes have a worse prognosis after vitrectomy when compared to idiopathic cases. Surgery might be performed in epiretinal membranes coexisting with vascular diseases, especially in tractional diabetic macular edema, or after retinal detachment surgery. However, visual acuity is often altered despite successful surgery because of the underlying disease.

Finally, epiretinal membranes may also coexist with other vitreoretinal interface diseases, such as macular holes or vitreomacular traction syndrome. They may also coexist with dry AMD.

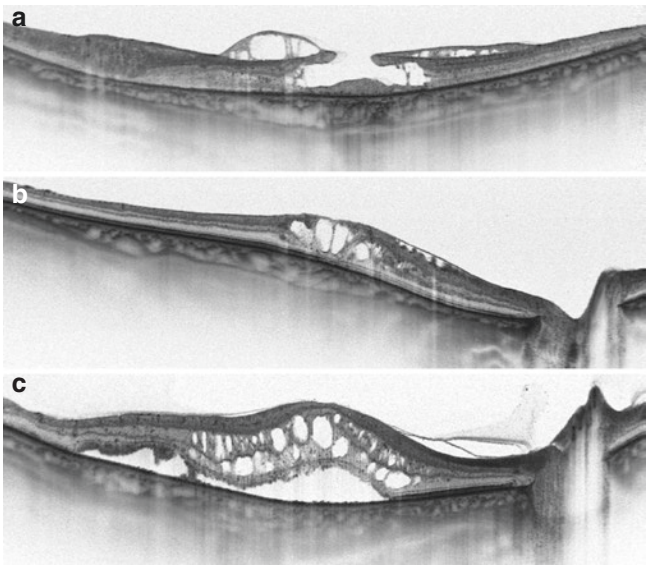

Fig. 10.7 Epiretinal membranes secondary to different diseases. (**a**) Lamellar macular hole and atypical (dense) epiretinal membrane secondary to severe age-related macular degeneration. (**b**) Tractional epiretinal membrane secondary to central retinal vein occlusion. (**c**) Partial posterior hyaloid detachment and epiretinal membrane secondary to diabetic macular edema

10.3 Swept Source OCT Angiography

Swept Source OCT Angiography (SS-OCTA) without dye is a novel, noninvasive technique that can present flow in retinal vessels. In eyes with epiretinal membranes, superficial vessels are much more tortuous when compared to a normal retina. Although diagnostic tools such as fluorescein angiography had shown irregularities of the superficial retinal vessels in the presence of epiretinal membranes, it was not possible to image the deep vessels before the advent of OCTA.

We also observed in SS-OCTA that vessels of the deeper retinal plexus (Fig. 10.8) are not as regular as in a healthy eye (Fig. 10.9). As this technique presents flow and not the morphology of retinal vessels, it might be extrapolated that blood flow in the deeper retinal plexus is disturbed in epiretinal membranes. This may correspond to SS-OCT findings that disturbances in the plexiform layers (Fig. 10.8, *arrows*) progress over time and are associated with a progressive decrease in visual acuity [7]. SS-OCT of epiretinal membranes secondary to vascular diseases, such as diabetic retinopathy with diabetic macular edema, present even more disturbances in blood flow (Fig. 10.10). Areas of reduced flow (hyporeflective areas) must be interpreted with caution. It must be considered that some of them are artifacts occurring due to erroneousness in the automatic layer segmentation.

Even if perfusion in the inner retinal plexus is good, some perfusion disturbances may occur in the deep retinal plexus (Fig. 10.11a). This perfusion deficit might even increase in the course of diabetes, even after successful removal of epiretinal membrane (Fig. 10.11b).

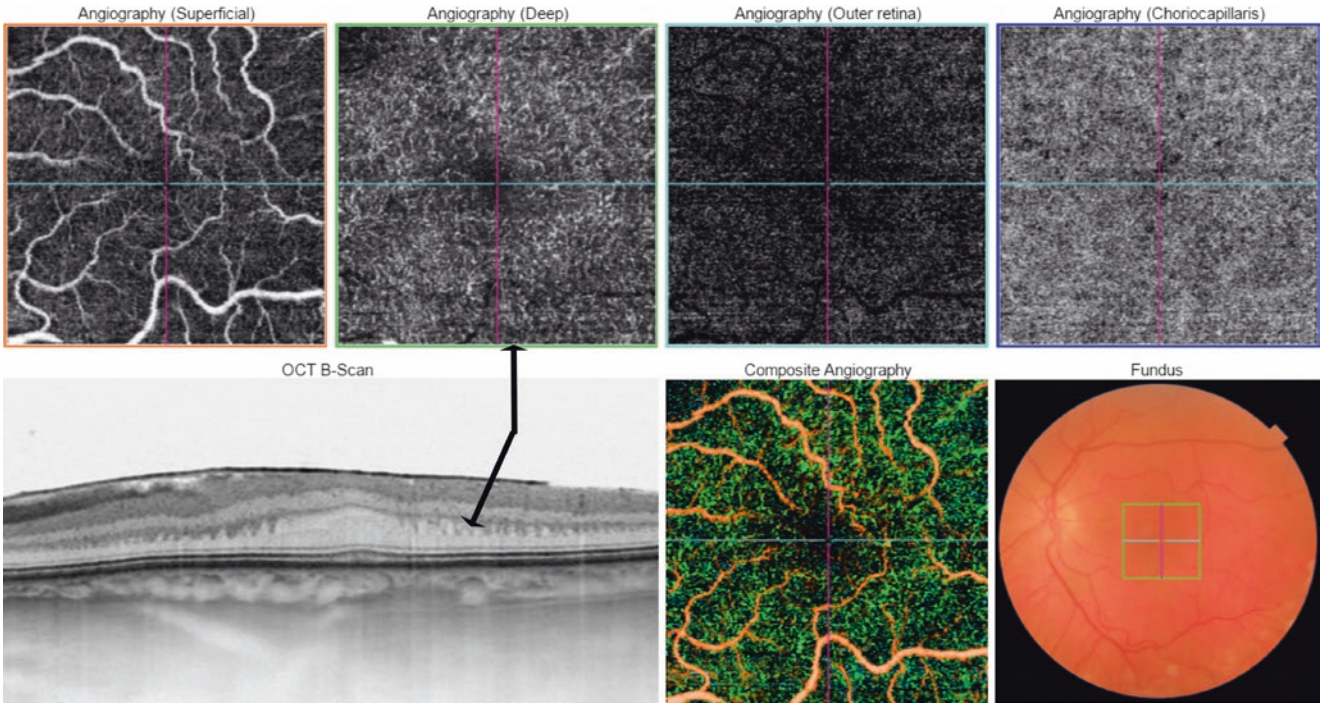

Fig. 10.8 SS-OCTA of an eye with epiretinal membrane. The orange box (angiography [superficial]) shows the superficial retinal vessels. The green box (angiography [deep]) shows the deep retinal plexus. Irregularities of deeper retinal vessels are visible. The light *blue box* (angiography [outer retina]) shows the avascular zone. The *dark blue* box (angiography [choriocapillaris]) shows the choriocapillaries

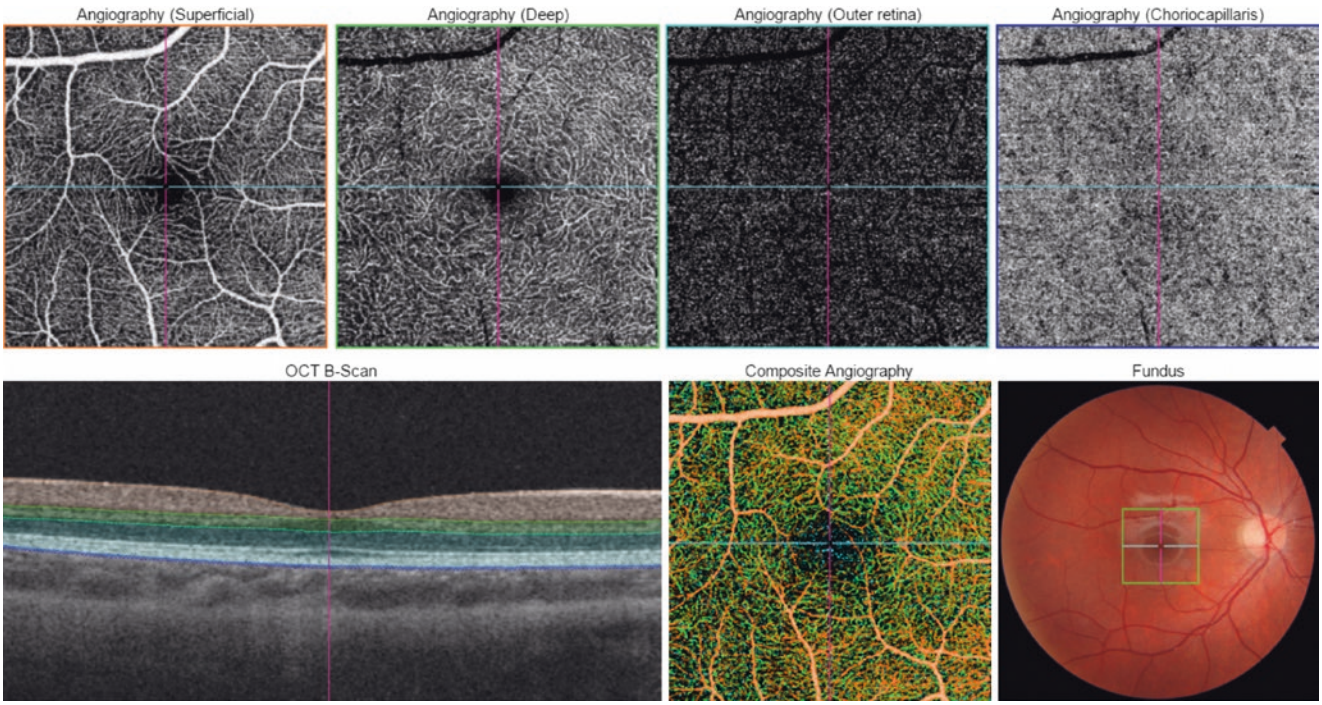

Fig. 10.9 SS-OCTA of a healthy eye. Orange box: superficial retinal vessels. Green box: deep retinal plexus. *Blue box*: avascular zone. *Dark blue box*: Choriocapillaries

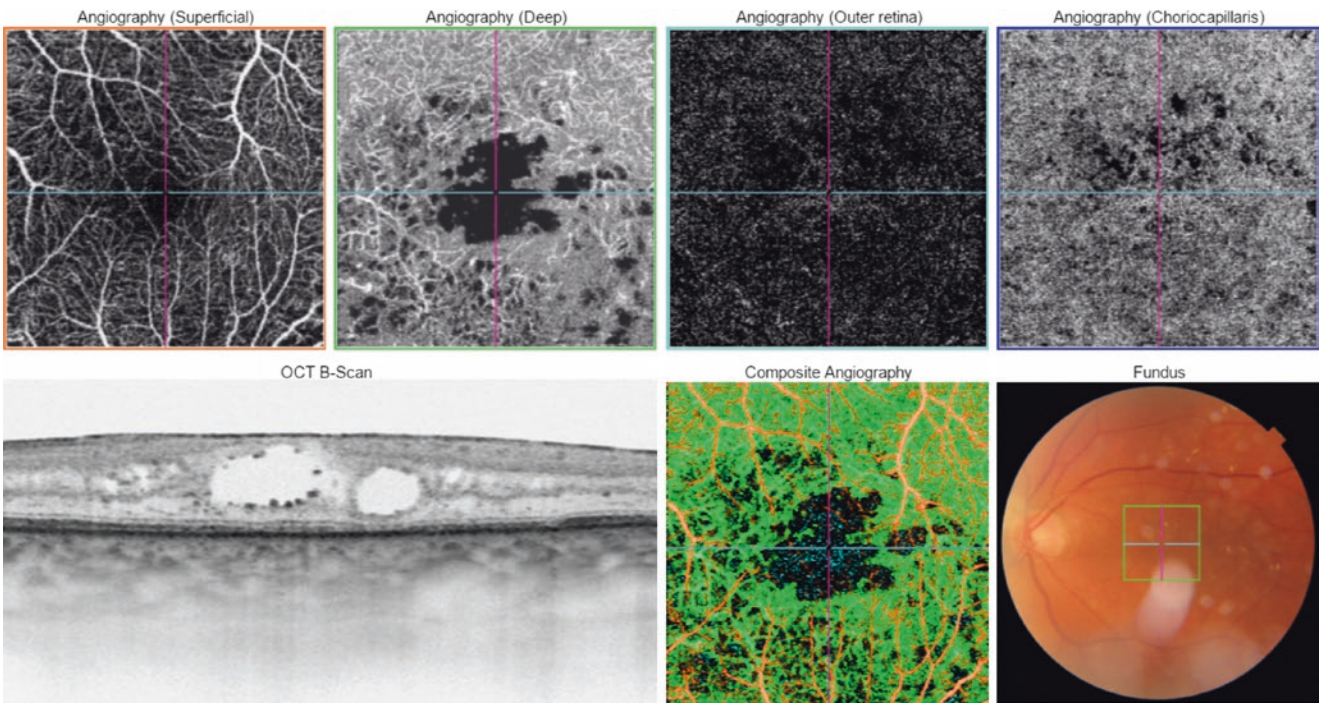

Fig. 10.10 SS-OCTA of epiretinal membrane secondary to diabetic macular edema. Cystoid spaces on SS-OCT correspond to spots of diminished visibility of deeper retinal vessels (*green box*)

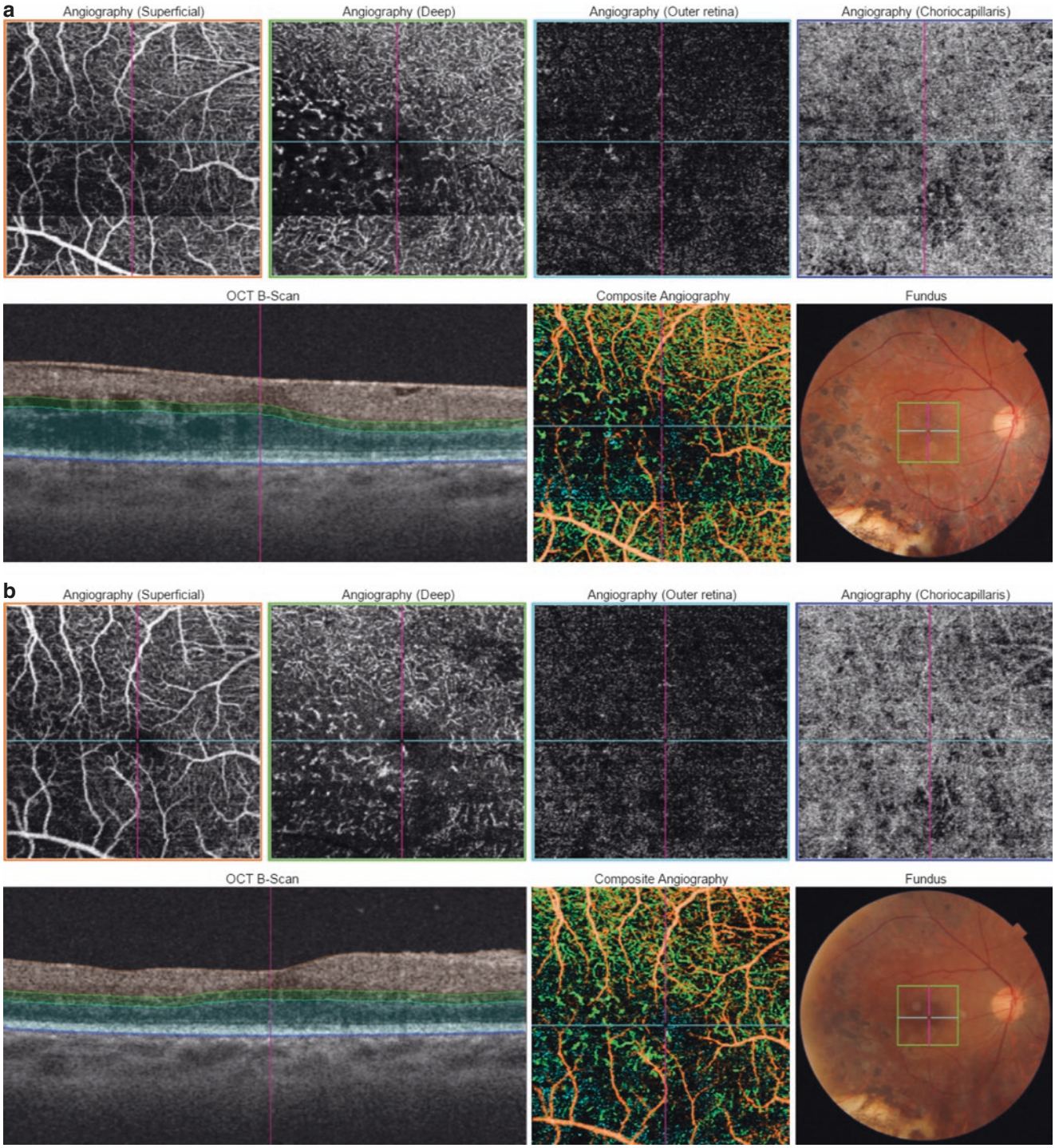

Fig. 10.11 (**a**) Pre-surgical SS-OCTA in a patient with diabetic macular edema and epiretinal membrane. Reduced perfusion is visible in the deeper retinal plexus. Visual acuity 0.01 Snellen. (**b**) Post-surgical SS-OCTA of the same patient with diabetic macular edema and epiretinal membrane. The area of reduced perfusion has increased in the deeper retinal plexus. Visual acuity is 0.15 Snellen

References

1. Klein R, Klein BE, Wang Q, Moss SE. The epidemiology of epiretinal membranes. Trans Am Ophthalmol Soc. 1994;92:403–30.
2. Meuer SM, Myers CE, Klein BE, Swift MK, Huang Y, Gangaputra S, et al. The epidemiology of vitreoretinal interface abnormalities as detected by SD-OCT: the Beaver Dam Eye Study. Ophthalmology. 2015;122:787–95.
3. Theodossiadis PG, Grigoropoulos VG, Emfietzoglou I, Nikolaidis P, Vergados I, Apostolopoulos M, et al. Evolution of lamellar macular hole studied by optical coherence tomography. Graefes Arch Clin Exp Ophthalmol. 2009;247:13–20.
4. Parolini B, Schumann RG, Cereda MG, Haritoglou C, Pertile G. Lamellar macular hole: a clinicopathologic correlation of surgically excised epiretinal membranes. Invest Ophthalmol Vis Sci. 2011;52:9074–83.
5. Schumann RG, Compera D, Schaumberger MM, Wolf A, Fazekas C, Mayer WJ, et al. Epiretinal membrane characteristics correlate with photoreceptor layer defects in lamellar macular holes and macular pseudoholes. Retina. 2015;35:727–35.
6. Pang CE, Spaide RF, Freund BK. Epiretinal proliferation seen in association with lamellar macular holes: a distinct clinical entity. Retina. 2014;34:1513–23.
7. Witkin AJ, Ko TH, Fujimoto JG. Redefining lamellar holes and the vitreomacular interface: an ultrahigh-resolution optical coherence tomography study. Ophthalmology. 2006;113:388–97.
8. Bottoni F, Deiro AP, Giani A, Orini C, Cigada M, Staurenghi G. The natural history of lamellar macular holes: a spectral domain optical coherence tomography study. Graefes Arch Clin Exp Ophthalmol. 2013;251:467–75.
9. Michalewska Z, Michalewski J, Ornafel-Sagan K, Nawrocki J. Swept-Source optical coherence tomography correlations between retina and choroid before and after vitrectomy for epiretinal membranes. Am J Ophthalmol. 2016;165:100–7.
10. Falkner-Radler CI, Glittenberg C, Binder S. Spectral domain high-definition optical coherence tomography in patients undergoing epiretinal membrane surgery. Ophthalmic Surg Lasers Imaging. 2009;40:270–6.
11. Michalewski J, Michalewska Z, Nawrocka Z, Bednarski M, Nawrocki J. Correlation of choroidal thickness and volume measurements with axial length and age using swept source optical coherence tomography and optical low-coherence reflectometry. Biomed Res Int. 2014;2014:639160.
12. Michalewska Z, Michalewski J, Adelman RA, Zawiślak E, Nawrocki J. Choroidal thickness measured with swept source optical coherence tomography before and after vitrectomy with internal limiting membrane peeling for idiopathic epiretinal membranes. Retina. 2015;35:487–91.
13. Michalewska Z, Michalewski J, Nawrocka Z, Dulczewska-Cichecka K, Nawrocki J. The outer choroidoscleral boundary in full-thickness macular holes before and after surgery - a swept-source OCT study. Graefes Arch Clin Exp Ophthalmol. 2015;253:2087–93.
14. Michalewska Z, Michalewski J, Nawrocka Z, Dulczewska-Cichecka K, Nawrocki J. Suprachoroidal layer and suprachoroidal space delineating the outer margin of the choroid in swept-source optical coherence tomography. Retina. 2015;35:244–9.
15. Michalewska Z, Michalewski J, Odrobina D, Nawrocki J. Non-full-thickness macular holes reassessed with spectral domain optical coherence tomography. Retina. 2012;32:922–9.
16. Gass JDM. Stereoscopic atlas of macular diseases. St. Louis: C. V. Mosby Co.; 1970.
17. Michalewski J, Michalewska Z, Dzięgielewski K, Nawrocki J. Evolution from a macular pseudohole to lamellar macular hole - spectral domain OCT study. Graefes Arch Clin Exp Ophthalmol. 2011;249:175–8.

Swept Source OCT for Macular Hole Treated with the Inverted Internal Limiting Membrane Flap Technique

11

Jerzy Nawrocki and Zofia Michalewska

The inverted internal limiting membrane flap technique (hereafter flap technique) was first performed by the author of this chapter in 2006 (JN). After performing several procedures and confirmation of good results, a comparative study was performed and presented at meetings of the European VitreoRetinal Society, the American Society of Retina Specialists, and the American Academy of Ophthalmology in 2009 and published by the authors of this chapter in 2010 [1]. The initial technique was based on using trimmed internal limiting membrane (ILM) flaps connected to the margins of a macular hole to cover the macular hole. During the following years we stopped trimming the flaps and decided to peel the ILM only from the temporal side [2]. The technique is growing in popularity among retina surgeons worldwide, which is confirmed by the growing number of publications on that topic (2010: one; 2013: three, 2014: five, 2015: nine, and ten papers in the first half of 2016).

All of the images in this chapter were obtained using the commercially available Swept Source OCT devices from Topcon, Japan: DRI OCT-1 Atlantis and DRI OCT Triton.

J. Nawrocki, MD, PhD (✉) • Z. Michalewska, MD, PhD
Jasne Blonia Ophthalmic Clinic, Lodz, Poland
e-mail: jerzy_n@poczta.onet.pl

© Springer International Publishing AG 2017

Z. Michalewska, J. Nawrocki (eds.), *Atlas of Swept Source Optical Coherence Tomography*,
DOI 10.1007/978-3-319-49840-9_11

11.1 Macular Hole Formation

Owing to its higher scanning speed, swept source OCT (SS-OCT) allows more details of retina tissue to be presented, which may play a role in treatment decisions. The aim of this chapter is to present details of SS-OCT images before and after treatment. An initial sign of macular hole formation in retina tissue, detected by SS-OCT, is an elevation of the photoreceptor layer from the pigment epithelium and the presence of traction (Fig. 11.1 a–c). This was described by our group in 2009 [3] and was confirmed by Takahashi in 2010 [4]. This may lead to the formation of an intraretinal cyst or intraretinal cystic spaces or the appearance of outer lamellar macular hole (Fig. 11.1 d–f).

The formation of a macular hole may be adequately visualized in three-dimensional mode. SS-OCT, due to its better resolution, enables us to present how the forces of traction are expressed by tissue connections; probably glial or neuronal cells. However, even if we have high-resolution pictures from SS-OCT, we cannot adequately explain the image in Fig. 11.1 b and the three-dimensional image in Fig. 11.1c, where a channel in the center of the fovea is formed with still-intact ILM. Perhaps some aspects of the hydration theory presented by Tornambe in 2003 may be considered to explain these images [5].

We also have very little information about the role of the choroid. Our group found that choroidal thickness did not change in any quadrant in eyes with full-thickness macular hole (FTMH) as compared with fellow eyes and healthy control (Fig. 11.2). However, in eyes with full-thickness macular holes, the lamina suprachoroidea was more often irregular and suprachoroidal space was more frequently visible when compared to healthy controls as previously described by Michalewska et al. [6]. Postoperatively the lamina suprachoroidea has a tendency to become more regular.

The fact that changes in the outer choroidoscleral boundary are more frequently observed in fellow eyes of FTMH than in healthy controls may indicate that the choroid has a role in FTMH etiopathogenesis. The normalization of the outer choroidoscleral boundary after vitrectomy may additionally indicate a role of the choroid in the healing process of FTMH [6].

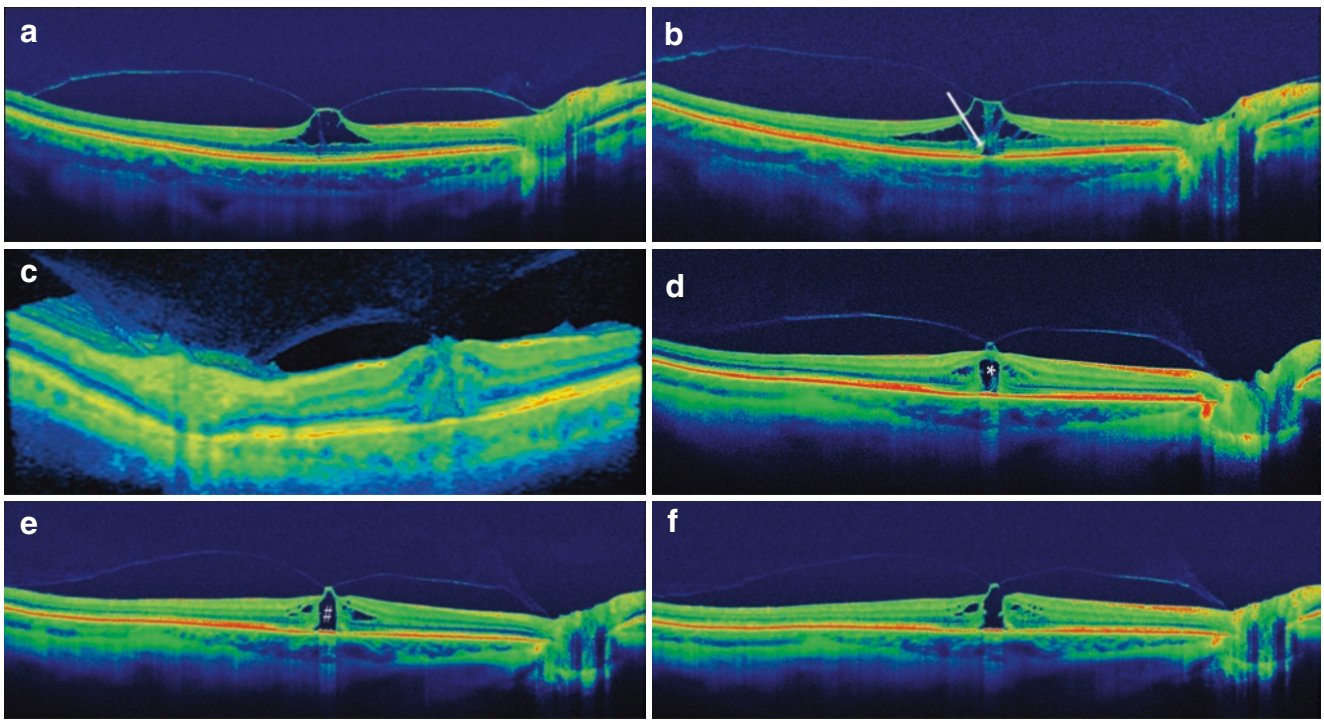

Fig. 11.1 SS-OCT images showing the sequence of macular hole formation, (**a**) beginning with vitreomacular traction. (**b**) Evolution from vitreomacular traction to idiopathic macular hole by formation of intraretinal channel. Image obtained two months after image (**a**) and shows elevation of photoreceptors (*white arrow*). Patient was operated on two weeks later for full-thickness macular hole. (**c**) Three-dimensional image of macular hole formation. (**d**) Cystic spaces (*white star*) seen prior to the formation of an outer lamellar macular hole. (**e**) Appearance of outer lamellar macular hole (*white hash*), just preceding full-thickness macular hole formation. (**f**) Full-thickness macular hole in the same eye

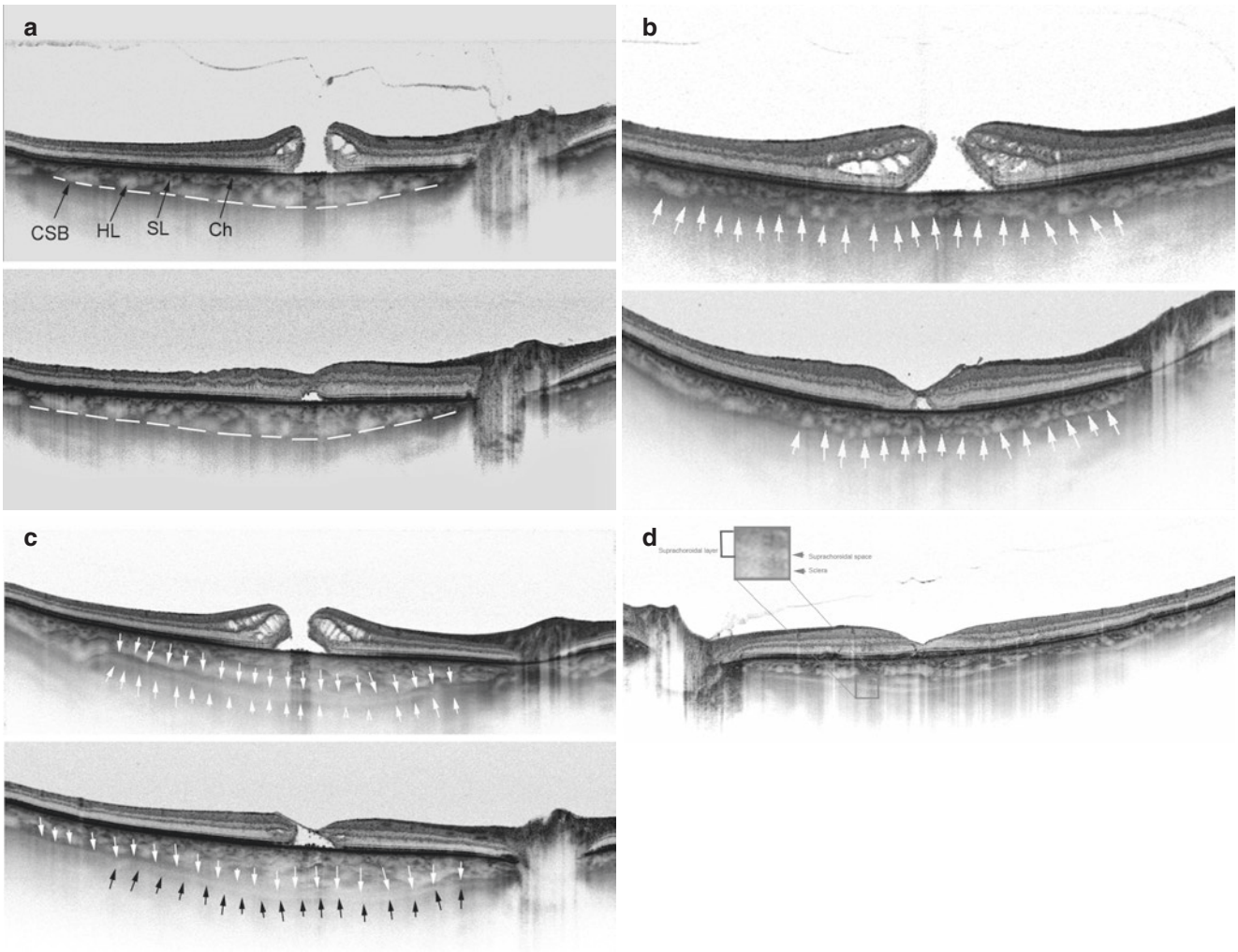

Fig. 11.2 **(a)** Swept source OCT of a macular hole before surgery (*upper image*) and after surgery (*lower image*). The *white lines* represent the regularity of the choroidoscleral boundary (CSB). *Ch* choriocapillaries; *HL* Haller layer; *SL* Sattler layer. **(b)** Swept source OCT of a macular hole before surgery (*upper image*) and after surgery (*lower image*). The *white arrows* indicate an irregular outer choroidoscleral boundary. the irregularities remained after surgery. **(c)** The *arrows* indicate the suprachoroidal space in an eye with full-thickness macular hole before (*upper image*) and after (*lower image*) surgery. **(d)** Fellow eye of an eye with a full-thickness macular hole. Posterior hyaloid is partially detached but adheres to the optic nerve. Irregular fovea contour and Drusen are visible. The enlarged area presents suprachoroidal layer and suprachoroidal space

11.1.1 Spontaneous Closure of Macular Holes

In very rare cases, the macular hole may close spontaneously without any surgery (Fig. 11.3). In these eyes, closure of macular hole begins at the inner layers of the retina. Our observations of these cases allow us to suggest that if the edges of macular hole are not completely smooth, spontaneous healing may occur [7].

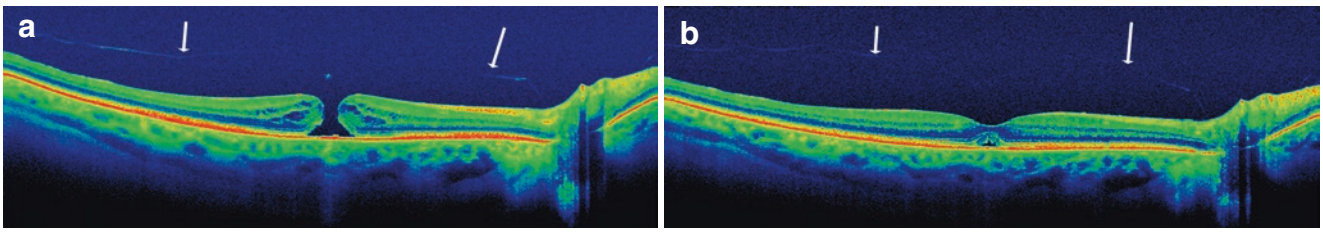

Fig. 11.3 (**a**) An SS-OCT scan from June 2015 and (**b**) SS-OCT scan from December 2015. No surgery was performed. Posterior hyaloid detachment is visible on both sides (*arrows*)

11.1.2 Surgical Closure of Macular Holes

After surgery, the macular hole closes during the first day in about 55% of cases and in 65–75% within 48 hours [8, 9]. This has been presented with a specially prepared OCT device, which allows OCT scans to be performed whilst the patient remains in a prone position [8]. Kikushima demonstrated that SS-OCT allows retina scans as early as 20 min after surgery in a gas-filled eye [9]. Because we perform the inverted ILM flap technique with an air tamponade in idiopathic macular hole cases, we can obtain good quality scans with the SS-OCT device after a few days. This is possible because air disappears quickly in the first days after surgery. We can observe U-type and V-type or irregular closure at the one-week follow-up visit. The best functional results are achieved with U-type closure [10]. Macular hole closure always begins in the inner retina layers (Fig. 11.4).

Interestingly, we may see at the one-week visit that macular hole is closed with ILM only (Fig. 11.4d). This may happen in 15–30% of cases (Nawrocki, unpublished data). We would like to suggest that those holes would not close or would stay flat open if a traditional approach was performed. Flat open macular hole appearance is defined as edges of the hole being flat on the pigment epithelium while bare pigment epithelium is visible in the center of the fovea (Fig. 11.4e). In the past this was considered as macular hole closure, but in our opinion such cases should rather be considered as surgical failures because visual acuity shows no improvement in follow-up.

In 2008, using spectral domain OCT, our group described different retina structure pathologies after macular hole surgery [10]. The following retinal abnormalities were observed: photoreceptor defect defined as linear lack of photoreceptors in the subfoveal area with normal retinal reflectivity; cysts in outer retinal layers; nerve fiber layer defect; elevation of all retinal layers in fovea; and retinal pigment epithelial defects. The study was performed after vitrectomy with ILM peeling and gas for idiopathic FTMH. Even at that time, we suggested some regeneration process occurred in the foveal architecture.

Due to the high resolution of SS-OCT, we can sometimes visualize the ILM flap covering the macular hole at the first post-operative follow-up (Fig. 11.5). After employing the inverted ILM flap technique, it is interesting that in many cases, such as U-type closure (Fig. 11.4a), we do not see any sign of the inverted ILM flap itself on the surface of the retina, whereas in V-type closure or irregular closure cases, we see some presence of ILM (Fig. 11.4b, c).

In some cases, during the first control after surgery the macular hole is closed with ILM flap only. We refer to these cases as "flap closure." During the next weeks or months of follow-up, we may observe almost complete regeneration of retinal tissue under the flap of ILM, and we suggest that this also confirms that ILM, as a base membrane, serves as a scaffold for retinal tissue to proliferate or migrate in the foveal area (Fig. 11.6).

During follow-up the ILM flap may become less visible but in some cases, after complete closure of macular hole, the ILM flap may change its position or even float above the surface of the retina. Interestingly, in macular holes initially closed with ILM only, we observe reappearance of retinal layers during the follow-up period and even the reformation of photoreceptor layers, even if the flap itself has become somewhat detached from the retinal surface (Fig. 11.7).

After surgery, or in rare cases with spontaneous resolution, macular hole closure always begins in the inner layers of the retina. During follow-up we observe healing of the inner and outer layers of the retina and photoreceptor layers. The process of regeneration lasts many months. We should usually reserve our judgment until 1 year after surgery, and in many cases complete reformation of the retina layers is not observed until even later. It is interesting to observe regeneration of retina tissue during follow-up. It was once thought that nervous tissue does not regenerate. We now know better, and looking at multiple examples after macular hole surgery we clearly see that as retina layers reappear the retina architecture normalizes and this correlates with improvement in visual acuity. These changes are clearly visualized with SS-OCT (Fig. 11.8).

With the new device we were also able to present that, contrary to the regeneration of foveal architecture, we see new defects in the nerve fiber layers as shown in Fig. 11.8c, d. These defects are known as dissociated nerve fiber layer (DONFL) [11]. DONFL is defined as indentation of inner retinal layer or formation of small dimples visible in the retinal nerve fiber layer, and can appear even 6–12 months after surgery. The most recent modification of the inverted ILM flap technique, called "the temporal inverted ILM flap technique," allows us to reduce the number and area of nerve fiber layer defects [2]. With this technique we observe DONFL only on the temporal side of the fovea where ILM had been peeled. We do not see them between the fovea and the optic nerve where ILM was not peeled.

When using the inverted ILM flap technique in reoperation cases, we do not observe pigment epithelium defects, which were seen in the past in cases of retinal massage or as a result of the mechanical decrease of the macular hole during repeated surgeries (Fig. 11.9).

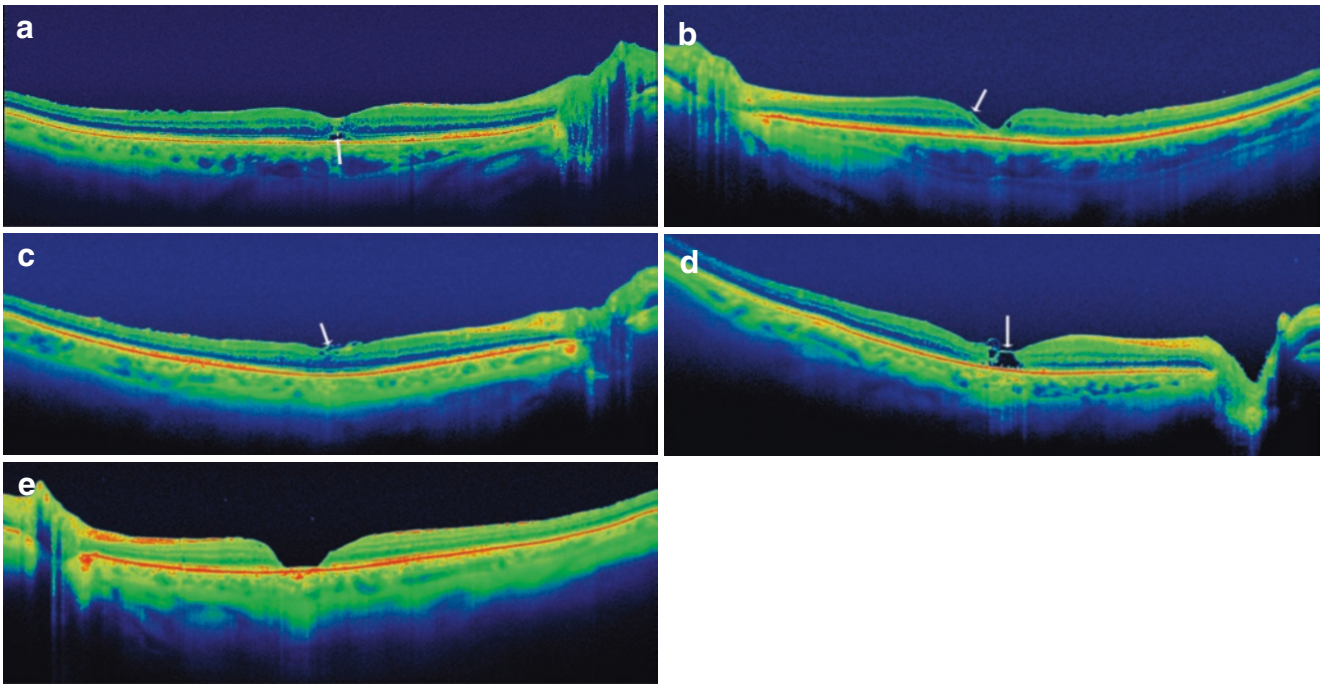

Fig. 11.4 (**a**), U-shape closure. Photoreceptor defect is visible in the fovea (*arrow*). (**b**) V-shape closure. ILM is visible on the surface of the retina (*arrow*). No photoreceptor layer is visible. (**c**) Irregular closure. ILM visible on the surface of fovea, photoreceptor layer almost intact. (**d**) ILM flap closure. Macular hole closed with the ILM only (*arrow*), no retina tissue visible in the center of fovea. (**e**) Flat open macular hole

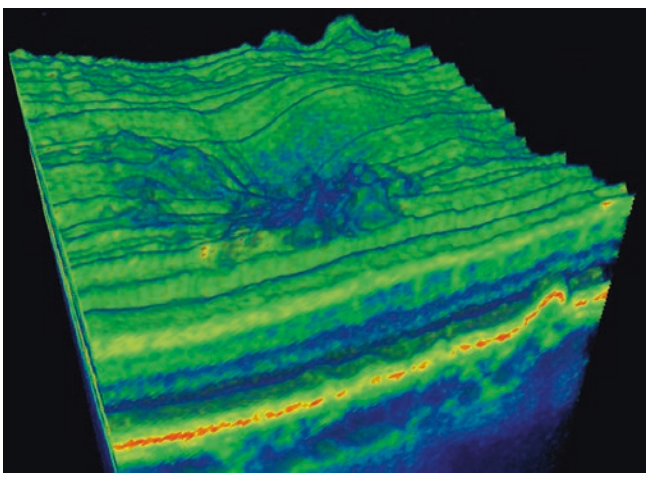

Fig. 11.5 3-D SS-OCT image showing an ILM flap on the surface of a macular hole

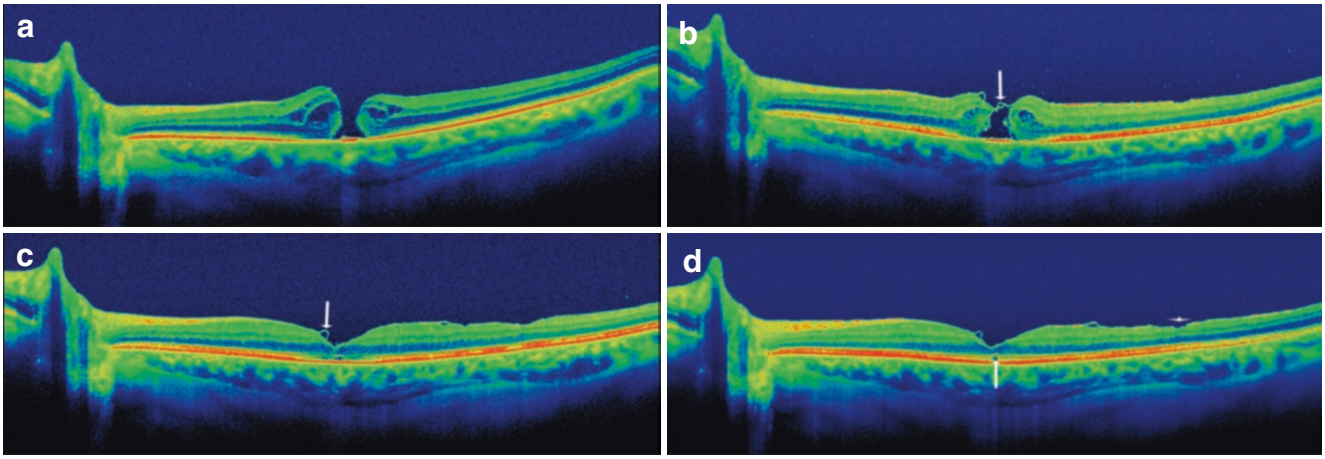

Fig. 11.6 (**a**) Macular hole preoperative view. (**b**) One-week postoperative view, macular hole closed with ILM flap only (*arrow*), visual acuity 20/100. (**c**) Six-week post-operative control, remnants of the ILM are visible (*arrow*), foveal layers of the retina are visible, defect in photoreceptor layer, visual acuity 20/50. (**d**) Twelve months after surgery defect in photoreceptor layer decreased in size (*arrow*). Visual acuity was 20/30. Please note the increase of nerve fiber layer defects during follow up at the temporal side of the fovea (*arrowhead*)

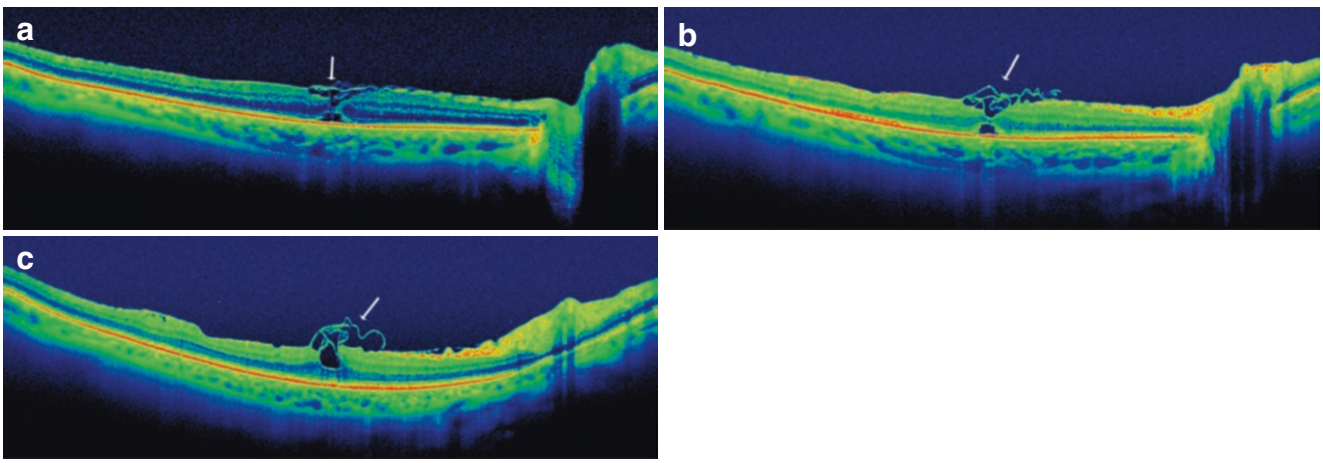

Fig. 11.7 (**a**), One week after surgery we see the macular hole closed with ILM flap (*arrow*). (**b**) One-month follow-up: we see reappearance of inner foveal layers and detachment of ILM flap from the surface of retina (*arrow*). (**c**) Two-year follow-up: almost complete recovery of foveal architecture with free-floating ILM (*arrow*)

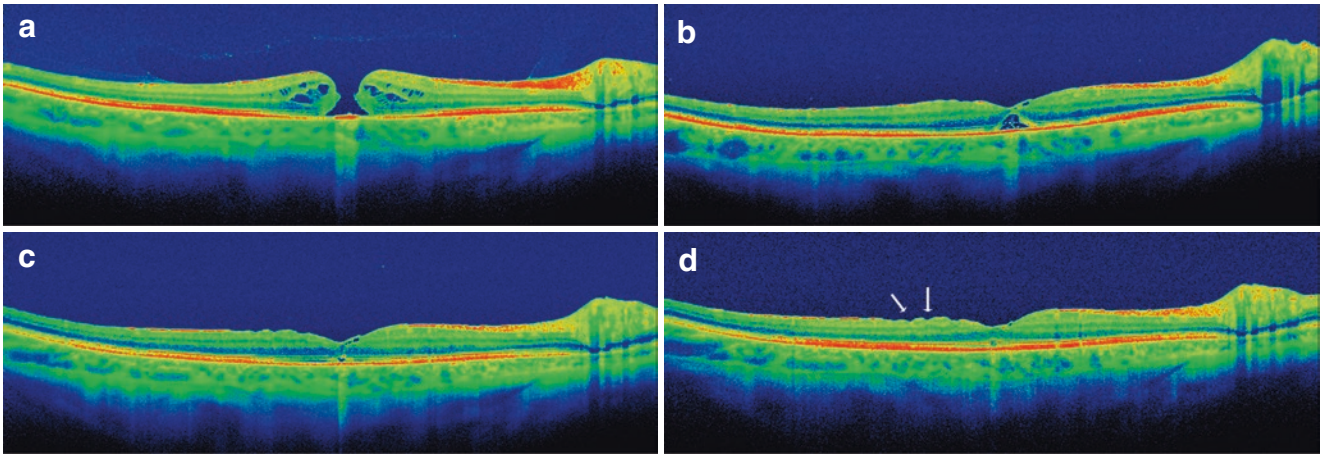

Fig. 11.8 (**a**) SS-OCT Preoperative appearance of a macular hole. (**b**) One-week postoperative B-scan shows closure of macular hole with ILM flap, some tissue appears on the outer surface of ILM, cystic space in the outer fovea is present. No defects in the nerve fiber layer. Visual acuity 20/100. (**c**) Two-month follow-up shows recovery of inner retinal layers defect in the photoreceptor layer is visible, visual acuity 20/40. (**d**) Two-year follow-up, almost complete recovery of retina tissue can be seen. The ILM flap is barely visible. A minimal defect in photoreceptor layer in fovea still persists. Visual acuity 20/30. Please note increased defects of nerve fiber layer during follow-up at the temporal side of the fovea (*arrows*)

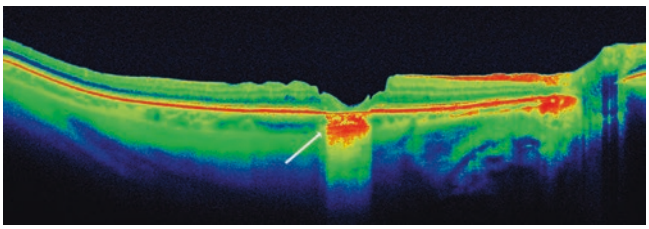

Fig. 11.9 A defect in the central retina and retinal pigment epithelium (*arrow*) caused by traumatic surgery can be beautifully presented with SS-OCT. Even if it has a tendency to decrease, it persists for years and limits visual acuity

11.2 Rare and Complicated Cases

In some cases, traumatic macular holes are associated with choroidal rupture and subsequent subretinal fibrosis. Such macular holes are difficult to close. We routinely use the inverted ILM flap technique in such cases as a primary approach. The vast majority of cases are healed and one advantage of the inverted ILM flap technique may be sparing the patient secondary surgery. In Fig. 11.10 we see SS-OCT images of a traumatic macular hole with subretinal fibrosis. Recently one such case was described by Morizane et al. His technique is a modification of the inverted ILM flap technique called "autologous transplantation of internal limiting membrane" [12]. It can be used in case of absence of ILM around the hole if the usual vitrectomy with ILM peeling had previously been performed.

Myopic macular hole retinal detachment is a surgical challenge. SS-OCT is one of the best tools for the examination of such cases because of the long scan (12 mm) and high depth of focus, which can present both elevated retina with macular hole as well as choroid with pigment epithelium in one B-scan.

The use of the inverted ILM flap technique not only allows us to close the macular hole but also reattach the posterior retina. Our own unpublished data show high success rates after the inverted ILM flap technique (Fig. 11.11). Recently Lai et al. have shown their modification of ILM repositioning and autologous blood clot, which allowed them to close macular holes and reattach the retina in 26 of 27 eyes (96%) after one surgery, and in 100% after additional surgery [13]. A high success rate of this method in closure of myopic macular holes without retinal detachment was demonstrated by Kuriyama et al. in 2013 and by our group, Michalewska et al., in 2014 [14, 15]. Additionally, Morizane et al. presented secondary macular holes after vitrectomy with ILM peeling for myopic foveoschisis [12]. According to their data, secondary macular holes are found in 19–27% of such cases. Those cases are difficult to treat because the ILM was already peeled. Morizane et al. achieved success in all four eyes treated with autologous transplantation of the ILM. Grewal and Mahmoud showed that autologous neurosensory retinal free flap may help to close refractory myopic macular holes [16].

No SS-OCT data is available in the literature on operations for full-thickness macular hole associated with drusen. Our unpublished data suggests that in these cases we can achieve similar anatomical results to those in a general group of patients. In Fig. 11.12 we present an example of one such case before and after surgery.

The flap technique may be also used in other relatively rare cases of full-thickness macular hole which can be diagnosed and presented with SS-OCT. In rare cases after retinal detachment surgery with scleral buckling and vitrectomy, a persistent full-thickness macular hole may be observed. In recent years we have collected three such cases (two of them were sent from other departments). The result of one such surgery is presented in Fig. 11.13.

We are also able to present a long-lasting full-thickness macular hole with localized retinal detachment in the course of severe proliferative diabetic retinopathy (Fig. 11.14). In this case the inverted ILM flap closed the macular hole, but at the last visit of the patient (after 10 months follow-up) a thin layer of subretinal fluid is still present.

Recovery of fovea architecture is also possible after a macular hole lasting several years. The case presented in Fig. 11.15 shows a macular hole diagnosed by myself in 2002 in a patient with mild myopia of −5 Diopters axial length 26.65 mm. The patient at that time did not wish to have surgery. She changed her mind in 2013. Vitrectomy with temporal inverted ILM flap was performed, phacoemulsification and intraocular (IOL) implantation after 1 year followed. Eighteen months after surgery foveal architecture was almost normal and visual acuity improved from 10/200 to 20/30.

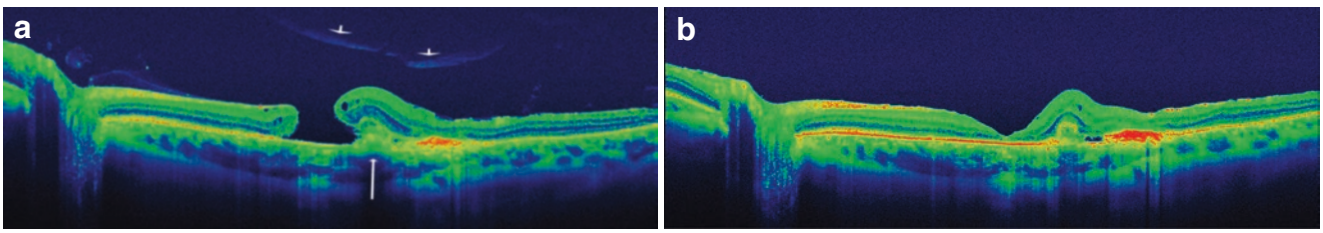

Fig. 11.10 (**a**) SS-OCT image of a traumatic macular hole with subretinal fibrosis (*arrow*), posterior hyaloid seems detached (*arrowheads*). (**b**) Four-month post-operative view, macular hole is closed. Subretinal fibrosis is still visible (*arrow*), recovery of photoreceptor layer is visible

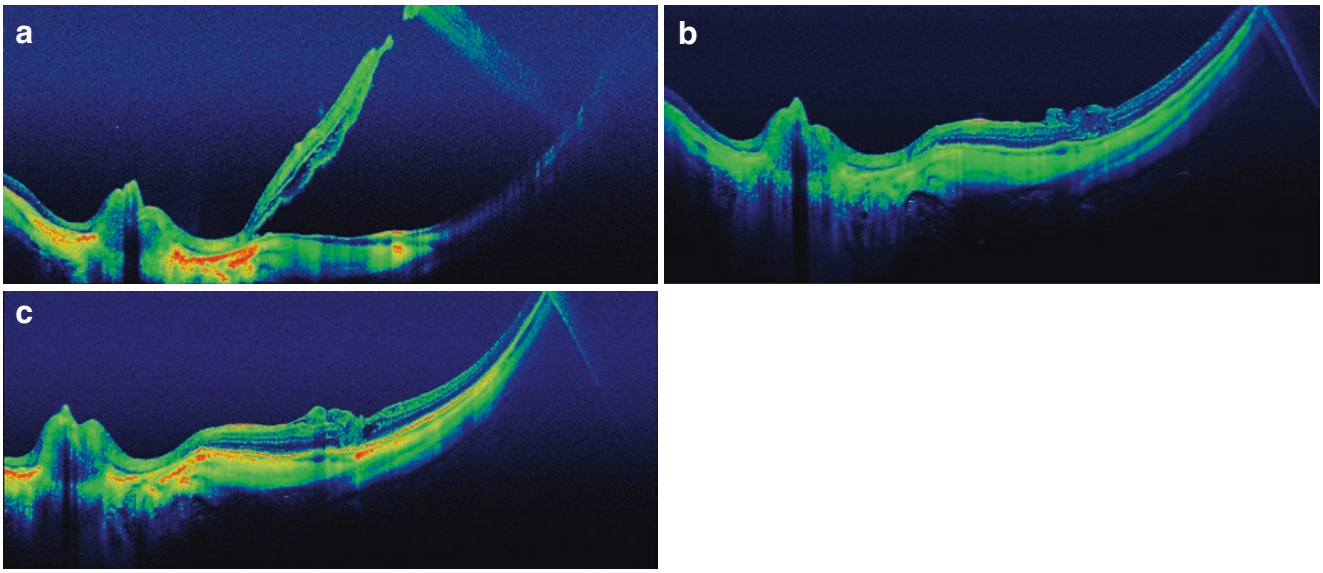

Fig. 11.11 (**a**), Myopic macular hole retinal detachment, elevated retina and full-thickness macular hole seen with SS-OCT. (**b**) One week post-operative. (**c**) Thirteen-month post-operative image. Visual acuity improved from 2/200 before surgery to 20/80 at the final control

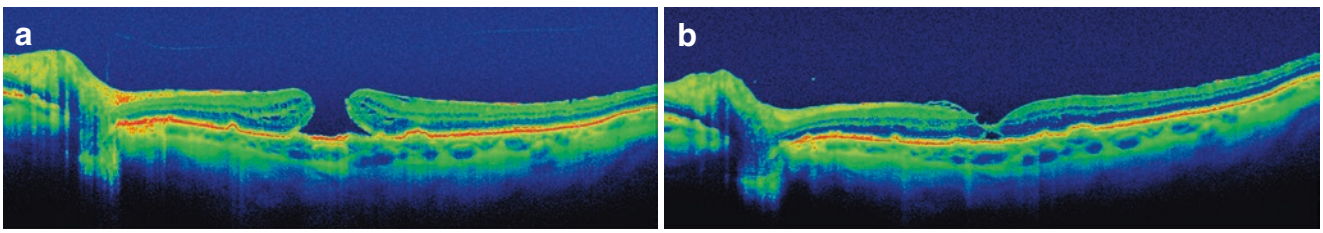

Fig. 11.12 (**a**) Macular hole with coexisting drusen before surgery. (**b**) At the one-week control

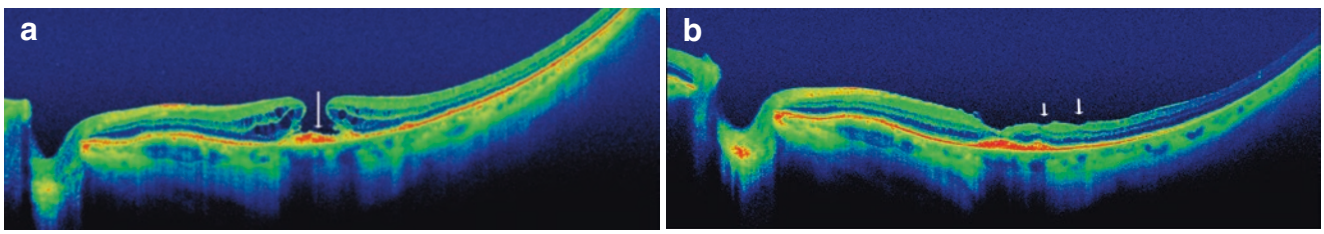

Fig. 11.13 (**a**) Persistent macular hole after scleral buckling and vitrectomy for retinal detachment. Retina is reattached, visual acuity 2/200. Note the thickening of retinal pigment epithelium (*arrow*). (**b**) Follow-up visit one year after repeated vitrectomy with temporal inverted ILM flap, cataract removal, and IOL implantation. Thickening of retinal pigment epithelium persists, macular hole is closed, foveal architecture improved, DONFL visible temporal to fovea (*arrow*); visual acuity 20/50

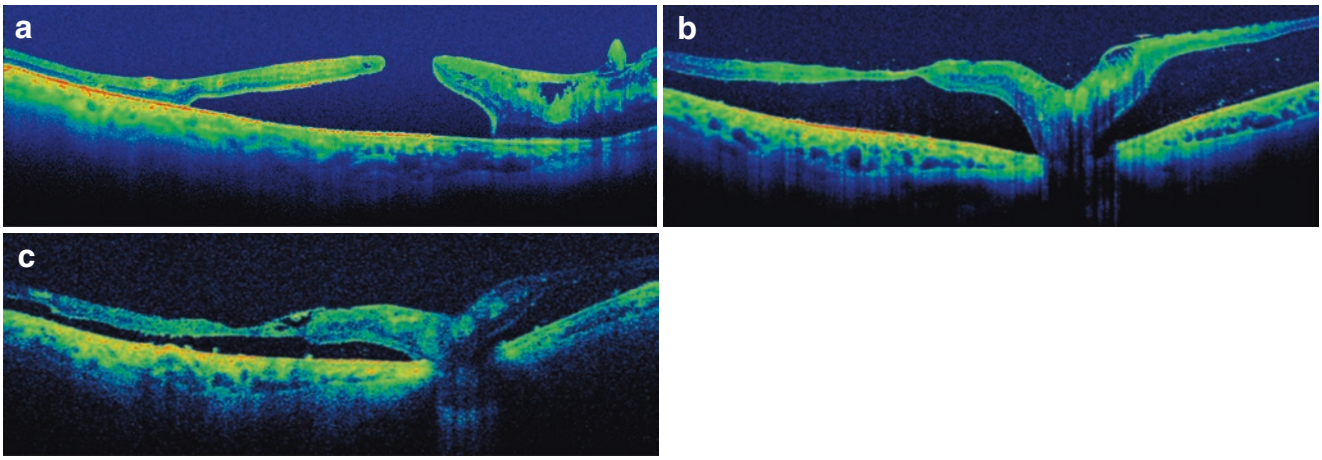

Fig. 11.14 (**a**) SS-OCT image of a full-thickness macular hole in course of proliferative diabetic retinopathy. (**b**) One-month follow-up, macular hole is closed, subretinal fluid is still present. (**c**) Ten-month follow-up, a thin layer of subretinal fluid is still present

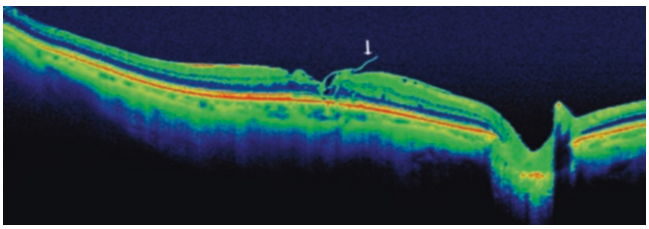

Fig. 11.15 SS-OCT 18 months after surgery. Control visit of a patient with myopia operated 11 years after onset of the macular hole. You can still see some visible flap remnants (*arrow*) and almost complete recovery of the photoreceptor lines in the center of the fovea. VA 20/30

11.3 SS-OCT Angiography

Despite the relatively simple pathology of macular holes, the device can experience difficulties in presenting the tissue. If we look at the SS-OCT angiography (OCTA) image of small stage 2 macular hole as presented in Fig. 11.16, even if the structural SS-OCT shows a full-thickness fovea defect, we do not see any pathology in the Angiography SS-OCT image.

If we look at the superficial vascular plexus image the vasculature is usually normal and the size of the avascular zone corresponds to the size of macular hole. However, in a Stage 3 macular hole (Fig. 11.17), when some tissue is present in the area of the full-thickness macular hole, the center of the fovea presents as a hyporeflective area both in the anterior vascular plexus image and deep vascular plexus image. The deep vascular plexus image shows an increased avascular zone with a strange defect outside of the partially preserved vasculature. Close to the center of the fovea we can just make out some vascular tissue, but with a very low signal. Looking at the segmentation lines on the B-scan, we can see that they move out of the firm tissue or go through cystic spaces. In the center of the fovea in the outer retina image, we notice the bright appearance of the choriocapillaris. The choriocapillaris in the center of fovea presents higher reflectivity when compared to the rest of the layer.

Next we present a case of a small Stage 4 macular hole (Fig. 11.18). The superficial vascular plexus is once again normal, but we see an enlarged fovea avascular zone in the deep vascular plexus. Looking more carefully at the deep angiography image there appears to be some vasculature close to the center of the fovea, but this is very pale and is probably a result of false detection of the vessels, as the scan has been affected by the cystic spaces around the macular hole.

In the outer retina, where usually we have no vessels, inaccurate segmentation can show vasculature to be present in the center of the fovea. If we look at the segmentation line in these instances, we are likely to see that it goes behind the outer retina to the choriocapillaris, and this observation indicates that the angiography image also shows an artifact. The laser is reflected from the surfaces of particular retinal and choroidal layers. Part of the laser beam is scattered in the tissue. In full-thickness macular holes, the lack of retinal tissue in the foveola means the laser beam has direct access to the retinal pigment epithelium and choriocapillaries. Therefore, we observe a circle of high hyperreflectance in the center of the fovea at the level of choriocapillaries.

Furthermore, if we have a stage 4 macular hole, especially larger-sized holes (Fig. 11.19), we see a normal superficial vascular plexus, but in the deep vascular plexus image we may see a hyperreflective area of vessels in the center of the fovea, where, we know, no vessels are present. This is caused by inaccurate segmentation, when the segmentation lines created automatically by the device might travel down under the retinal pigment epithelium and image choroidal vessels as if they were present in the center of the fovea. Such artifacts can be dealt with by manual correction of the shape of the segmentation line (scan line).

The choriocapillaris layer is more clearly visible in the center of fovea, when compared to other areas, in cases of full-thickness macular hole. This is probably due to the absence of retina tissue and vasculature in the center of fovea which do not produce any projection artifacts on the deeper layers.

These types of imaging complications are even better illustrated in this case of a full-thickness macular hole with surrounding cystic spaces (Fig. 11.20a). In such cases, the delicate appearance of deep vascular plexus may be presented around the cystic spaces. Initially the image may suggest that some abnormalities of the vasculature are actually present. However, we doubt that this is the case because we observe an immediate improvement after surgery following the disappearance of the cystic spaces (Fig. 11.20b). Thus we believe these are artifacts of segmentation.

Sometimes, in long-term follow-up, ILM flap may be floating in front of the retina, even if the macular hole is closed, and this can produce some projection artifacts. The B-scan in Fig. 11.21 shows that the ILM flap is free-floating, and this has possibly caused the dark shadows on the angiography images.

In very rare cases, the origin of the macular hole may be poor nutrition resulting from the presence of choroidal neovascularization in the course of age-related macular degeneration, and such cases can be beautifully detected with SS-OCT (Fig. 11.22).

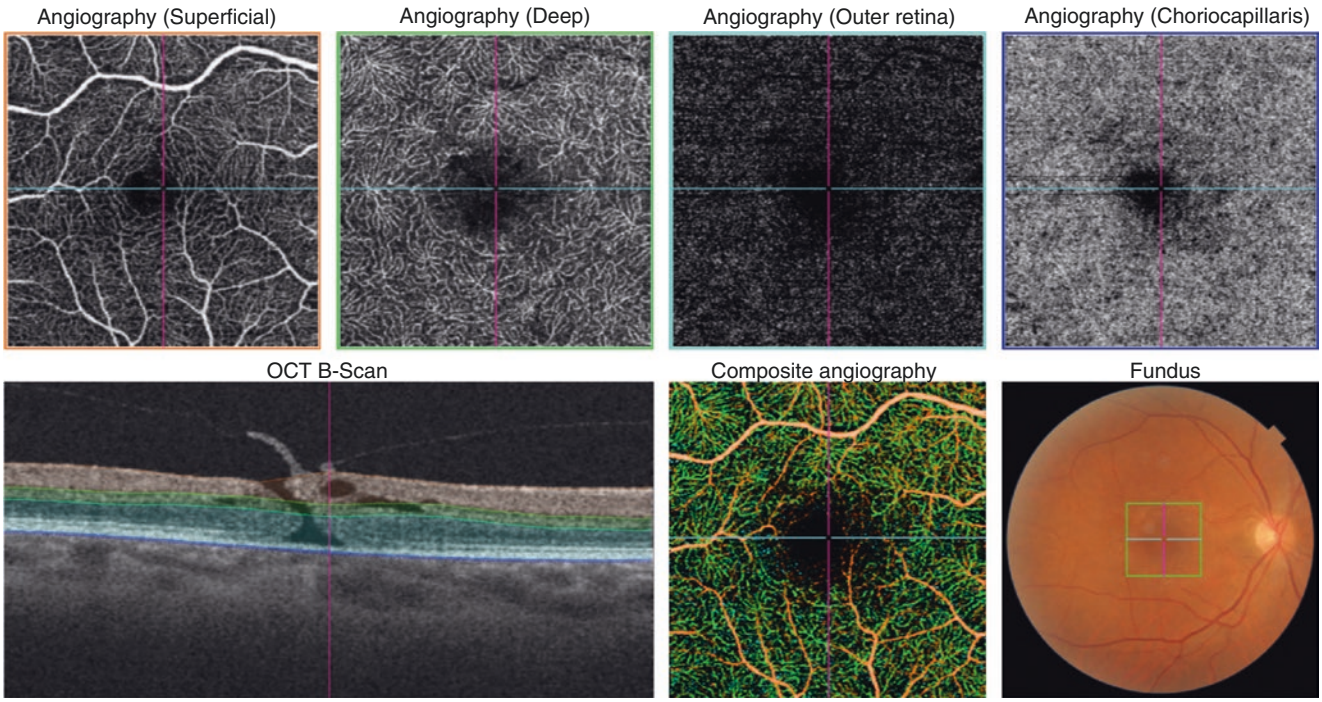

Fig. 11.16 SS-OCT angiography of a stage 2 macular hole

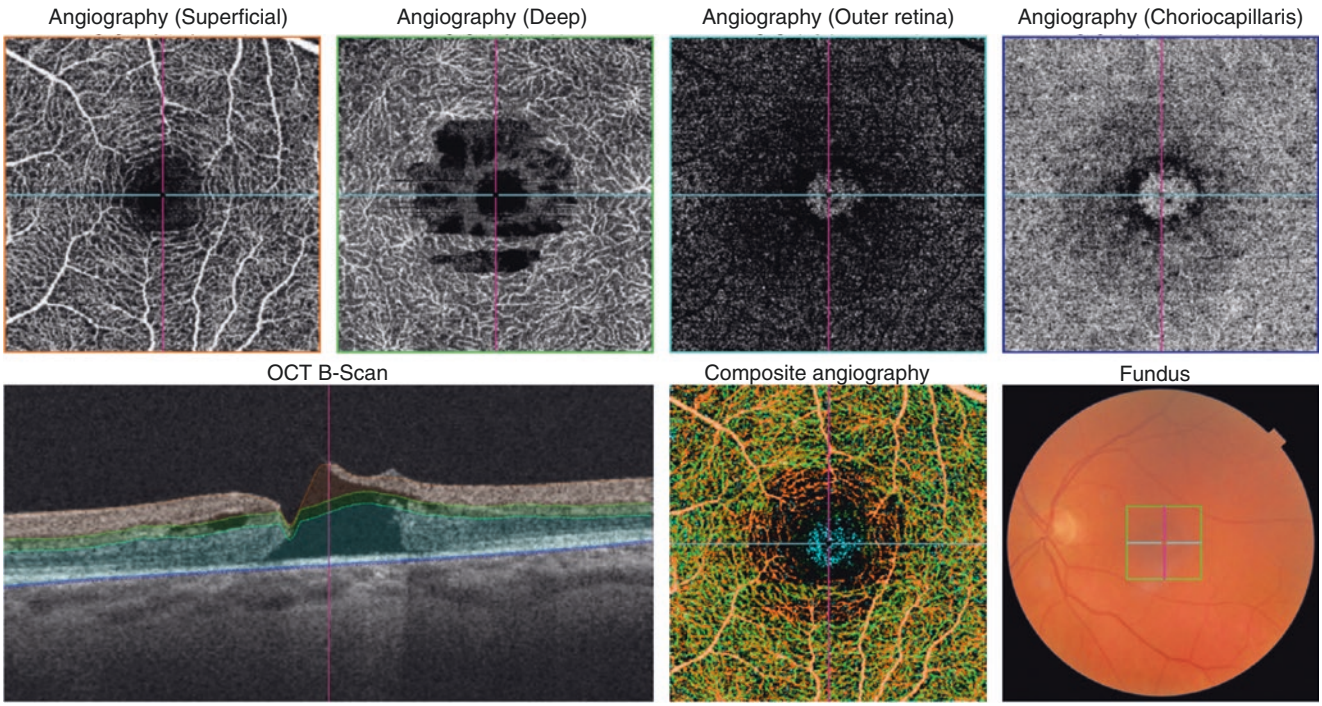

Fig. 11.17 SS-OCTA of a stage 3 macular hole with inaccurate segmentation of deep vascular plexus and choriocapillaris

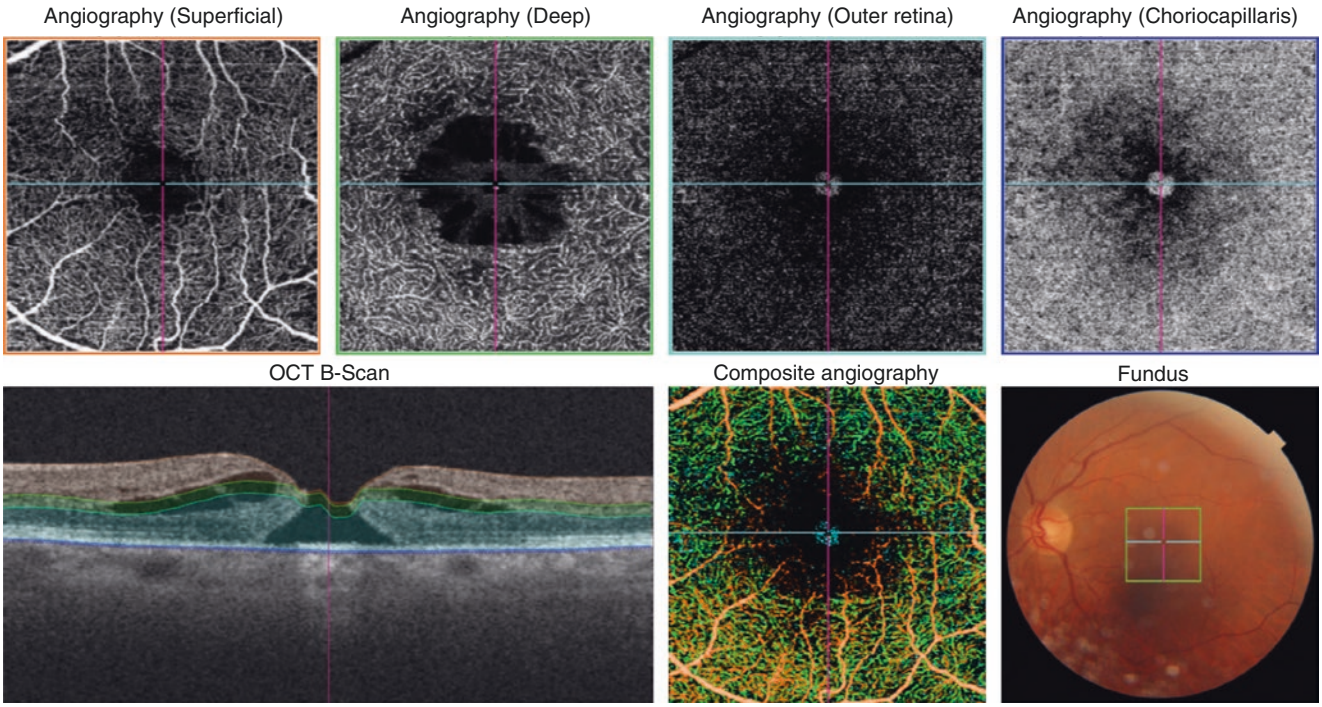

Fig. 11.18 SS-OCTA images of a stage 4 macular hole showing an artifact where the laser has reflected from the choriocapillaris

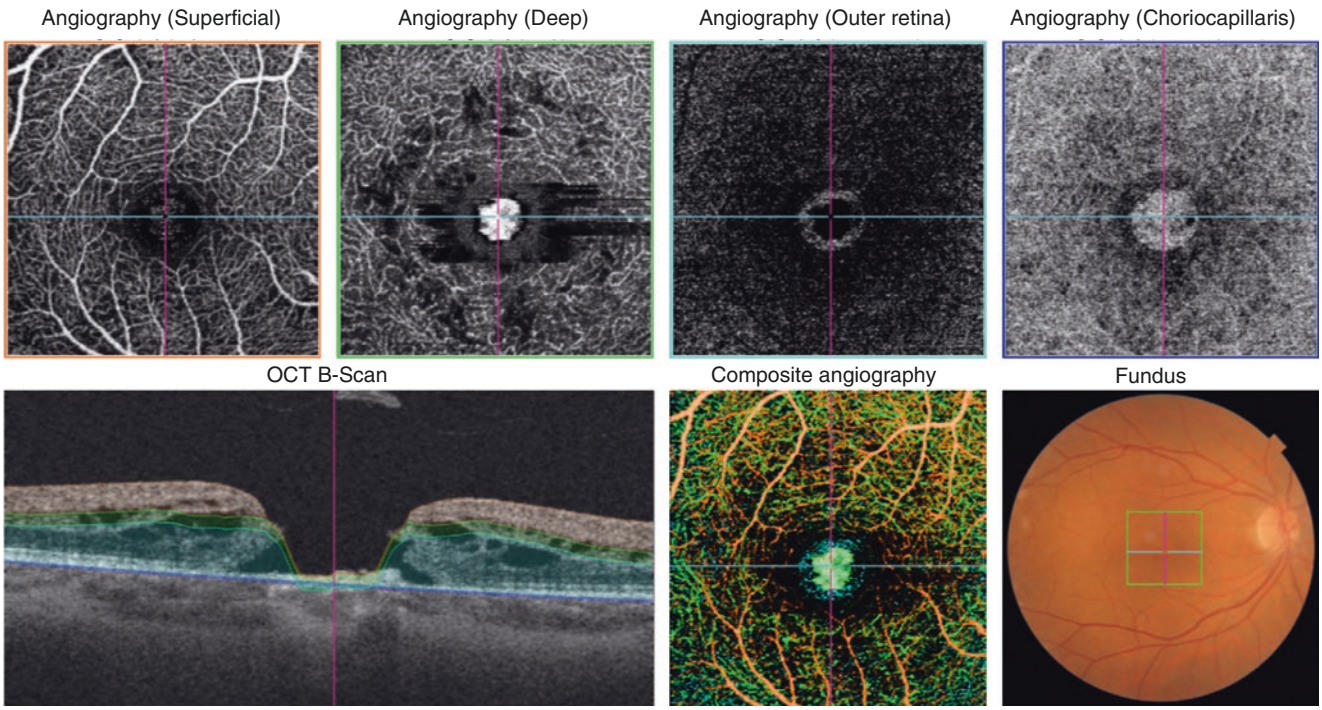

Fig. 11.19 Stage 4 macular hole SS-OCTA without manual correction where the segmentation has failed and the images present artifacts

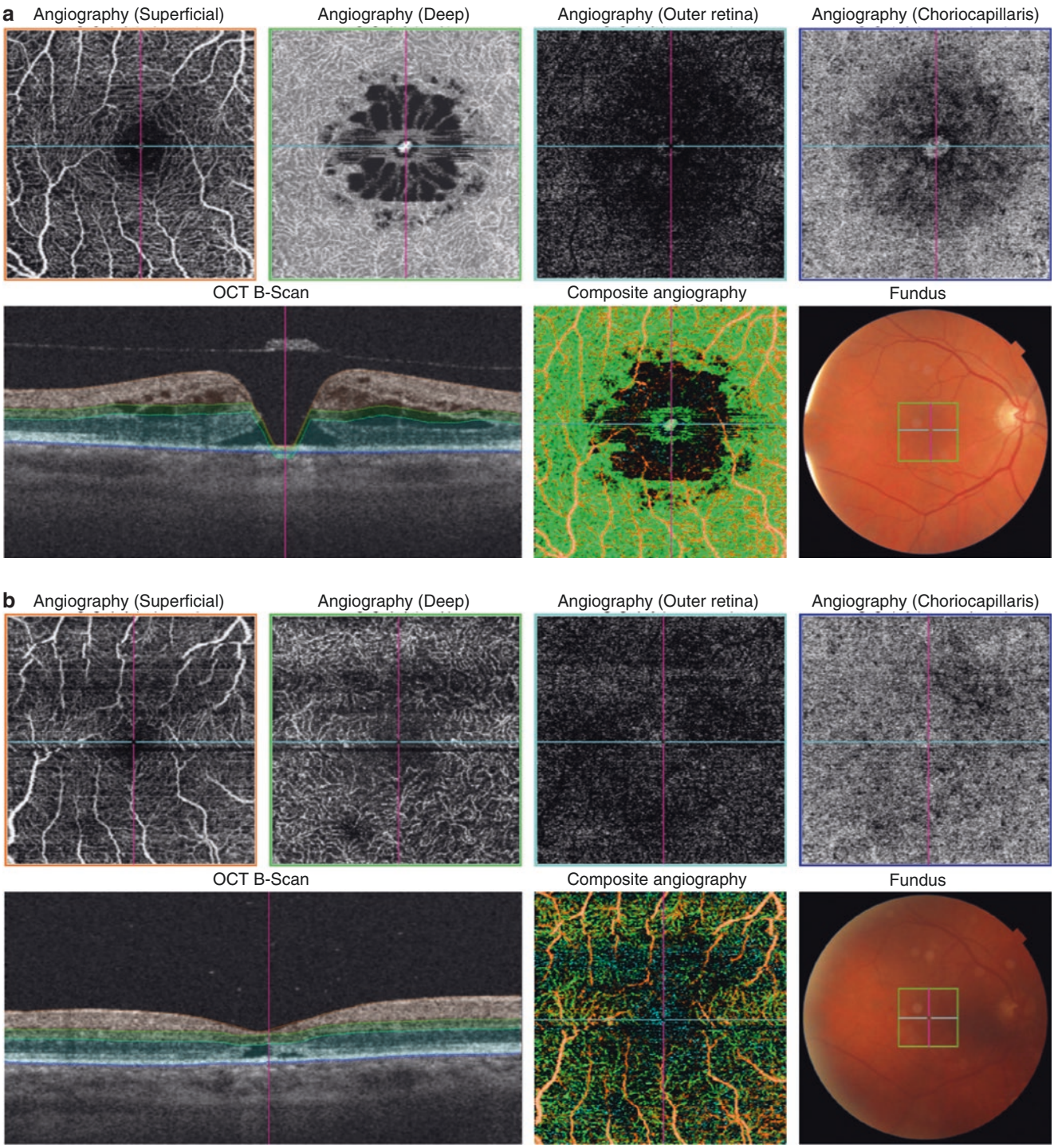

Fig. 11.20 (**a**) Apparent cystic spaces with vessel artifacts due to the scan lines having dropped into the hole resulting in poor segmentation. (**b**) Post-surgical SS-OCTA of the same eye. The macular hole has closed, cystic spaces have resolved and no vascular abnormalities are present in the deep angiography image

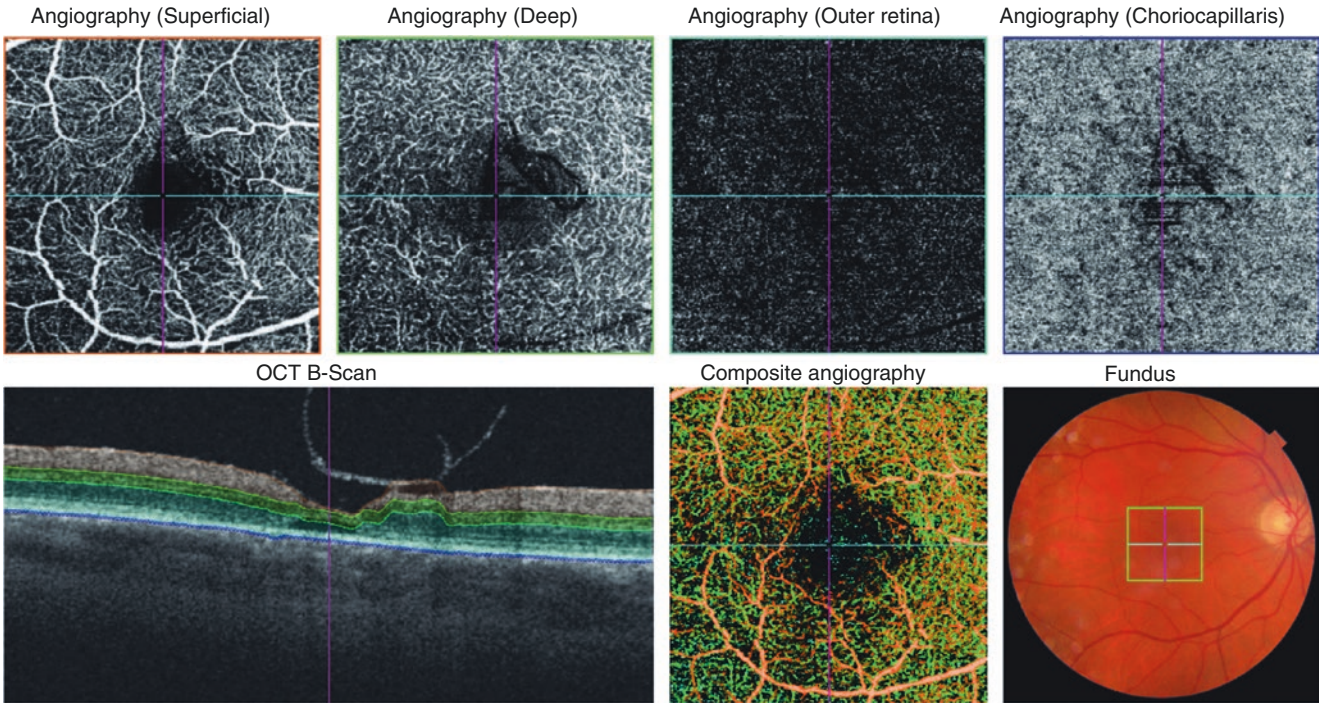

Fig. 11.21 Possible incorrect segmentation resulting in dark shadows on the angiography images

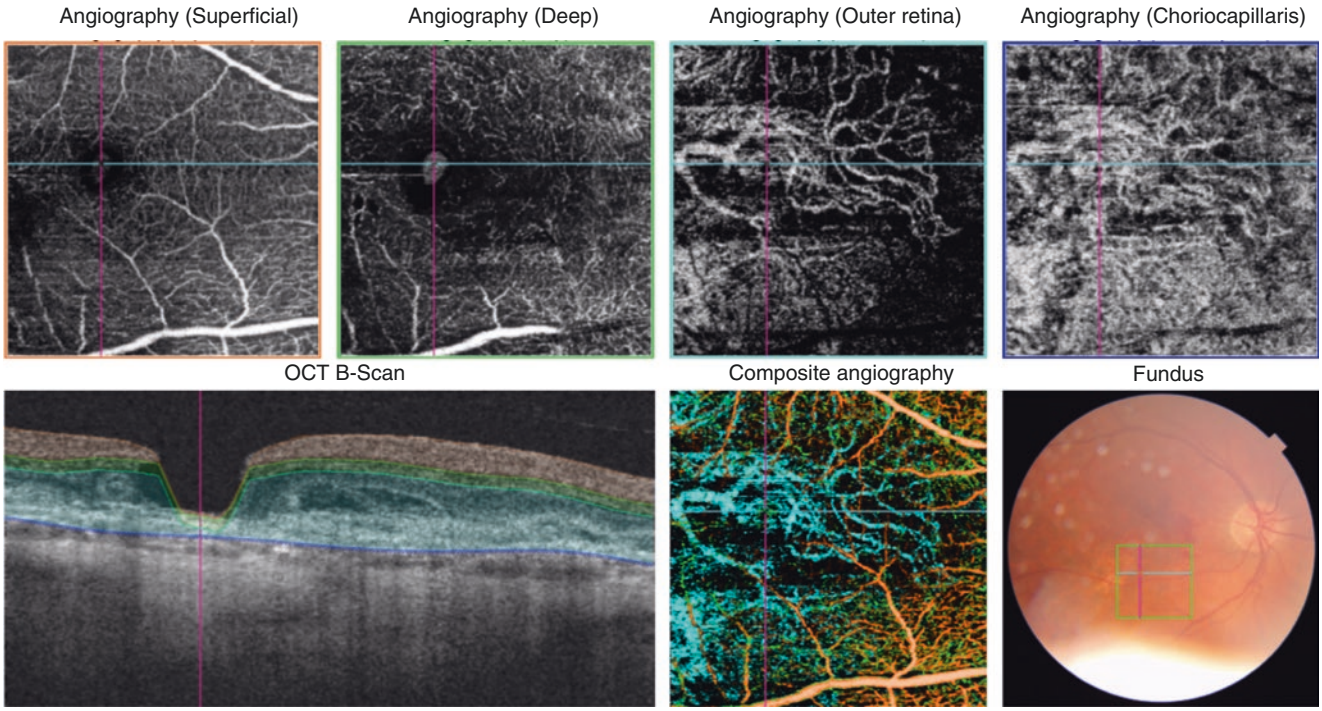

Fig. 11.22 Unique macular hole secondary to AMD subretinal vasculature—trophic hole not caused by traction

Conclusion

When compared to older imaging devices, the improved resolution and the excellent visualization of the vitreous, retina, and choroid provided by SS-OCT allows us to study cases of macular hole in greater detail. Additionally, the use of SS-OCTA in these cases allows us to better understand methods and to be more analytical with our observations.

References

1. Michalewska Z, Michalewski J, Adelman RA, Nawrocki J. Inverted Internal limiting membrane flap technique for large macular holes. Ophthalmology. 2010;117:2018–25.
2. Michalewska Z, Michalewski J, Dulczewska-Cichecka K, Adelman RA, Nawrocki J. Temporal inverted internal limiting membrane flap technique versus classic inverted internal limiting membrane flap technique. A comparative study. Retina. 2015;35(9):1844–50.
3. Michalewska Z, Michalewski J, Sikorski BI, Kałużny JJ, Wojtkowski M, Adelman RA, et al. A study of macular hole formation be serial spectral optical coherence tomography. Clin Exp Ophthalmol. 2009;37:373–83.
4. Takahashi A, Nagoaka T, Ishiko D, Kameyama D, Yoshida A. Foveal anatomic changes in progressing stage 1 macular hole documented by spectral-domain optical coherence tomography. Ophthalmology. 2010;117(4):806–10.
5. Tornambe PE. Macular hole genesis: the hydration theory. Retina. 2003;3:421–4.
6. Michalewska Z, Michalewski J, Nawrocka Z, Dulczewska-Cichecka K, Nawrocki J. The outer choroidoscleral boundary in full thickness macular holes before and after surgery, a swept source OCT study. Graefes Arch Clin Exp Ophthalmol. 2015;253(12):2087–93.
7. Michalewska Z, Cisiecki S, Sikorski B, Michalewski J, Kałużny JJ, Wojtkowski M, et al. Spontaneous closure of stage III and IV idiopathic full thickness macular holes – a two-case report. Graefes Arch Clin Exp Ophthalmol. 2008;246(1):99–104.
8. Eckardt C, Eckert T, Eckardt U, Porkert U, Gesser C. Macular hole surgery with air tamponade and optical coherence tomography based duration of face down positioning. Retina. 2008;28(8):1087–96.
9. Kikushima W, Imai A, Toriyama Y, Hirano T, Murata T, Ishibashi T. Dynamics of macular hole closure in gas filled eyes with 24 h of surgery observed with swept source optical coherence tomography. Ophthalmic Res. 2015;53(1):48–54.
10. Michalewska Z, Michalewski J, Cisiecki S, Adelman R, Nawrocki J. Correlation between foveal structure and visual outcome following macular hole surgery: a spectral optical coherence tomography study. Graefes Arch Clin Exp Ophthalmol. 2008;246(6):823–30.
11. Tadayoni R, Paques M, Massin P, Mouki-Benani S, Mikol J, Gaudric A. Dissociated optic nerve fiber layer appearance of the fundus after idiopathic epiretinal membrane removal. Ophthalmology. 2001;108:2279–83.
12. Morizane Y, Shiraga F, Kimura S, Hosokawa M, Shiode Y, Kawata HM, et al. Autologous transplantation of the internal limiting membrane for refractory macular holes. Am J Ophthalmol. 2014;157:861–9.
13. Lai C, Chen Y, Wang N, Chuang L, Liu L, Chen K, et al. Vitrectomy with internal limiting membrane repositioning and autologous blood for macular hole retinal detachment in highly myopic eyes. Ophthalmology. 2015;122:1889–98.
14. Kuriyama S, Hayashi H, Jingami Y, Kuramoto N, Akita J, Matsumoto M. Efficacy of inverted internal limiting membrane flap technique for treatment of macular hole in high myopia. Am J Ophthalmol. 2013;156:125–31.
15. Michalewska Z, Michalewski J, Dulczewska-Cichecka K, Nawrocki J. Inverted internal limiting membrane flap technique for surgical repair of myopic macular holes. Retina. 2014;34(4):664–9.
16. Grewal DS, Mahmoud TH. Autologous neurosensory retinal free flap for closure of refractory myopic macular holes. JAMA Ophthalmol. 2016;134(2):22930. doi:10.1001/jamaophthalmol.2015.5237.

Diabetic Macular Edema

12

Takafumi Hirashima, Masanori Hagihara, and Hideyasu Oh

Diabetic macular edema (DME) is one of the most common causes of visual impairment in patients with diabetes mellitus [1]. Physiologically, DME is reported to be induced by disruption of the blood-retinal barrier (BRB) secondary to retinal vessel leukostasis, pericyte loss, and increased permeability of retinal pigment epithelium cells [2]. The disruption of the BRB results in abnormal fluid leakage into the extracellular space and then leads to residual accumulation of fluid into the intraretinal layers [3]. Similarly, various choroidal abnormalities, including obstruction of the choriocapillaris, vascular degeneration, choroidal aneurysms, and choroidal neovascularization, have been reported [4–6]. The introduction of swept source OCT (SS-OCT) made it possible to detect these morphological features of the choroid in patients with DME, such as an irregular-shaped choroidoscleral interface, focal choroidal thinning, and reduction of choriocapillaris layer thickness [7].

The molecular mechanisms of DME involve chronic hyperglycemia, the accumulation of oxidative stress agents and protein kinase C formation, and the subsequent activations of various inflammatory factors, especially vascular endothelial growth factor (VEGF) [8–10].

12.1 Classification of Diabetic Macular Edema

Based on optical coherence tomography (OCT) images, DME is classified into six morphologic patterns: focal retinal thickening (Fig. 12.1), diffuse retinal thickening (Fig. 12.2a), cystoid macular edema (CME) (Fig. 12.2b), serous retinal detachment without posterior hyaloidal traction (PHT) (Fig. 12.2c), PHT without traction retinal detachment (TRD) (Fig. 12.2d), and PHT with TRD (Fig. 12.2e) [11, 12].

T. Hirashima, MD • M. Hagihara, MD • H. Oh, MD, PhD (✉)
Department of Ophthalmology, Hyogo Prefectural Amagasaki General Medical Center (AGMC), Amagasaki, Hyogo, Japan
e-mail: hideyasu@kuhp.kyoto-u.ac.jp

© Springer International Publishing AG 2017
Z. Michalewska, J. Nawrocki (eds.), *Atlas of Swept Source Optical Coherence Tomography*,
DOI 10.1007/978-3-319-49840-9_12

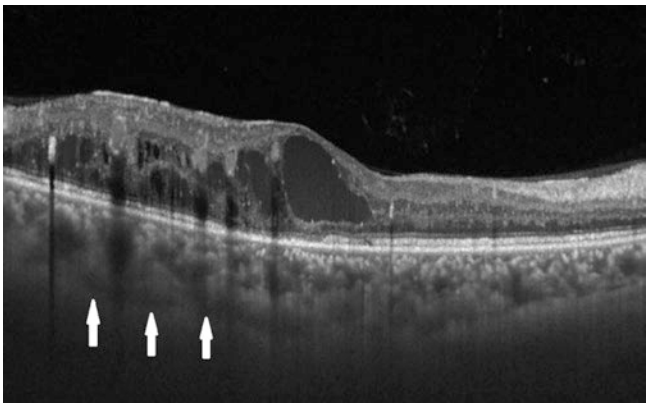

Fig. 12.1 Image of a case with focal diabetic macular edema (DME) by SS-OCT. *Arrows* indicate the region that has focal thickening of both the retina and choroid

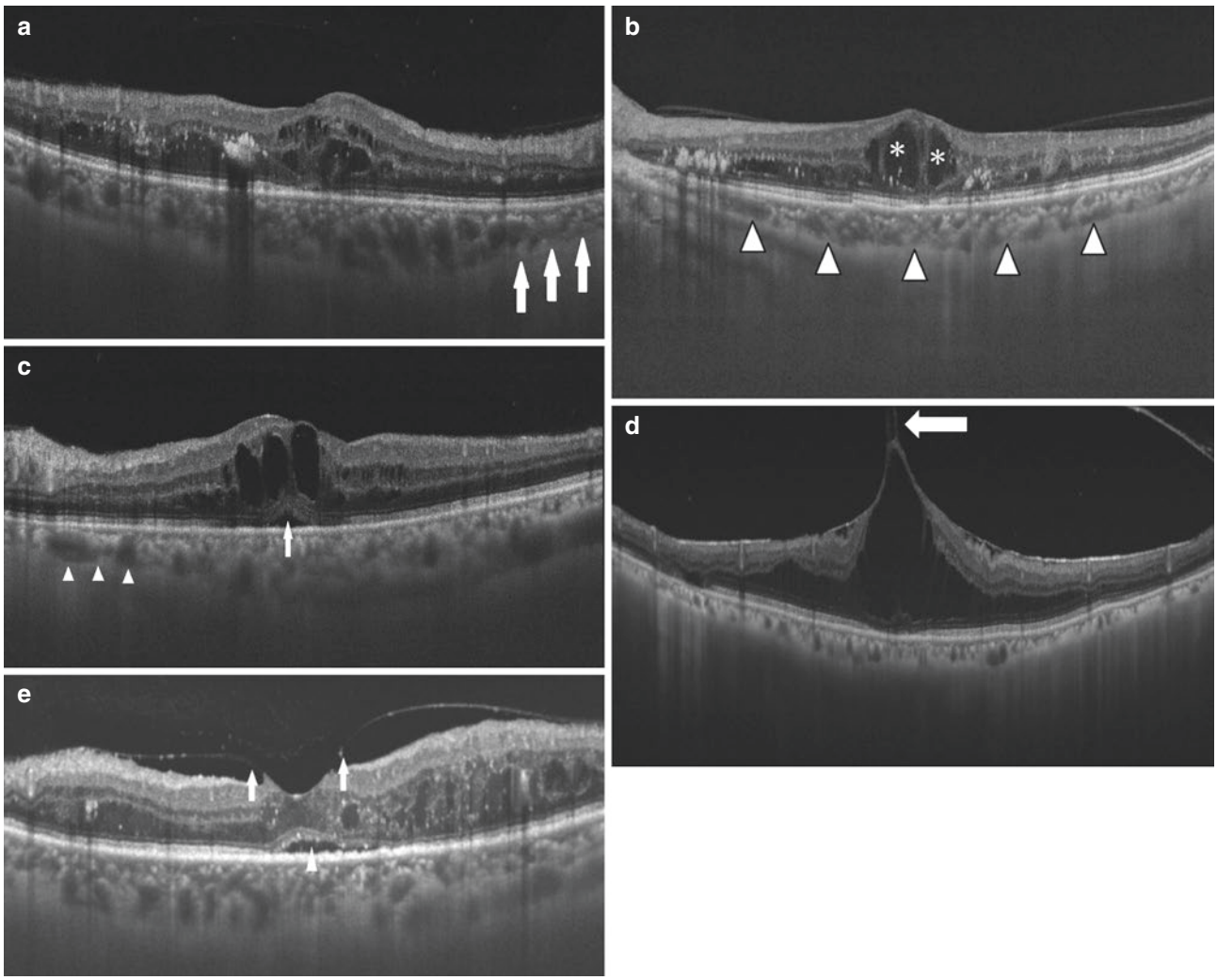

Fig. 12.2 **(a)** SS-OCT image of diffuse retinal thickening. Note the area of the thin choroid (*arrows*). **(b)** SS-OCT image of a case with cystoid macular edema. Both intraretinal cystoid cavities and choroidal vasculature are well documented. The chorio-scleral interface is indicated by *arrowheads*. **(c)** SS-OCT image of serous retinal detachment without posterior hyaloidal traction (PHT). A slight subretinal fluid is observed beneath the dome-like elevation of detached retina (*arrow*). *Arrowheads* indicate the region showing focal thinning of the choroid. (**d**) SS-OCT image of PHT without traction retinal detachment (TRD). The PHT is clearly identified as a highly reflective strand arising from the inner retinal surface (*arrow*). Note the relatively thin choroid. (**e**) SS-OCT image of PHT with TRD. The traction exerted by the PHT is identified as a highly reflective strand between the inner retinal surface and the posterior hyaloid (*arrows*). The TRD is detected as an area of low signal underlying the highly reflective border of detached retina (*arrowhead*)

12.2 Photocoagulation Treatment

Focal laser photocoagulation is the standard treatment for focal DME. The Early Treatment Diabetic Retinopathy Study (ETDRS) reported a 50% reduction in moderate vision loss (>3 lines) with laser treatment compared to observation (Figs. 12.3, 12.4, 12.5, and 12.6) [13]. In diffuse DME, however, the significant effectiveness of laser photocoagulation has not been demonstrated.

Recent reports showed a significant decrease in choroidal thickness in patients treated with pan-retinal coagulation (Figs. 12.7, 12.8, 12.9, and 12.10) [14, 15]. On the other hand, it has been reported that focal laser photocoagulation did not alter choroidal thickness in eyes with DME [16].

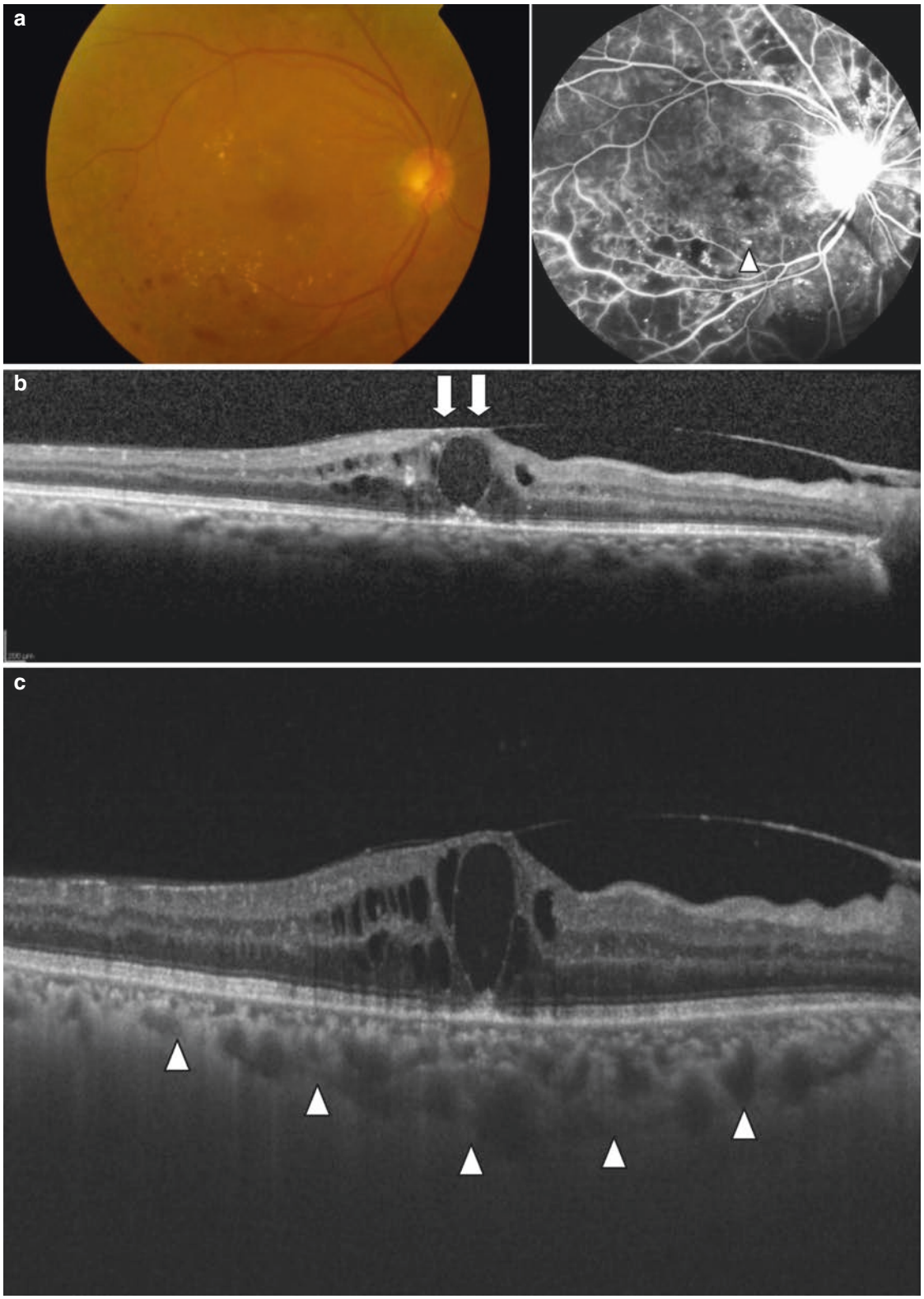

Fig. 12.3 (**a**) Fundus photograph (*left*) and fluorescent fundus angiography (*right*) of a case with CME. Note the microaneurysm (*arrowhead*) treated with focal laser photocoagulation. (**b**) Preoperative spectral-domain OCT image. Note the CME and the adhesion of posterior hyaloid membrane to the foveola (*arrows*). The choroidal vasculature is not well visualized. (**c**) Preoperative SS-OCT image. Note the detail structure of the choroid is well visualized, compared to (**b**) (*arrowheads*)

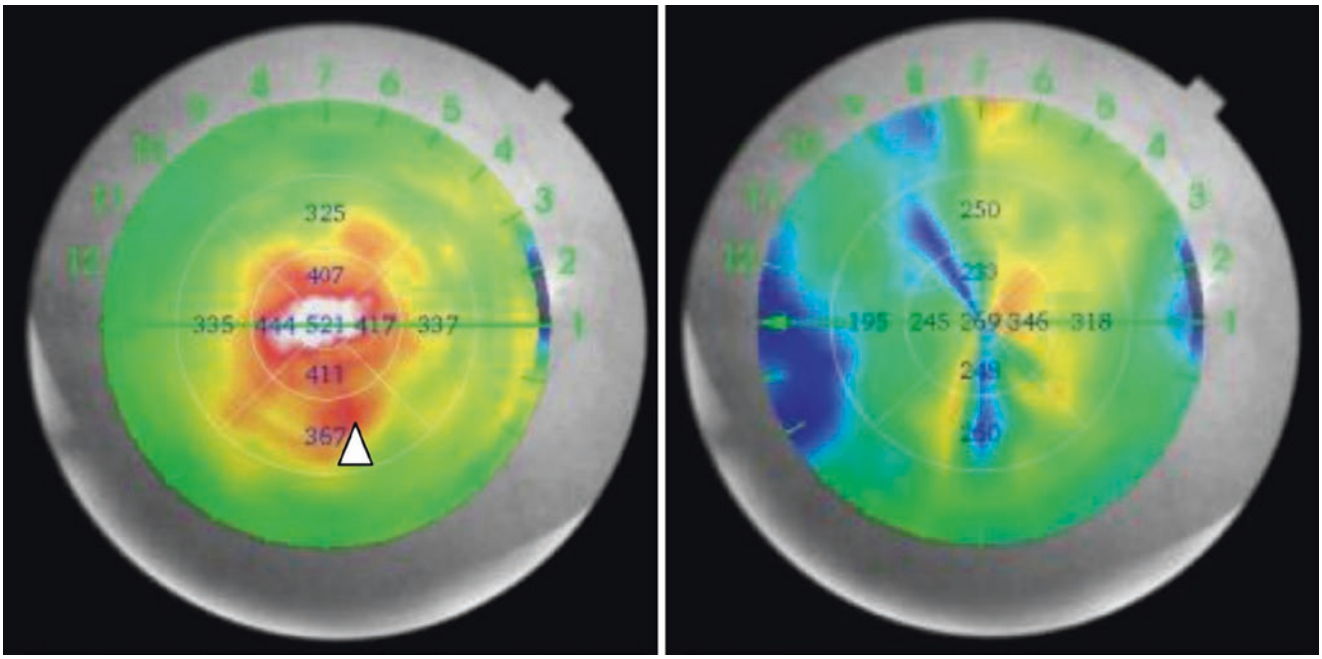

Fig. 12.4 Preoperative retinal (*left*) and choroidal thickness map (*right*) by SS-OCT. *Arrowhead* indicates the area where the photocoagulated microaneurysm is located

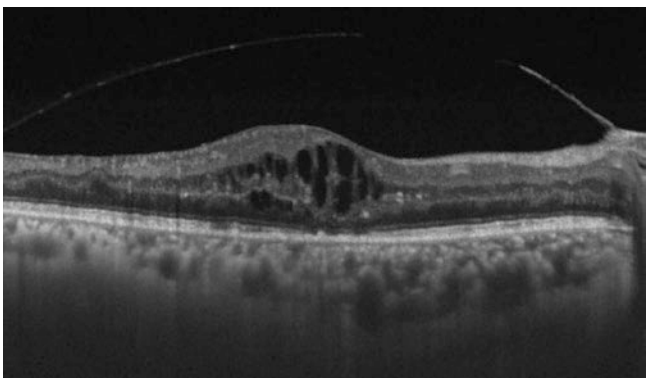

Fig. 12.5 SS-OCT at 1 month after focal photocoagulation. Note the adhesion of posterior hyaloid membrane is released

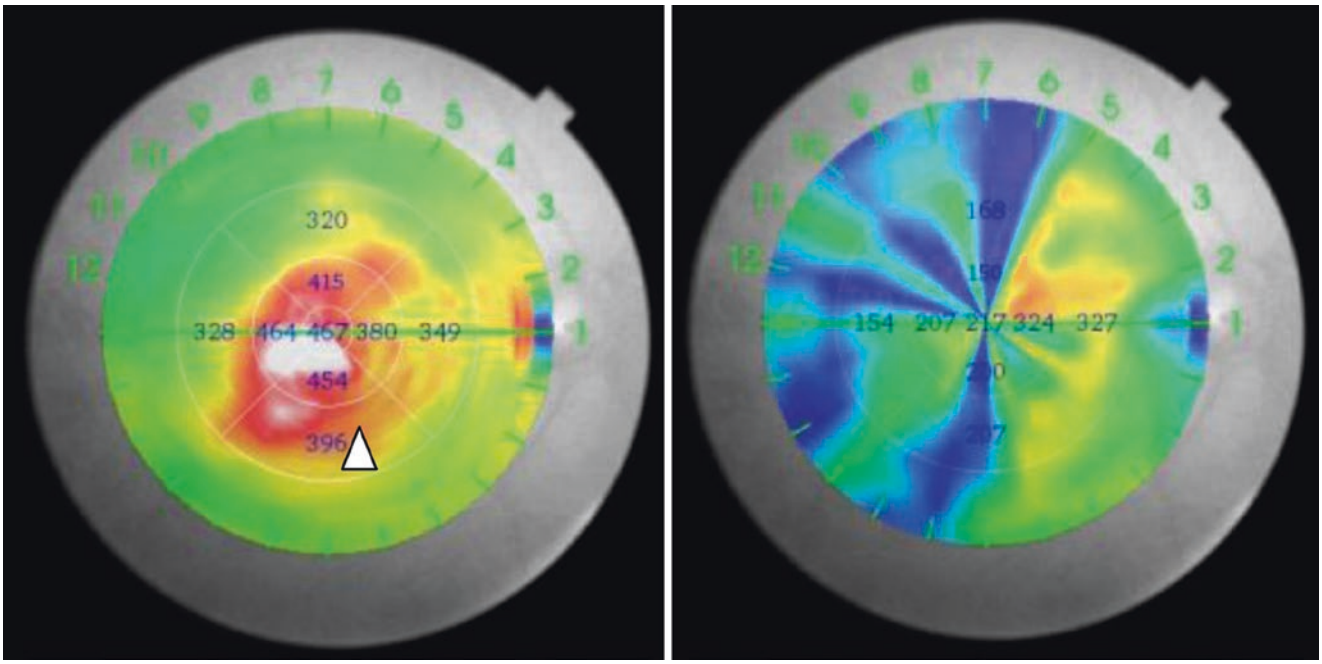

Fig. 12.6 Retinal thickness map (*left*) at 1 month after focal photocoagulation shows reduction of the retinal thickness in the photocoagulated area (*arrowhead*) and also the central fovea. The choroidal thickness map (*right*) shows that the choroidal thickness remains largely unchanged

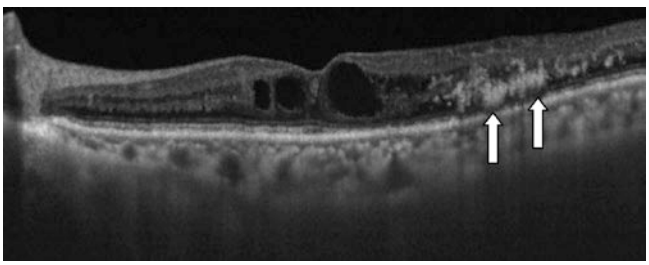

Fig. 12.7 A case that required pan-retinal photocoagulation. Preoperative SS-OCT shows CME and hard exudates (*arrows*)

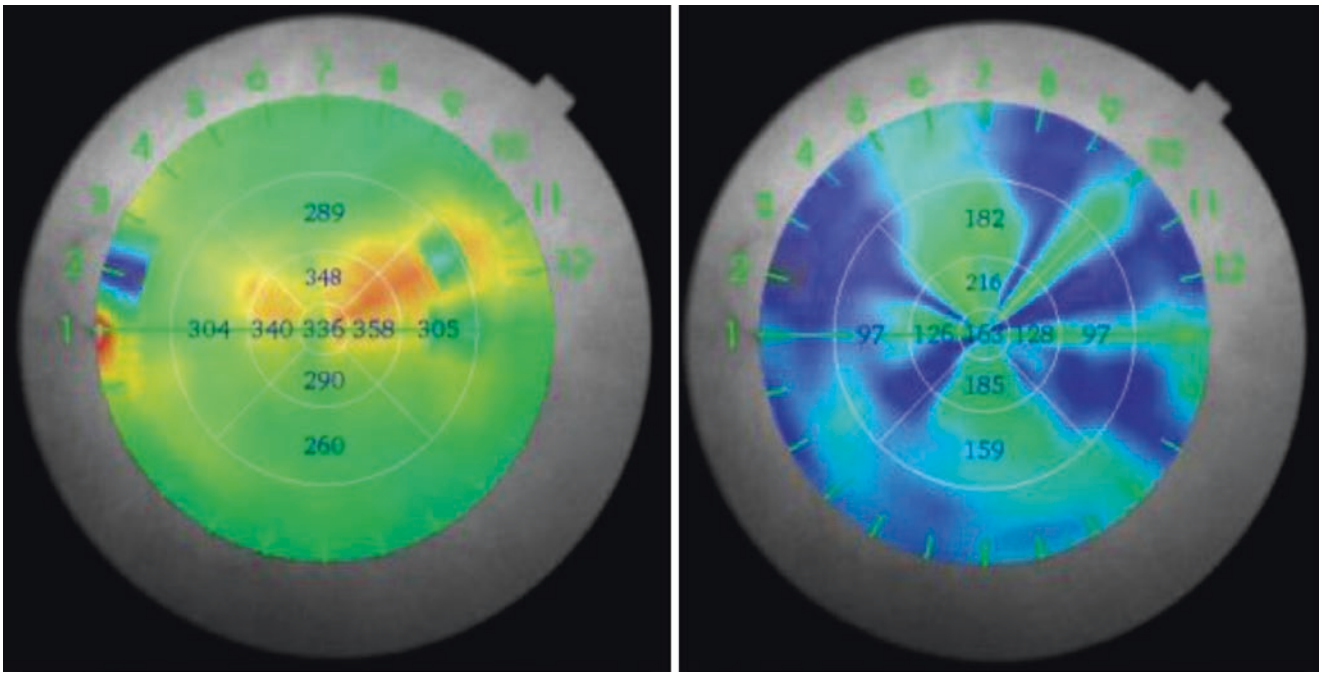

Fig. 12.8 Preoperative retinal (*right*) and choroidal thickness map (*left*)

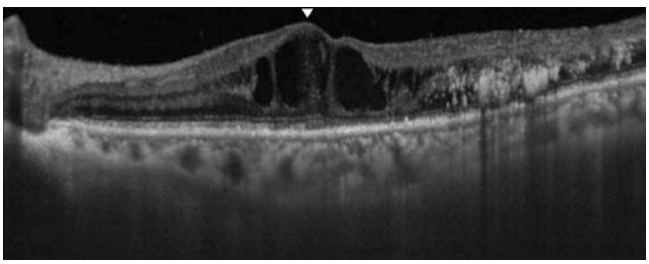

Fig. 12.9 SS-OCT at 2 weeks after pan-retinal photocoagulation. The increase of macular edema was observed (*arrowhead*)

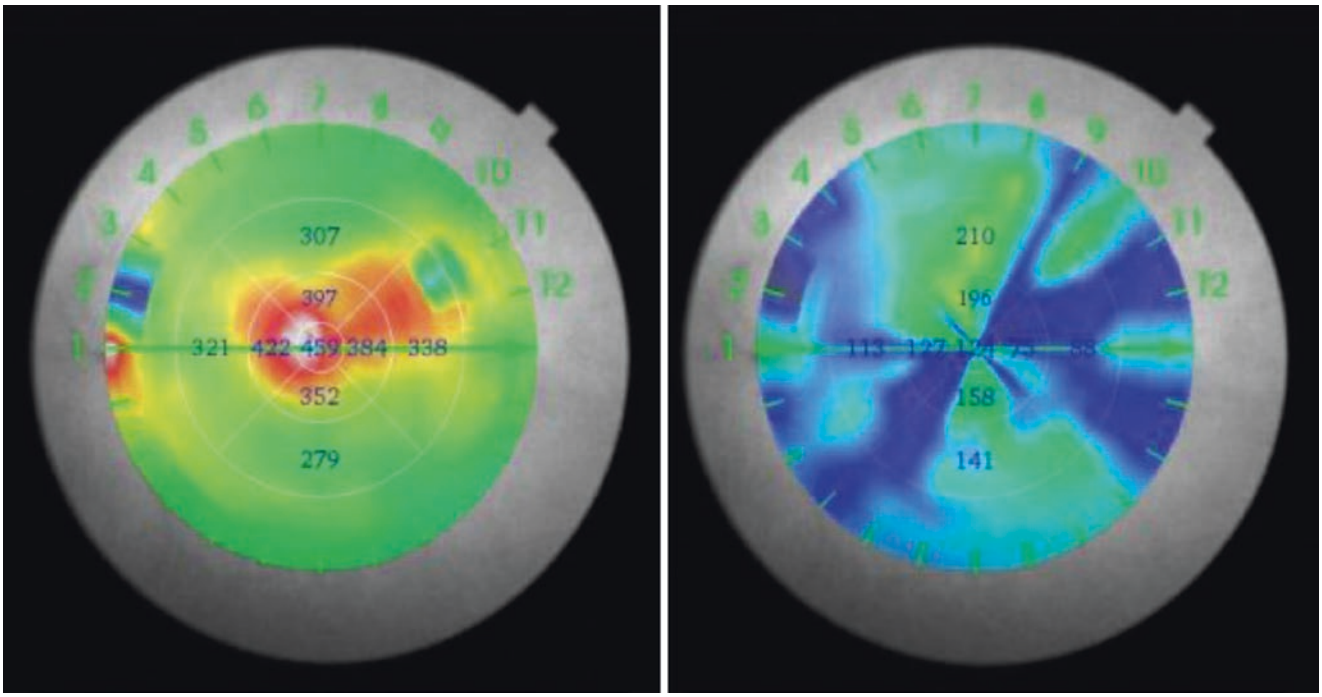

Fig. 12.10 Retinal thickness map (*left*) at 2 weeks after pan-retinal photocoagulation shows increase of the retinal thickness. The choroidal thickness map (*right*) shows that the choroidal thickness remains unchanged

12.3 Medical Treatment

The two major medical treatments for DME are corticosteroids and anti-VEGF agents. The anti-inflammatory effect of corticosteroids helps to reduce retinal edema and may also inhibit neovascularization [17, 18], while significant side effects, including cataracts and glaucoma, have been reported [19, 20].

The efficacy and safety of intravitreal anti-VEGF treatment for DME have recently been demonstrated by various clinical trials [21–23]. To date, both ranibizumab and aflibercept are approved for the treatment of DME by the U.S. Food and Drug Administration. The recent reports showed anti-VEGF treatment for DME reduces choroidal thickness (Figs. 12.11, 12.12, 12.13, and 12.14) [24–26].

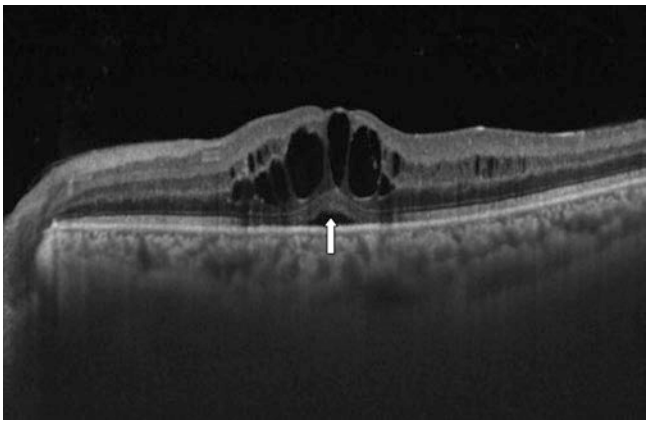

Fig. 12.11 A case treated with intravitreal injection of aflibercept (IVA). Preoperative SS-OCT shows CME and a slight subretinal fluid (*arrow*)

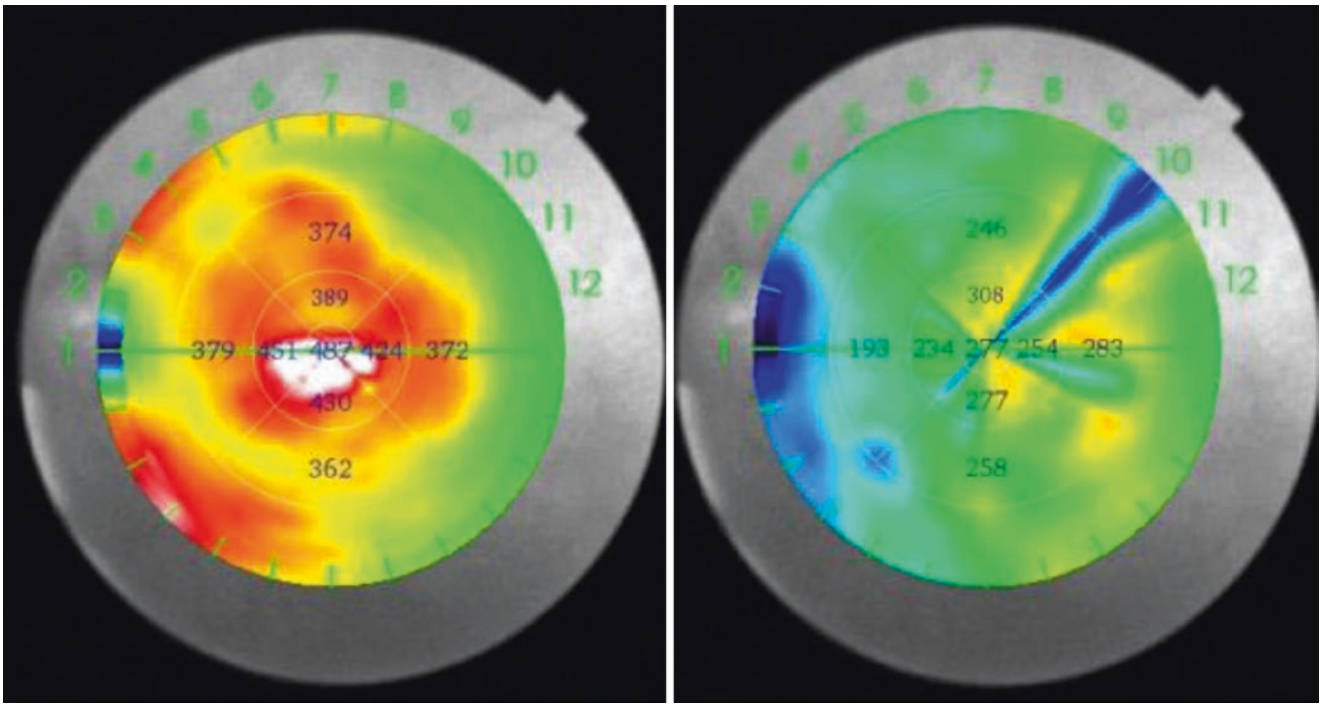

Fig. 12.12 Preoperative retinal (*left*) and choroidal thickness map (*right*) show diffuse retinal thickening and localized choroidal thickening in the fovea, respectively

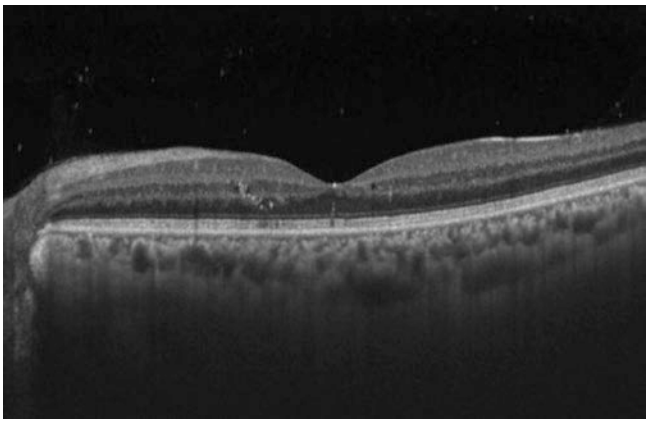

Fig. 12.13 SS-OCT image at 1 month after the initial IVA shows complete resolution of the macular edema

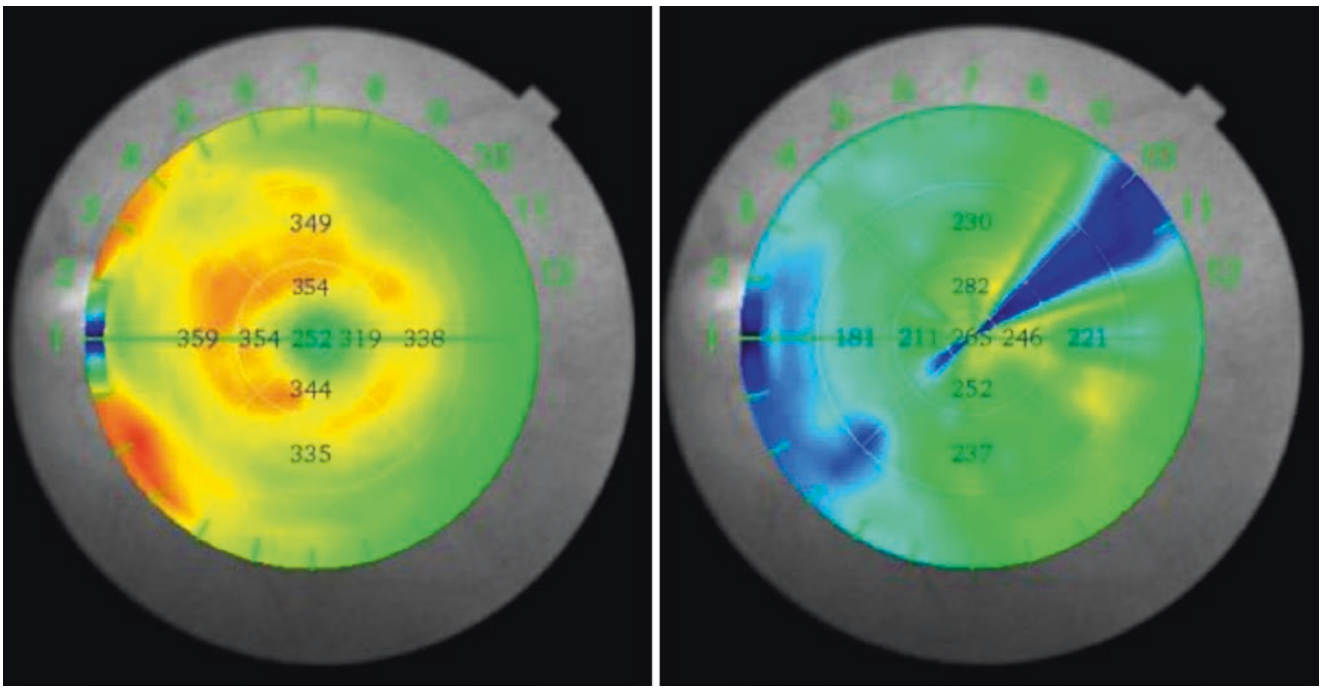

Fig. 12.14 Retinal thickness map (*left*) at 1 month after IVA shows a remarkable decrease of the retinal thickness and the choroidal thickness is also slightly reduced (*right*)

12.4 Vitrectomy

The vitreous is implicated as a cause of DME by some mechanical and physiologic mechanisms, all of which lead to increased vascular permeability [27–29]. When there is an evident traction over the macular, vitrectomy has been reported to be effective (Figs. 12.15, 12.16, 12.17, and 12.18) [30, 31]. Vitrectomy also can improve DME by removing the growth factors and cytokines such as VEGF, IL-6, and platelet-derived growth factor. These factors have been reported to be abundantly detected in the vitreous fluid of DME and associated with macular edema and retinal neovascularization [32]. Furthermore, the evidence that decreased oxygenation can exacerbate DME [33] supports an additional advantage of vitrectomy since it provides the inner retina with additional oxygen by improving the flow of oxygen rich aqueous into the vitreous cavity [34]. The increase of oxygen concentration at the inner retina can decrease the flow of oxygen from choroid to retina and constrict the choroidal vessels [35]. Nevertheless, the role of vitrectomy in treatment of DME remains elusive because the potential benefits and risks have not been clearly evaluated in long-term, adequately sized, randomized clinical trials.

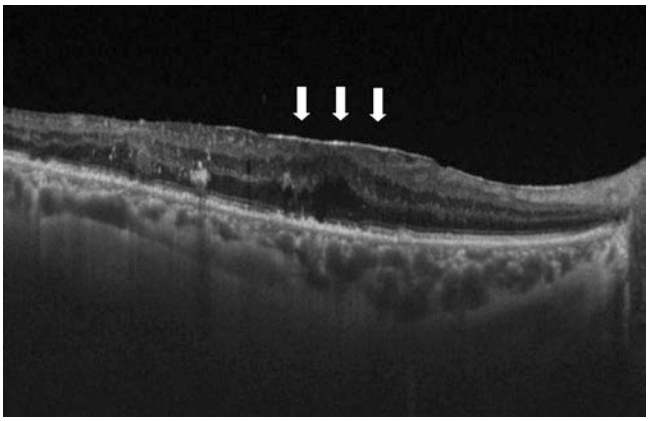

Fig. 12.15 A case treated with vitrectomy and internal limiting membrane peeling. Preoperative SS-OCT image shows diffuse retinal thickening, hard exudates, and an epiretinal membrane (*arrows*)

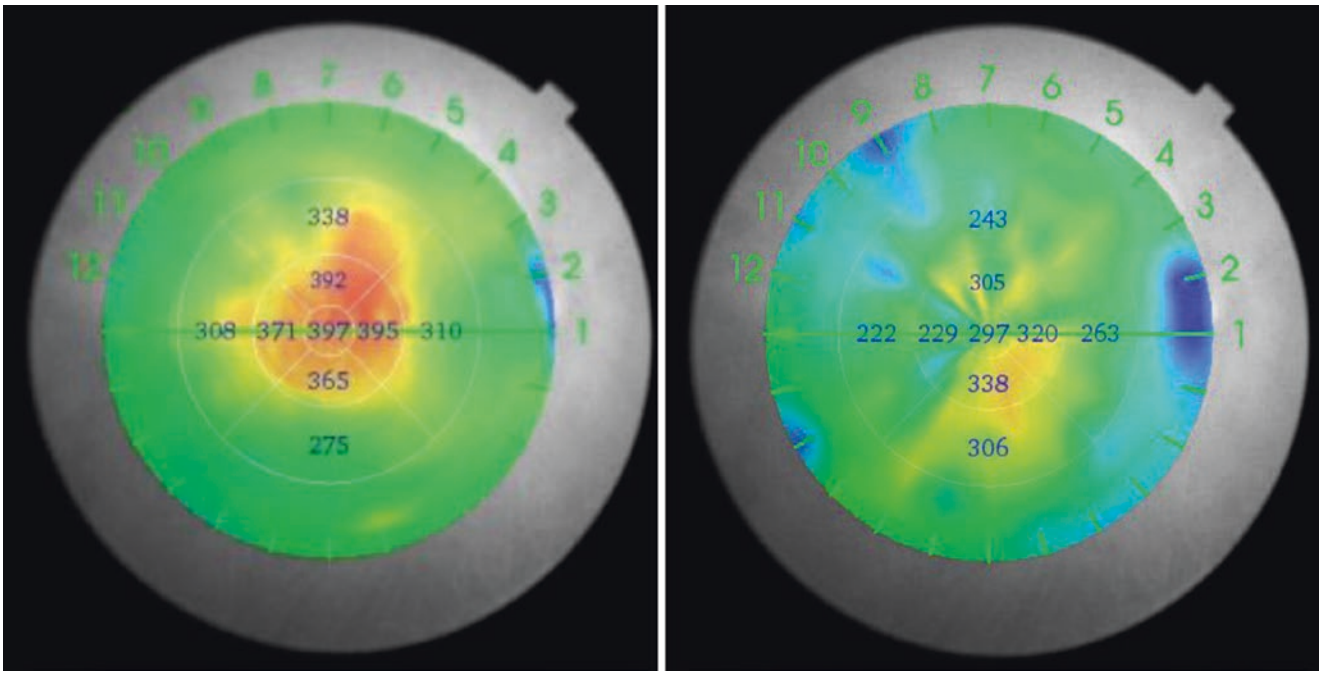

Fig. 12.16 Preoperative retinal thickness map (*left*) shows diffuse retinal thickening centered on the fovea. Preoperative choroidal thickness map (*right*)

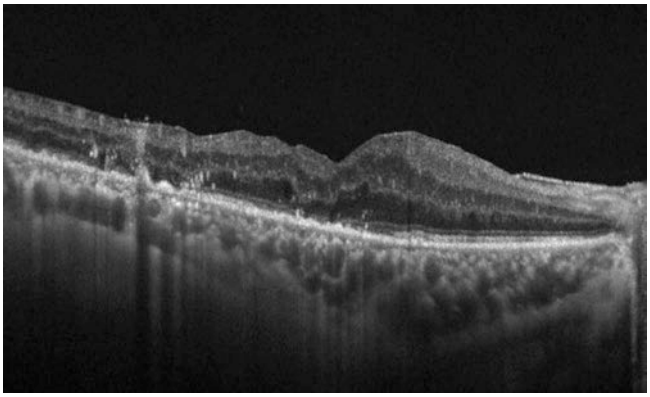

Fig. 12.17 SS-OCT image at 1 month after the surgery shows resolution of the retinal edema

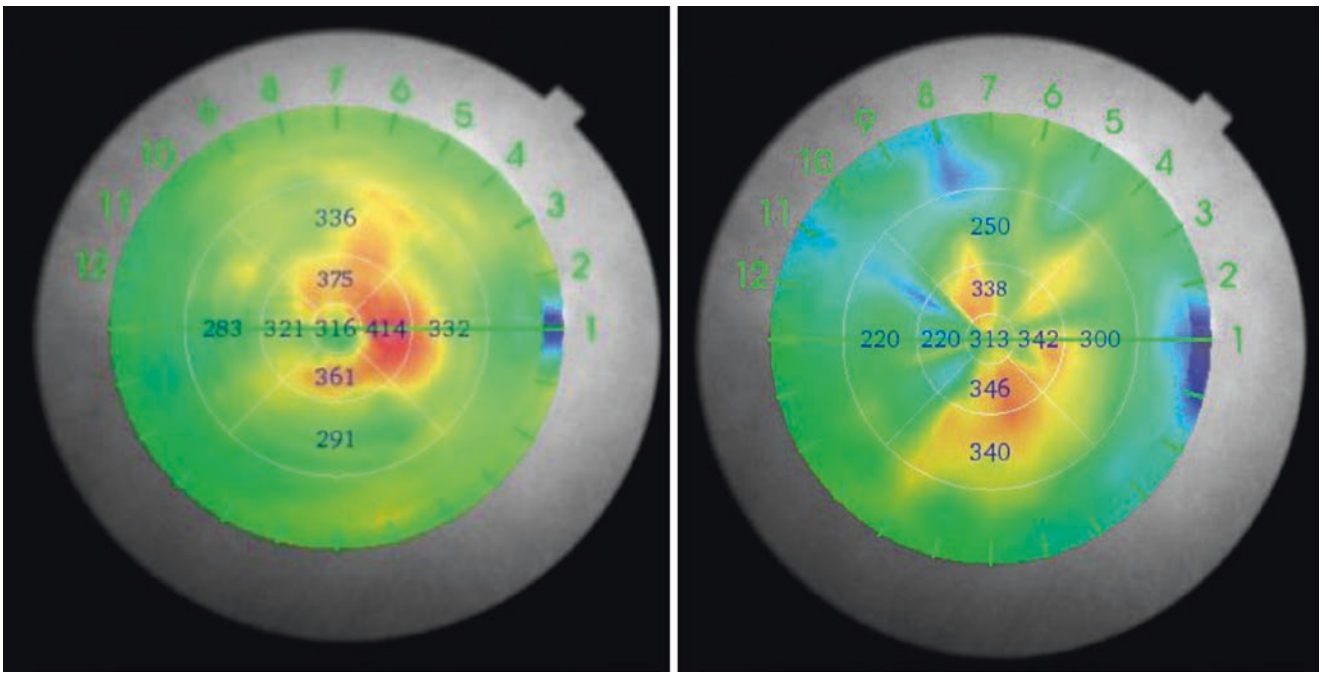

Fig. 12.18 Retinal thickness map (*left*) at 1 month after vitrectomy shows reduction of the retinal thickness in the central fovea. The choroidal thickness map (*right*) shows a slight increase of the choroidal thickness in the inferior parafoveal area

References

1. Klein R, Lee KE, Knudtson MD, Gangnon RE, Klein BE. Changes in visual impairment prevalence by period of diagnosis of diabetes: the Wisconsin Epidemiologic Study of Diabetic Retinopathy. Ophthalmology. 2009;116:1937–42.
2. Ciulla TA, Amador AG, Zinman B. Diabetic retinopathy and diabetic macular edema: pathophysiology, screening, and novel therapies. Diabetes Care. 2003;26:2653–64.
3. Knudsen ST, Bek T, Poulsen PL, Hove MN, Rehling M, Mogensen CE. Macular edema reflects generalized vascular hyperpermeability in type 2 diabetic patients with retinopathy. Diabetes Care. 2002;25:2328–34.
4. Hidayat AA, Fine BS. Diabetic choroidopathy. Light and electron microscopic observations of seven cases. Ophthalmology. 1985;92:512–22.
5. Cao J, McLeod S, Merges CA, Lutty GA. Choriocapillaris degeneration and related pathologic changes in human diabetic eyes. Arch Ophthalmol. 1998;116:589–97.
6. Fukushima I, McLeod DS, Lutty GA. Intrachoroidal microvascular abnormality: a previously unrecognized form of choroidal neovascularization. Am J Ophthalmol. 1997;124:473–87.
7. Adhi M, Brewer E, Waheed NK, Duker JS. Analysis of morphological features and vascular layers of choroid in diabetic retinopathy using spectral-domain optical coherence tomography. JAMA Ophthalmol. 2013;131:1267–74.
8. Morigi M, Angioletti S, Imberti B, Donadelli R, Micheletti G, Figliuzzi M, et al. Leukocyte-endothelial interaction is augmented by high glucose concentrations and hyperglycemia in a NF-kB-dependent fashion. J Clin Invest. 1998;101:1905–15.
9. Brownlee M. The pathobiology of diabetic complications: a unifying mechanism. Diabetes. 2005;54:1615–25.
10. Shams N, Ianchulev T. Role of vascular endothelial growth factor in ocular angiogenesis. Ophthalmol Clin N Am. 2006;19:335–44.
11. Otani T, Kishi S, Maruyama Y. Patterns of diabetic macular edema with optical coherence tomography. Am J Ophthalmol. 1999;127:688–93.
12. Kim BY, Smith SD, Kaiser PK. Optical coherence tomographic patterns of diabetic macular edema. Am J Ophthalmol. 2006;142:405–12.
13. Early Treatment Diabetic Retinopathy Study research group. Photocoagulation for diabetic macular edema. Early Treatment Diabetic Retinopathy Study report number 1. Arch Ophthalmol. 1985;103:1796–806.
14. Kim JT, Lee DH, Joe SG, Kim JG, Yoon YH. Changes in choroidal thickness in relation to the severity of retinopathy and macular edema in type 2 diabetic patients. Invest Ophthalmol Vis Sci. 2013;54:3378–84.
15. Zhu Y, Zhang T, Wang K, Xu G, Huang X. Changes in choroidal thickness after panretinal photocoagulation in patients with type 2 diabetes. Retina. 2015;35:695–703.
16. Adhi M, Alwassia AA, Duker JS. Analysis of choroidal thickness in eyes treated with focal laser photocoagulation using SD-OCT. Can J Ophthalmol. 2013;48:535–8.
17. Kompella UB, Bandi N, Ayalasomayajula SP. Subconjunctival nano- and microparticles sustain retinal delivery of budesonide, a corticosteroid capable of inhibiting VEGF expression. Invest Ophthalmol Vis Sci. 2003;44:1192–201.
18. Bhisitkul RB, Winn BJ, Lee OT, Wong J, Pereira Dde S, Porco TC, et al. Neuroprotective effect of intravitreal triamcinolone acetonide against photoreceptor apoptosis in a rabbit model of subretinal hemorrhage. Invest Ophthalmol Vis Sci. 2008;49:4071–7.
19. Martidis A, Duker JS, Greenberg PB, Rogers AH, Puliafito CA, Reichel E, et al. Intravitreal triamcinolone for refractory diabetic macular edema. Ophthalmology. 2002;109:920–7.
20. Jonas JB, Kreissig I, Degenring R. Intraocular pressure after intravitreal injection of triamcinolone acetonide. Br J Ophthalmol. 2003;87:24–7.
21. Michaelides M, Kaines A, Hamilton RD, Fraser-Bell S, Rajendram R, Quhill F, et al. A prospective randomized trial of intravitreal bevacizumab or laser therapy in the management of diabetic macular edema (BOLT study):12-month data. Report 2. Ophthalmology. 2010;117:1078–86.
22. Massin P. Safety and efficacy of ranibizumab in diabetic macular edema (RESOLVE study): a 12 month, randomized, controlled, double masked, muliticenter phase II study. Diabetes Care. 2010;33:2399–405.
23. Brown DM, Schmidt-Erfurth U, Do DV, Holz FG, Boyer DS, Midena E, et al. Intravitreal aflibercept for diabetic macular edema: 100-week results from the VISTA and VIVID studies. Ophthalmology. 2015;122:2044–52.
24. Sonoda S, Sakamoto T, Yamashita T, Otsuka H, Shirasawa M, Kakiuchi N, et al. Effect of intravitreal triamcinolone acetonide or bevacizumab on choroidal thickness in eyes with diabetic macular edema. Invest Ophthalmol Vis Sci. 2014;55:3979–85.
25. Laíns I, Figueira J, Santos AR, Baltar A, Costa M, Nunes S, et al. Choroidal thickness in diabetic retinopathy : the influence of anti-angiogenic therapy. Retina. 2014;34:1199–207.
26. Yiu G, Manjunath V, Chiu SJ, Farsiu S, Mahmoud TH. Effect of anti-vascular endothelial growth factor therapy on choroidal thickness in diabetic macular edema. Am J Ophthalmol. 2014;158:745–51.
27. Dillnger P, Mester U. Vitrectomy with removal of the internal limiting membrance in chronic diabetic macular oedema. Graefes Arch Clin Exp Opthalmol. 2004;242:630–7.
28. Otani T, Kishi S. A controlled study of vitrectomy for diabetic macular edema. Am J Opthalmol. 2002;134:214–9.
29. Lewis H, Abrams GW, Blumenkranz MS, Campo RV. Vitrectomy for diabetic macular traction and edema associated with posterior hyaloidal traction. Ophthalmology. 1992;99:753–9.
30. Figueroa MS, Contreras I, Noval S. Surgical and anatomical outcomes of pars plana vitrectomy of diffuse nontractional diabetic macular edema. Retina. 2008;28:420–6.
31. Massin P, Duguid G, Erginay A, Haouchine B, Gaudric A. Optical coherence tomography for evaluating diabetic macular edema before and after vitrectomy. Am J Opthalmol. 2003;135:169–77.
32. Funatsu H, Yamashita H, Ikeda T, Mimura T, Eguchi S, Hori S. Vitreous levels of interleukin-6 and vascular endothelial growth factor are related to diabetic macular edema. Ophthalmology. 2003;110:1690–6.
33. Lee DH, Kim JT, Jung DW, Joe SG, Yoon YH. The relationship between foveal ischemia and spectral-domain optical coherence tomography findings in ischemic diabetic macular edema. Invest Ophthalmol Vis Sci. 2013;7(54):1080–5.
34. Stefansson E, Landers 3rd MB, Wolbarsht ML. Vitrectomy, lensectomy, and ocular oxygenation. Retina. 1982;2:159–66.
35. Stefansson E, Landers 3rd MB, Wolbarsht ML. Increased retinal oxygen supply following pan-retinal photocoagulation and vitrectomy and lensectomy. Trans Am Ophthalmol Soc. 1981;79:307–34.

Swept Source OCT in Retinal Vein Occlusion

13

Mayss Al-Sheikh and SriniVas R. Sadda

Retinal vein occlusion (RVO) is the second-most-common retinal vascular disease after diabetic retinopathy [1]. Fluorescein angiography (FA), the current gold standard for diagnosis and management in retinal vascular diseases, provides excellent visualization of pathological alterations such as vessel leakage, non-perfusion, and neovascularization [2]. The assessment of microvasculature features and alterations using FA has been limited by the superimposition of various layers of capillary networks, as well as by capillary leakage [3]. Swept Source Optical coherence tomography angiography (SS-OCTA) is a new, noninvasive imaging modality that enables visualization of the retinal and choroidal vasculature based on isolation of motion signals (blood flow) from static (tissue) signals. Because of its high contrast and depth resolution, SS-OCTA can depict the capillary networks in specific retinal layers and allows the assessment of foveal avascular zone enlargement, capillary non-perfusion area, and vascular collateral formation. SS-OCTA *en face* images can be reviewed along with the structural B-scan SS-OCT to visualize changes such as increased retinal and choroidal thickness and intraretinal cysts and to correlate these with the microvascular changes visible on SS-OCTA.

13.1 SS-OCT Angiography Features in Vein Occlusion

High-density scanning of SS-OCTA can be used to identify the different vascular plexuses of the retina and the choroidal vasculature [4]. We can also observe features of vessel abnormalities that could not be detected using fluorescein angiography because of the dye leakage in the intermediate and late phases of the examination. SS-OCTA allows the detection of clinical features such as caliber changes, vessel tortuosity, vascular sheathing, alteration of the foveal microvascularization, and interruption of the capillary network.

13.1.1 Superficial Capillary Plexus

An enlargement of the foveal avascular zone (FAZ) can be observed based on capillary dropout with capillary non-perfusion areas around and outside the FAZ. Capillary non-perfusion is detected as regions of abrupt discontinuity of the capillary network. Vascular looping (Fig. 13.1), telangiectatic changes, collaterals, and focal dilations (microaneurysms) may all be identified with this technique.

Vessel wall staining on fluorescein angiography corresponds with a weak flow on SS-OCTA and may be visualized as a narrow vessel surrounded by a dark area that corresponds to the thickened vessel wall.

Macular cystoid spaces can also be seen by SS-OCTA as black, circular areas with no flow signal (Fig. 13.2). They have well-demarcated borders on the *en face* image.

13.1.2 Deep Capillary Plexus

The deep capillary plexus shows various alterations of the vasculature in RVO, including areas of non-perfusion with abrupt truncation of the capillary vessels and enlargement of the foveal avascular zone as a result of interruption of the parafoveal microcirculation (Figs. 13.1, 13.2 and 13.3). Collateral vessels may also be seen. Vascular congestion signs are mainly observed in the deep retinal plexus as dilated vessels with increased signal.

M. Al-Sheikh, MD
Doheny Image Reading Center, Doheny Eye Institute,
Los Angeles, California, United States

S.R. Sadda, MD (✉)
Department of Ophthalmology, David Geffen School of Medicine,
University of California Los Angeles,
Los Angeles, California, United States
e-mail: SSadda@doheny.org

© Springer International Publishing AG 2017

Z. Michalewska, J. Nawrocki (eds.), *Atlas of Swept Source Optical Coherence Tomography*,
DOI 10.1007/978-3-319-49840-9_13

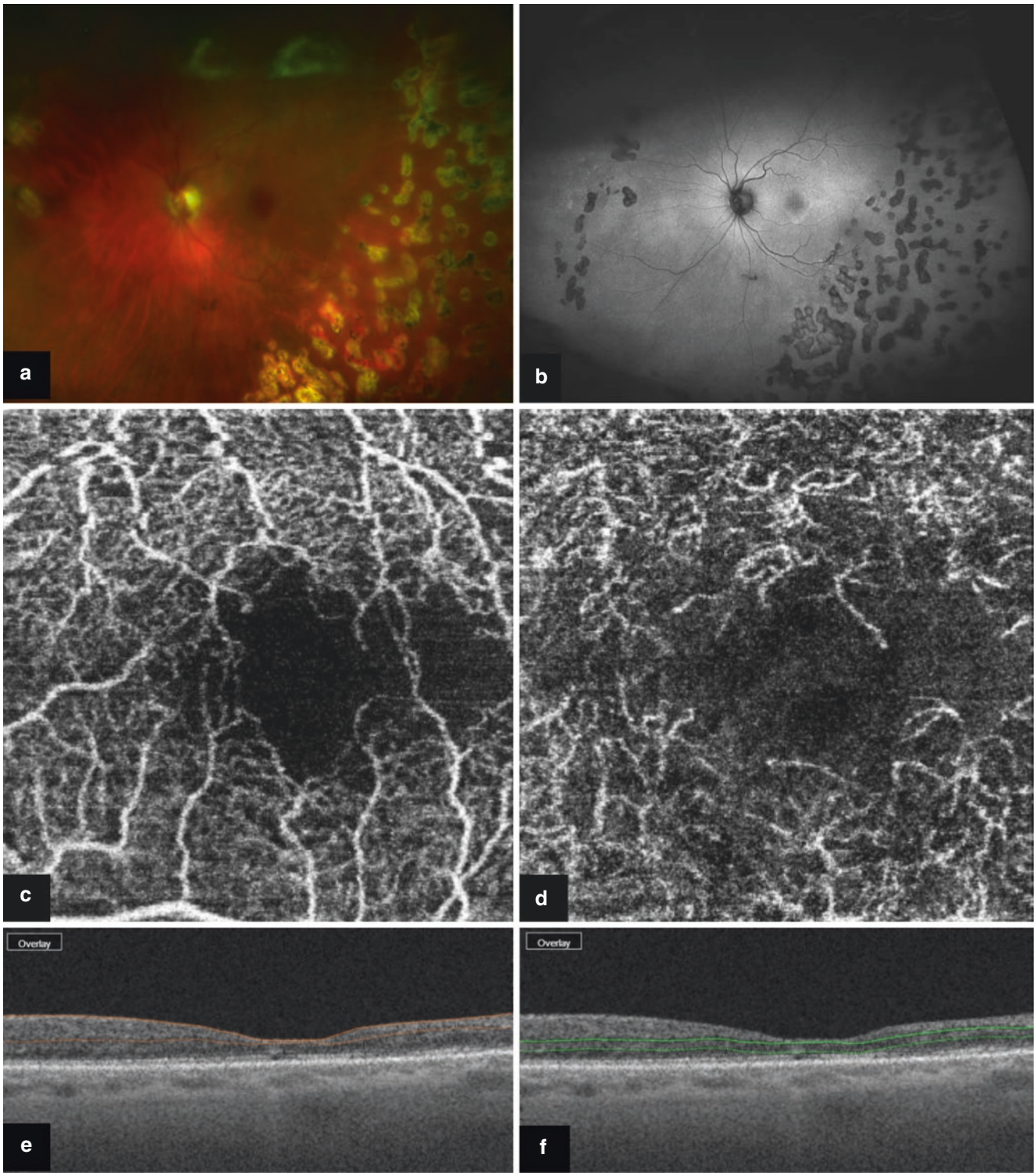

Fig. 13.1 Left eye of a 91-year-old woman with central retinal vein occlusion, first diagnosed 5 years ago, with a history of recurrent cystoid macular edema treated with multiple intravitreal anti-VEGF injections. (**a**) Color fundus photography. (**b**) Infra-red fundus image. (**c**) SS-OCTA of the superficial retinal layer with enlargement of the foveal avascular zone (FAZ) area and with capillary discontinuity perifoveally and temporal to the macula. (**d**) SS-OCTA of the deep retinal layer also shows an enlargement of the FAZ area, areas of capillary discontinuity, and dilation of superior macular capillaries with increased signal as a sign for vascular congestion. (**e**, **f**) Show the corresponding segmentation

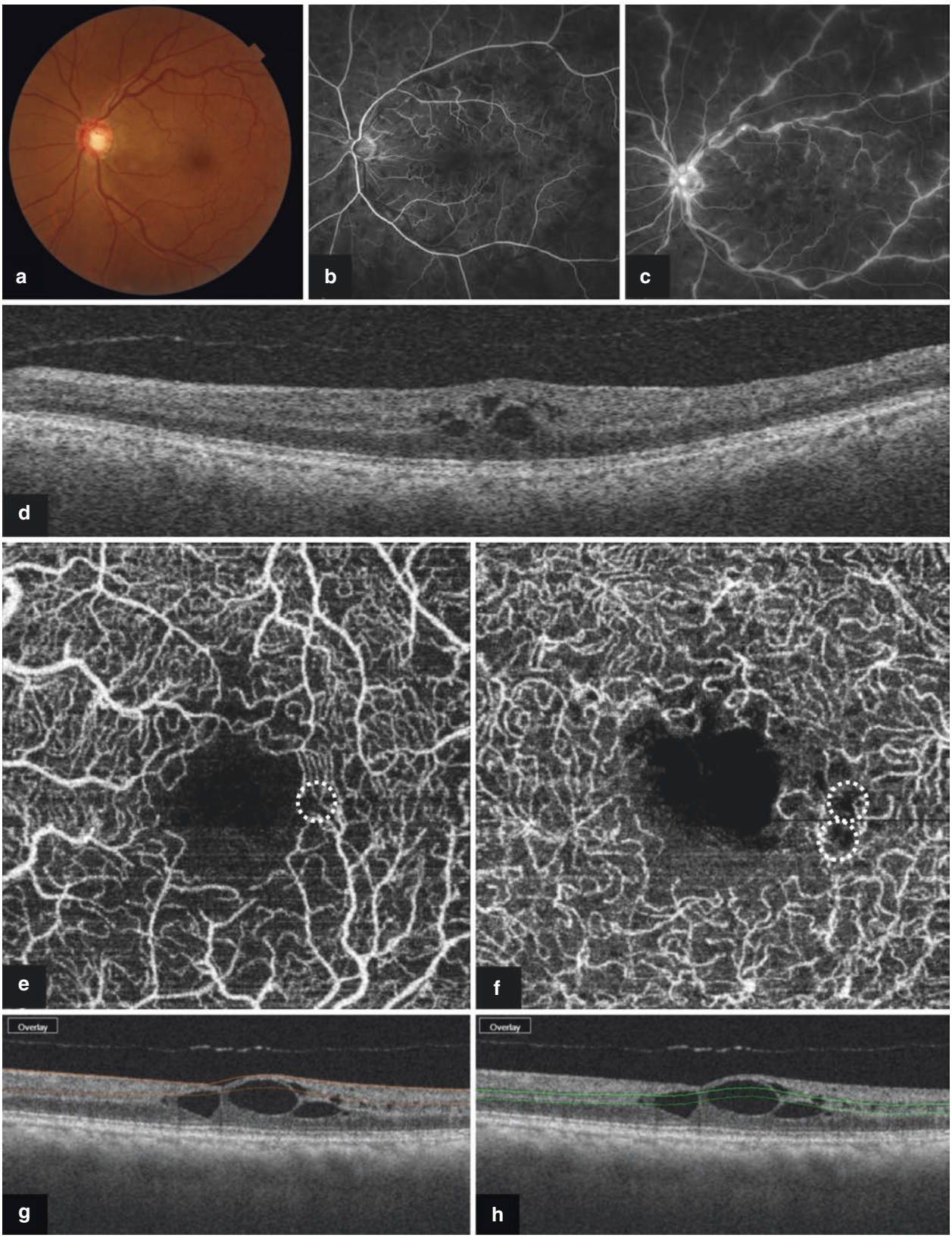

Fig. 13.2 A 56-year-old patient with central retinal vein occlusion in the left eye, which had first developed 1 year earlier. The patient has a history of recurrent macula edema treated with multiple anti-VEGF injections. (**a**) Color fundus photography. (**b**) Early and (**c**) late fluorescein angiography frames. (**d**) Structural optical coherence tomography (OCT) demonstrates cystoid macular edema. (**e**) SS-OCTA of the superficial retinal layer with enlargement of the foveal avascular zone (FAZ) area, capillary discontinuity and intraretinal cysts (*dashed circle*). (**f**) SS-OCTA of the deep retinal layer also shows an enlargement of the FAZ area, areas of capillary discontinuity and intraretinal cysts (*dashed circle*). (**g**, **h**) Show the corresponding slab segmentation

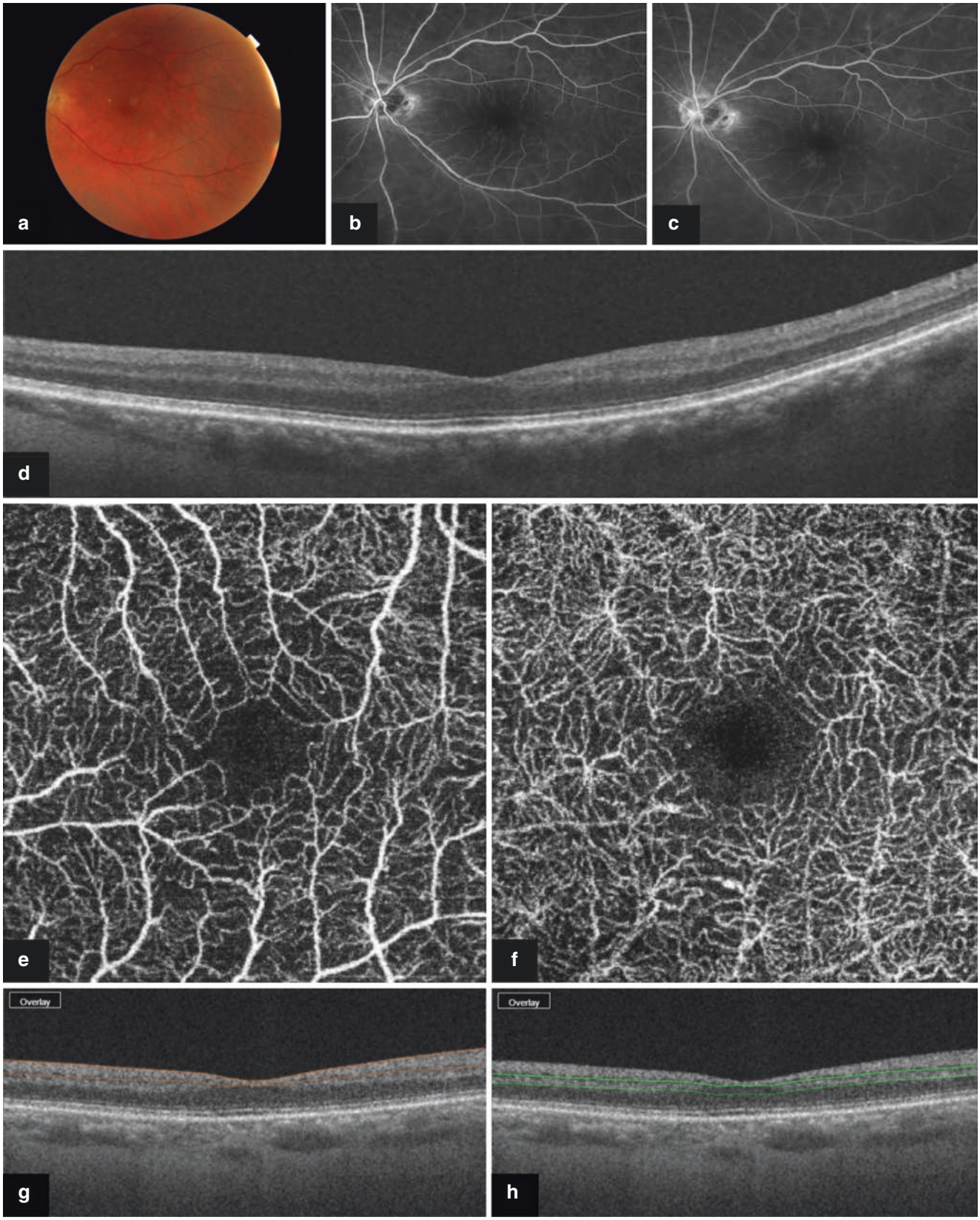

Fig. 13.3 A 79-year-old male with central retinal vein occlusion in the left eye. (**a**) Color fundus photography. (**b**) Early and (**c**) late fluorescein angiography frames. (**d**) Structural OCT. (**e**, **f**) SS-OCTA of the superficial and deep retinal layer with moderate enlargement of the foveal avascular zone area, some continuity of the perifoveal capillary network, and attenuation of the macular microvasculature. (**g**, **h**) Show the corresponding slab segmentation

13.2 Choroid

Changes in choroidal thickness in the eyes of patients with retinal vein occlusion have been previously described using enhanced depth imaging OCT. Tsuiki et al. [5], for example, observed increased choroidal thickness subfoveally in patients with central RVO, whereas others were only able to demonstrate increased choroidal thickness in the territory of the vascular occlusion. We have not observed significant alterations in the choriocapillaris or choroid by SS-OCTA in eyes with RVO; however, the edema from occlusion may cause a loss of signal that impairs the quality of the SS-OCTA.

13.3 Summary

In summary, the retinal microvascular alterations associated with RVO are well-demonstrated by SS-OCTA. Capillary non-perfusion can be detected in multiple layers, and previous reports have shown good correlation between SS-OCTA and FA [6].

These microvascular alterations can be quantified to more precisely describe the severity of the non-perfusion. An increase in the area of the FAZ was noted in the deep retinal layer but not in the superficial retinal layer of eyes with RVO, whereas decreased vessel density was observed in both the superficial and deep retinal layers [7]. Other morphological changes such as capillary dilation, as well as areas of non-flow, were present in the deep layer more frequently than in the superficial layer [8, 9].

One limitation of most current SS-OCTA systems is the relatively small field of view, as the best resolution scans are usually only 3 × 3 mm in size. Larger scans (9 × 9 mm or possibly 12 × 12 mm) still provide little more than a 30° field of view and sacrifice resolution for this size of field. Ultra-widefield SS-OCTA is not yet available, though larger fields may be studied by montaging multiple smaller cans together. Evaluation of larger and more peripheral regions of the retina by SS-OCTA are important goals for the future, as the extent of the peripheral non-perfusion has been shown to influence the severity of macular edema in patients with RVO [10].

References

1. Rehak M, Wiedemann P. Retinal vein thrombosis: pathogenesis and management. J Thromb Haemost. 2010;8:1886–94.
2. Coscas G, Loewenstein A, Augustin A, Bandello F, Battaglia Parodi M, Lanzetta P, et al. Management of retinal vein occlusion--consensus document. Ophthalmologica. 2011;226:4–28.
3. Mendis KR, Balaratnasingam C, Yu P, Barry CJ, McAllister IL, Cringle SJ, et al. Correlation of histologic and clinical images to determine the diagnostic value of fluorescein angiography for studying retinal capillary detail. Invest Ophthalmol Vis Sci. 2010;51:5864–9.
4. Spaide RF, Klancnik Jr JM, Cooney MJ. Retinal vascular layers imaged by fluorescein angiography and optical coherence tomography angiography. JAMA Ophthalmol. 2015;133:45–50.
5. Tsuiki E, Suzuma K, Ueki R, Maekawa Y, Kitaoka T. Enhanced depth imaging optical coherence tomography of the choroid in central retinal vein occlusion. Am J Ophthalmol. 2013;156:543–7.
6. Kuehlewein L, An L, Durbin MK, Sadda SR. Imaging areas of retinal nonperfusion in ischemic branch retinal vein occlusion with swept-source OCT microangiography. Ophthalmic Surg Lasers Imaging Retina. 2015;46:249–52.
7. Samara WA, Shahlaee A, Sridhar J, Khan MA, Ho AC, Hsu J. Quantitative optical coherence tomography angiography features and visual function in eyes with branch retinal vein occlusion. Am J Ophthalmol. 2016;166:76–83.
8. Coscas F, Glacet-Bernard A, Miere A, Caillaux V, Uzzan J, Lupidi M, et al. Optical coherence tomography angiography in retinal vein occlusion: evaluation of superficial and deep capillary plexa. Am J Ophthalmol. 2016;161:160–71.
9. Rispoli M, Savastano MC, Lumbroso B. Capillary network anomalies in branch retinal vein occlusion on optical coherence tomography angiography. Retina. 2015;35:2332–8.
10. Singer M, Tan CS, Bell D, Sadda SR. Area of peripheral retinal nonperfusion and treatment response in branch and central retinal vein occlusion. Retina. 2014;34:1736–42.

Swept Source OCT of Choroidal Nevi

14

Kunal K. Dansingani and K. Bailey Freund

Choroidal nevus is the most common type of intraocular tumor with an estimated prevalence of 6.5% and 1.4% in Caucasian and Asian populations, respectively [1]. Due to pigmentation, melanotic choroidal nevi are relatively opaque to internal examination under white light.

Imaging in the near-infrared, optical coherence tomography (OCT) achieves greater tissue penetration than technologies which use visible light, but is still hindered by the retinal pigment epithelium and by the melanin within nevi. Time domain and spectral domain OCT (SD-OCT) have therefore revealed much about secondary changes to tissues adjacent to choroidal nevi but relatively little about the internal structures of the nevi themselves, even with the addition of enhanced depth-imaging protocols.

Long wavelength swept source OCT (SS-OCT) achieves even greater tissue penetration than enhanced depth-imaging spectral domain OCT and, in the case of melanotic choroidal nevi, has been shown to be better than spectral domain OCT at demonstrating the internal features of nevi, such as blood vessels and granularity, as well as choriocapillaris abnormalities [2].

An additional benefit of SS-OCT is the higher scan speeds achieved as compared to SD-OCT. Although higher scan speeds compromise signal-to-noise ratio they allow for acquisition of dense raster patterns, providing volumetric reflectivity data that can then be segmented in various planes. *En face* segmentation of SS-OCT scans of choroidal nevi demonstrates tissue relationships *in vivo* that and fundus autofluorescence with earlier imaging modalities.

Figure 14.1 illustrates a subfoveal choroidal nevus in the right eye of a 65-year-old female. Color and red-free photography show associated drusen and fundus autofluorescence imaging shows mottled pigment epitheliopathy.

Cross-sectional SS-OCT shows anterior bowing of Bruch's membrane due to the bulk of the nevus, with an overlying shallow irregular pigment epithelial detachment with intermediately reflective contents. Extreme thinning of the residual choroid is noted over the temporal aspect of the nevus with distended vessels and choroidal thickening immediately adjacent to the nevus. One prominent vessel within the nevus substance appears to be a Haller vessel around which the nevus has grown.

En face segmentation of the volume scan data through the deep choroid shows the arrangement of enlarged choroidal vessels surrounding the nevus.

Figure 14.2 illustrates a subfoveal amelanotic choroidal nevus in the left eye of a 41-year-old male. Color and red-free photography show the amelanotic lesion and an area of altered coloration temporal to the lesion, corresponding with chronic shallow subretinal fluid. A horizontal cross-sectional SS-OCT line scan shows the distentive effects of the nevus on tissues related to it anteriorly, and related to the sclera posteriorly. Shallow neurosensory detachment is seen nasal to the nevus and ellipsoid loss is seen temporal to the nevus, presumed secondary to regressed chronic subretinal fluid. A shallow irregular pigment epithelial detachment is seen at the apex of the nevus, the contents of which are intermediately reflective.

The granularity of the nevus manifests as heterogeneous internal reflectivity. Dilated choroidal vessels are noted at the lateral borders of the nevus, with some vascular markings also

K.K. Dansingani, MA, FRCOphth (✉) • K.B. Freund, MD
Vitreous Retina Macula Consultants of New York,
New York, NY, USA
e-mail: kkd@doctor.com

© Springer International Publishing AG 2017
Z. Michalewska, J. Nawrocki (eds.), *Atlas of Swept Source Optical Coherence Tomography*,
DOI 10.1007/978-3-319-49840-9_14

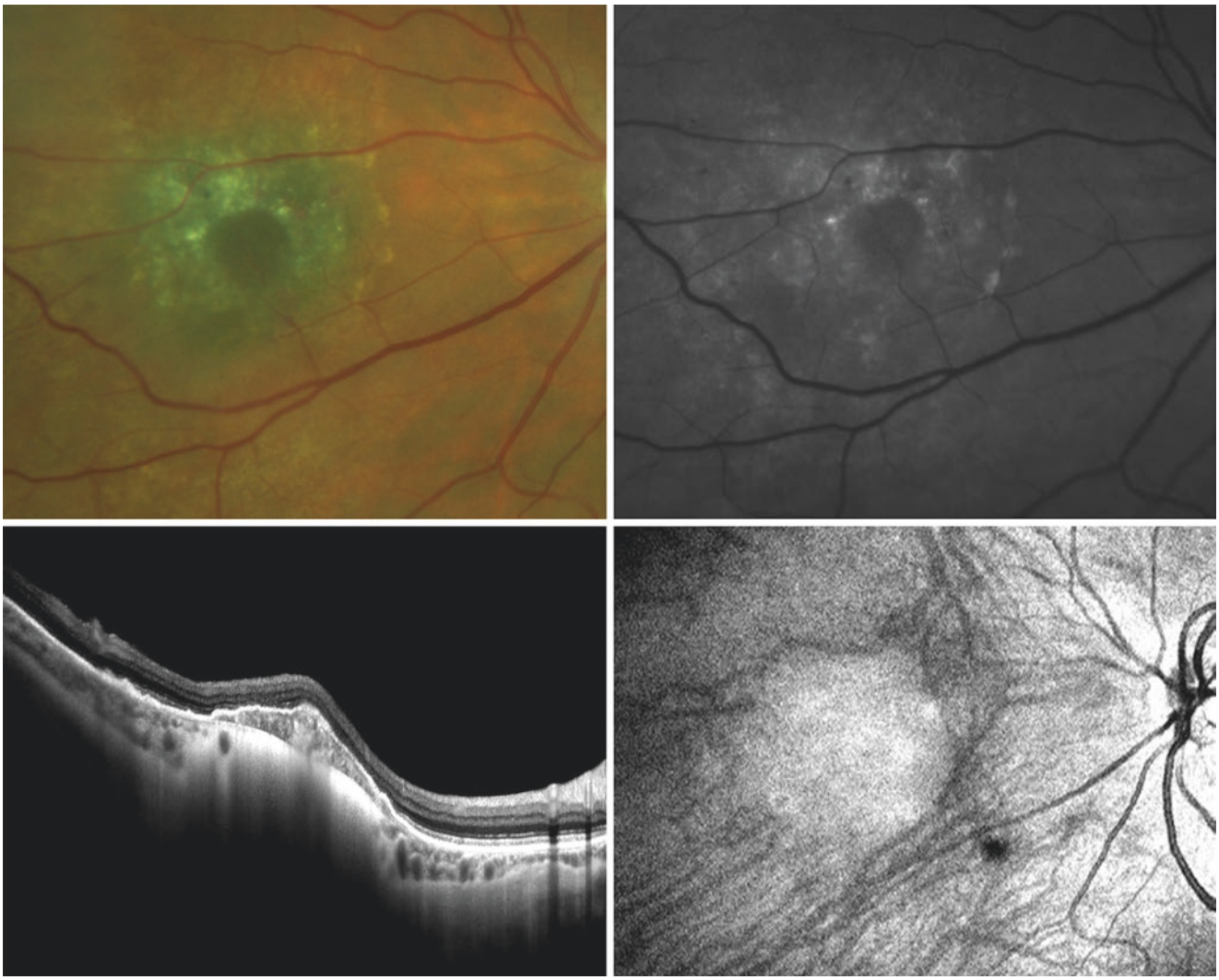

Fig. 14.1 Multimodal imaging of the right eye of a 65-year-old-female with melanotic choroidal nevus. *Top row*, Color and red-free photographs. *Lower left*, Horizontal SS-OCT line scan (12 mm) through the center of the nevus. *Lower right*, *En face* SS-OCT segmented at the level of the mid-choroid (12 × 9 mm)

visualized within the lesion. *En face* segmentation through the deep choroid reveals the diagonal orientation of these vessels, which appear to be draining toward the vortex veins.

The visualization of features intrinsic and related to amelanotic choroidal nevi in cross-sectional SS-OCT is similar to that achieved by SD-OCT. For melanotic lesions, the superior tissue penetration of long wavelength SS-OCT enables detection of features not seen by SD-OCT.

The morphology and significance of dilated Haller vessels with accompanying inner choroidal attenuation has been discussed previously in the context of chronic central serous chorioretinopathy and pachychoroid disease, and the finding of similar features localized to the immediate vicinity of choroidal nevi suggests that the space-occupying effects of the nevi can alter choroidal hemodynamics [3]. Additionally, shallow irregular pigment epithelial detachments have been shown with high probability to contain neovascular tissue in both age-related macular degeneration (AMD) and pachychoroid disease [4–6]. The clinical value of these observations in the context of choroidal nevi remains to be determined, and would require longitudinal study of large series.

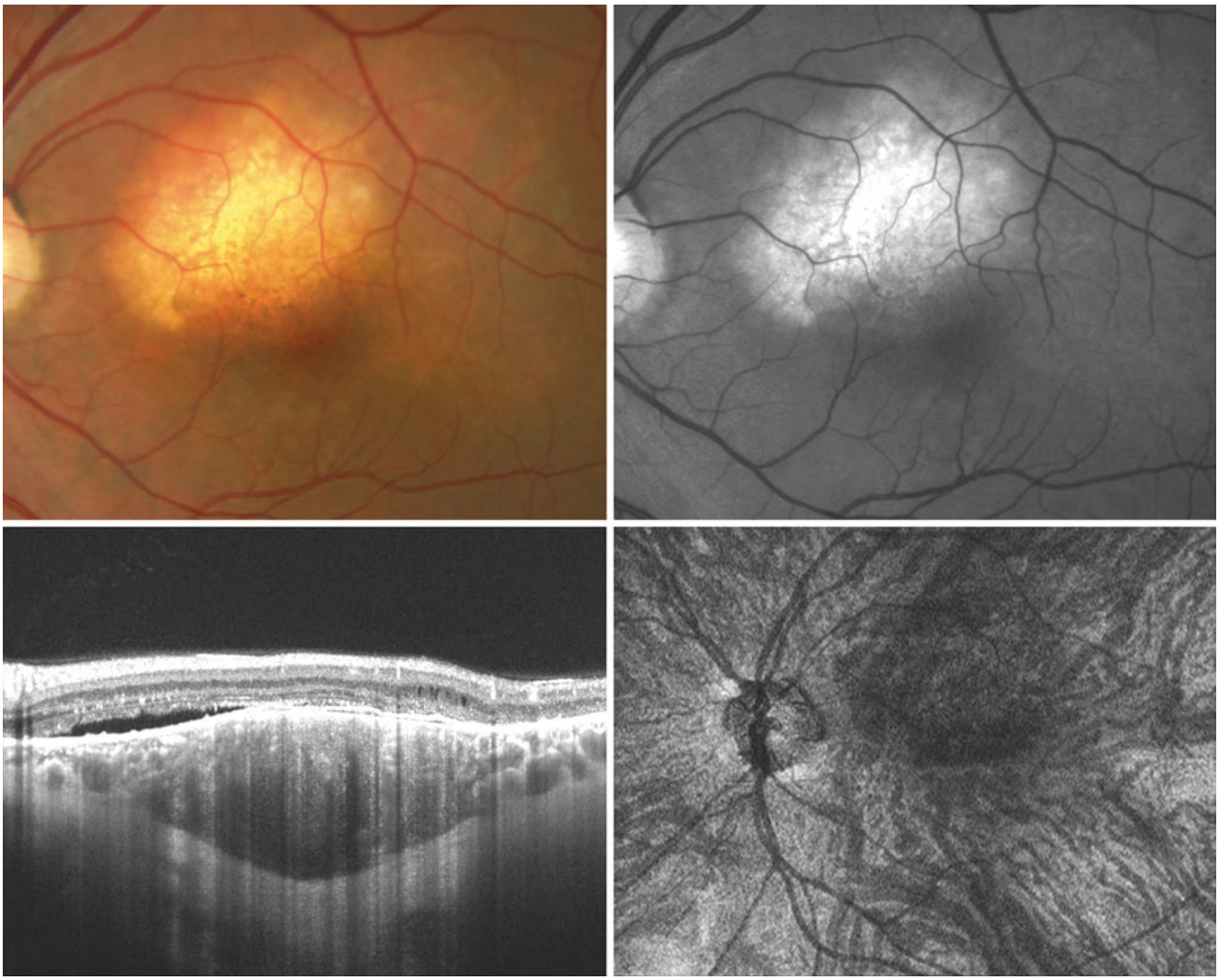

Fig. 14.2 Multimodal imaging of the left eye of a 41-year old male with amelanotic choroidal nevus. *Top row*, Color and red-free photographs. *Lower left*, Horizontal SS-OCT line scan (12 mm) through the center of the nevus. *Lower right*, *En face* SS-OCT segmented at the level of the mid-choroid (12 × 9 mm)

References

1. Qiu M, Shields CL. Choroidal nevus in the United States adult population: racial disparities and associated factors in the National Health and Nutrition Examination Survey. Ophthalmology. 2015; 122(10):2071–83.
2. Francis JH, Pang CE, Abramson DH, Milman T, Folberg R, Mrejen S, et al. Swept-source optical coherence tomography features of choroidal nevi. Am J Ophthalmol. 2015;159(1):169–76.
3. Dansingani KK, Balaratnasingam C, Naysan J, Freund KB. En face imaging of pachychoroid spectrum disorders with swept-source optical coherence tomography. Retina. 2015;6(3):499–516.
4. Spaide RF. Optical coherence tomography angiography signs of vascular abnormalization with antiangiogenic therapy for choroidal neovascularization. Am J Ophthalmol. 2015;160(1):6–16.
5. Kuehlewein L, Bansal M, Lenis TL, Iafe NA, Sadda SR, Bonini Filho MA, et al. Optical coherence tomography angiography of type 1 neovascularization in age-related macular degeneration. Am J Ophthalmol. 2015;160(4):739–48.
6. Dansingani KK, Balaratnasingam C, Klufas MA, Sarraf D, Freund KB. Optical coherence tomography angiography of shallow irregular pigment epithelial detachments in pachychoroid spectrum disease. Am J Ophthalmol. 2015;160(6):1243–54.

Intraocular Tumors Using Swept Source OCT

15

Ignacio Flores-Moreno, Luis Arias-Barquet, Josep M. Caminal, Jorge Ruiz-Medrano, and José M. Ruiz-Moreno

Swept source optical coherence tomography (SS-OCT) permits a complementary study of retinal and choroidal lesions and diseases, including intraocular tumors. Due to the longer wavelength (1050 nm) employed, SS-OCT allows the visualization of the internal configuration of the tumors, and even the extent of the lesion in small and medium tumors, up to a thickness of around 500 μm in pigmented lesions and up to 1600 μm in non-pigmented lesions [1, 2]. The high-quality images and resolution obtained with SS-OCT allow a better study of the tumors, helping at the time of diagnosis and showing complementary information such as intraretinal edema, subretinal fluid, photoreceptor atrophy, and retinal pigment epithelium (RPE) atrophy or detachments, which will guide physicians to the best treatment.

15.1 Choroidal Nevus

Choroidal nevus is a relatively frequent intraocular tumor, benign in nature and usually pigmented. SS-OCT shows a homogeneous, hyperreflective mass, clearly well-defined from the surrounding choroid and the choriocapillaris preserved (Fig. 15.1) [1]. RPE and ellipsoid zone are in most cases damaged, resulting in atrophy or irregularity of both layers [3, 4]. Drusen are usually present, and are clearly defined in the scan (Fig. 15.2). Three different configurations have been defined: "plateau," where the nevus has a distention in the sclera only; "dome," with a distention into the retina only; and the most common configuration, "almond," where the lesion presses both the retina and the sclera [3].

I. Flores-Moreno, MD, PhD
Clínico San Carlos University Hospital, Madrid, Spain

Bellvitge University Hospital, Hospitalet de Llobregat, Barcelona, Spain

L. Arias-Barquet, MD, PhD • J.M. Caminal, MD, PhD
Bellvitge University Hospital, Hospitalet de Llobregat, Barcelona, Spain

J. Ruiz-Medrano, MD (✉)
Clínico San Carlos University Hospital, Madrid, Spain
e-mail: jorge.ruizmedrano@gmail.com

J.M. Ruiz-Moreno, MD, PhD
Castilla La Mancha University, Albacete, Spain

© Springer International Publishing AG 2017
Z. Michalewska, J. Nawrocki (eds.), *Atlas of Swept Source Optical Coherence Tomography*,
DOI 10.1007/978-3-319-49840-9_15

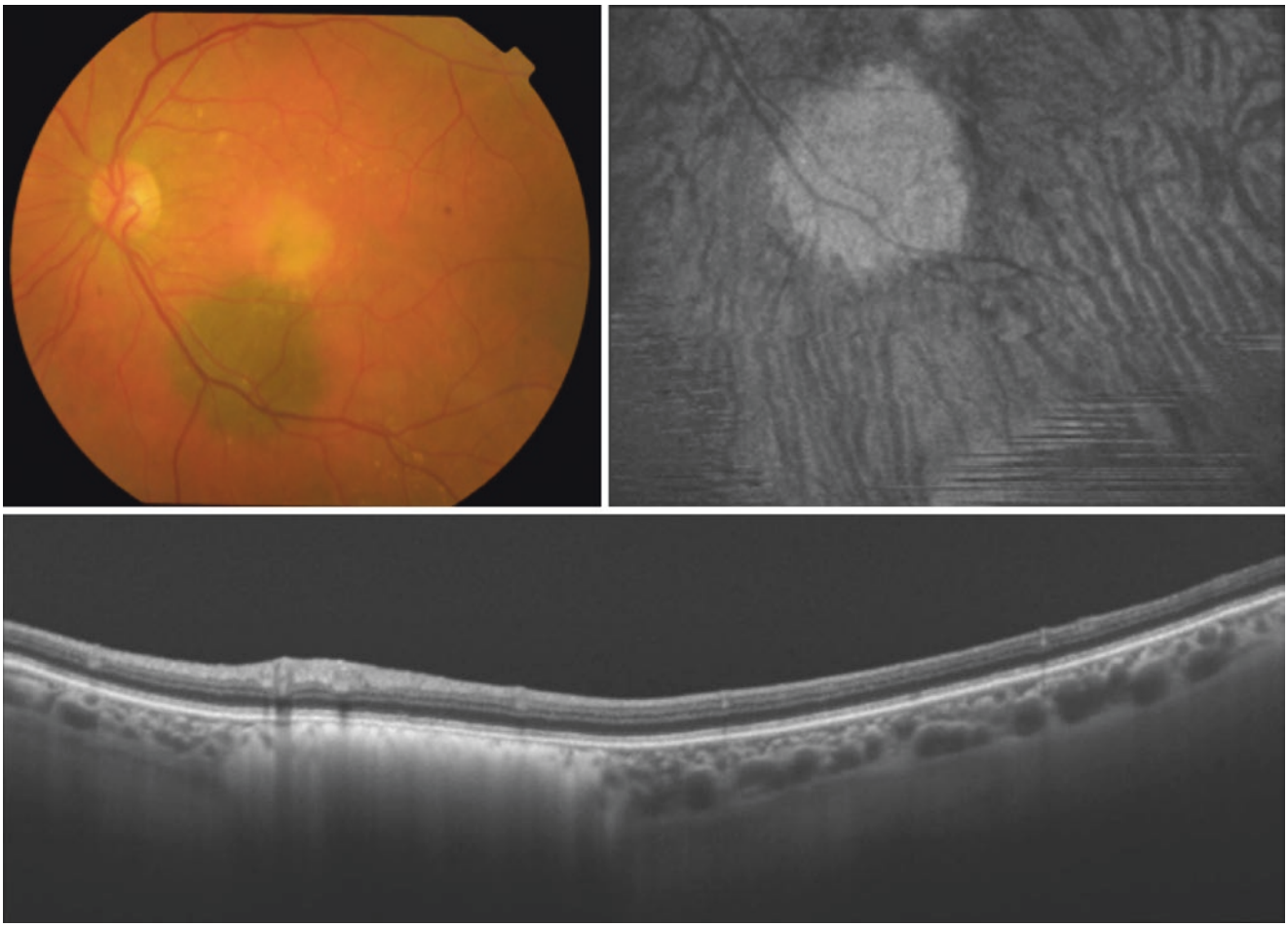

Fig. 15.1 A choroidal nevus located at the inferior temporal arcade is shown in the fundus photograph (*top left*). *En face* SS-OCT shows a hyperreflective lesion, perfectly delimited from the surrounding choroid (*top right*). B-scan SS-OCT shows a homogeneous, hyperreflective mass, with the choriocapillaris preserved

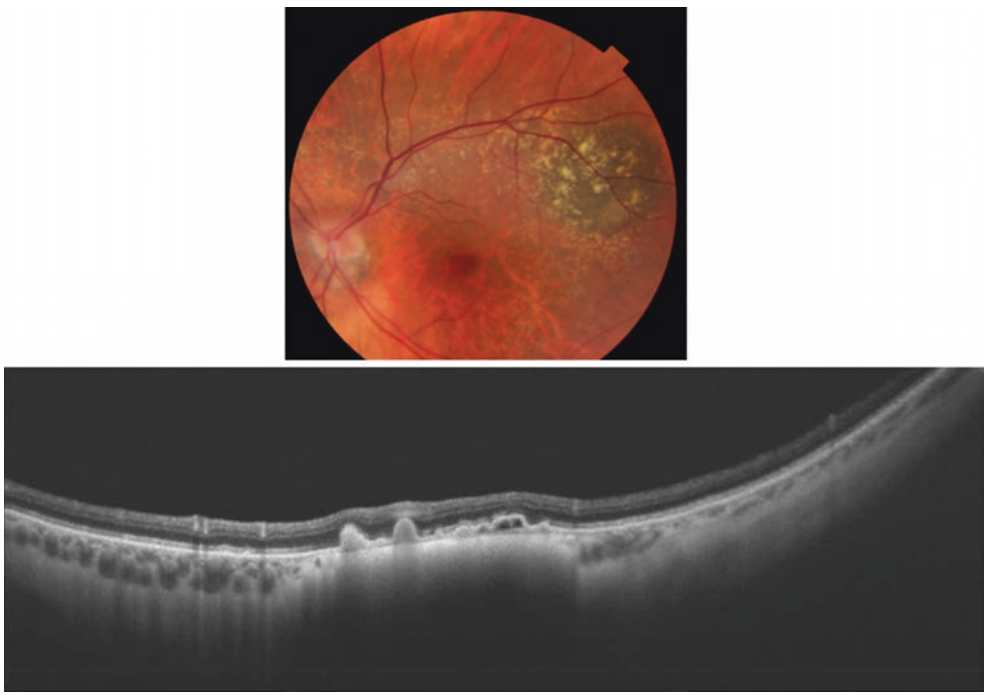

Fig. 15.2 Several drusen over the choroidal nevus are clearly defined in the fundus and SS-OCT B-scan

15.2 Choroidal Nevus with Risk Factors for Growth

Choroidal nevus can turn into choroidal melanoma. Shields et al. [5] described eight clinical signs and features that predict malignant transformation of nevus, including thickness over 2 mm, subretinal fluid, symptoms, orange pigment, tumor proximity to optic nerve, ultrasound hollowness, halo absent, and drusen absent. These lesions show intermediate features between nevus and melanoma using SS-OCT. They have more regular internal structure than melanoma, but the choriocapillaris is not visible in most patients, whereas it is visible in nevus (Figs. 15.3 and 15.4) [1].

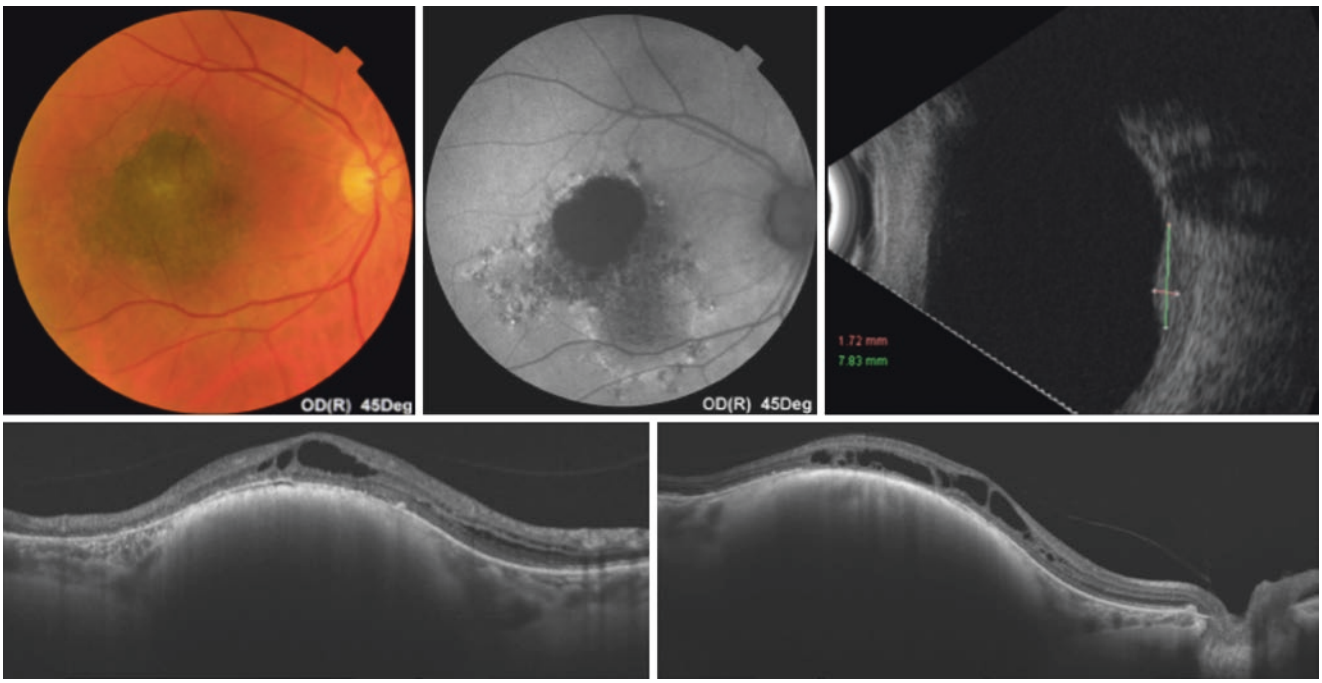

Fig. 15.3 Choroidal nevus with risk factors for growth at the posterior pole (*top left*). A patch of RPE and areas of hyper/hypo-autofluorescence is shown in the autofluorescence image (*top middle*). B-mode of ultrasound shows a lesion thinner than 2 mm (*top right*). B-scan SS-OCT presents intraretinal chronic cysts in vertical scan (*bottom left*) and horizontal scan (*bottom right*). An RPE alteration in the center of the lesion, with most of the choriocapillaris disappeared. The intrinsic features of the tumor show a hyperreflective lesion with some hyporeflective areas along the nevus, with corresponding shadowing

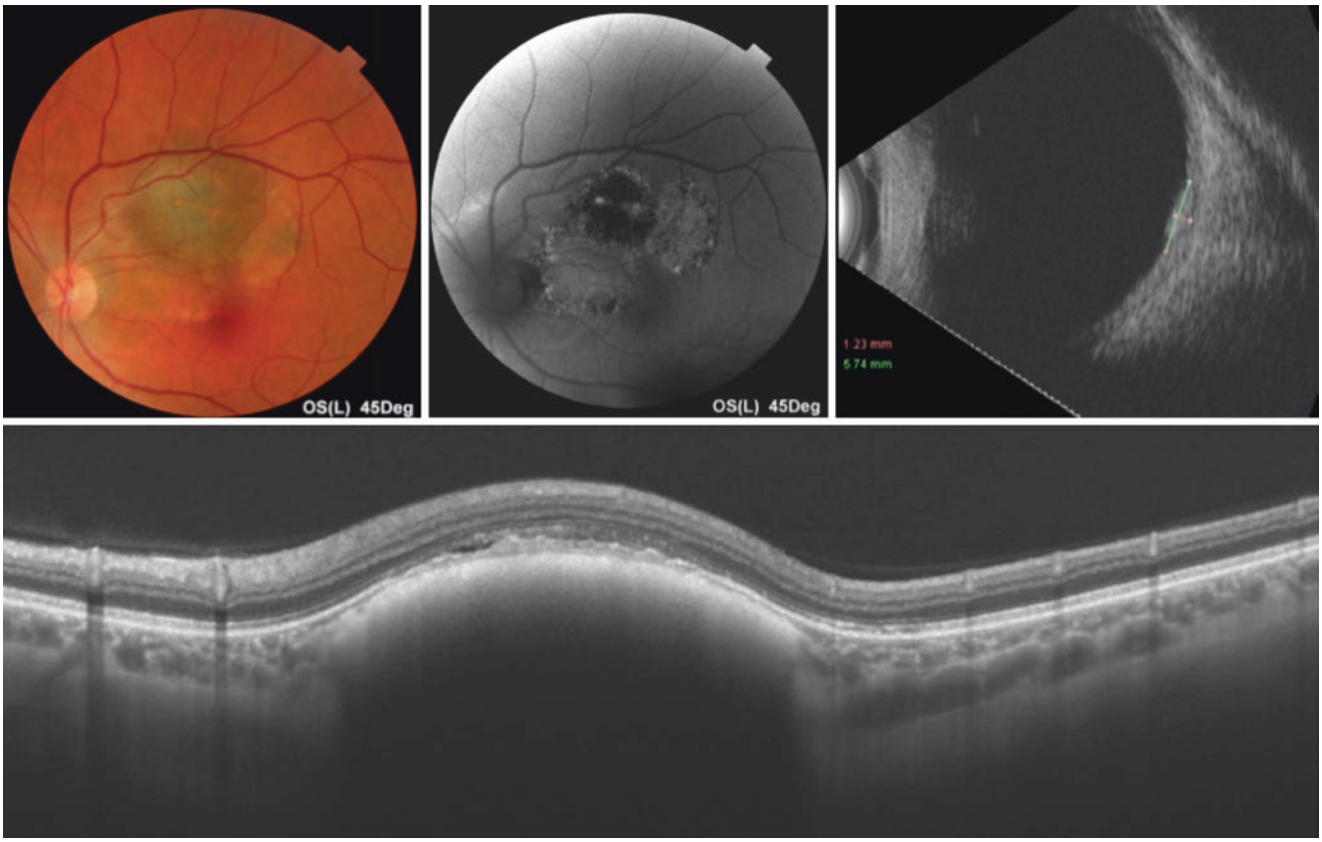

Fig. 15.4 Pigmented lesion located at the superior temporal arcade, with orange pigmentation and chronic subretinal fluid (*top left*). Autofluorescence image shows a patch of RPE atrophy and areas of hyper/hypo-autofluorescence (*top middle*). B-mode of ultrasound shows a small lesion thinner than 1.5 mm (*top right*). Outer retina alterations associated to subretinal fluid and RPE undulation are the retinal changes observed. Choriocapillaris layer is preserved along the full hyperreflective lesion, which can be clearly differentiated from the healthy choroid

15.3 Choroidal Melanoma

Imaging choroidal melanoma presents a lesion with a dome-shaped configuration with highly reflective lesion, deep optical shadowing, subretinal fluid, and shaggy photoreceptors [5, 6]. The tumor compresses the choriocapillaris in 100% of cases, resulting in an invisible choriocapillaris in SS-OCT scans [1]. Melanomas have a heterogeneous configuration on SS-OCT (Fig. 15.5), and irregularities are always present in the internal space, which differentiates from choroidal nevus that are homogeneous in their configuration (Fig. 15.6).

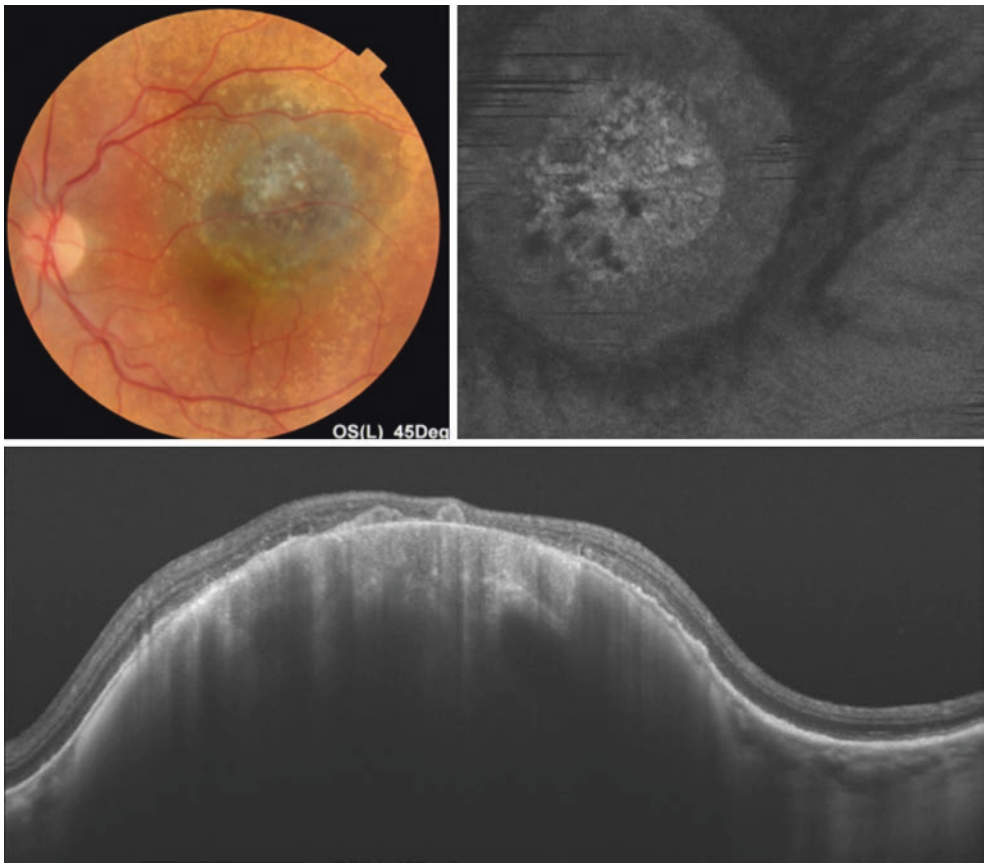

Fig. 15.5 Choroidal melanoma located at the posterior pole (*top left*). *En face* SS-OCT (*top right*) shows two areas clearly differentiated, an outer halo with a homogeneous pattern and a circular central hyperreflective area with hyporeflective lacunae. B-scan SS-OCT (*bottom*) presents an atrophic retina thickness with retinal pigment epithelium atrophy, no choriocapillaris preservation and a dome-shape lesion with hyper/hyporeflective areas

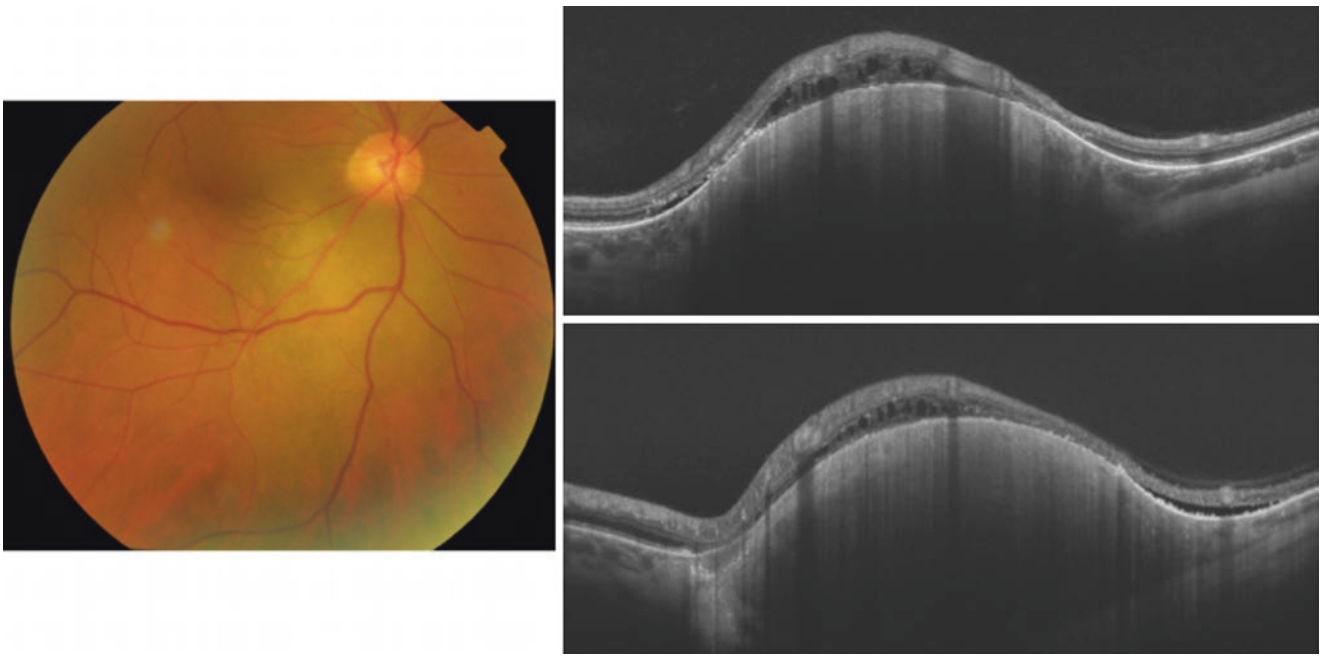

Fig. 15.6 Choroidal melanoma inferior to the optic nerve, which has been previously treated with brachytherapy. Chronic retinal edema and subretinal fluid is noticed in SS-OCT B-scan. Retinal pigment epithelium is shown as an irregular hyperreflective line, and choriocapillaris cannot be distinguished. The melanoma has a homogeneous configuration although some irregularities are present in the internal space

15.4 Choroidal Metastasis

Choroidal metastasis originates most frequently from lung or breast carcinoma, usually affecting the posterior pole and a profuse exudative retinal detachment. SS-OCT scans show a dome-shaped or "lumpy-bumpy" mass with low internal reflectivity, well delimitated from the surrounding choroid and with irregular clumps, compression of the overlaying choriocapillaris, and posterior shadowing (Fig. 15.7) [1, 5].

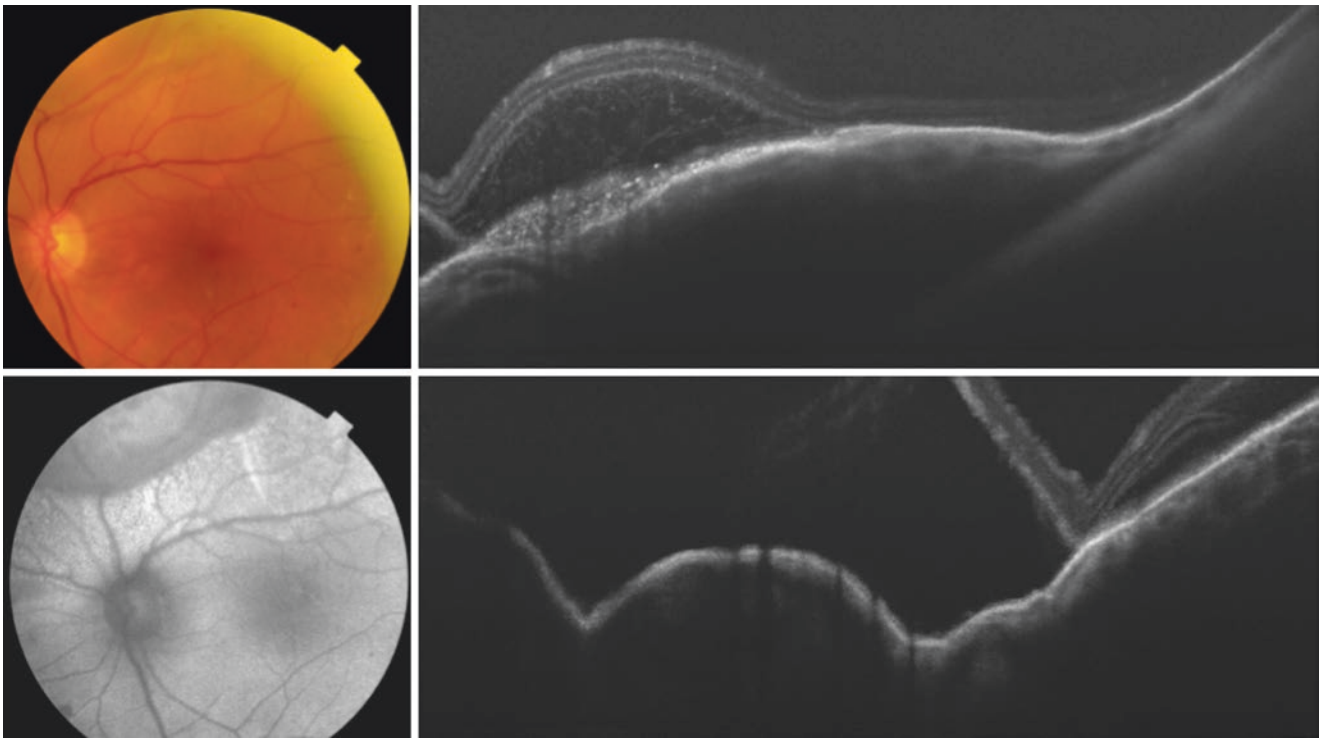

Fig. 15.7 Choroidal metastasis from lung cancer is shown as an amelanotic, yellow mass, with an extensive exudative retinal detachment (*top left*). SS-OCT B-scan shows a lesion with a "lumpy-bumpy" configuration, low internal reflectivity, and irregular clumps

15.5 Circumscribed Choroidal Hemangioma

Choroidal hemangioma is a benign, vascular tumor, round or oval in configuration and orange-red in appearance. The study of this lesion with SS-OCT shows a dome-shaped configuration with preservation of the choriocapillaris and expanded vascular spaces in the interior of the mass, which resemble a sponge-like pattern (Figs. 15.8 and 15.9). The lesion can be clearly differentiated from the surrounding choroidal vessels [1, 2, 5].

En face SS-OCT permits a coronal view of the lesion. A multilobular pattern, similar to a honeycomb or a sponge—with hyporeflective, confluent, round, or oval vascular spaces, and hyperreflective zones, presumably the vessel walls and connective tissue of the tumor—can be differentiated in the *en face* scan (Fig. 15.10). This rapid, non-invasive method helps us differentiate choroidal hemangioma from other tumors [2].

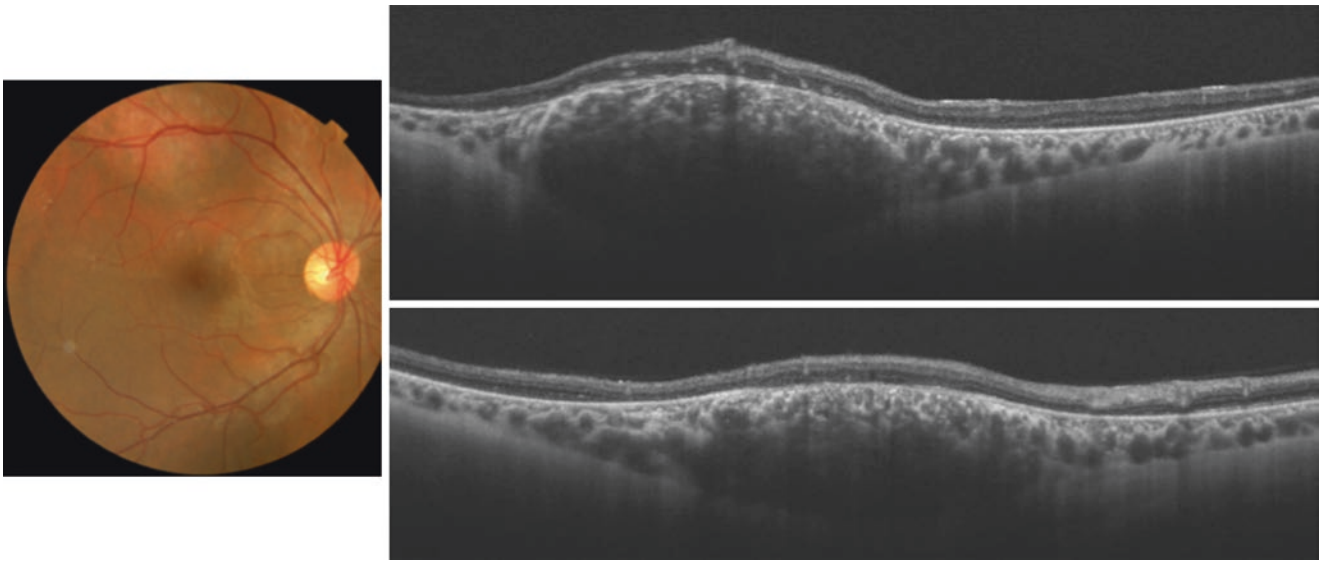

Fig. 15.8 Circumscribed choroidal hemangioma located at the superior temporal arcade. Vertical (*top right*) and horizontal (*bottom right*) SS-OCT B-scan shows a dome-shaped configuration with preservation of the choriocapillaris and expanded vascular spaces in the interior of the tumor, in a "sponge"-like pattern. The lesion can be perfectly defined in size

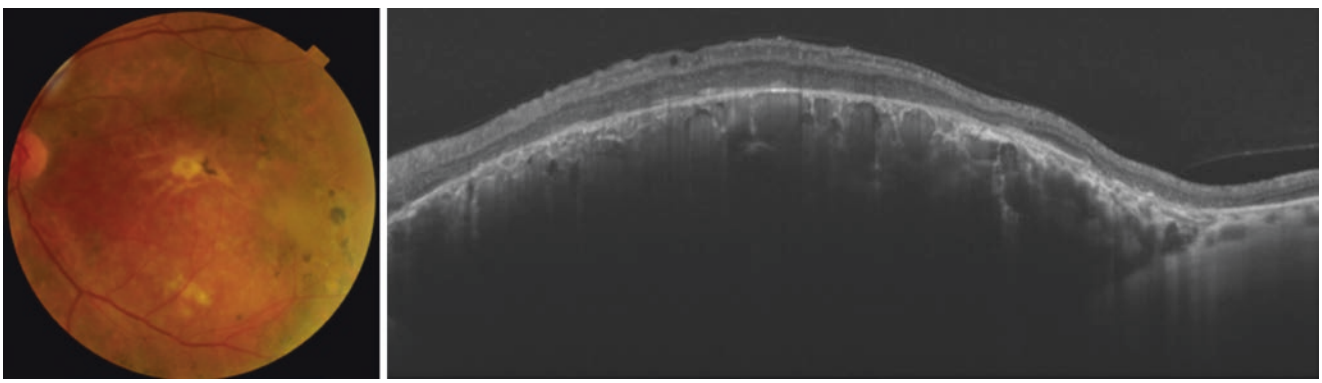

Fig. 15.9 Circumscribed choroidal hemangioma after photodynamic therapy. SS-OCT B-scan shows long vascular spaces across the lesion

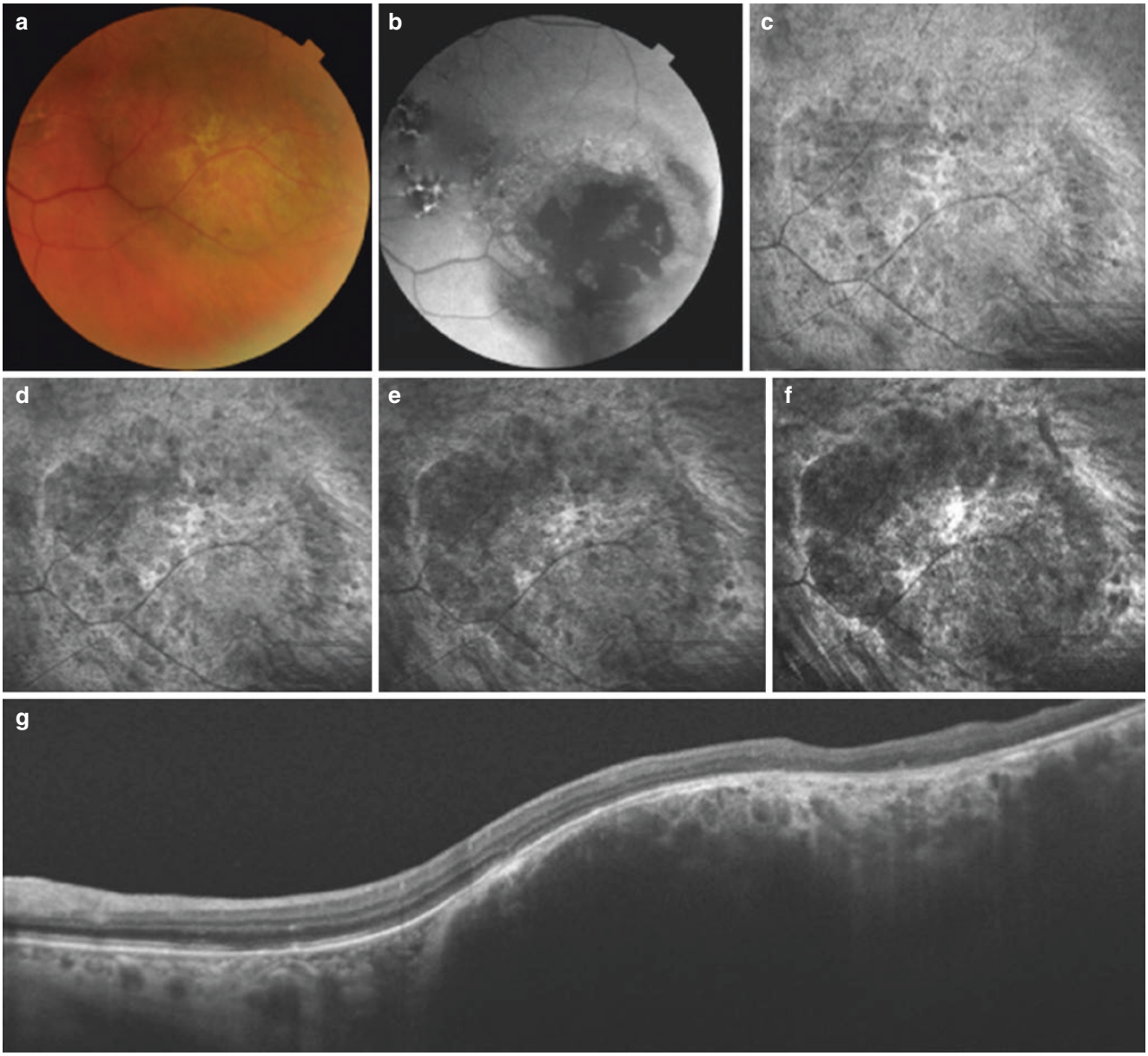

Fig. 15.10 Multimodal imaging of circumscribed choroidal hemangioma. (**a**) Color fundus showing the circumscribed choroidal hemangioma at the superior temporal arcade. (**b**) Autofluorescence image with retinal pigment epithelium atrophy and changes around the lesion. (**c**, **d**) *En face* SS-OCT images from the inner zone of the tumor (**c**) to deeper zone (**d**). (**e**, **f**) A multi-lobular pattern, or "honeycomb" pattern, is seen in the images (**e**), and an enlargement of the vascular spaces from the inner to the outer zone of the tumor is observed (**f**). (**g**) SS-OCT B-scan across the tumor showing the enlargement of the vascular spaces

References

1. Filloy A, Caminal JM, Arias L, Jordán S, Català J. Swept source optical coherence tomography imaging of a series of choroidal tumours. Can J Ophthalmol. 2015;50:242–8.
2. Flores-Moreno I, Caminal JM, Arias-Barquet L, Rubio-Caso MJ, Catala-Mora J, Vidal-Martí M, et al. En face mode of swept-source optical coherence tomography in circumscribed choroidal haemangioma. Br J Ophthalmol. 2016;100:360–4.
3. Francis JH, Pang CE, Abramson DH, Milman T, Folberg R, Mrejen S, et al. Swept-source optical coherence tomography features of choroidal nevi. Am J Ophthalmol. 2015;159:169–76.
4. Shields CL, Pellegrini M, Ferenczy SR, Shields JA. Enhanced depth imaging optical coherence tomography of intraocular tumors: from placid to seasick to rock and rolling topography—the 2013 Francesco Orzalesi Lecture. Retina. 2014;34:1495–512.
5. Shields CL, Manalac J, Das C, Ferguson K, Shields JA. Choroidal melanoma: clinical features, classification, and top 10 pseudomelanomas. Curr Opin Ophthalmol. 2014;25:177–85.
6. Torres VLL, Brugnoni N, Kaiser PK, Singh AD. Optical coherence tomography enhanced depth imaging of choroidal tumors. Am J Ophthalmol. 2011;151:586–93.

Intraocular Inflammation

16

Roberto Gallego-Pinazo, Rosa Dolz-Marco,
Enrique España-Gregori, and Alejandro Fonollosa

Intraocular inflammatory diseases, especially posterior uveitis, are associated with a variety of retinal morphometric changes. Optical coherence tomography (OCT), given its high sensitivity in terms of finding any vitreomacular, retinal, or choroidal disturbance, has become an essential tool in the evaluation of patients with uveitis.

With the new high-penetration swept source OCT (SS-OCT) technology, the choroidal tissue can be analyzed easily, even in the presence of preretinal or intraretinal moderately hyperreflective lesions. Thus, a complete map of macular choroidal thickness may be obtained to evaluate a certain case or even to monitor the therapeutic response of the choroid [1]. OCT can establish the diagnosis of a certain etiology based on pattern recognition of typical characteristics and hallmark features. The main tomographic signs associated with uveitis can be classified into vitreomacular interface, retinal and choroidal thickness changes, and qualitative retinal and retinal pigment epithelium changes.

The present chapter aims to summarize the main SS-OCT changes in patients with intraocular inflammation: vitreomacular interface abnormalities; uveitic macular edema; inflammatory choroidal neovascularization; and a myriad of other retinal changes [2–4].

R. Gallego-Pinazo, MD (✉) • R. Dolz-Marco, MD, PhD
Unit of Macula, Department of Ophthalmology,
University and Polytechnic Hospital La Fe, Valencia, Spain
e-mail: robertogallego@comv.es

E. España-Gregori, MD
Department of Ophthalmology, Faculty of Medicine,
University of Valencia, Valencia, Spain

A. Fonollosa, MD, PhD
Department of Ophthalmology, BioCruces Health Research Institute,
Cruces University Hospital, Vizcaya, Spain

© Springer International Publishing AG 2017
Z. Michalewska, J. Nawrocki (eds.), *Atlas of Swept Source Optical Coherence Tomography*,
DOI 10.1007/978-3-319-49840-9_16

16.1 Vitreomacular Interface Abnormalities in Patients with Uveitis

The swept source OCT imaging achieves a 12 mm-length scanning area. This is of great relevance in the assessment of the status of vitreomacular interface abnormalities. Besides the conventional vitreomacular adhesions and vitreomacular tractions (Fig. 16.1), patients with intraocular inflammation are at a higher risk of developing secondary epiretinal membranes (Fig. 16.2) [5].

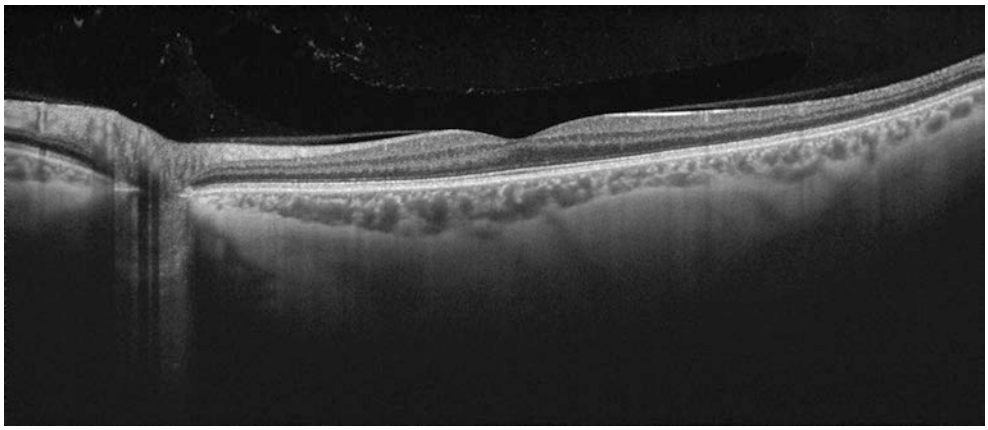

Fig. 16.1 Subclinical broad vitreomacular adhesion in a 34-year-old female with pars planitis. Visual acuity was 20/25

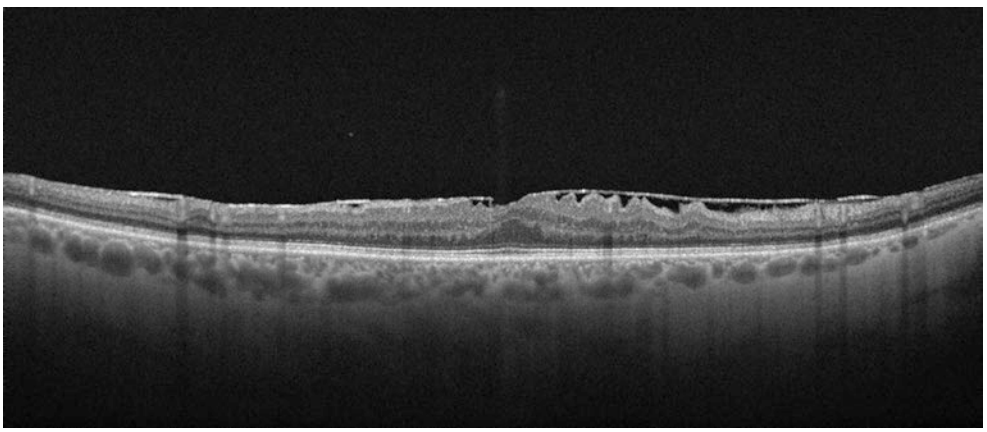

Fig. 16.2 Epiretinal membrane in a 56-year-old male with Eales disease treated with pan-retinal photocoagulation. Visual acuity was 20/40

16.2 Uveitic Macular Edema

Morphometric macular changes can be easily observed and analyzed with SS-OCT. More than this, the follow-up of such changes makes it possible to reliably monitor the therapeutic response to any treatment administered with high precision.

Increased macular thickness in patients with uveitis may appear as one of three different patterns in SS-OCT images [6–10].

16.2.1 Diffuse Macular Thickening

Diffuse macular thickening is the most frequent pattern of uveitic macular edema, accounting for 55% of these cases. It is characterized by increased retinal thickness with disturbance of the layered retinal structure, or sponge-like low reflective areas, without intraretinal cystoid cavities, within the thickened area (Fig. 16.3).

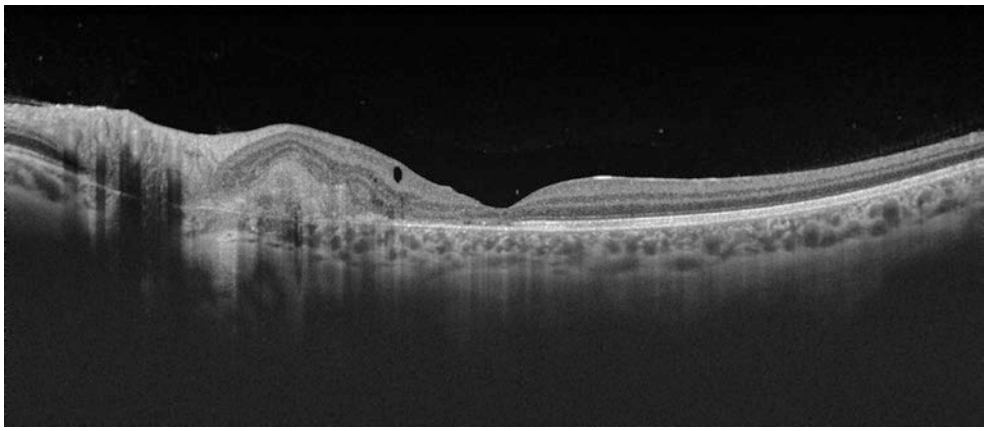

Fig. 16.3 Diffuse macular thickening associated with inflammatory juxtapapillary choroidal neovascularization in a 29-year-old female. Visual acuity was 20/30

16.2.2 Cystoid Macular Edema

Cystoid macular edema is present in up to 25% of cases of uveitic macular edema. Although it is usually associated with diffuse macular thickening, the presence of intraretinal cystoid spaces is associated with worse visual prognosis when compared to pure diffuse thickenings (Fig. 16.4). The response to local and systemic therapies of cystoid macular edema is usually good, but recurrences are frequent throughout the follow-up. Although basically any intraocular inflammatory disease may associate cystoid macular edema, this is a typical feature of Birdshot choroidopathy [11, 12] and juvenile idiopathic arthritis [13].

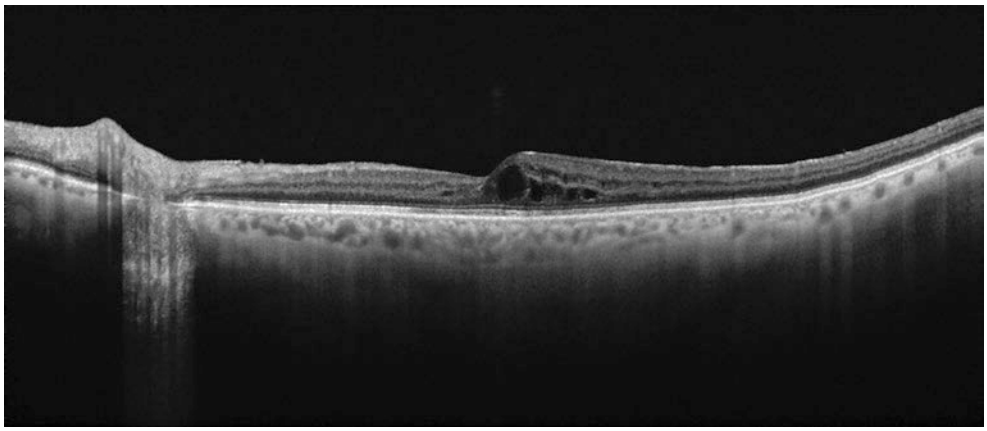

Fig. 16.4 Foveal cystoid macular edema in a 62-year-old female with chronic Birdshot choroidopathy. Visual acuity was 20/40

16.2.3 Subretinal Fluid

The presence of fluid between the photoreceptors and the retinal pigment epithelium is infrequent in patients with uveitis, accounting for 6% of all cases. However, the detection of subretinal fluid has a relevant prognostic impact, as it is the macular edema pattern associated with the worst visual outcome; therefore, therapeutic interventions should be considered immediately after diagnosing its presence (Fig. 16.5). Vogt-Koyanagi-Harada disease is characterized by a particular appearance of large subretinal fluid spaces fenestrated by fibrinous tissue associated with a significant increase of choroidal thickness; both findings respond to systemic steroid-intensive therapy. Other entities that may exhibit subretinal fluid in the SS-OCT images are posterior scleritis [14], sympathetic ophthalmia [15], and neuroretinitis, among others [16].

In addition, choroidal involvement by granulomatous diseases (Fig. 16.6) or lymphoproliferative disorders may also induce serous retinal detachment (Figs. 16.7 and 16.8).

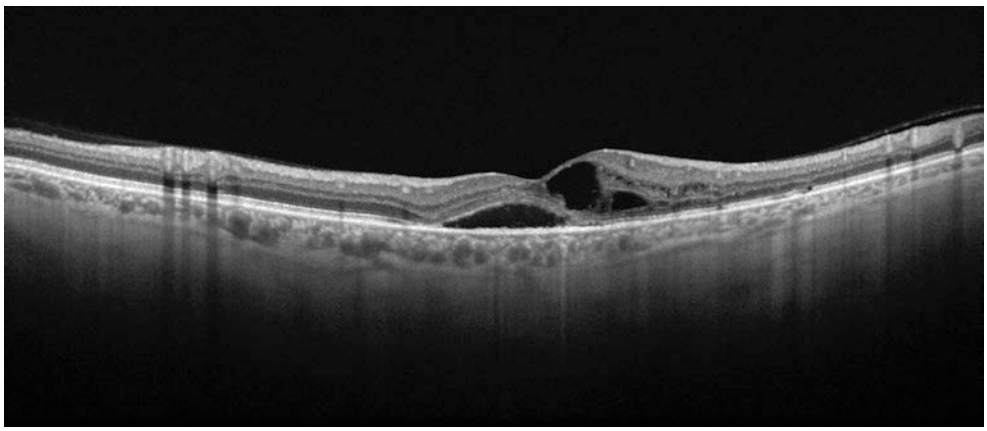

Fig. 16.5 Subfoveal fluid associated with cystoid macular edema in a 38-year-old patient with posterior scleritis. Visual acuity was 20/6

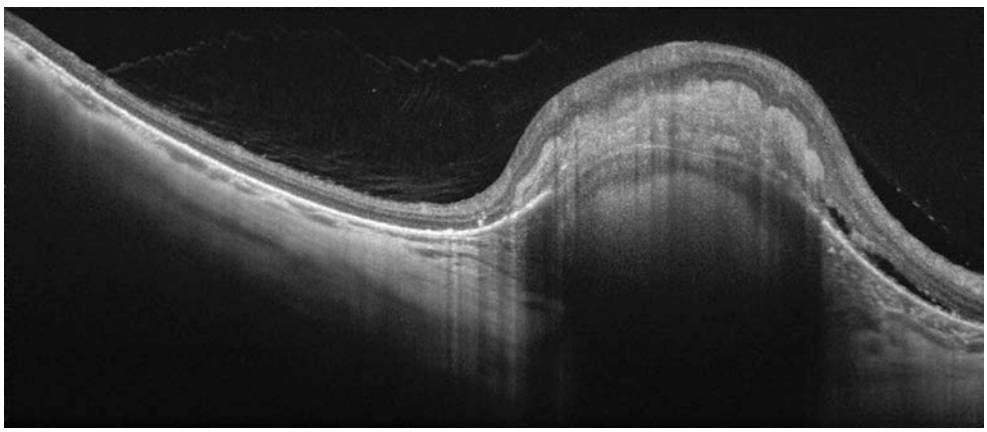

Fig. 16.6 Subretinal fluid secondary to tuberculous choroidal granuloma in a 27-year-old male with miliary tuberculosis. Visual acuity was 20/20

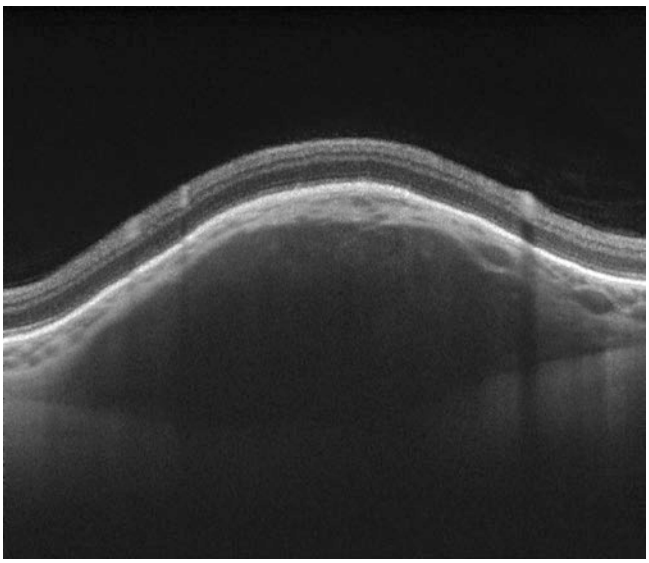

Fig. 16.7 Focal choroidal lesion in a 62-year-old male with systemic follicular lymphoma. Visual acuity was 20/20

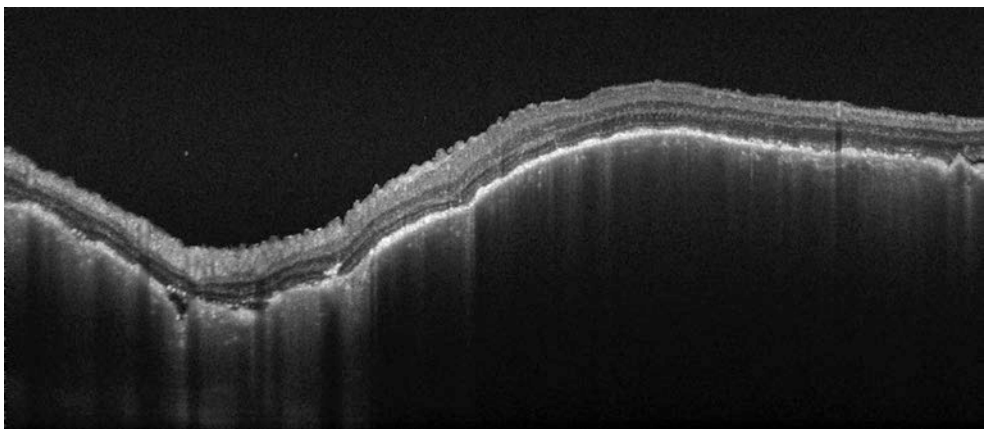

Fig. 16.8 Subretinal fluid and severe choroidal involvement with the typical seasick appearance in a patient with extranodal marginal zone MALT lymphoma. Visual acuity was 20/200

16.3 Inflammatory Choroidal Neovascularization

Choroidal neovascularization (CNV) is present in several intraocular inflammatory diseases (Fig. 16.9). The main uveitis associated with inflammatory CNV are multifocal choroiditis (30%), punctate inner choroidopathy (70%), and presumed ocular histoplasmosis syndrome (30%) [17–19].

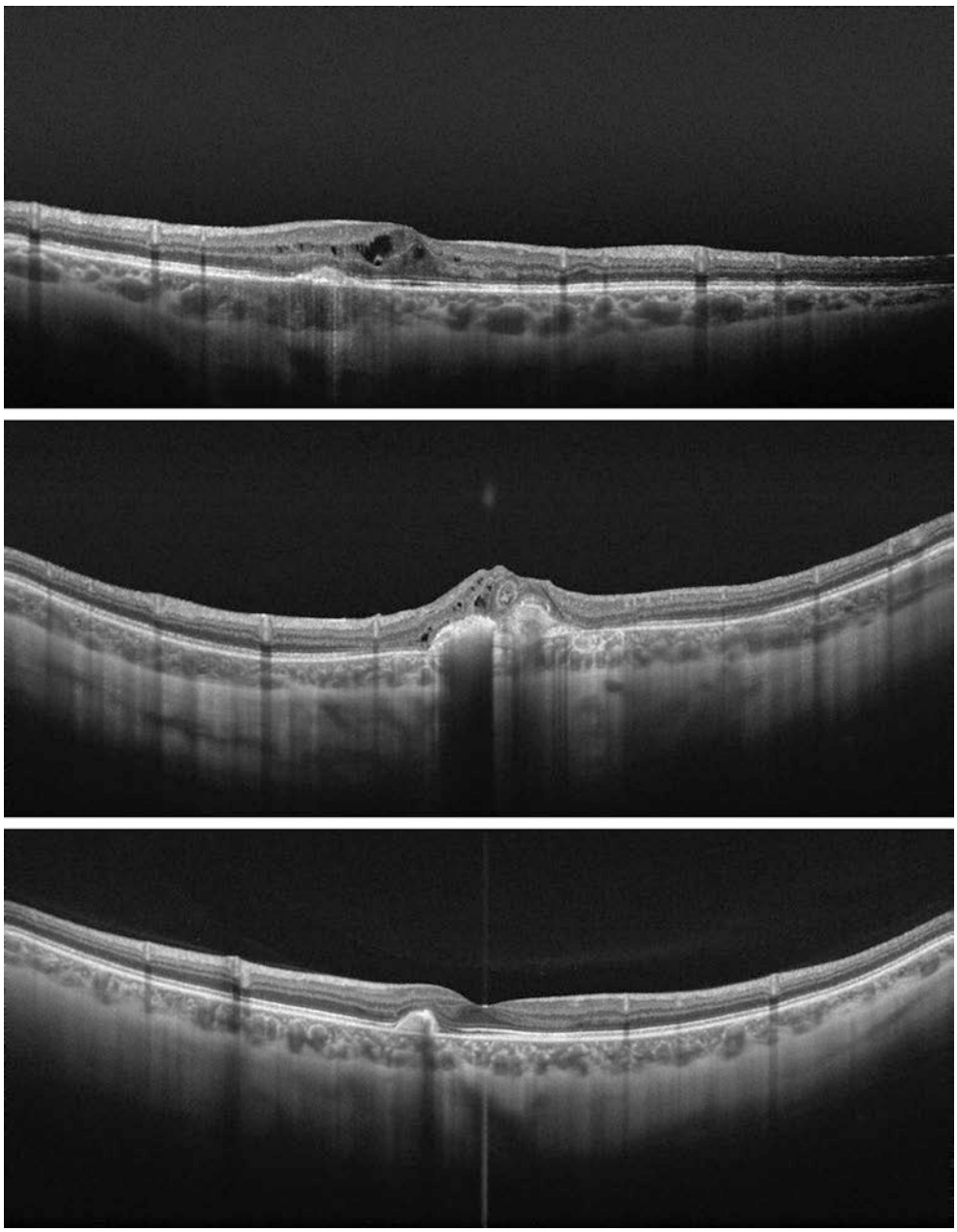

Fig. 16.9 Illustrative cases of choroidal neovascularization (CNV) in patients with multifocal choroiditis. *Top*: Active CNV with ill-defined neovascular complex and cystoid macular edema (visual acuity 20/50); *Middle*: Inactive CNV with outer retinal tubulations and degenerative pseudocysts (visual acuity 20/30); *Bottom*: Consolidated and healed CNV with complete retinal pigment epithelium envelopment of the CNV and no evidence of neovascular activity (visual acuity 20/20)

16.4 Other Retinal Changes in Patients with Uveitis

16.4.1 Topographic Characterization of Chorioretinal Inflammation

The cautious observation of SS-OCT scans is useful in order to determine the exact composition of inflammatory lesions, thus making possible the differentiation between *retinitis* (hyperreflective lesions within the neurosensory retina), *choroiditis* (increased choroidal thickness with hyperreflective foci at the level of the choriocapillaris), and *chorioretinitis* (combination of the aforementioned lesions) [20].

Also, there are some typical tomographic signs highly suggestive of particular entities: hyperreflective evanescent lesions on top of the retinal pigment epithelium (RPE), eventually in a columnar disposition, in patients with multiple evanescent white dots syndrome [21]; hyperreflective banded lesions from the inner plexiform layer to the outer nuclear layer in patients with acute macular neuroretinopathy [22].

16.4.2 Retinal Pigment Epithelium Atrophy

Chorioretinitis may lead to widespread punched-out lesions at the level of the retinal pigment epithelium that can be identified and evaluated by SS-OCT (Fig. 16.10). These are typical of multifocal choroiditis, punctate inner choroidopathy, and presumed ocular histoplasmosis syndrome [23, 24]. Also, zonal atrophic lesions of the RPE may be observed in acute multifocal placoid pigment epitheliopathy (APMPPE) [25], acute zonal occult outer retinopathy (AZOOR) [26], and serpiginoid syndromes (serpiginous choroiditis, ampiginous chorioretinopathy) [27].

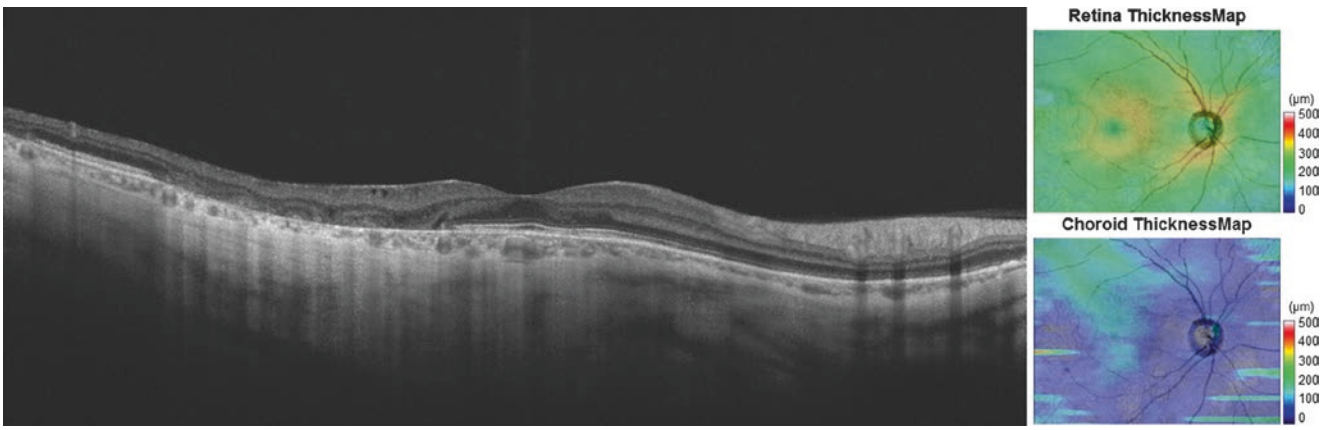

Fig. 16.10 Atrophic changes at the level of the outer retinal layers, retinal pigment epithelium (RPE) and choroid in a 47-year-old patient with relentless placoid chorioretinitis (ampiginous choroiditis). Visual acuity was 20/25

16.4.3 Retinal Atrophic Changes

Retinal atrophy may develop secondary to vascular ischemia or to progressive atrophy of the choroid and the RPE. In cases secondary to retinal ischemia, the area of thinning usually follows the involved vessels, making it easy to recognize the underlying process (Fig. 16.11). On the other hand, zonal atrophic areas correspond to the retina overlying atrophic choroid and/or RPE regions (Fig. 16.10) [28–30].

16.5 Assessment of the Choroid in Uveitis

Among the several goals of using imaging techniques in uveitis, one of the most important is to achieve a precise characterization of the pathologic processes that happen in the choroid. Angiographic techniques have traditionally been the only way to explore the choroid. Fluorescein angiography is especially useful for retinal pathology, though signs of choroidal abnormalities may also be observed. Indocyanine green angiography reveals predominantly pathology of the choroid and has been shown to provide valuable data regarding pathogenesis and the monitoring of patients with uveitis. However, some caveats include that this technique is invasive, time-consuming, and difficult to perform repeatedly during the patient's follow-up. Moreover, it does not provide sufficient information regarding cross-sectional imaging of the choroid, and it does not provide quantitative data. Choroidal structure can be easily observed and analyzed by SS-OCT. Moreover, measurement of its thickness can be performed. Hence, OCT is an excellent tool for both detection of inflammation and monitoring therapeutic response, as it has been shown in several publications. Kim et al. [31] found greater choroidal thickness in patients with Behçet's disease in active disease as compared to quiescent phase. Ishikawa et al. [32] assessed the effect of treatment with Infliximab in patients with Behçet's uveitis by measuring changes in choroidal thickness. This treatment reduced the choroidal thickness from week two after the first infusion and the reduced choroidal thickness was maintained thereafter. Zarranz-Ventura et al. [33] showed, in a large series of patients with presumably inactive punctate inner choroiditis, that one-fifth of the lesions analyzed by OCT revealed signs of activity (retinal pigment epithelium elevation with underlying hyporeflective space). Sakata et al. [34] described a new OCT finding that may indicate ongoing inflammation in patients with Vogt-Koyanagi-Harada (VKH) disease in the chronic stage consisting of a localized choroidal thickening or bulging. Sequelae of choroidal chronic inflammation has also been assessed by OCT. Patients with ocular sarcoidosis present thinner choroids in the quiescent stage [35]. Patients with longstanding VKH disease also have thinner choroids [36].

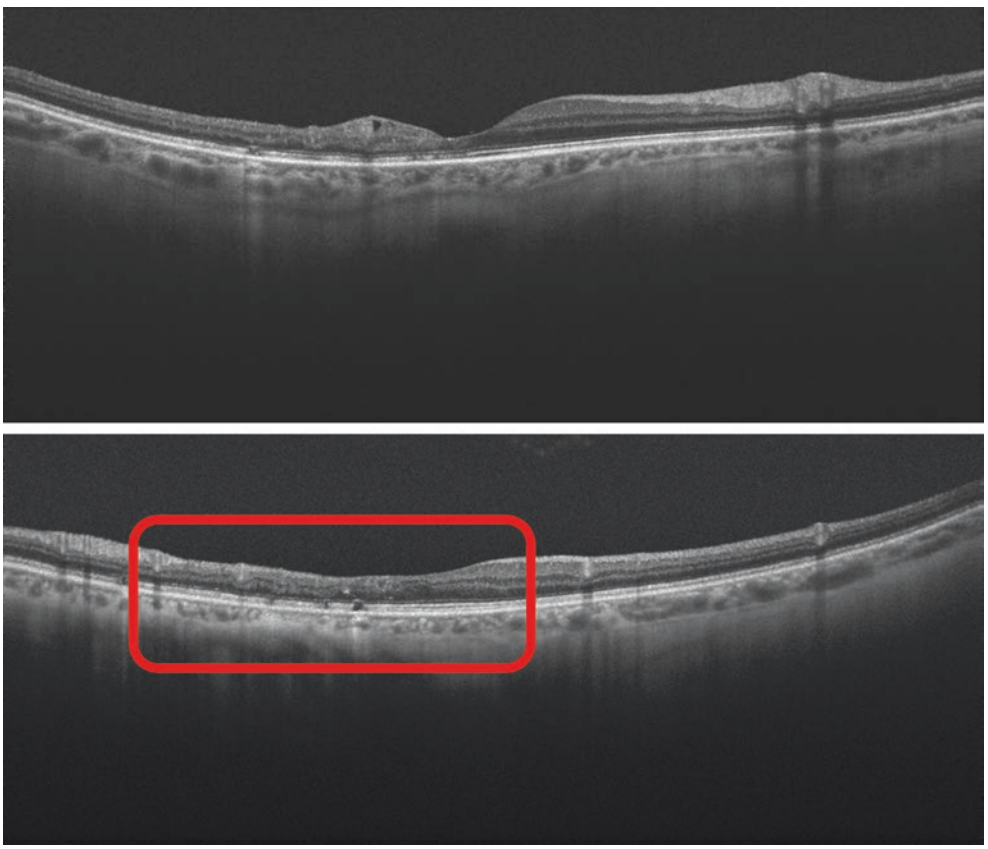

Fig. 16.11 Zonal retinal atrophy secondary to vascular ischemia due to thrombophlebitis secondary to Behçet disease in a 48-year-old female. The atrophic changes are clearly visible rastering the superior temporal macular area (*bottom image*). Visual acuity was 20/80

References

1. Michalewski J, Michalewska Z, Nawrocka Z, Bednarski M, Nawrocki J. Correlation of choroidal thickness and volume measurements with axial length and age using swept source optical coherence tomography and optical low-coherence reflectometry. Biomed Res Int. 2014;2014:639160.
2. Cunningham Jr ET, van Velthoven ME, Zierhut M. Spectral-domain-optical coherence tomography in uveitis. Ocul Immunol Inflamm. 2014;22(6):425–8.
3. Pakzad-Vaezi K, Or C, Yeh S, Forooghian F. Optical coherence tomography in the diagnosis and management of uveitis. Can J Ophthalmol. 2014;49(1):18–29.
4. Onal S, Tugal-Tutkun I, Neri P. P Herbort C. Optical coherence tomography imaging in uveitis. Int Ophthalmol. 2014;34(2):401–35.
5. Odrobina D, Michalewska Z, Michalewski J, Dzięgielewski K, Nawrocki J. Long-term evaluation of vitreomacular traction disorder in spectral-domain optical coherence tomography. Retina. 2011;31(2):324–31.
6. Tranos PG, Wickremasinghe SS, Stangos NT, Topouzis F, Tsinopoulos I, Pavesio CE. Macular edema. Surv Ophthalmol. 2004;49(5):470–90.
7. Gupta V, Gupta A, Dogra MR. Chapter 19. Inflammatory diseases of retina-choroid. In: Atlas optical coherence tomography of macular diseases and glaucoma. 4th ed. New Delhi: Jaypee-Highlights Medical Publishers; 2012. p. 458–540.
8. Antcliff RJ, Stanford MR, Chauhan DS, Graham EM, Spalton DJ, Shilling JS, et al. Comparison between optical coherence tomography and fundus fluorescein angiography for the detection of cystoid macular edema in patients with uveitis. Ophthalmology. 2000; 107(3):593–9.
9. Markomichelakis NN, Halkiadakis I, Pantelia E, Peponis V, Patelis A, Theodossiadis P, et al. Patterns of macular edema in patients with uveitis: Qualitative and quantitative assessment using optical coherence tomography. Ophthalmology. 2004;111(5):946–53.
10. Fardeau C, Champion E, Massamba N, LeHoang P. Uveitic macular edema. J Fr Ophtalmol. 2015;38(1):74–81.
11. Shao EH, Menezo V, Taylor SR. Birdshot chorioretinopathy. Curr Opin Ophthalmol. 2014;25(6):488–94.
12. Comander J, Loewenstein J, Sobrin L. Diagnostic testing and disease monitoring in birdshot chorioretinopathy. Semin Ophthalmol. 2011;26(4–5):329–36.
13. Vitale AT, Graham E, de Boer JH. Juvenile idiopathic arthritis-associated uveitis: clinical features and complications, risk factors for severe course, and visual outcome. Ocul Immunol Inflamm. 2013;21(6):478–85.
14. Oellers P, Jaffe GJ, Proia AD. Clinical-pathological correlation of Vogt-Koyanagi-Harada disease. JAMA Ophthalmol. 2016;134(3): 343–5.
15. Papakostas TD, Chee YE, Vavvas D. Posterior nodular scleritis. JAMA Ophthalmol. 2015;133(1):e141801.
16. Magalhães FP, Lavinsky D, Rossi LV, Barbosa L, Moraes N. Sympathetic ophthalmia after penetrating keratoplasty: a case report evaluated by spectral-domain optical coherence tomography. Retin Cases Brief Rep. 2012;6(1):11–5.
17. D'Ambrosio E, Tortorella P, Iannetti L. Management of uveitis-related choroidal neovascularization: from the pathogenesis to the therapy. J Ophthalmol. 2014;2014:450428.
18. Dhingra N, Kelly S, Majid MA, Bailey CB, Dick AD. Inflammatory choroidal neovascular membrane in posterior uveitis-pathogenesis and treatment. Indian J Ophthalmol. 2010;58(1):3–10.
19. Matsumoto Y, Haen SP, Spaide RF. The white dot syndromes. Compr Ophthalmol Updat. 2007;8(4):179–200.
20. Gallagher MJ, Yilmaz T, Cervantes-Castañeda RA, Foster CS. The characteristic features of optical coherence tomography in posterior uveitis. Br J Ophthalmol. 2007;91(12):1680–5.
21. Marsiglia M, Gallego-Pinazo R, Cunha de Souza E, Munk MR, Yu S, Mrejen S, et al. Expanded clinical spectrum of multiple evanescent white dot syndrome with multimodal imaging. Retina 2016;36(1):64–74.
22. Mrejen S, Pang CE, Sarraf D, Goldberg NR, Gallego-Pinazo R, Klancnik JM, et al. Adaptive optics imaging of cone mosaic abnormalities in acute macular neuroretinopathy. Ophthalmic Surg Lasers Imaging Retina. 2014;45(6):562–9.
23. Yasuno Y, Okamoto F, Kawana K, Yatagai T, Oshika T. Investigation of multifocal choroiditis with panuveitis by three-dimensional high-penetration optical coherence tomography. J Biophotonics. 2009;2(6–7):435–41.
24. Jung JJ, Khan S, Mrejen S, Gallego-Pinazo R, Cunningham Jr ET, Freund KB, et al. Idiopathic multifocal choroiditis with outer retinal or chorioretinal atrophy. Retina. 2014;34(7):1439–50.
25. Mrejen S, Gallego-Pinazo R, Wald KJ, Freund KB. Acute posterior multifocal placoid pigment epitheliopathy as a choroidopathy: what we learned from adaptive optics imaging. JAMA Ophthalmol. 2013;131(10):1363–4.
26. Mrejen S, Khan S, Gallego-Pinazo R, Jampol LM, Yannuzzi LA. Acute zonal occult outer retinopathy: a classification based on multimodal imaging. JAMA Ophthalmol. 2014;132(9):1089–98.
27. Dolz-Marco R, Rodríguez-Ratón A, Hernández-Martínez P, Pascual-Camps I, Andreu-Fenoll M, Gallego-Pinazo R. Macular retinal and choroidal thickness in unilateral relentless placoid chorioretinitis analyzed by swept-source optical coherence tomography. J Ophthalmic Inflamm Infect. 2014;4:24.
28. Abu El-Asrar AM, Herbort CP, Tabbara KF. Differential diagnosis of retinal vasculitis. Middle East Afr J Ophthalmol. 2009;16(4):202–18.
29. Arantes TE, Matos K, Garcia CR, Silva TG, Sabrosa AS, Muccioli C. Fundus autofluorescence and spectral domain optical coherence tomography in recurrent serpiginous choroiditis: case report. Ocul Immunol Inflamm. 2011;19(1):39–41.
30. Spaide RF, Goldberg N, Freund KB. Redefining multifocal choroiditis and panuveitis and punctate inner choroidopathy through multimodal imaging. Retina. 2013;33(7):1315–24.
31. Kim M, Kim H, Kwon HJ, Kim SS, Koh HJ, Lee SC. Choroidal thickness in Behcet's uveitis: an enhanced depth imaging-optical coherence tomography and its association with angiographic changes. Invest Ophthalmol Vis Sci. 2013;54:6033–9.
32. Ishikawa S, Taguchi M, Muraoka T, Sakurai Y, Kanda T, Takeuchi M. Changes in subfoveal choroidal thickness associated with uveitis activity in patients with Behçet's disease. Br J Ophthalmol. 2014;98:1508–13.
33. Zarranz-Ventura J, Sim DA, Keane PA, Patel PJ, Westcott MC, Lee RW, et al. Characterization of punctate inner choroidopathy using enhanced depth imaging optical coherence tomography. Ophthalmology. 2014;121:1790–7.
34. Sakata VM, da Silva FT, Hirata CE, Takahashi WY, Costa RA, Yamamoto JH. Choroidal bulging in patients with Vogt-Koyanagi-Harada disease in the non-acute uveitic stage. J Ophthalmic Inflamm Infect. 2014;4:1–6.
35. Güngör SG, Akkoyun I, Reyhan NH, Yeşilırmak N, Yılmaz G. Choroidal thickness in ocular sarcoidosis during quiescent phase using enhanced depth imaging optical coherence tomography. Ocul Immunol Inflamm. 2014;22:287–93.
36. da Silva FT, Sakata VM, Nakashima A, Hirata CE, Olivalves E, Takahashi WY, et al. Enhanced depth imaging optical coherence tomography in long-standing Vogt-Koyanagi-Harada disease. Br J Ophthalmol. 2013;97:70–4.

17 Central Serous Chorioretinopathy, Polypoidal Choroidal Vasculopathy, and Rare Cases Imaged with Swept Source OCT and SS-OCTA

Zofia Michalewska and Jerzy Nawrocki

17.1 Central Serous Chorioretinopathy

Central serous chorioretinopathy (CSC) (*see* Figs. 17.1 and 17.2) is characterized by serous retinal detachment and is most often observed in young men. Gass [1] suspected that abnormalities of choroidal vasculature were primary to this disease. His suspicions were confirmed with indocyanine green angiography [2].

Choroidal thickness is crucial in distinguishing CSC from age-related macular degeneration (AMD) in doubtful cases. The choroid is always thickened is CSC (*see* Fig. 17.1, *double-headed arrow*) and thinned in AMD. These suggest that CSC might be associated with increased hydrostatic pressure in the choroid [3]. As the disease is self-limiting in most cases, the common practice is to observe acute cases for about 3 months.

Treatment of CSC is still being discussed. Choroidal thickness does not decrease after laser photocoagulation, but choroidal thickness normalizes after photodynamic therapy (PDT). Theoretically, PDT should occlude only choriocapillaries without affecting deep choroidal vessels. However, Izumi et al. [4] reported that especially the diameter of large choroidal vessels decreased after PDT.

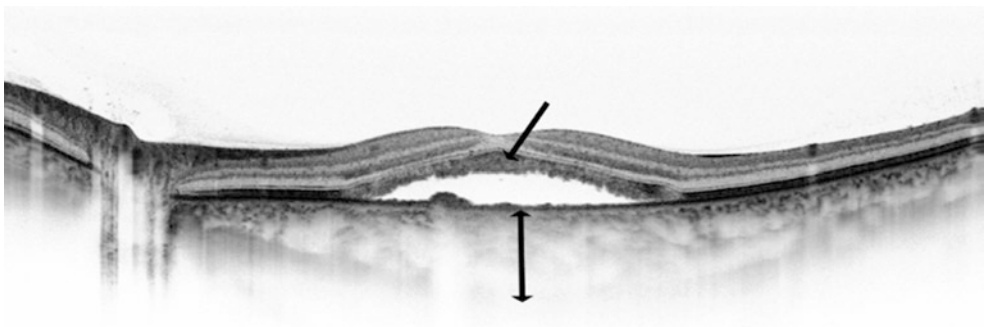

Fig. 17.1 Central serous chorioretinopathy in swept source optical coherence tomography (SS-OCT). This image presents long-standing CSC with elongated photoreceptors (*top arrow*)

Z. Michalewska, MD, PhD (✉) • J. Nawrocki, MD, PhD
Jasne Blonia Ophthalmic Clinic, Rojna 90, 91-162 Lodz, Poland
e-mail: zosia_n@yahoo.com

© Springer International Publishing AG 2017

Z. Michalewska, J. Nawrocki (eds.), *Atlas of Swept Source Optical Coherence Tomography*,
DOI 10.1007/978-3-319-49840-9_17

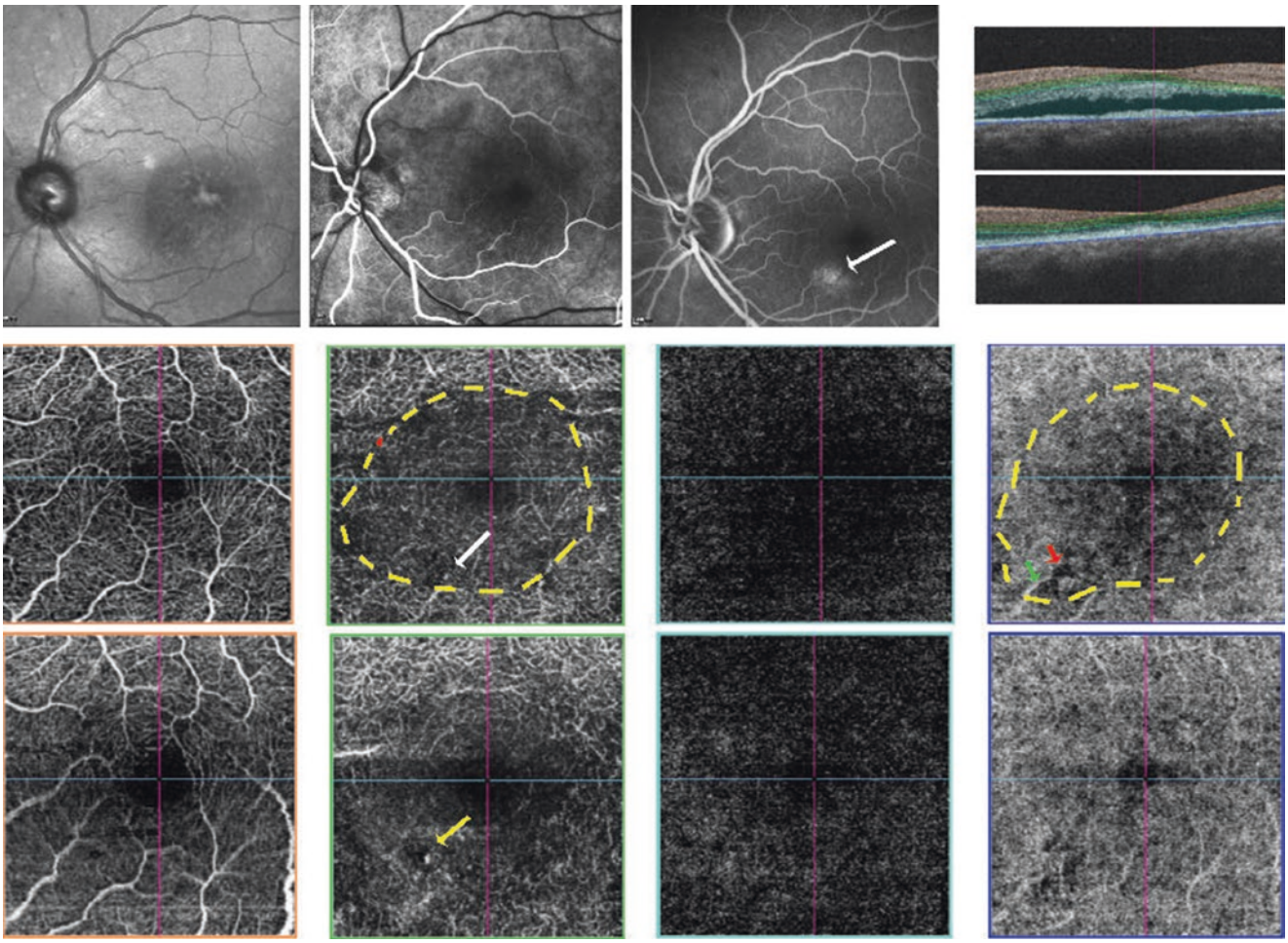

Fig. 17.2 Central serous chorioretinopathy. *Top left*, Scanning laser ophthalmoscopy and fluorescein angiography showing pooling. *Arrow* added to the fluorescein angiography early phase indicates the spot to be lasered. *Top right*, SS-OCT before and after laser photocoagulation. Please note that choroidal thickness did not change after laser photocoagulation. *Middle row,* Swept source optical coherence tomography angiography (SS-OCTA) performed on the same day as fluorescein angiography. *Middle row from left to right*, Superficial retinal vessels; deep retina vessels (*white arrow* indicates the spot to be lasered, corresponding to early phase of fluorescein angiography, the central area with decreased vessels visibility, marked with yellow lines, corresponds to serous retinal detachment); avascular retinal pigment epithelium; choroidal vasculature presents a hyporeflective central area, corresponding to serous retinal detachment (*yellow lines*), additionally a dilated vessel (*green arrow*), which probably is leaking, attached to a hyporeflective spot (*red arrow*), probably the leakage site. Please note that in spectral-domain OCTA leakage sites are very rarely observed [5, 6]. *Bottom row*, SS-OCTA after laser photocoagulation. *Bottom row from left*, Superficial retinal vessels; deep retina vessels (*yellow arrow* indicates the lasered spot); avascular retinal pigment epithelium; choroidal vessels

17.2 Polypoidal Choroidal Vasculopathy

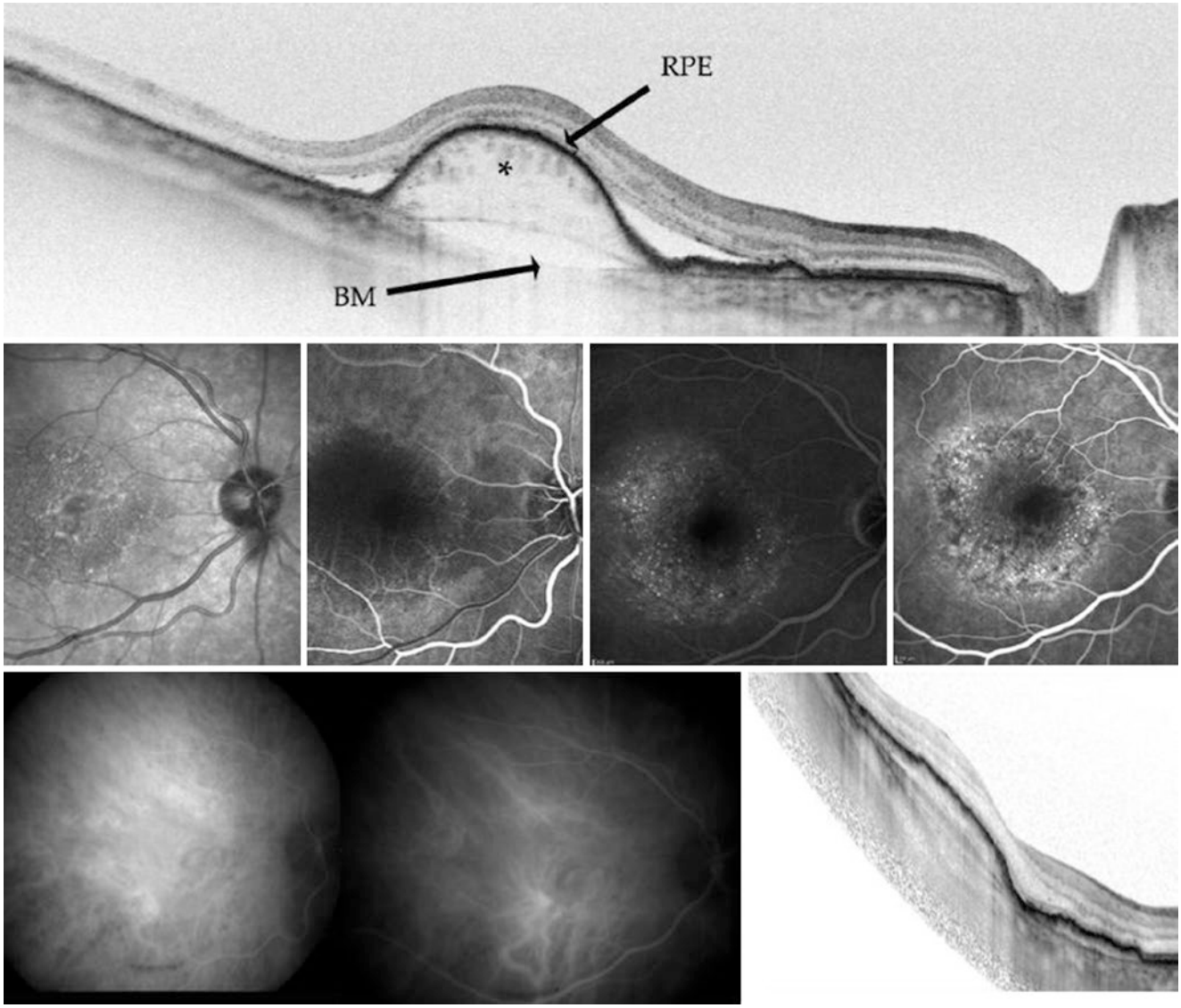

Fig. 17.3 Polypoidal choroidal vasculopathy. *Top*, SS-OCT image showing the double layer sign—typical for PCV. It seems as though the retinal pigment epithelium (*RPE*) is split into two layers, whereas in fact we can see RPE and Bruch's membrane (*BM*). Another pathognomonic feature of PCV are polypoidal lesions filled with moderately hyperreflective material (*asterisk*) [7]. *Middle*, Fluorescein angiography. *Lower left*, SS-OCT after photodynamic therapy in this patient. *Lower right*, Indocyanine green angiography

17.3 Rare Cases Imaged with SS-OCT and SS-OCTA

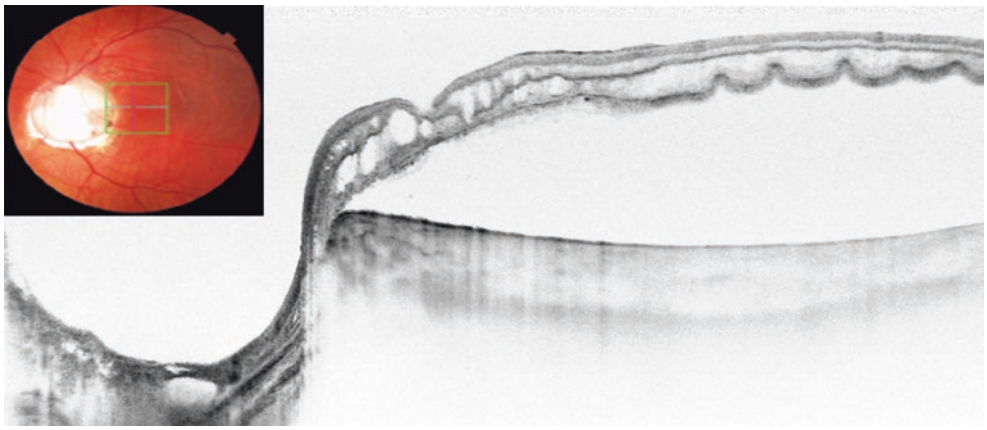

Fig. 17.4 Morning glory syndrome in SS-OCT

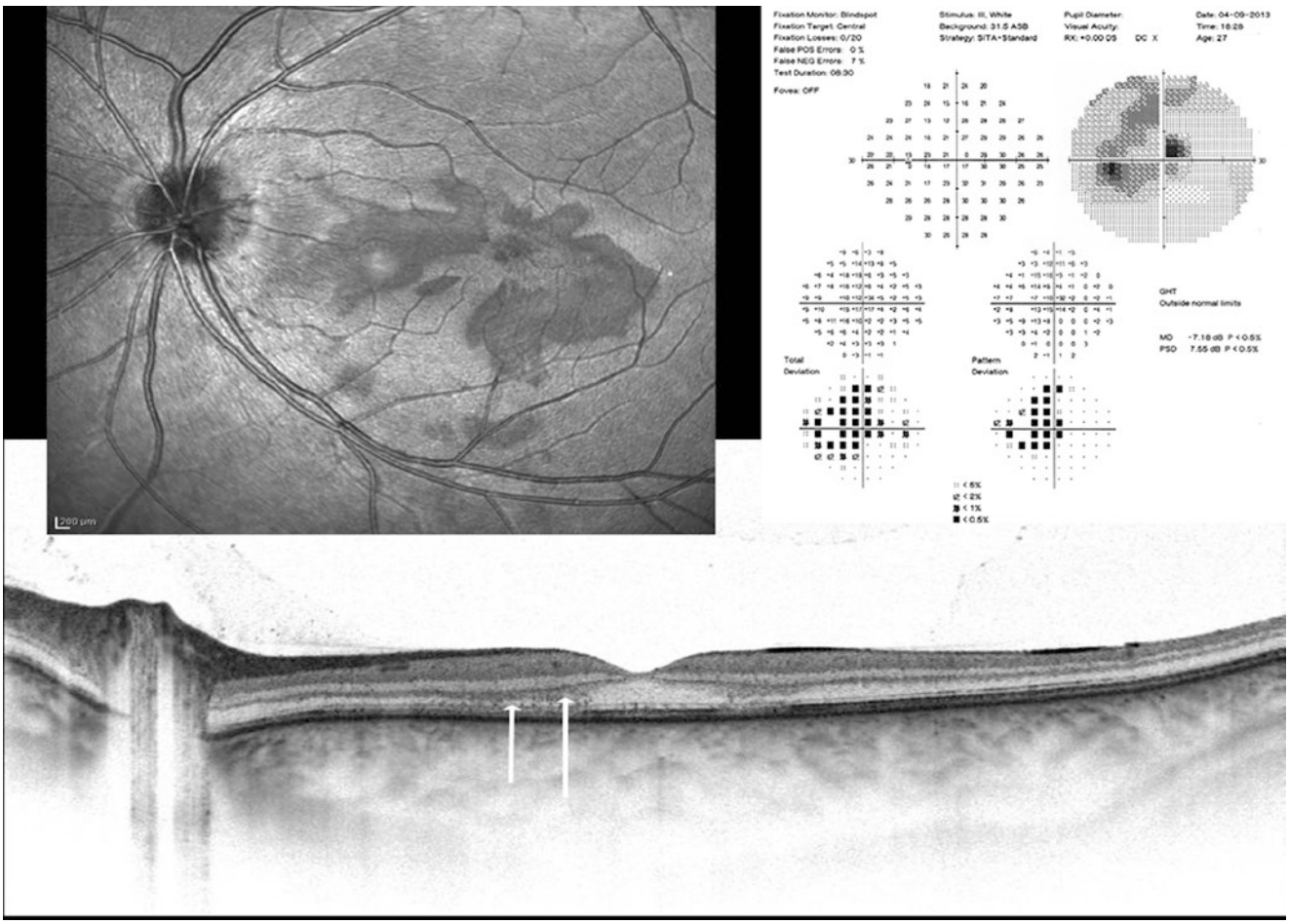

Fig. 17.5 Acute macular neuroretinopathy. *Upper left*, Scanning laser ophthalmoscopy. *Upper right*, Visual field. *Lower image*, SS-OCT. *Arrows* indicate deformation of the outer plexiform layer

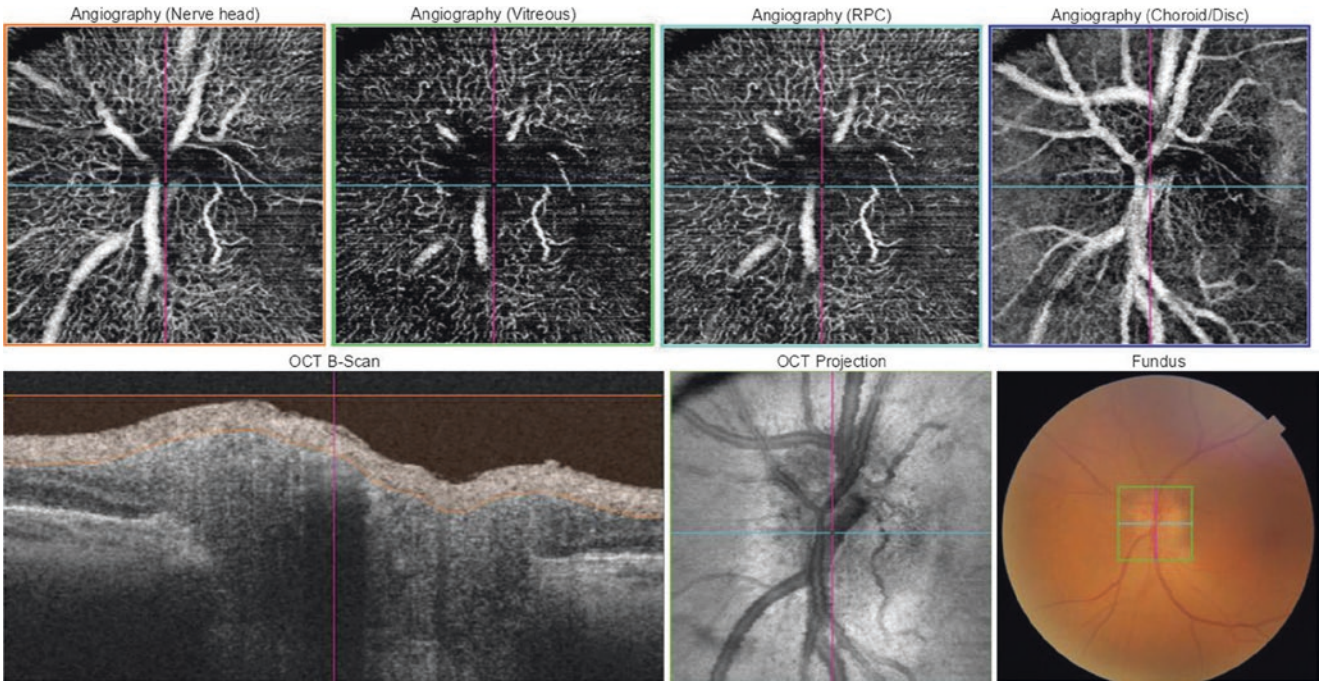

Fig. 17.6 Optic disc edema in SS-OCTA

Fig. 17.7 Subfoveal melanoma after proton beam therapy

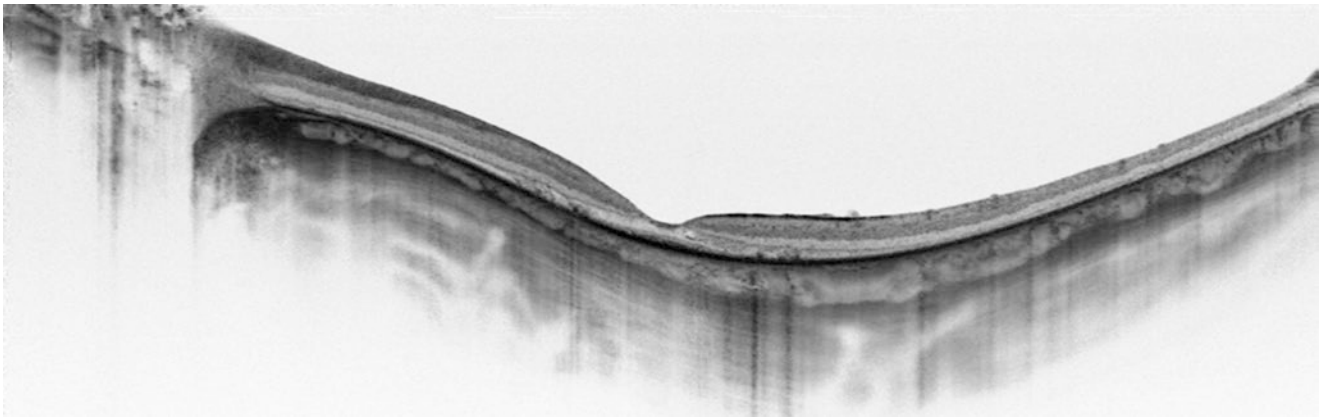

Fig. 17.8 Retinitis pigmentosa. External limiting membrane and photoreceptors are visible in the fovea, but diminish peripherally. The choroid is thinned

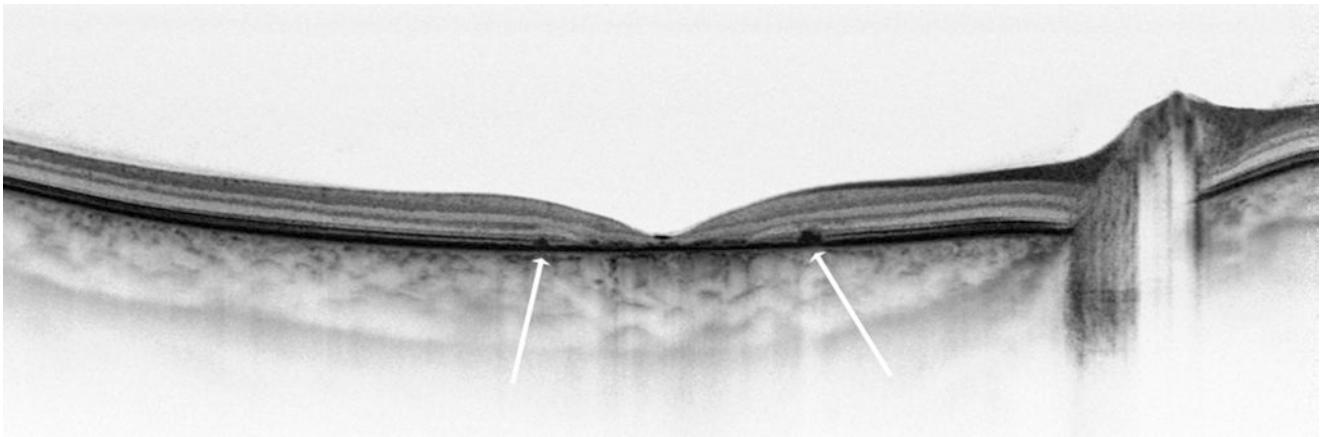

Fig. 17.9 Stargardt disease. Photoreceptors and the external limiting membrane are absent in the fovea and present peripherally. *Arrows* indicate the margins between present and absent photoreceptors. Choroidal thickness is normal

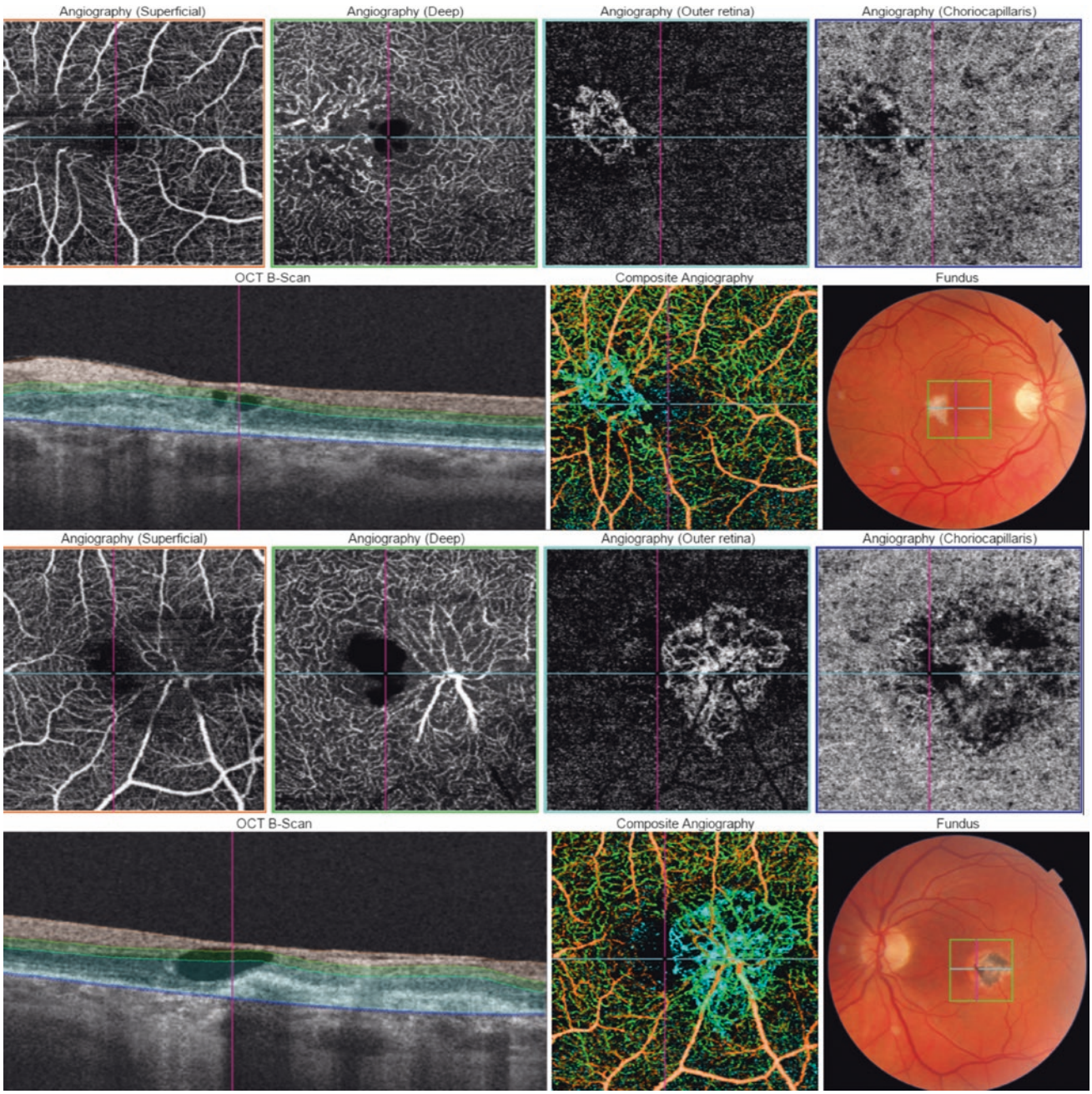

Fig. 17.10 Bilateral macular telangiectasia in SS-OCTA

References

1. Gass JD. Pathogenesis of disciform detachment of neuroepithelium. Am J Ophthalmol. 1967;63:1–139.
2. Piccoline FC, Borgia L. Central serous chorioretinopathy and indocyanine green angiography. Retina. 1994;14:231–42.
3. Imamura Y, Fujiwara T, Margolis R, Spaide RF. Enhanced depth imaging optical coherence tomography of the choroid in central serous chorioretinopathy. Retina. 2009;29(10):1469–73.
4. Izumi T, Koizumi H, Maruko I, Takahashi Y, Sonoda S, Sakamoto T, Iida T. Structural analyses of choroid after half-dose verteporfin photodynamic therapy for central serous chorioretinopathy. Br J Ophthalmol. 2016. pii: bjophthalmol-2016-308921. doi:10.1136/bjophthalmol-2016-308921. [Epub ahead of print].
5. Feucht N, Maier M, Lohmann CP, Reznicek L. OCT angiography findings in acute central serous chorioretinopathy. Ophthalmic Surg Lasers Imaging Retina. 2016;47(4):322–7.
6. Costanzo E, Cohen SY, Miere A, Querques G, Capuano V, Semoun O, et al. Optical coherence tomography angiography in central serous chorioretinopathy. J Ophthalmol. 2015; doi:10.1155/2015/134783.
7. St Martin JM, Rodman J, Pizzimenti JJ, Duchnowski E. The "double-layer sign": in vivo imaging of polypoidal choroidal vasculopathy. Optom Vis Sci. 2013;90(12):e293–300.

Swept Source OCT and Glaucoma

18

Kaweh Mansouri, Kirsten Hoskens,
and Robert N. Weinreb

Glaucoma is a leading cause of blindness worldwide [1]. It is defined as a group of progressive optic neuropathies with characteristic retinal ganglion cell damage at the optic disc and a concomitant pattern of visual field loss [2]. Structural measurements have become more important for glaucoma diagnosis and follow-up. The introduction of optical coherence tomography (OCT) has contributed to better understanding and management of glaucoma [3]. The assessment of structural damage of the retinal nerve fiber layer (RNFL) using OCT has become a critical part of glaucoma diagnosis and follow-up. The new generation of OCT, swept source OCT (SS-OCT), has recently been developed to enhance the visualization of the deep optic nerve head and deep parapapillary structures such as the lamina cribrosa (LC) and the choroid, which have been postulated to play a role in glaucoma pathogenesis [4, 5].

K. Mansouri, MD (✉) • K. Hoskens
Glaucoma Center, Montchoisi Clinic, Lausanne, Switzerland
e-mail: kmansouri@ucsd.edu

R.N. Weinreb, MD
Department of Ophthalmology, Hamilton Glaucoma Center and Shiley Eye Center, University of California, San Diego, La Jolla, CA, USA

18.1 Posterior Segment Imaging

Visualization of the deeper ocular structures has been improved thanks to the development of two different imaging techniques, enhanced depth imaging OCT (EDI-OCT) and swept source OCT (SS-OCT). Spaide et al. first described the technique of EDI-OCT in 2008 to improve visualization of posterior ocular structures [6]. With this technique, the spectral-domain OCT (SD-OCT) device is pushed close enough to the eye to create an inverted fundus image, which places the deeper ocular structures closer to the zero-delay. Images acquired with EDI-OCT allow better visualization of the choroid, and choroidal thickness can be measured [7].

The new generation of high-penetration OCT, SS-OCT, has a longer center wavelength (1040–1060 nm instead of 840 nm) to improve tissue penetration and allow better visualization of the deeper ocular structures such as the choroid [8, 9].

Light scattering and absorption at the photoreceptors and retinal pigment epithelium are limited due to the longer wavelength of this imaging technique [10]. Miki et al. [11] compared both imaging techniques, using subjective grading systems, and showed that both are useful for evaluating the deep optic nerve head and the deep parapapillary structures. Visualization of the prelaminar tissue surface was excellent with both EDI-OCT and SS-OCT. Mean visibility scores were reported to be 1.04 in the EDI-OCT images and 1.02 in the SS-OCT images. The mean visibility scores for the anterior laminar border (1.33), the posterior laminar border (2.10), and the laminar pores (1.99) were significantly better in the EDI-OCT images as compared to the SS-OCT images (mean visibility scores 1.52, 2.62, and 2.13, respectively). Mean visibility scores for the intrascleral vessels (2.26) and the choroid (1.02) were better in the SS-OCT images compared with those in the EDI-OCT images (2.82 and 1.47, respectively).

The longer-wavelength light used in the SS-OCT makes the images less susceptible to scattering by the choroid and

© Springer International Publishing AG 2017

Z. Michalewska, J. Nawrocki (eds.), *Atlas of Swept Source Optical Coherence Tomography*,
DOI 10.1007/978-3-319-49840-9_18

the sclera and to absorptions by the retinal pigment epithelium and the choroid. Park et al. compared the detection rates of identifying the posterior border of the sclera and LC using EDI-OCT and SS-OCT in myopic glaucoma patients [12]. The posterior borders of the sclera were visible in 31% of the eyes using EDI-OCT versus 53% of the eyes using SS-OCT. Imaging of the sclera in highly myopic eyes did not differ between EDI-OCT and SS-OCT. Since SS-OCT has a long width and depth of the scan window, it is possible to visualize the whole sclera at the posterior segment. The detection rates of the posterior border of the LC using EDI-OCT (75%) and SS-OCT (81%) were similar. Interobserver intraclass correlation coefficients (ICC) were reported to be 0.925 (95% CI, 0.846–0.963) using EDI-OCT and 0.929 (95% CI, 0.862–0.971) using SS-OCT for subfoveal choroidal thickness; 0.890 (95% CI, 0.742–0.908) using EDI-OCT and 0.897 (95% CI, 0.863–0.911) using SS-OCT for subfoveal scleral thickness; 0.906 (95% CI, 0.890–0.921) using EDI-OCT and 0.907 (95% CI, 0.895–0.930) using SS-OCT for laminar thickness. Intersystem ICCs were reported to be 0.936 (95% CI, 0.936–0.978) for subfoveal choroidal thickness; 0.769 (95% CI, 0.710–0.854) for subfoveal scleral thickness; and 0.900 (95% CI, 0.887–0.917) for laminar thickness.

18.1.1 Imaging the Lamina Cribrosa

The axons of the retinal ganglion cells converge to form the neuroretinal rim of the optic disc before exiting the eye through the LC, a scleral structure at the optic nerve head that is characterized by sheets of porous connective tissue. The LC is presumed to provide mechanical support to these optic nerve fibers within the deep optic disc region [13]. Structural thinning of the LC, via deformation and compression, has been associated with glaucoma [14, 15]. Changes in the LC pore shape and size also have been correlated with progression of the disease [16–18]. Overall, deformation of the LC likely impedes axoplasmic flow, disrupting transport of trophic factors important to survival of retinal ganglion cells [19, 20]. Thus, structural changes in the LC may play a role in neuronal death characteristic of glaucoma. Also, from a biomechanical perspective, the LC represents a discontinuity in the spherical casing of the eye, which makes it more vulnerable to the stress-loading that may play a role in glaucoma [21]. Therefore, understanding the forces that affect the structure of the LC will further elucidate the mechanisms of glaucoma.

Characterization of both focal defects and general morphologic changes may provide valuable insight into specific glaucomatous mechanisms at this site of presumed axonal injury. A study evaluating focal LC defects in glaucoma using EDI-OCT reported the presence of various shapes of focal LC defects in 34 of 38 eyes with glaucoma, versus none in the healthy eyes. Altered laminar insertion was the most common type of defect identified (59%). Focal LC defects were demonstrated to have a good structure-function relationship with visual field (VF) defects. The location of the focal LC defect in either the superior or inferior half of the LC corresponded to visual hemifield with a greater sensitivity loss in the pattern deviation plot. The investigators reported the number of focal LC defects to be significantly correlated with the VF mean deviation (MD) before ($p = 0.003$) and after ($p = 0.002$) controlling for age [22]. A detailed study of the LC, however, requires accurate visualization of this anatomical structure. SS-OCT has been developed to enhance visualization of posterior ocular layers, including the LC.

Earlier postmortem analysis of glaucomatous human eyes has shown morphological changes of the LC such as posterior displacement of laminar insertion [23]. Recent development of posterior segment imaging using SS-OCT has made the evaluation of the LC structure possible in vivo. The location of the anterior LC insertion has recently been shown to be more posterior in eyes with primary open angle glaucoma (POAG) as compared to healthy controls [24]. In another study, SS-OCT has been used to demonstrate that the peripheral LC was displaced more posteriorly in POAG eyes compared with age-matched healthy eyes [25]. The vertical peripheral LC was found to be located more posteriorly than the horizontal peripheral LC, and the vertical-horizontal peripheral LC depth difference was significantly larger in POAG eyes compared to healthy controls. The authors suggested that the peripheral LC in the vertical meridian may have increased strain related to intraocular pressure (IOP) compared to the horizontal meridian in glaucomatous eyes.

Focal LC defects have also been shown to be associated with glaucomatous optic neuropathy [22]. Takayama et al. demonstrated that three-dimensional SS-OCT volume rendering is also a useful method to identify focal full-thickness LC defects [26]. A focal full thickness LC defect was defined as a hyporeflective spot, much larger in size and much lower in reflectivity than a laminar pore, showing a full-thickness defect in the highly reflective LC on serial B-images. Two types of full-thickness LC defects were analyzed: the lamina cavity and lamina disinsertion. LC defects spatially corresponded with clinical signs of localized glaucomatous damage (neuroretinal rim thinning, localized RNFL defects, abnormal circumpapillary RNFL, and disc hemorrhages).

In multivariate logistic regression analyses, LC defects were significantly associated with concurrent or previous disc hemorrhages and longer axial length. Kim et al. [27] found that a focal LC defect was more frequently visible in eyes with a disc hemorrhage than in eyes without a disc hemorrhage (80.6% versus 39.7%). LC defects also showed a significant rate of spatial relationship with disc hemorrhages (62.1%).

Miki et al. [28] have shown LC defects to be associated with corresponding visual field damage in glaucomatous eyes and highly myopic eyes with glaucoma. LC defects could also be demonstrated in highly myopic eyes without any sign of glaucomatous optic neuropathy. It is still unclear whether these LC defects are pathologically related to glaucoma or not. Since LC defects in myopia could be an early sign of glaucoma, evaluation of the LC seems to be important in glaucoma and myopia patients.

Omodaka et al. [29] developed a new software to measure the average thickness of the LC within a validated area of an SS-OCT disc scan image. Reconstructed B- and *en-face* images could be synchronized and simultaneously visualized using this software. The anterior border of the LC was defined as the point where the pores became visible in the images, and the posterior border as the point where the pores ceased to be visible. Measurements of the LC thickness using this method of defining the outer border of the LC were found highly reproducible and correlated to glaucoma severity. The investigators reported a coefficient of variation for LC thickness measurements of 5.1%. LC thickness and circumpapillary RNFL thickness were shown to be closely correlated (0.64, $p < 0.01$).

SS-OCT enables good visualization of the anterior LC, while the posterior borders remain insufficiently visible in many eyes (Figs. 18.1, 18.2, and 18.3).

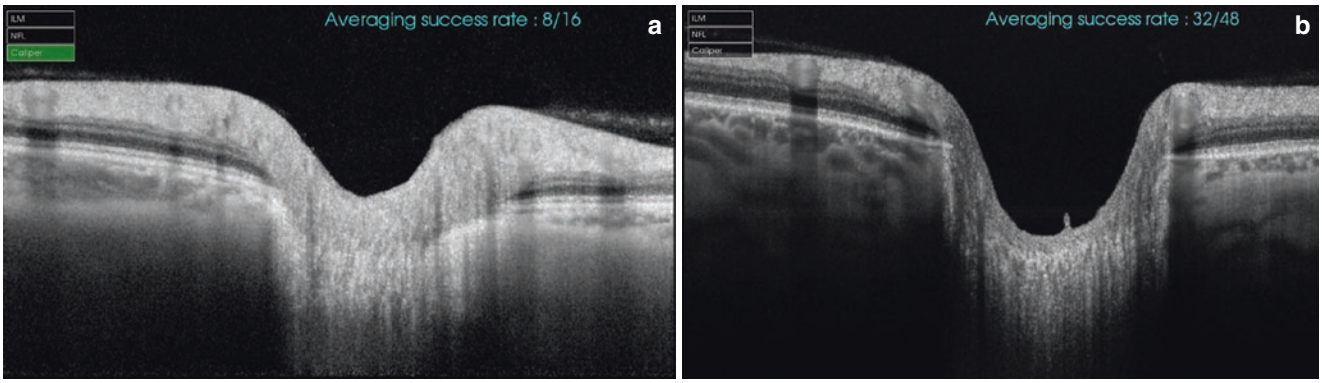

Fig. 18.1 SS-OCT scans of optic nerve head of a healthy individual (**a**) and of a glaucoma patient (**b**). Both anterior and (to some degree) posterior borders of the lamina cribrosa are visible

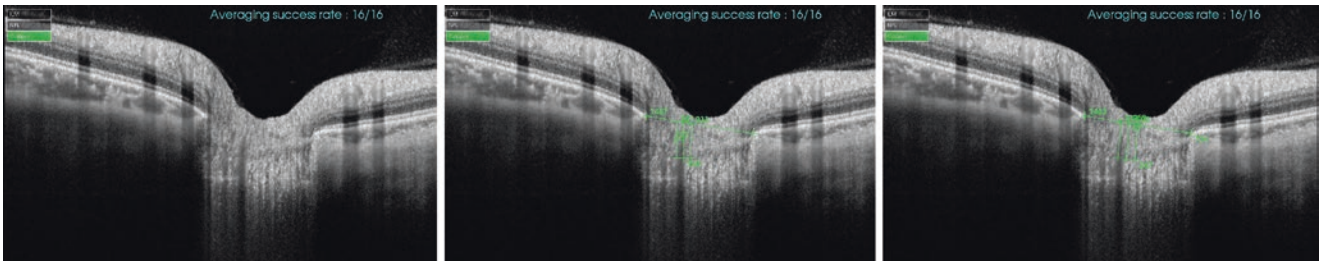

Fig. 18.2 SS-OCT scan of optic nerve head of a healthy eye. Two graders independently used manual calibers to measure depth of the lamina cribrosa. At present, no automated segmentation is available for that purpose

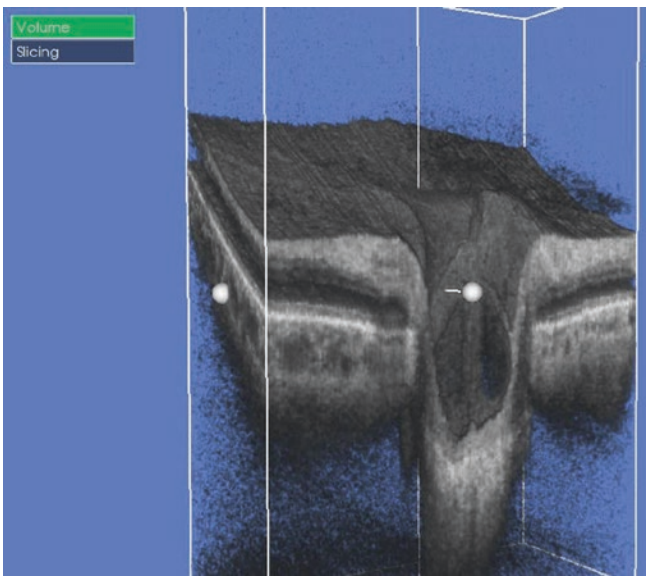

Fig. 18.3 Three dimensional SS-OCT scan of optic nerve head of a glaucoma patient. Specific regions of interest can be exposed using the crop function

18.1.2 Imaging the Choroid

The choroid is a vascular meshwork between the retina and sclera and plays a vital role in ocular metabolism, volume regulation, and temperature control. Abnormalities of the choroid have been implicated in several ophthalmic diseases, most importantly in the pathophysiology of retinal conditions [30, 31]. In addition, changes in choroidal structure and function have also been postulated to play a role in glaucoma [32, 33]. Study of this structure was until recently limited to postmortem histological studies [32, 34] and ultrasonography [35]. An important source of uncertainty about the cause-and-effect relationship of choroidal changes and disease processes arises from the lack of precision and effect of artifacts on these methods [36].

Imaging with SS-OCT has been shown to enhance the visualization of the choroid (Fig. 18.4). The use of SS-OCT has been evaluated in choroidal and retinal thickness measurements. Automated measurements of choroidal and retinal thickness have been shown to be highly repeatable [37]. The frequency and type of artifacts have also been assessed: the most frequent image artifact was signal loss resulting from blinking. Other artifacts that occurred were segmentation failure and motion artifacts. SS-OCT has been used to measure choroidal thickness in healthy and glaucomatous eyes [38]. A relationship was demonstrated between increasing age, longer axial length, and thinner choroid. No association was found between glaucoma and choroidal thickness after accounting for differences in age and axial length. Choroidal thickness has also been evaluated using SS-OCT after the water-drinking test [39]. The water-drinking test has been used to estimate the magnitude of peaks in IOP, and consists of ingestion of 1000 mL of water within a period of 5–15 min. A consistent and statistically significant increase of peripapillary and macular choroidal thickness and volume after the water-drinking test has been demonstrated. However, this phenomenon was of small magnitude and unlikely to explain the observed IOP increase by itself.

To determine whether the choroid plays a role in glaucoma, longitudinal studies are needed to evaluate the correlation between choroidal changes and glaucoma progression.

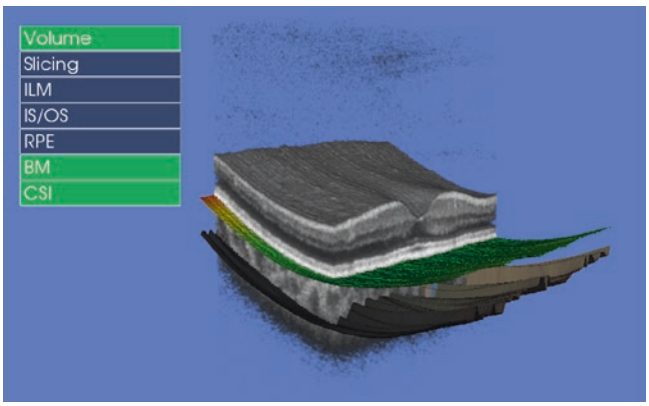

Fig. 18.4 Three-dimensional SS-OCT scan of the macular region, showing the retina and choroid. The colored lines represent automated segmentation of the choroid

18.1.3 Imaging the Retinal Nerve Fiber Layer

Less attention has been paid to the ability of SS-OCT to evaluate the RNFL, as it is widely presumed that no additional benefit for this parameter is provided compared to SD-OCT. Yang et al. assessed the ability of SS-OCT RNFL measurements to differentiate glaucomatous eyes from healthy eyes [40]. Wide-angle and peripapillary RNFL thickness were assessed. The diagnostic accuracy of the RNFL thickness measurements by SS-OCT was similar to that of peripapillary RNFL measurements by SD-OCT. The same group also evaluated the diagnostic ability of macular ganglion cell and inner plexiform layer measurements using SS-OCT [41]. The thickness of the macular ganglion cell complex (mGCC) and the macular ganglion cell inner plexiform layer (mGCIPL) were shown to be significantly reduced in glaucomatous compared to healthy eyes. Diagnostic accuracies for both parameters from both SS-OCT and SD-OCT showed a similar ability to detect glaucoma as circumpapillary RNFL. Good diagnostic performance was also shown for early glaucoma.

18.2 Anterior Segment Imaging

Evaluation of the anterior chamber angle is an important part of glaucoma management and diagnosis. Although gonioscopy remains the clinical gold standard for the visualization of the angle structures, anterior segment optical coherence tomography (AS-OCT) has become available for the evaluation of the anterior chamber angle. This imaging technique enables the obtention of objective and reproducible measurements of the anterior chamber angle, and has improved the diagnostic performance to detect angle closure [42].

Studies generally use the scleral spur as a reference point for evaluation of the angle. Parameters to measure the angle dimensions including the angle-opening distance, trabecular iris angle, angle recess area, and trabecular iris space area are measured with reference to the scleral spur [42]. The scleral spur may not always be visible with time domain AS-OCT [43, 44]. Using the Casia SS-OCT (Tomey, Nagoya, Japan), McKee et al. [45] visualized the scleral spur in over 95% of all examined quadrants in HD scan images. In addition to the scleral spur, Schwalbe's line and the Schlemm's canal could also be visualized. Their visibility was influenced by the scan location and the scan density: images obtained with HD scan in the nasal and temporal quadrants had superior visibility of the angle landmarks compared with those obtained with LD scan in the superior and inferior quadrants. The ability to visualize both the scleral spur and Schwalbe's line by SS-OCT makes it possible to measure the length of the trabecular meshwork. This may improve the precision of angle measurements and detection of angle closure [42].

Anterior chamber angle measurements using SS-OCT were shown to have low variability. Liu et al. [46] measured the angle opening distance, the trabecular iris space area, and the trabecular-iris angle at four quadrants, and found intraclass correlation coefficients of all angle parameters to be $\geq$0.83. Iris thickness, scan location, angle dimension, and axial length were associated with increased variance of angle measurements, but overall SS-OCT was found to be a reliable technique for the evaluation and measurement of the anterior chamber angle.

Peripheral anterior synechiae (PAS) are adhesions between the peripheral iris and cornea that can be found in different forms of angle-closure glaucoma. The fast scan speed of SS-OCT enables the acquisition of multiple high-resolution cross-sectional images of the angle, and facilitates evaluation of PAS. Lai et al. used SS-OCT to evaluate the area and degree of PAS involvement in patients with angle-closure glaucoma [47]. The measurements of the area and degree of PAS involvement were found to be reproducible. Synechial and appositional angle closure could be discriminated by variation of the lighting condition during OCT imaging: in appositional angle closure the angle is closed in the dark and open in the light, whereas in synechial closure the angle remains closed.

OCT evaluation of PAS has an advantage over gonioscopy in that it is a non-contact method and provides precise quantitative measurements of PAS. These measurements could be useful in the monitoring of PAS progression over time. Another group evaluated the use of SS-OCT in detection of iridotrabecular contact (ITC) in eyes with shallow peripheral anterior chamber and compared the results to these obtained with ultrasound biomicroscopy (UBM) [48]. The prevalence of ITC, which involves both PAS and appositional angle closure, in eyes with shallow peripheral anterior chambers was found to be significantly higher with SS-OCT as compared to UBM under light conditions, but not under dark conditions. The ITC range evaluated by SS-OCT was greater in the dark than in the light. PAS-positive eyes had a greater range of ITC than PAS-negative eyes under light conditions.

The high scan speed of SS-OCT also facilitates a more complete imaging of the iris and measurement of iris volume as compared to time-domain OCT. Mak et al. measured iris volume using SS-OCT and assessed the relationship with primary angle closure [49]. A larger iris volume was found to be associated with a smaller angle width, a smaller pupil diameter, smaller anterior chamber volume, and a longer axial length. After pharmacological dilatation, mean iris volume significantly decreased in all eyes independent of angle status (angle closure, POAG, and normal eyes). From light to dark 19.4% of angle closure eyes, 16.7% of normal eyes, and 19.4% of POAG eyes showed an increase in iris volume. SS-OCT iris volume

measurements can provide useful information for a better understanding of the pathophysiology of angle-closure glaucoma.

Conclusion

In conclusion, SS-OCT has the potential to add important information to the understanding of structural changes in glaucoma. Longitudinal data are needed to evaluate its benefits in respects to SD-OCT for the diagnosis and management of glaucoma.

References

1. Resnikoff S, Pascolini D, Etya'ale D, Kocur I, Pararajasegaram R, Pokharel GP, et al. Global data on visual impairment in the year 2002. Bull World Health Organ. 2004; 82(11):844–51. Epub 2004 Dec.
2. Weinreb RN, Khaw PT. Primary open-angle glaucoma. Lancet. 2004;363(9422):1711–20.
3. Leung CK. Diagnosing glaucoma progression with optical coherence tomography. Curr Opin Ophthalmol. 2014;25(2):104–11.
4. Quigley HA, Addicks EM. Regional differences in the structure of the lamina cribrosa and their relation to glaucomatous optic nerve damage. Arch Ophthalmol. 1981;99(1):137–43.
5. Banitt M. The choroid in glaucoma. Curr Opin Ophthalmol. 2013;24(2):125–9.
6. Spaide RF, Koizumi H, Pozzoni MC. Enhanced depth imaging spectral-domain optical coherence tomography. Am J Ophthalmol. 2008;146(4):496–500.
7. Margolis R, Spaide RF. A pilot study of enhanced depth imaging optical coherence tomography of the choroid in normal eyes. Am J Ophthalmol. 2009;147(5):811–5.
8. Yasuno Y, Hong Y, Makita S, Yamanari M, Akiba M, Miura M, et al. In vivo high-contrast imaging of deep posterior eye by 1-microm swept source optical coherence tomography and scattering optical coherence angiography. Opt Express. 2007;15(10):61.
9. Unterhuber A, Povazay B, Hermann B, Sattmann H, Chavez-Pirson A, Drexler W. In vivo retinal optical coherence tomography at 1040 nm – enhanced penetration into the choroid. Opt Express. 2005;13(9):3252–8.
10. Chen Y, Burnes DL, de Bruin M, Mujat M, de Boer JF. Three-dimensional pointwise comparison of human retinal optical property at 845 and 1060 nm using optical frequency domain imaging. J Biomed Opt. 2009;14(2):024016.
11. Miki A, Ikuno Y, Jo Y, Nishida K. Comparison of enhanced depth imaging and high-penetration optical coherence tomography for imaging deep optic nerve head and parapapillary structures. Clin Ophthalmol. 2013;7:1995–2001.
12. Park HY, Shin HY, Park CK. Imaging the posterior segment of the eye using swept-source optical coherence tomography in myopic glaucoma eyes: comparison with enhanced-depth imaging. Am J Ophthalmol. 2014;157(3):550–7.
13. Grytz R, Meschke G, Jonas JB. The collagen fibril architecture in the lamina cribrosa and peripapillary sclera predicted by a computational remodeling approach. Biomech Model Mechanobiol. 2011;10(3):371–82.
14. Radius RL. Regional specificity in anatomy at the lamina cribrosa. Arch Ophthalmol. 1981;99(3):478–80.
15. Radius RL, Gonzales M. Anatomy of the lamina cribrosa in human eyes. ArchOphthalmol. 1981;99(12):2159–62.
16. Tezel G, Trinkaus K, Wax MB. Alterations in the morphology of lamina cribrosa pores in glaucomatous eyes. Br J Ophthalmol. 2004;88(2):251–6.
17. Miller KM, Quigley HA. Comparison of optic disc features in low-tension and typical open-angle glaucoma. Ophthalmic Surg. 1987; 18(12):882–9.
18. Fontana L, Bhandari A, Fitzke FW, Hitchings RA. In vivo morphometry of the lamina cribrosa and its relation to visual field loss in glaucoma. Curr Eye Res. 1998;17(4):363–9.
19. Quigley HA. Glaucoma. Lancet. 2011;377(9774):1367–77.
20. Burgoyne CF. A biomechanical paradigm for axonal insult within the optic nerve head in aging and glaucoma. Exp Eye Res. 2011;93(2):120–32.
21. Downs JC, Roberts MD, Sigal IA. Glaucomatous cupping of the lamina cribrosa: a review of the evidence for active progressive remodeling as a mechanism. Exp Eye Res. 2011;93(2):133–40.
22. Kiumehr S, Park SC, Syril D, Teng CC, Tello C, Liebmann JM, Ritch R. In vivo evaluation of focal lamina cribrosa defects in glaucoma. Arch Ophthalmol. 2012;130(5):552–9.
23. Quigley HA, Addicks EM, Green WR, Maumenee AE. Optic nerve damage in human glaucoma. II. The site of injury and susceptibility to damage. Arch Ophthalmol. 1981;99(4):635–49.
24. Lee KM, Kim TW, Weinreb RN, Lee EJ, Girard MJ, Mari JM. Anterior lamina cribrosa insertion in primary open-angle glaucoma patients and healthy subjects. PLoS One. 2014;9(12): e114935.
25. Kim YW, Kim DW, Jeoung JW, Kim DM, Park KH. Peripheral lamina cribrosa depth in primary open-angle glaucoma: a swept-source optical coherence tomography study of lamina cribrosa. Eye (Lond). 2015;29(10):1368–74.
26. Takayama K, Hangai M, Kimura Y, Morooka S, Nukada M, Akagi T, et al. Three-dimensional imaging of lamina cribrosa defects in glaucoma using swept-source optical coherence tomography. Invest Ophthalmol Vis Sci. 2013;54(7):4798–807.
27. Kim YK, Park KH. Lamina cribrosa defects in eyes with glaucomatous disc haemorrhage. Acta Ophthalmol. 2015; doi:10.1111/aos.12903.
28. Miki A, Ikuno Y, Asai T, Usui S, Nishida K. Defects of the lamina cribrosa in high myopia and glaucoma. PLoS One. 2015;10(9): e0137909.
29. Omodaka K, Horii T, Takahashi S, Kikawa T, Matsumoto A, Shiga Y, et al. 3D evaluation of the lamina cribrosa with swept-source optical coherence tomography in normal tension glaucoma. PLoS One. 2015;10(4):e0122347.
30. Spaide RF. Age-related choroidal atrophy. Am J Ophthalmol. 2009;147(5):801–10.
31. Imamura Y, Fujiwara T, Margolis R, Spaide RF. Enhanced depth imaging optical coherence tomography of the choroid in central serous chorioretinopathy. Retina. 2009;29(10):1469–73.
32. Haefliger IO, Flammer J, Luscher TF. Heterogeneity of endothelium-dependent regulation in ophthalmic and ciliary arteries. Invest Ophthalmol Vis Sci. 1993;34(5):1722–30.
33. Hayreh SS. Blood supply of the optic nerve head and its role in optic atrophy, glaucoma, and oedema of the optic disc. Br J Ophthalmol. 1969;53(11):721–48.
34. Yin ZQ, Vaegan, Millar TJ, Beaumont P, Sarks S. Widespread choroidal insufficiency in primary open-angle glaucoma. J Glaucoma 1997;6(1):23–32.
35. Hung LF, Wallman J, Smith 3rd EL. Vision-dependent changes in the choroidal thickness of macaque monkeys. Invest Ophthalmol Vis Sci. 2000;41(6):1259–69.
36. Gloesmann M, Hermann B, Schubert C, Sattmann H, Ahnelt PK, Drexler W. Histologic correlation of pig retina radial stratification with ultrahigh-resolution optical coherence tomography. Invest Ophthalmol Vis Sci. 2003;44(4):1696–703.
37. Mansouri K, Medeiros FA, Tatham AJ, Marchase N, Weinreb RN. Evaluation of retinal and choroidal thickness by swept-source optical coherence tomography: repeatability and assessment of artifacts. Am J Ophthalmol. 2014;157(5):1022–32.

38. Zhang C, Tatham AJ, Medeiros FA, Zangwill LM, Yang Z, Weinreb RN. Assessment of choroidal thickness in healthy and glaucomatous eyes using swept source optical coherence tomography. PLoS One. 2014;9(10):e109683.
39. Mansouri K, Medeiros FA, Marchase N, Tatham AJ, Auerbach D, Weinreb RN. Assessment of choroidal thickness and volume during the water drinking test by swept-source optical coherence tomography. Ophthalmology. 2013;120(12):2508–16.
40. Yang Z, Tatham AJ, Zangwill LM, Weinreb RN, Zhang C, Medeiros FA. Diagnostic ability of retinal nerve fiber layer imaging by swept-source optical coherence tomography in glaucoma. Am J Ophthalmol. 2015;159(1):193–201.
41. Yang Z, Tatham AJ, Weinreb RN, Medeiros FA, Liu T, Zangwill LM. Diagnostic ability of macular ganglion cell inner plexiform layer measurements in glaucoma using swept source and spectral domain optical coherence tomography. PLoS One. 2015;10(5):e0125957.
42. Leung CK, Weinreb RN. Anterior chamber angle imaging with optical coherence tomography. Eye (Lond). 2011;25(3):261–7.
43. Sakata LM, Lavanya R, Friedman DS, Aung HT, Seah SK, Foster PJ, et al. Assessment of the scleral spur in anterior segment optical coherence tomography images. Arch Ophthalmol. 2008;126(2):181–5.
44. Liu S, Li H, Dorairaj S, Cheung CY, Rousso J, Liebmann J, et al. Assessment of scleral spur visibility with anterior segment optical coherence tomography. J Glaucoma. 2010;19(2):132–5.
45. McKee H, Ye C, Yu M, Liu S, Lam DS, Leung CK. Anterior chamber angle imaging with swept-source optical coherence tomography: detecting the scleral spur, Schwalbe's Line, and Schlemm's Canal. J Glaucoma. 2013;22(6):468–72.
46. Liu S, Yu M, Ye C, Lam DS, Leung CK. Anterior chamber angle imaging with swept-source optical coherence tomography: an investigation on variability of angle measurement. Invest Ophthalmol Vis Sci. 2011;52(12):8598–603.
47. Lai I, Mak H, Lai G, Yu M, Lam DS, Leung CK. Anterior chamber angle imaging with swept-source optical coherence tomography: measuring peripheral anterior synechia in glaucoma. Ophthalmology. 2013;120(6):1144–9.
48. Mishima K, Tomidokoro A, Suramethakul P, Mataki N, Kurita N, Mayama C, et al. Iridotrabecular contact observed using anterior segment three-dimensional OCT in eyes with a shallow peripheral anterior chamber. Invest Ophthalmol Vis Sci. 2013;54(7):4628–35.
49. Mak H, Xu G, Leung CK. Imaging the iris with swept-source optical coherence tomography: relationship between iris volume and primary angle closure. Ophthalmology. 2013;120(12):2517–24.

Index

A
Age-related macular degeneration (AMD)
  classification, 57
  dry, 57
  early and intermediate, 58–60
  late, 61–63
  non-neovascular, 28–29
  wet, 57
Anterior segment optical coherence tomography (AS-OCT), 172

B
Basal laminar drusen (cuticular drusen), 59

C
Capillary layer, retina
  deep, 38
  superficial, 38
Capillary plexus
  deep, 129–132
  superficial, 129
Central serous chorioretinopathy (CSC), 159–160
Central serous choroidal retinopathy (CSCR)
  choroidal neovascularization, 30
  FA, 30
  ICGA, 30
  SS-OCTA imaging, 30–33
Choriocapillaris, 39–40
Choroid
  imaging, 171
  thickness, retinal vein occlusion, 133
Choroidal hemangioma, circumscribed, 146–147
Choroidal melanoma, 143–144
Choroidal metastasis, 145
Choroidal neovascularization (CNV), 30, 69, 155
Choroidal neovascular membranes (CNVMs), 10
Choroidal nevi, 35
  amelanotic, 137
  benefit, 135
  en face segmentation, 135, 136
  granularity, 135
  melanotic, 136
  prevalence, 135
  with risk factors for growth, 141–142
  SS-OCT, 139–140
Circumscribed choroidal hemangioma, 146–147

D
Deep capillary plexus (DCP), 10
Diabetic macular edema (DME)
  blood-retinal barrier (BRB), 115
  classification, 115–116
  medical treatment, 123–124
  molecular mechanisms, 115
  photocoagulation treatment, 117–122
  vitrectomy, 125–126
Dome-shaped macula (DSM), 70

E
En face optical coherence tomography, 12
En face swept source OCT study
  neovascular age-related macular degeneration, 49–52
  type 1 neovascularization, 50
  type 2 neovascularization, 51
Enhanced vitreous visualization (EVV), 10, 13
Epiretinal membranes
  choroid alteration, 90–92
  classification, 87–89
  and macular hole classification guides, 88
  and non-full-thickness macular holes, 91
  and non-full-thickness macular holes secondary to retinal diseases, 92
  swept source OCT angiography, 93–95

F
Fluorescein angiography (FA), 10, 27
Fourier-domain optical coherence tomography (FD-OCT), 1, 4
Fundus guided acquisition™ (FGA), 10

G
Geographic atrophy (GA), 28, 29, 63
Glaucoma
  anterior segment imaging, 172–173
  posterior segment imaging, 167–172

H
Hood Report, 10, 16

I
Idiopathic vitreomacular traction syndrome, 80
Inner plexiform layer/inner nuclear layer border (IPL/INL), 10
Internal limiting membrane (ILM), 10
Intrachoroidal cavitation (ICC), 70

© Springer International Publishing AG 2017
Z. Michalewska, J. Nawrocki (eds.), *Atlas of Swept Source Optical Coherence Tomography*,
DOI 10.1007/978-3-319-49840-9

Intraocular inflammation
choroidal neovascularization (CNV), 155
uveitic macular edema, 151–154
uveitis
choroid assessment, 157
retinal changes in patients with, 156–157
vitreomacular interface abnormalities in patients with, 150
Intraocular lens (IOL)
glistenings, 21
and macular hole, 106
phacoemulsification and, 105
Intraocular tumors
choroidal hemangioma, circumscribed, 146–147
choroidal melanoma, 143–144
choroidal metastasis, 145
choroidal nevus, 139–140
with risk factors for growth, 141–142
Inverted internal limiting membrane flap technique, macular hole, 105

L
Lamina cribrosa imaging, 168–170

M
Macular edema and uveitis
cystoid macular edema, 152
diffuse macular thickening, 151
subretinal fluid, 153–154
Macular hole. *See also* Epiretinal membranes
classification guides, 88
with coexisting drusen before surgery, 106
formation, 98–104
fovea architecture recovery, 105
inverted ILM flap technique, 105
myopic macular hole retinal detachment, 105, 106
non-full-thickness, 91
preoperative view, 103
retinal detachment, 68
secondary to retinal diseases, non-full-thickness, 92
spontaneous closure, 100
SS-OCT angiography, 108–112
stage 2, 109
stage 3, 109
stage 4, 110
surgical closure, 101–104
U-shape closure, 102
Macular neuroretinopathy, acute, 162
Macular telangiectasia, bilateral, 165
Michelson interferometer design, 3
Morning glory syndrome, 162
Myopia
high, 66, 70
LC defects, 169
mild, 105
pathological (*see* Pathological myopia)
Myopic traction maculopathy (MTM)
macular hole retinal detachment, 68
retinal schisis, 67–68

N
Neovascular age-related macular degeneration (nvAMD)
definition, 61
en face swept source OCT study, 49–52
SS-OCT angiography, 53–55
type 1, 61, 62
type 2, 61, 62
type 3, 62
Non-neovascular age-related macular degeneration
advanced dry AMD, 29
geographic atrophy (GA), 28

O
OCT angiography (OCT-A), 10, 14
OCTARA™, 10
Optic disc edema, 163

P
Pathological myopia
choroidal neovascularization, 69
dome-shaped macula, 70
intrachoroidal cavitation, 70
myopic traction maculopathy, 67–68
posterior staphyloma, 66
prevalence, 65
Peripheral anterior synechiae (PAS), 172
Pigment epithelium detachment (PED), 60
Polypoidal choroidal vasculopathy (PCV), 34, 161
Proliferative diabetic retinopathy (PDR), 18
Pseudodrusen, SS-OCT
choroidal correlations, 48
classification, 43–47
clinical implications, 45–47
dot, 43
ribbon, 43

R
Reticular pseudodrusen (RPD), 59
Retinal angiomatous proliferation (RAP), 62
Retinal artery occlusion (RAO), 27
Retinal-choroidal anastomosis (RCA), 62
Retinal layers, 9
Retinal nerve fiber layer (RNFL), 9, 172
Retinal pigment epithelium atrophy, 156
Retinal vasculature
choriocapillaris, 39–40
deep capillary layer, 38
outer retina, 39
superficial capillary layer, 38
vitreous, 41
Retinal vein occlusion (RVO)
branch, 24, 25
central, 24, 26
choroidal thickness, 133
fluorescein angiography, 24
foveal vascular zone enlargement, 24
internal limiting membrane (ILM), 25
OCTA orthogonal view, 26
SS-OCTA, 130–132
vasculature, 129
Retina pigment epithelium (RPE), 2
Retinitis pigmentosa, 164

S
Signal-to-noise ratio (SNR), 2
SMARTTrack™, 10
Spectral-domain optical coherence tomography (SD-OCT), 1–2

finite pixels, different wavelength light, 5
retinal images, 7
signal roll-off, 5
Staphyloma, posterior, 66
Stargardt disease, 164
Subfoveal melanoma after proton beam therapy, 163
Superficial capillary plexus (SCP), 10
Superluminescent diode (SLD), 2
Swept source optical coherence tomography (SS-OCT), 1–3
after aflibercept treatment, neovascular AMD, 55
development, 3
en face mode (*see En face* swept source OCT study)
glistenings, IOL, 21
human retina angiography, 14
1 μm wavelength, 7
myopic macular hole repair, 20
retinal images, 7
signal roll-off, 6
silicone oil placement, 19
vs. spectral domain, 12
subhyaloid hemorrhage, PDR, 18
wide-field, 11
Swept source optical coherence tomography angiography (SS-OCTA)
central serous choroidal retinopathy, 30–33
choroidal nevi, 35
epiretinal membranes, 93–95
hardware components, 23
macular hole, 108–112
neovascular age-related macular degeneration, 53–55
non-neovascular age-related macular degeneration, 28–29
polypoidal choroidal vasculopathy, 34
software components, 23
vascular occlusions, 24–27
vitreomacular traction syndrome, 82–84

T
Time-domain optical coherence tomography (TD-OCT), 1
Topcon DRI Triton, 9
Triton optical coherence tomography, 9
advantages, 18
anterior segment images, 17
en face mode, 10
wide combination report, 15

U
Uveitis
choroid assessment, 157
and macular edema
cystoid macular edema, 152
diffuse macular thickening, 151
subretinal fluid, 153–154
retinal changes in patients with, 156–157
vitreomacular interface abnormalities in patients with, 150

V
Variable interscan time analysis (VISTA) algorithm, 23–24
Vascular occlusions, SS-OCTA
retinal artery occlusion, 27
retina vein occlusion, 24–26
Vein occlusion
choroid, 133
deep capillary plexus, 129–132
retinal (*see* Retinal vein occlusion)
superficial capillary plexus, 129
Vertical-cavity surface-emitting laser (VCSEL), 23
Vitrectomy and diabetic macular edema, 125–126
Vitreomacular traction syndrome (VMT)
B-scan, 77
classification, 73–74
clinical appearance, 75–79
with epiretinal membrane, 79
focal vitreomacular traction, 75
idiopathic, 80
swept source OCT angiography, 82–84
three-dimensional imaging, 76
treatment, 81
Vitreous body, 41